“Solvothermal Synthesis and Characterisation of Novel Gallium-Sulphide Compounds”

Maria Lucia Romero Perez

Thesis Submitted for the Degree of Doctor of Philosophy

Heriot-Watt University

Department of Chemistry

April 2010

Abstract

In this thesis, novel supertetrahedral gallium-sulphide compounds were synthesised under solvothermal conditions. Three-dimensional frameworks, which are analogous to previously reported structures, along with a large number of new hybrid supertetrahedral compounds were produced. Inorganic three-dimensional structures were obtained using dimethylamine as a template/solvent. In total, four different inorganic frameworks were prepared. They consist of double interpenetrated diamond lattices, containing diverse building units. The first two are formed of $[Ga_{10}S_{20}]^{10-}$ and $[Ga_{10}S_{19}O]^{10-}$ respectively, while the other two consist of alternating clusters of $[M_4Ga_{16}S_{35}]^{14-}$ (M= Zn or Co) and $[Ga_{10}S_{20}]^{10-}$. To date, only one type of hybrid gallium-sulphide supertetrahedral cluster with stoichiometry $[Ga_4S_6L_4]$ (L= N-coordinated amine) has been described in the literature. The hybrid gallium-sulphide supertetrahedral structures, reported in Chapter 4, are based on clusters of general stoichiometry $[Ga_{10}S_{16}L_4]^{2-}$. It is shown that the combination of mono and polydentate pyridine ligands leads to formation of multi-functionalised clusters. These multi-functionalised clusters are connected through the ligands, building extended structures. In most cases, the structures are formed by interpenetrated elements such as quadruple-stranted helical nano-tubes. These nano-tubes are extremely rare and consist of organically functionalised supertetrahedra connected through 1,2-di(4-pyridyl)ethylene, $[C_2H_8N]_2[Ga_{10}S_{16}(N_2C_{12}H_{12})(NC_2H_7)_2]$. In addition, the structure is non-centrosymmetric and a chiral solid. Other extended structures consist of two-dimensional covalent organic-inorganic networks such as $[C_7H_{10}N]_2[Ga_{10}S_{16}(NC_7H_9)(N_2C_{12}H_{10})_{3/2}]$, containing layers with a honey-comb topology. Also, $[C_5H_6N]_3[Ga_{10}S_{16}(OH)(N_2C_{13}H_{14})]$ is formed by supertetrahedral composite layers consist of a corrugated two-dimensional network with a (4, 4) topology. Structures containing other building blocks have also been produced. These contain one-dimensional chains which are based on edge-sharing GaS_4 tetrahedra along with a two-dimensional structure consisting of neutral hybrid layers of $[(C_6H_{14}N_2)_4Ga_6S_9]$. The materials have been characterised by powder and single crystal X-ray diffraction, elemental analysis, thermogravimetry and FTIR. The optical properties have been studied using UV-Vis Diffuse Reflectance Spectroscopy. Ion-exchange experiments and BET surface area/pore size distribution analysis have been carried out to determine the ion-exchange capacity for the three-dimensional structure.

Acknowledgements

I would like to express my gratitude to Dr Paz Vaqueiro for the opportunity of completing this PhD, her commitment and dedication to research and science; without her help this project could not be possible. Also, I would like to thank Dr Valeria Arrighi for her support and EPSRC for supporting me through a studentship.

I would like to thank the staff at Heriot-Watt University for their assistance and advice during these years, especially to Dr Georgina Rosair, Mrs Christina Graham, Mrs Mary Pratt and Mr John MacConnachie, Mr Alan Burton, Mr Paul Allan, Mr Iain Drummond and Mr Tom Doherty.

I would like to acknowledge all the members of the Solid State Group and the other PhD colleagues at Heriot-Watt University because we have supported, understood and helped each other creating a more pleasing environment.

I thank all people I have been so lucky to meet at Edinburgh to share my experiences and friendship (Elena, Isaela, Victor, Amalia, Camino, Veronica, Rafa, Angel, Iwona, Alberto, Rachel, Robert, Michaela, Fernando and to those that always have time for a coffee or a smile).

I would like to specially thank my friends and colleagues Miss Patricia Leyva Bailen and Mr Santiago Gomez Quero, because they have been by my side all the time and I know that they will be there for long.

Finally, I would like to dedicate this thesis to my family and friends in Spain because of their unconditional support and love despite the distance and the time. And especially, I dedicate this thesis to my partner Mr Charis Niotis because of his love, support, patience and understanding.

M. Lucia Romero

DECLARATION STATEMENT

ACADEMIC REGISTRY
Research Thesis Submission

Name*:*	Maria Lucia Romero Perez		
School/PGI:	Chemistry/EPS		
Version: *(i.e. First, Resubmission, Final)*	Final	Degree Sought (Award **and** Subject area)	PhD Chemistry

Declaration

In accordance with the appropriate regulations I hereby submit my thesis and I declare that:

1) the thesis embodies the results of my own work and has been composed by myself
2) where appropriate, I have made acknowledgement of the work of others and have made reference to work carried out in collaboration with other persons
3) the thesis is the correct version of the thesis for submission and is the same version as any electronic versions submitted*.
4) my thesis for the award referred to, deposited in the Heriot-Watt University Library, should be made available for loan or photocopying and be available via the Institutional Repository, subject to such conditions as the Librarian may require
5) I understand that as a student of the University I am required to abide by the Regulations of the University and to conform to its discipline.

* *Please note that it is the responsibility of the candidate to ensure that the correct version of the thesis is submitted.*

Signature of Candidate*:*		Date:	

Submission

Submitted By *(name in capitals):*	
Signature of Individual Submitting:	
Date Submitted:	

For Completion in Academic Registry

Received in the Academic Registry by *(name in capitals):*			
Method of Submission *(Handed in to Academic Registry; posted through internal/external mail):*			
*E-thesis Submitted (**mandatory for final theses from January 2009)***			
Signature:		Date:	

Table of Contents

Chapter 5: Non-Supertetrahedral gallium-sulphide structures

Chapter 6: Conclusions and Further work

List of Publications by the Candidate

- P. Vaqueiro, M. L. Romero, "Three-dimensional gallium sulphide open frameworks", *J. Phy. Chem. Of Solids*, **68**, 5-6, (2007).

- P. Vaqueiro, M. L. Romero, "Catena-Poly[piperaziniumdi-mu-sulfido-gallium]", *Acta Cryst. E*, **63**, M1700-U1094, (2007).

- P. Vaqueiro, M. L. Romero. "$[Ga_{10}S_{16}(NC_7H_9)_4]^{2-}$: a hybrid supertetrahedral nanocluster", *Chem. Comm.,* 3282-3284 (2007).

- P. Vaqueiro; M. L. Romero, "Gallium-sulfide supertetrahedral clusters as building blocks of covalent organic-inorganic networks", *J. Am. Chem. Soc*., **130**, 9630-9632 (2008).

- P. Vaqueiro; M. L. Romero, "Zero-Dimensional Units of Ligand-Bridged Gallium-Sulfide Supertetrahedra", *Inorg. Chem*., **48**, 810-812 (2009).

- P. Vaqueiro; M. L. Romero, "Organically-functionalised supertetrahedra as building blocks for hybrid materials", *Mater. Res. Soc. Symp. Proc.*, **1148E**, 1148-PP10-07 (2009).

- P. Vaqueiro; M. L. Romero; B. C. Rowan and B. S. Richards, "Arrays of Chiral Nanotubes and a Layered Coordination Polymer Containing Gallium-Sulfide Supertetrahedral Clusters", *Chem. Eur. J*., DOI: 10.1002/chem.200903425 (2010).

Chapter 1: Introduction

1.1. Background

During the last century solid-state chemistry has an exponential development closely aligned with emerging technologies. New materials with interesting properties have been applied in diverse fields with a high demand. Some of the most relevant highlights have been: (i) the use of semiconductors to produce apparatus for controlling electric current [1] such as transistors (which is the key active component in the majority of all modern electronics) and (ii) the development of superconductor materials [2,3], which constitute the most powerful electromagnets known and form integral parts of precision instruments (such as NMR, spectrometers and SQUID) applied to the physical characterisation of materials.

The approaches in the synthesis of solid state materials include: (a) the preparation of new materials, exploring different chemical systems directed towards the synthesis, and (b) the design of materials with specific properties. The techniques employed in solid state synthesis [4] include (i) high temperature methods, involving fluxes, melts and molten salts which cover the temperature window between 573-1273 K; (ii) soft reaction conditions, which are based on the use of solutions and suspensions to favour the diffusion between reagents and reduce the temperatures required. In solvothermal and hydrothermal methods, the thermodynamic control competes with the kinetic factors, and metastable phases can be produced in addition to stable ones. As a consequence, a large number of different compounds can be obtained, such as nanocrystalline materials [5], inter-metallic compounds [6] and a variety of open-framework materials [7,8]. Hydrothermal and solvothermal methods are the most employed techniques due to their versatility and potential for the production of new materials.

In the literature, there is a large interest in producing porous solid materials due to their multiple applications in catalysis, sorption, gas sensing, optics and photovoltaic materials. Zeolites [9] were the first family of compounds which were discovered with these characteristics. These materials are synthetically produced using the hydrothermal method. The development of analogous compounds resulted in the synthesis of alumino- and gallophosphates [10], and more recently, in the production of hybrid metal-organic materials [11]. The majority of these compounds are based on oxygen frameworks. In 1989, Berard and co-workers [12] extended the synthesis of zeolites to non-oxide inorganic frameworks. Compounds with chalcogenides and other main group elements are remarkable for their variable bonding characteristics, which range

from ionic sulphides to the polymeric extended structures. Their bonding capability leads to a wide range of chemical and physical characteristics and as a consequence, into a variety of multifunctional materials which include open-framework metal chalcogenides. These materials differ from the traditional open-framework compounds in two aspects: (i) whilst zeolites, microporous oxides and metal oxides are intrinsic electrical insulators in their nature, porous metal chalcogenides present semiconducting behaviour [13]; (ii) chalcogenide frameworks have higher anionic framework polarizability than zeolites [14] and the migration of mobile cations in the open-framework is facilitated, which is quite desirable for certain applications such as ion-exchange.

The design of metal-chalcogenide favour the formation of clusters and the crystallisation of modular solids [15] under solvothermal conditions. This approach constitutes a challenge in the design of porous materials, which is initially based on atoms or small units. The exploration of new systems capable to produce this type of materials is very attractive, offers boundless applications and is still in an early stage. This thesis will explore the synthesis of new gallium-sulphide materials, using solvothermal synthesis.

1.2. Solvothermal synthesis

Solvothermal synthesis is typically carried out in the temperature range of 393-533 K in a closed system under autogeneous pressure. The conditions in these systems are mainly controlled by two sets of parameters: (i) thermodynamic (pressure and temperature) and (ii) chemical. The combination of both can produce a system with supercritical conditions. Organic and/or inorganic species are part of the system, acting as precursors and/or as templates and supporting the crystallization process. The reactions usually give rise to non-equilibrium crystallization states, promoting metastable kinetic phases rather than the thermodynamic phases [16] and small changes in one or more of the reaction variables (time, temperature, pH, stoichiometry or template) can have a profound influence on the resulting product. Hence, quantitative prediction of the final products is not often possible and guidelines for the design of new compounds are based on the experience, the geometric constraints of the template and/or the coordination requirements of the cations employed.

1.2.1. Parameters

Although solvothermal synthesis is considered as a 'black box' due to the impossibility of an accurate prediction of the final product, there are some factors which can be adjusted, favouring certain conditions:

- Solvent: this is the reaction media. A liquid organic compound is used in solvothermal reactions and water for hydrothermal reactions.
- Template: this is usually an organic molecule with functional groups and acid/base properties. Several roles have been associated with it such as a counter-ion, space filler and directing-agent. The selection of a template depends on the following physical properties: size, shape and distribution of the charge. Size and shape will influence the dimensions of the potential cavities, distance between layers in two-dimensional structures or the packing in the final structure. The type of interactions establishes the neutral balance in the structure and the most favourable packing.
- pH: the formation of certain species is related to the exact control of the pH; for example the precipitation of thiogermannates and thiostannates from aqueous solution [17]. Therefore, the production of specific types of building units may be suitable under a certain range of the pH. This can be regulated by the solvent or the template. For example, it was found that at low pH amines are hydrated and exhibit different p*Ka*, aliphatic diamines lie between $7< pK_a <10$ while cyclic diamines have $4< pK_a <6$ [18].
- Time and Temperature: solvothermal synthesis temperatures lie in the range 373-573 K, depending on the procedure. The physical properties of the reaction vessel materials usually limit the temperature i.e. Teflon. A Teflon vessel starts deforming at *ca.* 473 K while Pyrex tubes can be heated maximum at *ca.* 800 K and silica tubes at *ca.* 1200 K in extreme conditions. The stability of the template has to be considered as well, and under certain conditions the template can be transformed and produce unexpected species or even be pyrolised.

The time of reaction varies from few hours to weeks. Generally, the crystallisation process of the different types of open frameworks can take short times especially for light structures with large cavities. Short reaction times could also result in incomplete nucleation of the inorganic structures and therefore, collapse of the structure of the final product. On the other hand, longer times favour the formation of dense phases and interpenetration [19-21].

Exploring a large number of variables is time consuming and expensive when the reaction is carried out in a single pot. Combinatorial and parallel synthesis [22] (widely used in drug discovery by pharmaceutical companies) followed by high-throughput

structural determination have become a widely used methodology. These methods allow the researcher to carry out a large amount of reactions at the same time in small reaction chambers. Materials with optimum composition and/or properties are scaled up to quantities that are sufficient for their characterisation and after, the identified products are collected in libraries for further use. This combinatorial technology has been applied to the discovery and optimisation of superconducting [23], magneto-resistive [24], ferroelectric [25], dielectric and luminescent materials [26]. The synthesis of zeolites has also been carried out successfully using multi-autoclaves [27,28]. This type of synthesis can be extended to other materials produced by hydrothermal and solvothermal methods.

1.2.2. Mechanism

Solvothermal reaction parameters have an intense influence on the reaction product. Consequently, quantitative predictions of reaction products are generally not possible. It is known that there is a synergism between the main inorganic components and the template that makes an important contribution in controlling the nucleation and growth of the inorganic frameworks. Several authors carried out different experiments to explain the obscure process involved in the reaction pot, with the hope of finding the guidelines for future design of three-dimensional structures. Several hypotheses were proposed to rationalise the process in the synthesis of zeolites. The first one [29] proposes the formation of a precursor gel-state (which includes all the reaction components) and from which nucleation takes place. The second hypothesis [30,31] considers the diffusion of all the reagents in the liquid phase to initiate the reaction. Additionally, David and Lobo [32] proposed different roles of the template according to the flexibility and geometry of the potential structure. If the structure is flexible, the template acts as space-filling agent and when the shape of the template and the framework are correlated, the template is a structure-directing agent.

The analysis of the interactions between the parameters in the synthesis and the structural characteristics of the family of compounds ULM-n resulted in a new hypothesised mechanism [33]. It considers that the reaction is governed by different elements: first there should be a match between the charge of the template and the oligomeric building species (which would control the size and shape of the building unit of the structure). Then, the cation-building unit pair (which is an intermediate, neutral, metastable phase) facilitates the precipitation of the solid whose structure presents the lowest lattice energy, satisfying constraints imposed by the size, shape and plasticity of

the pair. This hypothesis is supported by experimental data obtained by *in situ* NMR [34-36] and EDXRD [37]. Regardless of these hypotheses, all the authors reach the same conclusion: the template is, in one way or another, the driving and limiting factor in the synthesis.

When the crystallisation of a three-dimensional framework is achieved the template is usually located in the cavities to stabilise the structure. Its charge induces strong electrostatic interactions with the framework and makes its extraction after the synthesis difficult, reducing the number of potential applications. In some occasions, the template/solvent molecules are small molecules and do not fill the cavities; therefore, once crystallization has taken place and as soon as the dimension of the cages becomes a little larger, the cavities are usually filled by one or more interpenetrated sub-networks [38]. This phenomenon could represent an impediment on the design of large microporous materials. Nevertheless, there are a large amount of interpenetrated structure which present interesting properties [39,40].

1.3. Structures based on metal-chalcogenide supertetrahedral clusters

1.3.1. Types of metal chalcogenide clusters

The structure of clusters is influenced by the geometry and reactivity of their components. Tetrahedral coordination is one of the most common coordination spheres that metal or semimetal chalcogenides usually present. It provides adequate functionality and stereochemistry that allows metal or semimetal chalcogenides to be perfect candidates to produce networks, as zeolites and aluminophosphates which are formed from secondary building units (SBU) sharing corners and forming.

Previous classifications [41] divided the family of tetrahedral clusters into three types: Regular supertetrahedral clusters, Penta-supertetrahedral clusters and Capped clusters. However, after a large number of recent structures were found, it was difficult to classify them using this system. It has been more convenient to separate two main types of clusters depending on if organic moieties that form part of the cluster. The modified classification is shown in Figure 1.1:

Inorganic Supertetrahedral Clusters

- Regular Supertetrahedral Clusters: regular supertetrahedral units are denoted as Tn, where T is the tetrahedral fragment and n is the number of tetrahedra along the edge (Figure 1.2). These clusters are regular tetrahedrally shaped fragments of the cubic ZnS-type lattice.

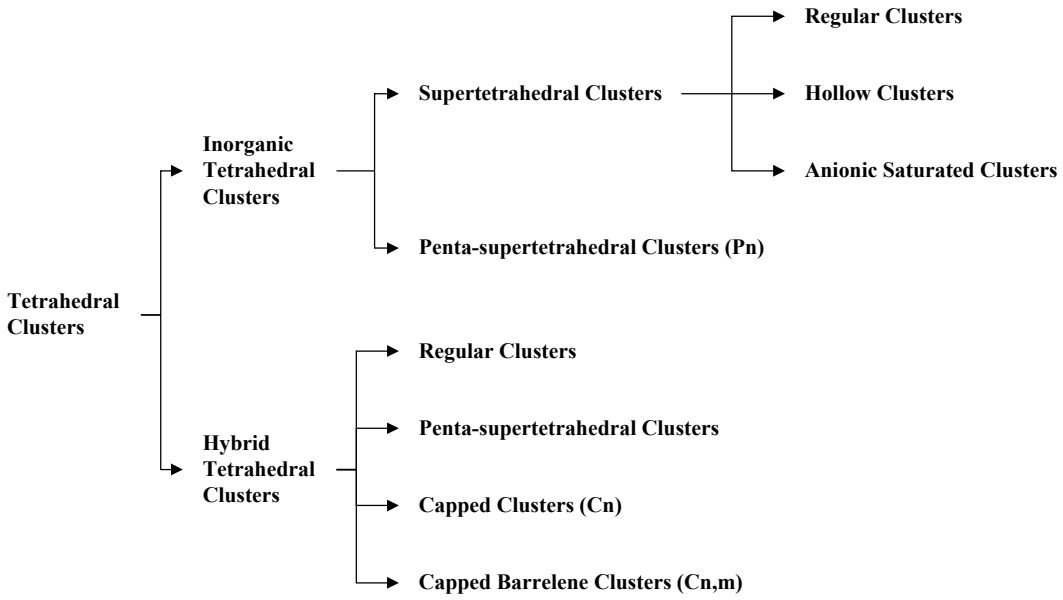

Figure 1.1. Classification of Tetrahedral metal chalcogenide clusters.

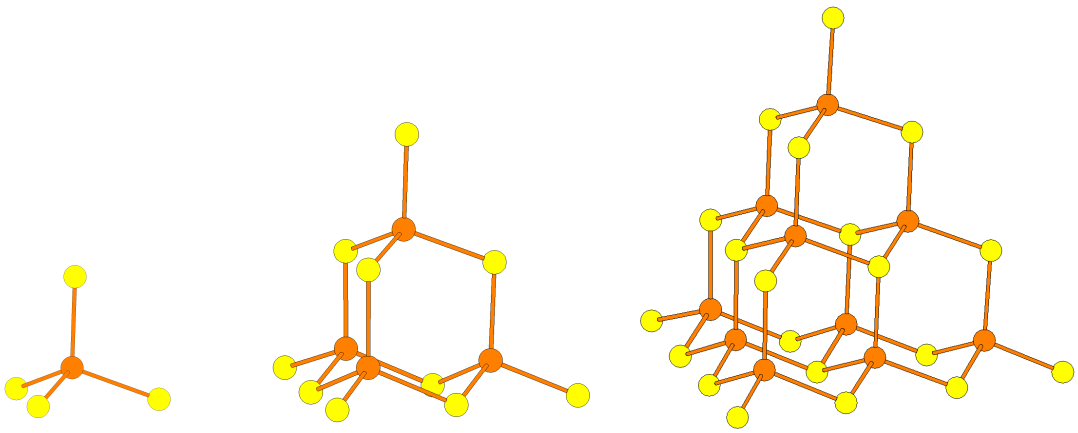

Figure 1.2. View of supertetrahedral clusters. From left to right, T1, T2 and T3; chalcogenide atoms are shown in yellow and metal atoms in orange.

Supertetrahedral chalcogenide clusters have been produced with metal cations from groups 12-14 (Zn, Cd, Ge, In, Ga and Sn) and the insertion of transition metals from the first row (Mn, Co, Fe and Cu) has been achieved. The dimensionality of the supertetrahedral unit is related to the charge of the elements that constitute the cluster. They follow Pauling's electrostatic rule and the bond valence of each atom can be precisely determined following the empirical model proposed by Brown [42] for the individual bond length. Therefore, the positions of the atoms and their coordination are in agreement with the charge they can be surrounded by. Inorganic T2 clusters usually involve M^{4+} cations because they present a localised high density of charge and the formation of a higher cluster implies a more homogeneous distribution of charge. T3

clusters are exclusively formed by M^{3+} (generally In^{3+} or/and Ga^{3+}). T4 clusters are caused by the combination of M^{2+} and M^{3+} cations and T5 clusters are usually caused by the insertion of monovalent cations. At the moment, the maximum size found for supertetrahedral clusters is T5.

- Hollow Supertetrahedral Clusters: (Figure 1.3): these clusters consist of regular supertetrahedral clusters with vacant positions. These vacancies are frequently found in clusters of high dimensionality. For example, $[In_{22}S_{36}]^{6-}$ units are constituted by T5 clusters where the S atom that should occupy the central core is missing [43]. In extreme cases the super-supertetrahedral clusters are formed by supertetrahedra that are connected forming a supertetrahedral unit and due to geometrical reasons, a large cavity is produced in the center of the unit. The only inorganic cluster reported to date is the $[Cd_{16}In_{64}S_{134}]^{44-}$ a T4 cluster formed by four $[Cd_4In_{16}S_{37}]^{18-}$ T2 clusters [44].

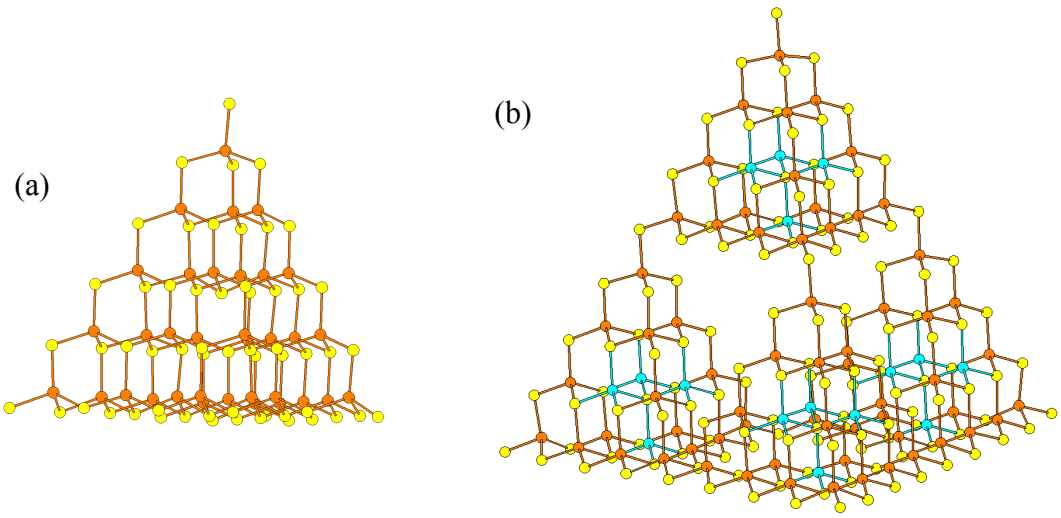

Figure 1.3. Ball-stick diagrams of supertetrahedral clusters. (a) Coreless T5 cluster $[In_{22}S_{36}]^{6-}$ and (b) super-supertetrahedral cluster $[Cd_{16}In_{64}S_{134}]^{44-}$. In atoms are shown in orange, S in yellow and Cd in blue.

- Anionic saturated clusters: these are regular clusters containing additional anions within the unit. The dimensions of a supertetrahedral unit are related to the internal charge balance between cations and anions, generally the cluster is negatively charged and cations has high valence such as M^{4+} to produce T2 clusters. Additional anions within the cluster can compensate an excess of positive charge and increase the size of the cluster. The most common example is the case of the $[Sn_{10}S_{20}O_4]^{8-}$ cluster (Figure 1.4), which is found in several compounds [45-47]. Sn^{4+} usually form T2 clusters in

combination with S^{2-}, but the presence of four O^{2-} atoms reduces the positive charge of the unit and the size of the cluster increases up to T3.

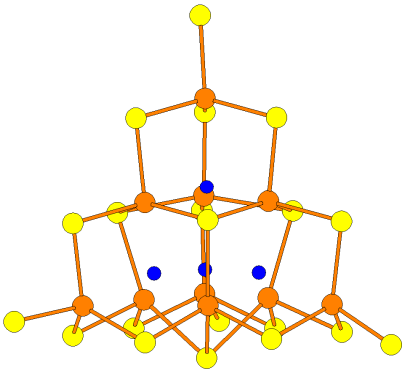

Figure 1.4. Ball-stick representation of $[Sn_{10}S_{20}O_4]^{8-}$. S atoms are shown in yellow, Sn in orange and O in blue.

- Penta-supertetrahedral Clusters (Figure 1.5): these are denoted by Pn. These clusters can be described as fragments of Tn linked together to form a different unit building. The core is formed by an anti-Tn cluster, which is defined as a Tn cluster where the cationic and anionic positions are exchanged. The faces of the anti-cluster are fused to four regular Tn fragments (n indicates the same order in all the fragments). Then, a P1 cluster consists of the merging of four T1 clusters, with an anti-T1 in the centre. Examples of this type of units are the compounds of formula $[M_4Sn_4S_{17}]^{10-}$ (M= Mn, Fe, Co, Zn) [48]. The maximum dimensionality in this type of clusters is P2, for example $[Li_4In_{22}S_{44}]^{18-}$ [49], which can be described as four merged $[In_4S_{10}]^{8-}$ T2 clusters connected through an inverted T2 cluster of Li^+, In^{3+} and S^{2-}.

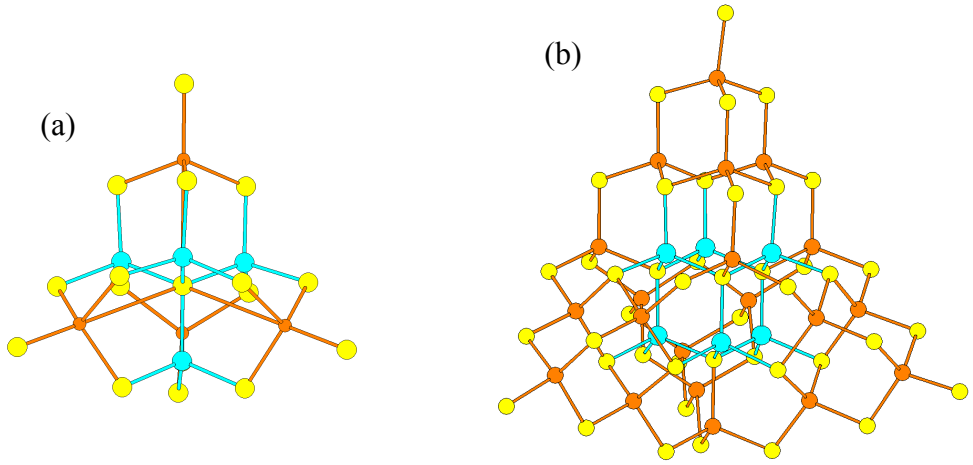

Figure 1.5. Ball-stick diagrams of penta-supertetrahedral clusters: (a) example of P1 $[M_4Sn_4S_{17}]^{10-}$ (M= Mn, Fe, Co, Zn). (b) P2 cluster $[Li_4In_{22}S_{44}]^{18-}$. S atoms are shown in yellow, Sn and In in orange and metal atoms (M and Li) in blue.

Hybrid Tetrahedral Clusters

- Hybrid regular clusters: hybrid clusters are all the supertetrahedral clusters which contain organic molecules covalently bonded to the cluster. The first hybrid tetrahedral compound [50] (Figure 1.6) was produced using thiolates (HS-R) as source of sulphur instead of elemental S (usually employed in the synthesis of inorganic supertetrahedral clusters). It consists of discrete $[Co_4S_{10}C_{60}H_{50}]^{2-}$ T2 clusters charge balanced by tetramethylammonium cations. Other hybrid T2 clusters were synthesised with Zn, Cd and Fe [51,52]. These clusters can reach the same dimensions as the inorganic regular supertetrahedral clusters by the mixture of transition metals from the first row [53,54].

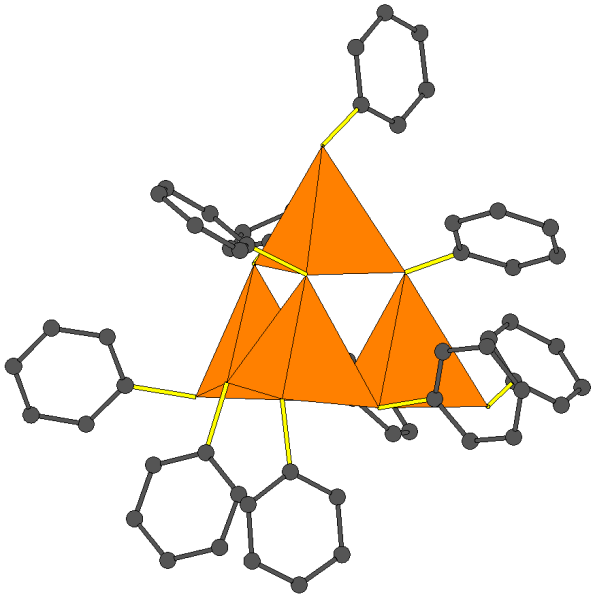

Figure 1.6. Polyhedral representation of $[Co_4S_{10}C_{60}H_{50}]^{2-}$ hybrid cluster. CoS_4 tetrahedra are shown in orange and C atoms in grey. H atoms are omitted for clarity.

The capacity of bonding is related to the acidity of the metal which forms the clusters. A mixture of ligands produces the compound $[Cu_9In_{10}S_9(SC_2H_5)(PPh_3)_3]$ [55]. It consists of tetrahedral clusters, where triphenylphosphine (PPh_3) ligands are covalently-bonded to Cu^+ in three of the corner positions (Figure 1.7). Ethyl molecules shield the core and the corners of the supertetrahedra are coordinated by triphenylphosphine (PPh_3) ligands, showing there are other effective ligands apart from thiolates.

Pyridine derivatives have also been found to be effective ligands for the synthesis of hybrid materials. Initial attempts used a mixture of thiophenyl groups and pyridyl ligands. While thiophenyl groups shield the faces of the clusters, pyridyl ligands substitute the S atoms in the corners (Figure 1.8). The employment of polydentate

ligands allows different coordination positions which may favour connections between clusters and therefore, the probability of building extended structures.

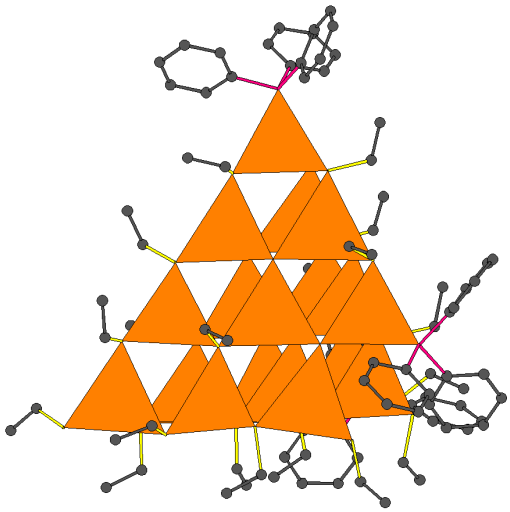

Figure 1.7. Polyhedral representation of $[Cu_9In_{10}S_9(SC_2H_5)(PPh_3)_3]$ hybrid capped supertetrahedral cluster. MS_4 and MS_3P clusters are shown in orange, S-C bonds in yellow, Cu-P bonds in pink and C atoms in grey. H atoms are omitted for clarity.

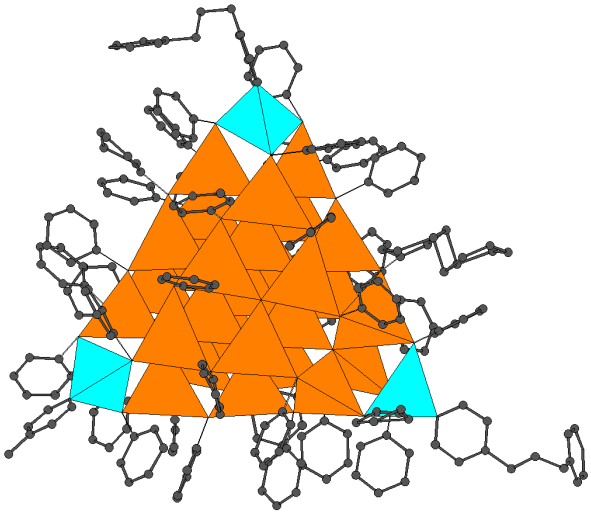

Figure 1.8. Polyhedral representation of Hybrid T5 with four covalent-bonded TMDPyr molecules. CdS_4 tetrahedra are shown in orange, CdS_3N tetrahedra in blue and C atoms in grey. H atoms are omitted for clarity.

However, the coordination of tetrahedral clusters can be oriented and only take place in the corners of the cluster, producing hybrid clusters which surface is not shielded by organic molecules. This type of cluster has been reported using pyridine ligands and has been observed when Ga^{3+} is used as metal source. The first hybrid cluster consists of $[Ga_4S_6(NC_9H_{15}N_2)]$ discrete units [56]. The unit consists of gallium sulphide T2 cluster, where the four terminal S atoms in the corners are substituted by N

covalent-bonded organic moieties (Figure 1.9). This is a neutral cluster, although the interaction of the organic groups promotes the crystallisation as a solvated covalent crystal.

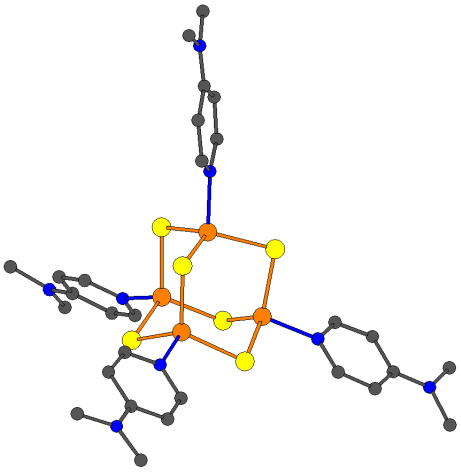

Figure 1.9. Ball-stick representation of $[Ga_4S_6(NC_9H_{15}N_2)]$. Ga atoms are shown in orange, S in yellow, N in blue and C in grey. H atoms have been omitted for clarity.

- Hybrid Penta-supertetrahedral Cluster: these are units analogous to the regular Pn clusters, where n indicates the dimensionality of the cluster. However, the central core is shielded by organic groups. These clusters are usually P_2, for example $[Cd_{17}S_4(SC_6H_5)_{28}]^{2-}$ [57] (Figure 1.10).

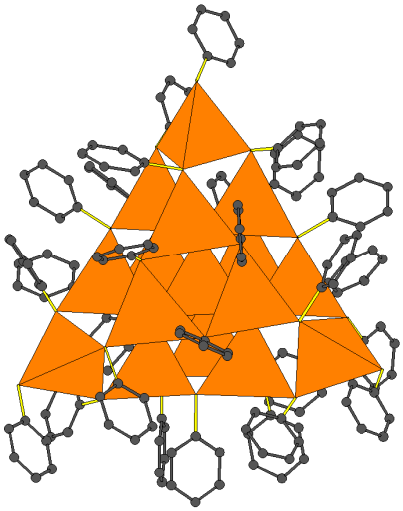

Figure 1.10. Polyhedral representation of the $[Cd_{17}S_4(SC_6H_5)_{28}]^{2-}$ hybrid cluster. CdS_4 tetrahedra are shown in orange and C atoms in grey. H atoms are omitted for clarity.

- Capped cluster: these are denoted by Cn. They consist of regular hybrid clusters in which one or several of the tetrahedra allocated in the corner positions are missing,

producing a truncated supertetrahedron. This type of cluster is exclusively constituted by cadmium-sulphide tetrahedral clusters such as $[S_4Cd_{17}(SPh)_{28}]^{2-}$ [58]. No analogous inorganic capped cluster has been reported to date.

- Capped barrelene clusters: these are denoted by Cn,m. They can be considered as a variation of the Cn series because they present capped corners. The structure of the unit is a consequence of the arrangement of two types of fragments with different ZnS type lattices. The first fragment shows the cubic-ZnS type lattice and has a tetrahedral shape; while the second fragment can be described as fragments of a wurzite-ZnS type lattice with a barrelene-like shape and formula M_4Q_5 (M = Cd or Zn and Q = S or Se). The Cn,m cluster is formed by a main fragment of the cubic-ZnS fragment corresponding to one of the supertetrahedral cluster corners that can be fused to other fragments with cubic-ZnS lattice or one, two or three M_4Q_5 groups (Figure 1.11). Therefore, n indicates the order of the cluster and m the number of M_4Q_5 groups. Cn,m clusters have been prepared with elements from group 10 [59,60].

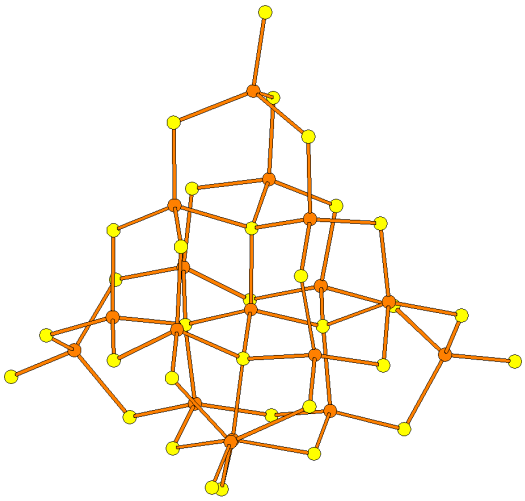

Figure 1.11. Ball-stick representation of the $C_{4,1}$ cluster $[Cd_{17}S_4(SPh)_{28}]^{2-}$. S atoms are shown in yellow and Cd atoms in orange. Phenyl groups are omitted for clarity.

1.3.2. Structures containing inorganic tetrahedral clusters

This family of compounds has been extensively studied to produce porous materials with conducting properties. Materials presenting cavities such as zeolites, microporous oxides and metal oxides are intrinsic insulators due to their composition and so open-frameworks based on chalcogenides are potential candidates to optimize the electric behaviour. Most of the materials have been based on sulphur frameworks [14] because:

- Sulphur has a larger ionic radius than oxide and fluoride ion; the steric impediment to locate large cations is decreased favouring tetrahedral coordination.

- Sulphur shows higher polarisability than the others chalcogenides and the tetrahedra angles should be more flexible [14]. However, M-S-M angles found in tetrahedral materials (90-115°) [61,39] are slightly less flexible when are compared with M-O-M angles in oxide-based silicates (120-180°) [12,62].
- The tetrahedral chalcogenide cluster structures present the same arrangement of atoms as the raw dense matter (sphalerite-type).

The rest of the chalcogenides share the same characteristics as sulphur, although, under the same reaction conditions, the number of metal selenide frameworks analogous to sulphides is less than the sulphur but greater than the tellurium ones.

Discrete units

Before the use of solvothermal synthesis, supertetrahedral chalcogenides species were known [17] from the degradation of condensed materials in alkaline conditions. Ternary gallium and indium chalcogenides $[M_4Q_{10}]^{8-}$ (M = Ga or In and Q = S or Se) [63] consist of discrete T2 clusters, with an ideal Td symmetry, and separated by alkali-metal cations (Na^+ and K^+) (Figure 1.12).

A number of Sn and Ge compounds, containing isolated tetrahedra MQ_4^{4-} (M = Sn or Ge and Q= S or Se) [64-67], larger clusters such as tetrameric adamantane-like units $[M_4Q_{10}]^{4-}$ (M = Sn or Ge and Q= S or Se) [68,69], dimeric T2 clusters $[Ge_8S_{19}]^{6-}$ [70] or isolated T3 clusters $[Sn_{10}O_4S_{20}]^{8-}$ units [70] have been reported. These species condense in different ranges of pH, which are shifted to lower values when compared to the oxoanions.

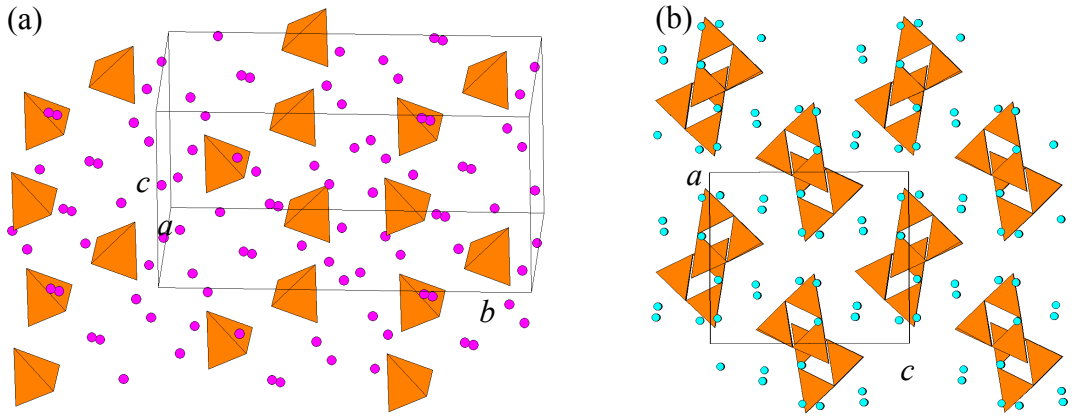

Figure 1.12. Polyhedral representation of compounds containing isolated clusters. (a) $Na_4SnS_4 \cdot (H_2O)_{14}$ and (b)$K_8Ga_4S_{10} \cdot (H_2O)_{15}$. MS_4 tetrahedra are shown in orange, Na^+ cations in pink and K^+ cations in blue. H_2O molecules are omitted for clarity.

Under solvothermal conditions, only discrete indium-sulphide supertetrahedral clusters have been produced [71]. These compounds are formed by arrangement of T2 clusters $[In_4S_{10}H]^{4-}$ in a *c*-stacked sequence separated by organic molecules (Figure 1.13). Discrete T3 clusters were produced using divalent transition metals from the first row [48,72] (M^{2+} = Mn, Fe, Zn, Co). Clusters are charge balanced by the presence of Na^+ or K^+ cations.

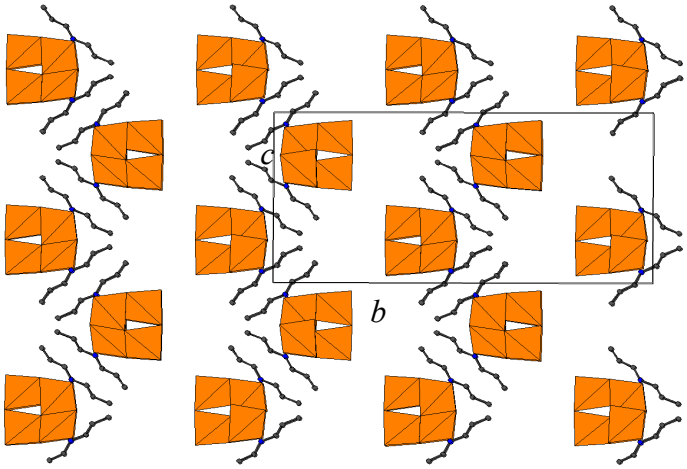

Figure 1.13. View on the (100) plane of $(C_6H_{16}N)_4(In_4S_{10}H)$. InS_4 tetrahedra are shown in orange, N atoms in blue and C atoms in dark grey. H atoms are omitted for clarity.

Under mild conditions and using organic molecules as templates, the insertion of transition metals M^{2+} (M = Cd, Zn, Co, Fe) into supertetrahedral clusters results in other types of isolated units. The first of them is the Super-supertetrahedral cluster [44], $[Cd_{16}In_{64}S_{134}]^{44-}$. The crystal structure of this material consists of clusters composed of metal–centred tetrahedra placed along the *c*-axis (Figure 1.14).

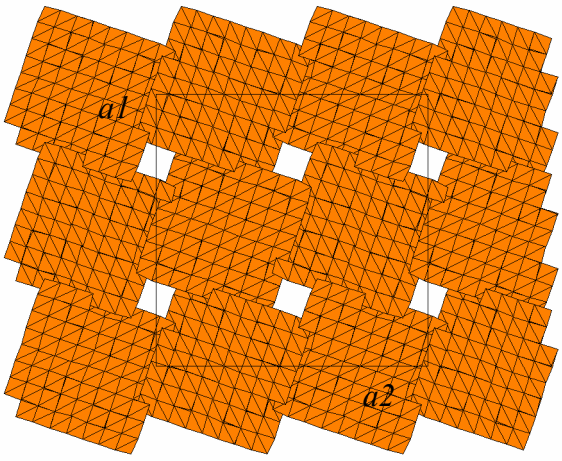

Figure 1.14. View on the (001) plane of the super-super tetrahedral cluster $[Cd_{16}In_{64}S_{134}]^{44-}$. Tetrahedra are shown in orange. Organic moieties are omitted for clarity.

A compound containing isolated P1 clusters, which crystallises in the presence of inorganic cations, has also been reported [73]. It has been described as clusters organised in a similar manner to the rock-salt lattice, where Na^+ and Cl^- ions are substituted by $[Zn_4Sn_4S_{17}]^{10-}$ clusters and where K^+ cations surround each cluster (Figure 1.15). Other more complex lattices based on Pn cluster can be found in [72]. Other routes to produce discrete supertetrahedral clusters compounds involve applying surfactants as templates [74].

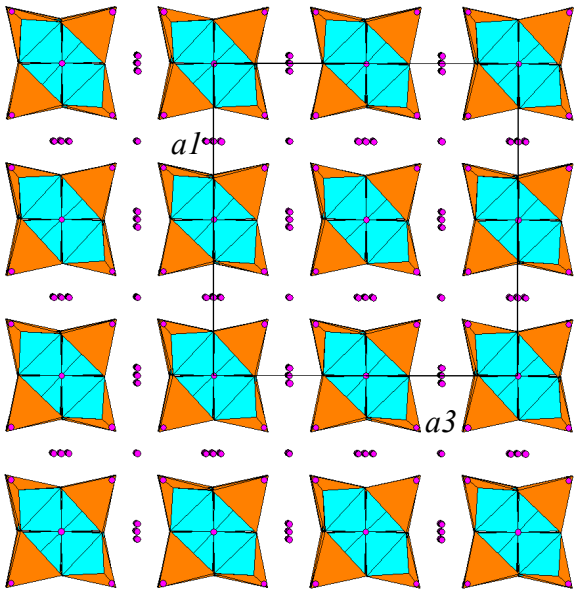

Figure 1.15. Packing of $K_{10}[Zn_4Sn_4S_{17}]$ on the (010) plane. SnS_4 tetrahedra are shown in orange, ZnS_4 tetrahedra in blue and K^+ cations in pink.

Two dimensional structures

There are a large number of structurally related layered compounds that are composed from supertetrahedral T2. They are mainly obtained in sealed tubes at high temperatures. These compounds have the general formula AMQ_2, where A is an alkali cation (A = K, Rb, Li, Tl, Cs, Na), M can be an element from group 13 (M = Al, Ga, In or Tl) and Q is a chalcogen (Q = S or Se) [17,75-77]. The structure of this family of materials consists of $[MQ_2]^-$ T2 supertetrahedral clusters, which are connected by sharing three of their corners through S atoms, forming layers. These layers are usually stacked along one of the axes and the supertetrahedral clusters in each sheet points towards the pores in the next sheet. Layers are paired forming a double layer with metal cations placed between them, forming a sandwich-type structure (Figure 1.16). Twining and stacking faults are common in this type of crystal [78].

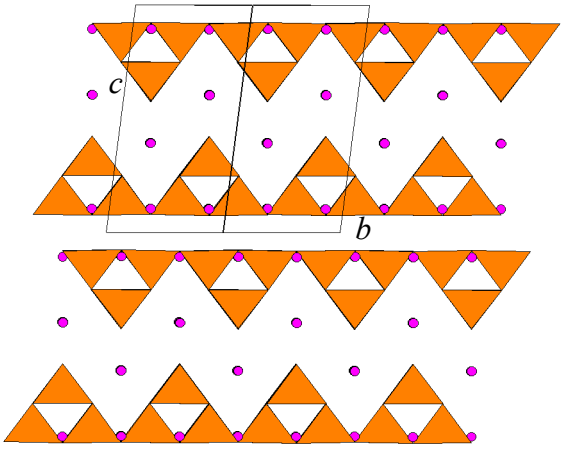

Figure1.16. Packing of the supertetrahedral layer $RbGaS_2$ along the [111] direction. GaS_4 tetrahedra are shown in orange and Rb^+ cations in pink.

Using solvothermal conditions, a related layered structure of composition $[C_6H_{24}N_4][Ga_4Se_{10}]$ was reported [79]. This material adopts the same structure as the AMQ_2 phases prepared using high-temperature methods. However, protonated organic moieties are placed between the layers instead of inorganic cations. Two-dimensional structures containing larger T5 clusters $[Cu_5In_{30}S_{54}]^{13-}$ [80] and $[Cd_6In_{28}S_{54}]^{12-}$ [81] have been also described. These materials contain layers in which four-connected clusters form a chessboard pattern (Figure 1.17). Only one structure formed exclusively of Pn clusters has been reported [71]. The clusters are four-connected through S bridges, forming a square grid parallel to the plane (010) and stacked along the *c*-axis. 4,4'-trimethylenedipyridine (TMPyr) protonated moieties are placed between the layers (Figure 1.18).

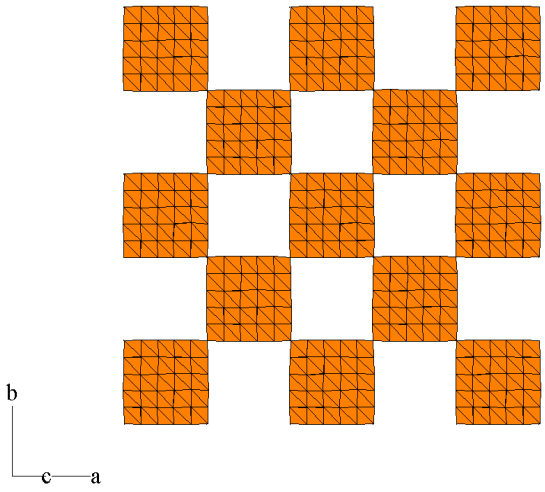

Figure 1.17. Polyhedral representation on the $(\bar{1}\,\bar{1}\,0)$ plane of the structure containing $[In_{28}Cd_6S_{54}]^{12-}$ clusters forming a chess-board pattern sheet. Tetrahedra are shown in orange.

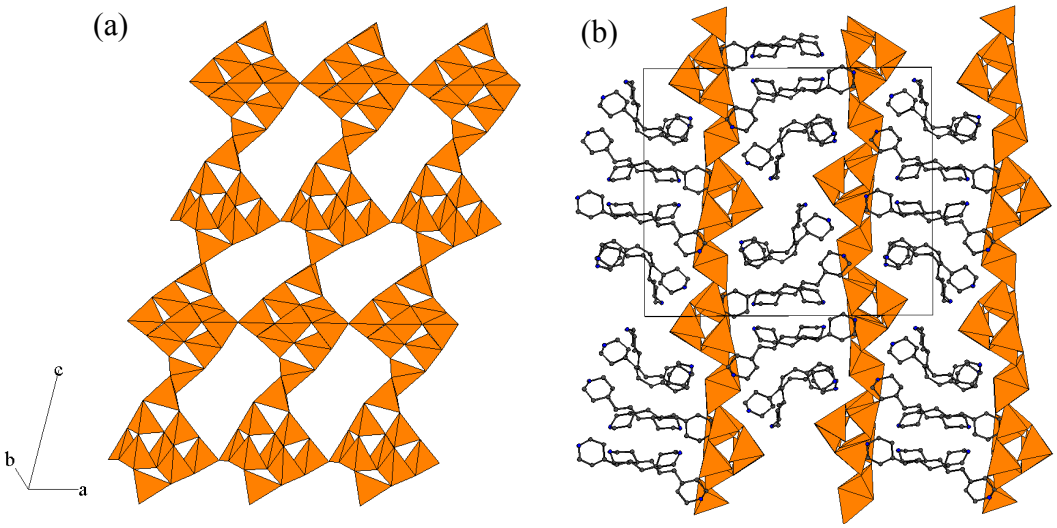

Figure 1.18. Polyhedral representation of compound $[C_{13}H_{14}N_2][In_9S_{17}]$. (a) View of a single layer on the (001) plane. (b) View of the packing on (001) plane. Tetrahedra are shown in orange, C atoms in dark grey and N in blue. H atoms are omitted for clarity.

Other types of two-dimensional structures are formed by alternating clusters of different sizes. Two types of layers have been described. The first one is constituted by T1 and T3 clusters [82], where T3 clusters of composition $[In_{10}S_{20}]^{10-}$ are three-coordinated to InS_4 tetrahedra forming six-membered rings and layers are produced within the (001) plane, showing large pores with a diameter of approximately 15 × 15 Å. The layers are stacked in pairs with the T3 building blocks pointing towards the pores of the neighbouring layer, forming double inorganic layers placed perpendicular to the *c*-axis. The protonated $[(C_2H_5)_2NH_2]^+$ cations are located in the pores of the layers and within slabs between successive double layers (Figure 1.19).

The second compound, which is denoted by HFC-1, contains P1 clusters of composition $[In_6S_{17}H]^{9-}$,which are corner linked to T2 clusters, ($[In_4S_{10}H]^{7-}$) forming six-membered rings, constituting a single infinite two-dimensional sheet stacked also along the *c*-axis (Figure 1.20) [83]. For the synthesis of this compound, two templates were used simultaneously, 4,4'-trimethylene dipiperidine (TMDP) and tetraethylenetetramine (TETA)). TMDP was located between the layers. However, the presence of TETA was not determined and latter experiments demonstrated that the same compound can be produced substituting this amine with 1,4-Bis-(3-aminopropyl piperazine) (BAPP), 1,4-diazabicyclo(2,2,2) octane (DABCO) or triethylenetetramine (TRIEN).

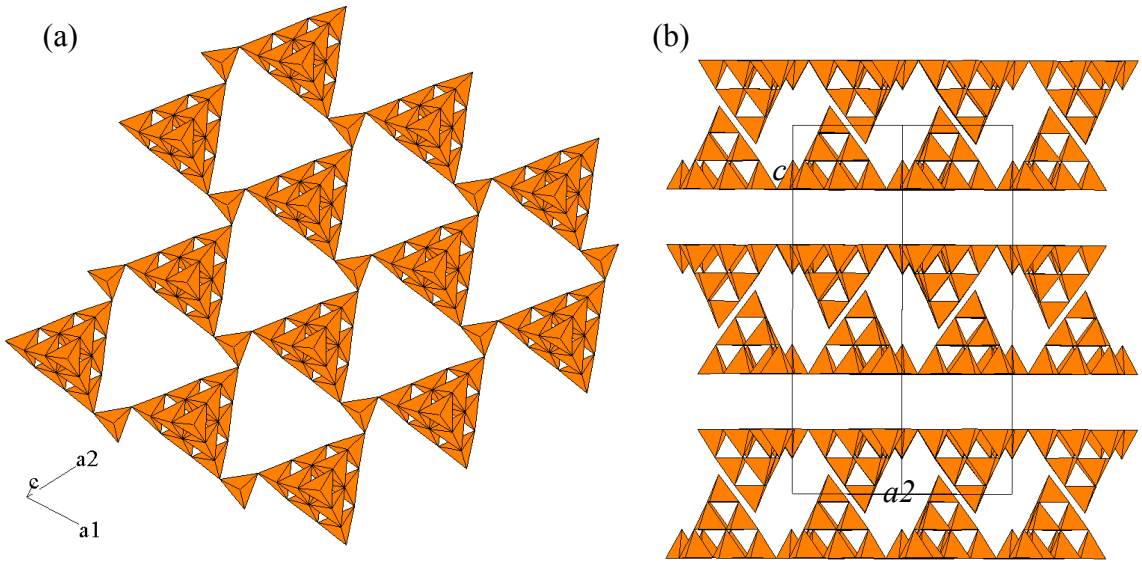

Figure 1.19. Polyhedral representation of compound $(DEA-H)_7^+[In_{11}S_{21}H_2]$. (a) Two-dimensional layer of supertetrahedra on the (001) plane. (b) Packing of the structure along the *c*-axis. InS_4 tetrahedra are shown in orange. Organic molecules have been omitted for clarity.

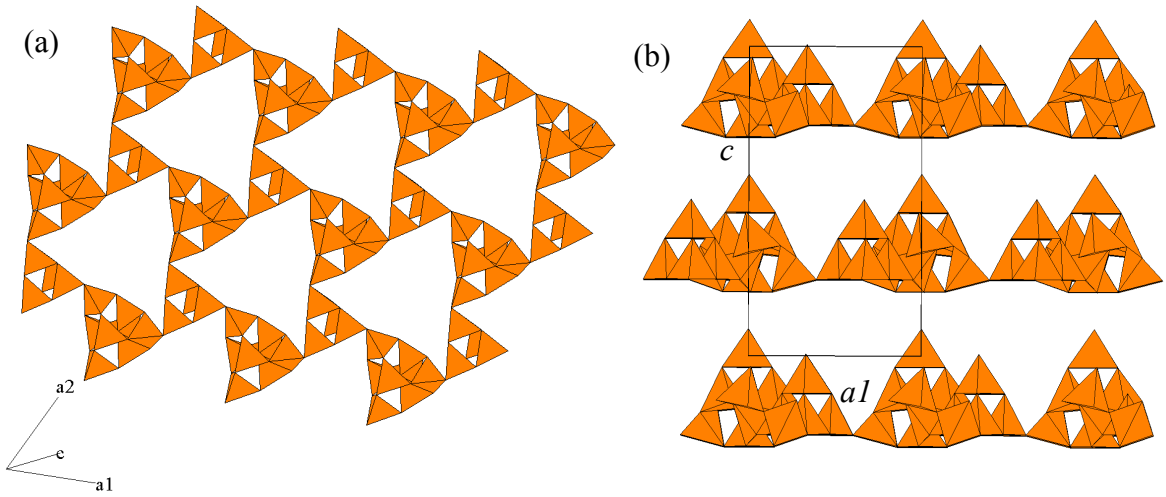

Figure 1.20. Polyhedral representation of HFC-1. (a) Single layer on of the (111) plane. (b) Stacking of the layers within the (001) plane. Tetrahedra are shown in orange.

Three-dimensional structures

Inorganic supertetrahedral clusters can be linked into extended structures by sharing corners (Figure 1.21). The most commonly observed linkage is that involving a single S^{2-} (or Se^{2-}) bridge, which joins two supertetrahedra. This type of connection is also found in two-dimensional structures. Other linkages are provided by polysulfide ions

(S_3^{2-}) as reported in UCR-18 [84], where one fourth of the connections are provided by the polysulphide bridge and the rest are linked by S^{2-} bridges as in UCR-8 [85].

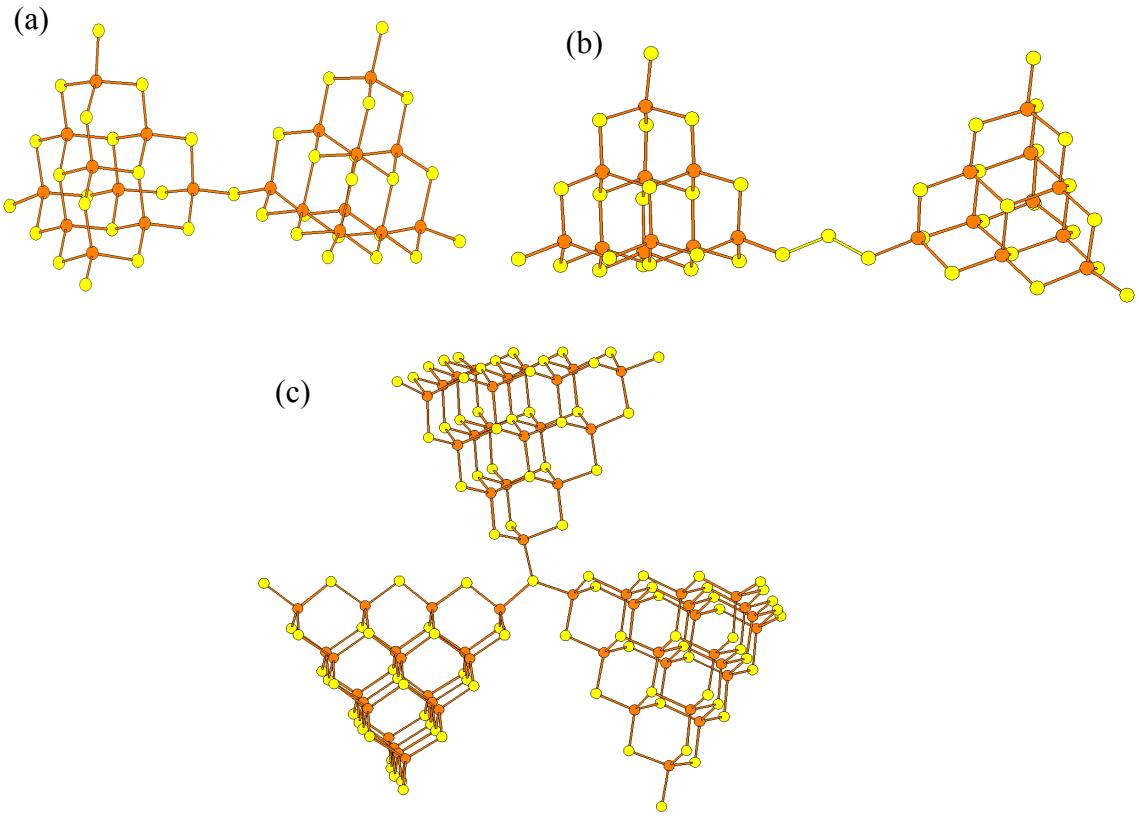

Figure 1.21. Examples of different bridging patterns between supertetrahedral clusters: (a) through S^{2-}, (b) polysulfide bridge S_3^{2-} and (c) through tri-coordinate S^{2-}. Metal atoms are shown in orange and S atoms in yellow.

Each three-dimensional structure can be considered as a covalent network of nanoclusters without the dispersion and orientation problems caused by a random distribution [86]. However, their properties sometimes differ from individual clusters of the bulk material [43,49]. The presence of large cavities within the structure may affect the electrical properties producing weak dipole-dipole interactions [87]. The approach in the design of these materials in which each cluster is considered as a single identity forming a super-lattice is denoted by the term 'Decoration' [88,89]. When each cluster is replaced by a node, the structures can be classified as belonging to seven topological types (Figure 1.22): single and double diamond lattice, cristobalite, sodalite, ABW-zeolite, CrB_4 and cubic-C_3N_4. The single and double diamond-type lattices are the most common.

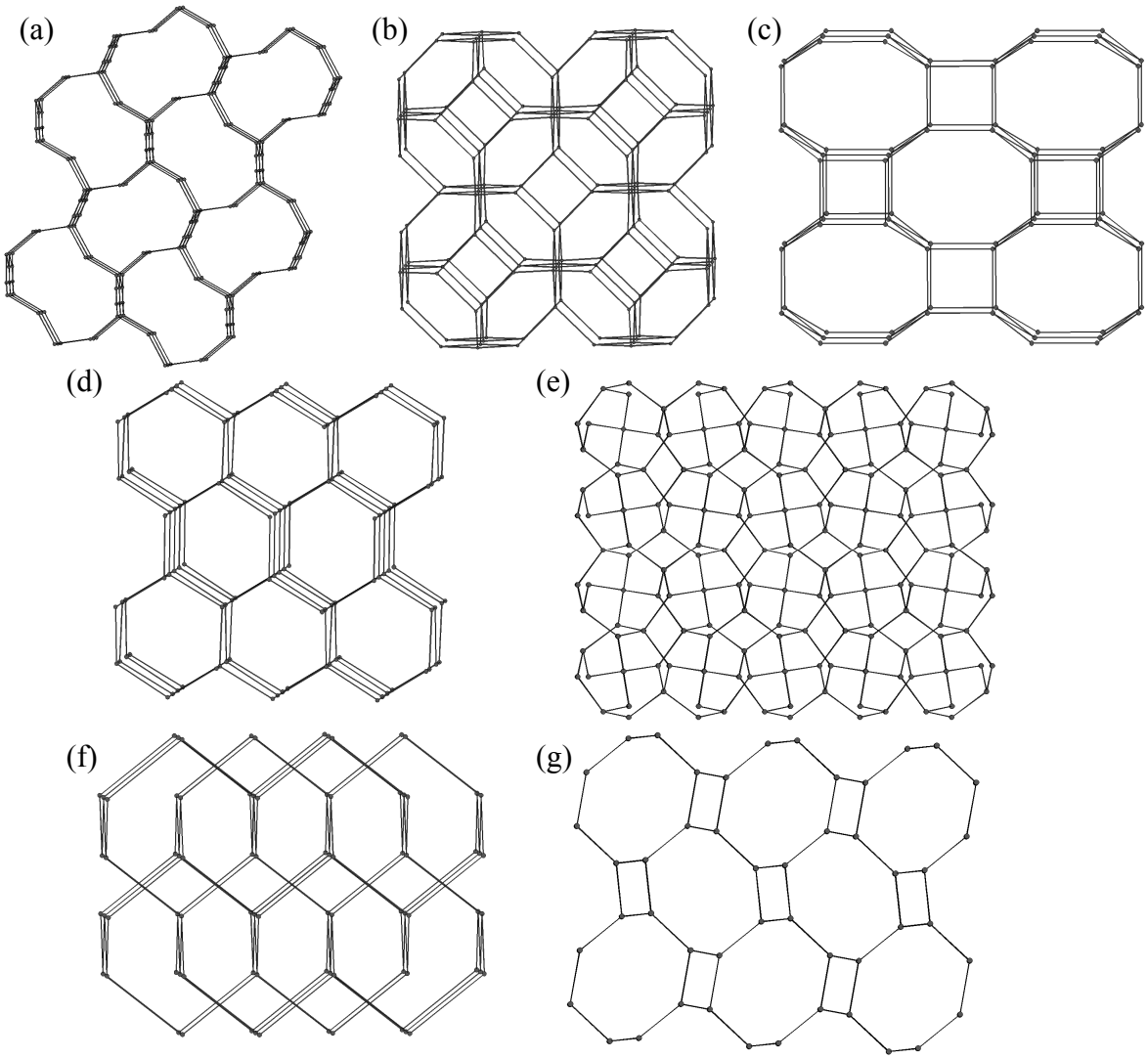

Figure 1.22. Examples of the three-dimensional framework topologies formed from tetrahedral clusters. From top to bottom and left to right: (a) cristobalite, (b) sodalite, (c) CrB_4, (d) diamond lattice, (e) cubic-C_3N_4, (f) double diamond lattice and (g) ABW topology.

Cristobalite lattice

The first cristobalite-type structure, denoted by ASU-34 [90], consists of T3 supertetrahedral units of $[In_{10}S_{20}]^{10-}$ (Figure 1.23). Four-connected clusters produce a cristobalite lattice. Experiments with cations of difference valences were carried out in order to produce structures containing other members of the Tn family in the networks and try to increase the porosity. Initially, it was demonstrated that a mixture of In^{3+} and Ge^{4+} produces structures with reduced dimensions on the cristobalite lattice [91]; this effect may be attributed to the formation of a T2 cluster as a building unit. The insertion of transition metals M^{2+} produces larger T4 clusters such as $[M_4In_{16}S_{35}]^{14-}$ (M

= Cd, Mn, Co or Zn) [92,86]. However, a cristobalite-type lattice based on T4 clusters would contain a large percentage of void space favouring the formation of two interpenetrating cristobalite networks.

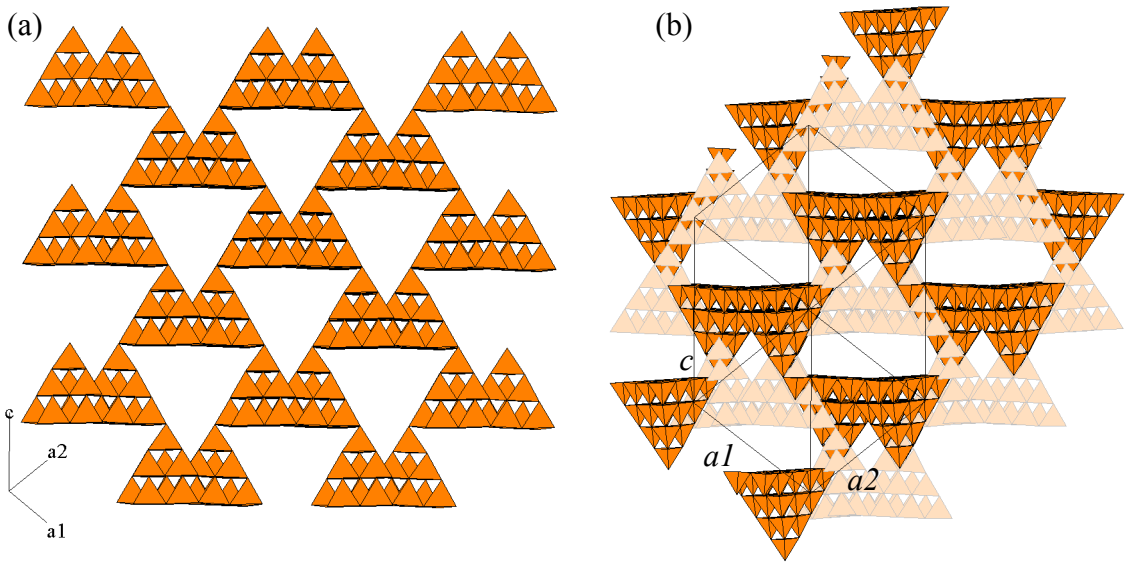

Figure 1.23. Polyhedral representation of a supertetrahedral cristobalite-type network. (a) View of a single net and (b) double cristobalite network formed by supertetrahedral clusters. MS_4 units are shown in orange. Organic molecules are omitted for clarity.

Sodalite lattice

Structures analogous to zeolites were initially reported by Yaghi and co-workers [93]. The compound, which is denoted by ASU-31, is constituted of $[In_{10}S_{20}]^{10-}$ T3 supertetrahedral clusters, which replace the SiO_4 and AlO_4 tetrahedra in a sodalite-type lattice. The T3 clusters are four-coordinated and build alternating four- and six membered rings, yielding a three-dimensional structure with large cavities (*ca.* 25.6 Å). Other materials have been synthesised by Feng and co-workers [94], who have produced metal chalcogenides with a zeolite-like structure using mixture of M^{3+} (M^{3+} = In or Ga), M^{4+} (M^{4+} = Sn or Ge) cations and Q^{2-} (S^{2-} = S or Se). One of these families consists of materials with a sodalite structure. These compounds are denoted by UCR-20 and consist of T2 clusters with composition $[M_4Q_{10}]^{6-}$ four-connected by sulphur bridges forming the sodalite lattice (Figure 1.24).

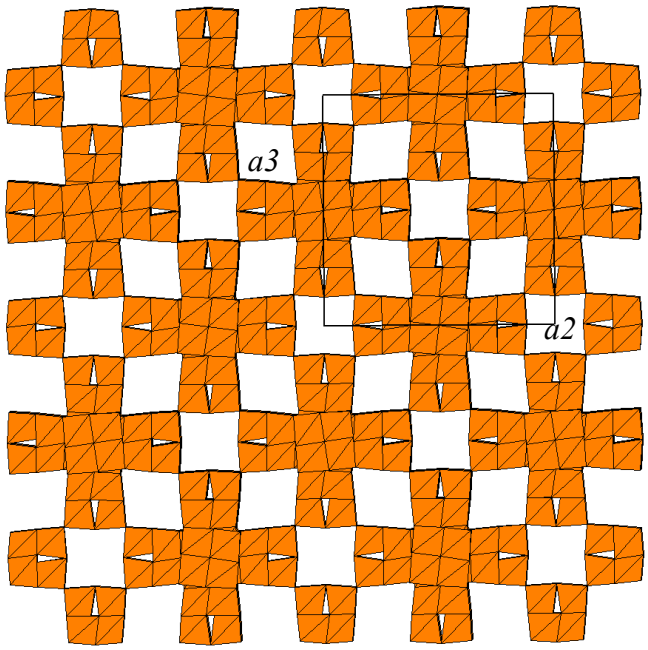

Figure 1.24. Polyhedral representation of $[Ga_2Ge_2S_8]^{2-}$ clusters on the (100) plane forming a sodalite-type structure. MS_4 tetrahedral are shown in orange. Organic components were omitted for clarity.

CrB_4 lattice

The CrB_4 lattice is a common topology also found in zeolites, such as the aluminosilicate $CaAl_2Si_2O_8$ in the monoclinic form [95]. The first supertetrahedral chalcogenide with this structure was formed by $[In_{10}S_{20}]^{10-}$ T3 clusters denoted by ASU-32 [93]. The same cluster was previously observed in cristobalite [90] and sodalite-like [93] structures with different templates under the same reaction conditions. The coordination of the clusters was the same, but the three-dimensional arrangement has changed, forming only six-membered rings. Analogous materials were produced by substituting cationic and anionic positions with elements of the same groups. The new material OCF-13 is formed by T3 clusters of $[Ga_{10}Se_{20}]^{10-}$ [96] (Figure 1.25). The family of compounds UCR-23 [94] has also the decorated CrB_4-type network, where the boron atoms are replaced by T2 clusters of various compositions.

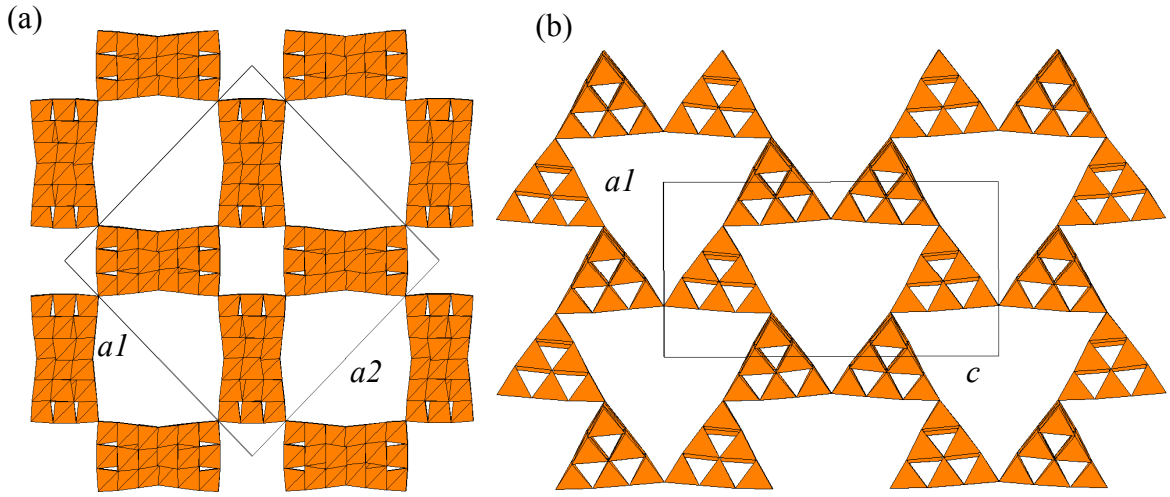

Figure 1.25. Polyhedral representation of $[Ga_{10}Se_{20}]^{10-}$ forming the CrB_4-type structure, (a) perpendicular view of the (001) plane showing the cubic channel along the *c*-axis and (b) view on the (010) plane, showing the six-membered rings connections. GaS_4 tetrahedra are shown in orange, and organic molecules are omitted for clarity.

ABW lattice

The insertion of transition metals into the framework does not always result in an increase in the size of the supertetrahedral cluster. The compound $[MnGe_4S_{10}](C_6H_{14}N_2)\cdot 3H_2O$ (denoted by Dabco-MnGs-SB1 [97]) is synthesised under solvothermal conditions and is formed by $[Ge_4S_{10}]^{4-}$ T2 adamantine clusters, four-connected through Mn^{2+} cations. The result is a framework topology analogous to that of zeolites Li-ABW [9] in which the AlO_4 and SiO_4 tetrahedra are substituted by $[Ge_4S_{10}]^{4-}$ clusters and $[MnS_4]^{6-}$ tetrahedra, respectively. The ABW topology in this case presents elliptical eight-membered rings due to the differences in size of the T2 and T1 (Figure 1.26). The use of mild conditions and surfactants as templates [98] resulted in a mesostructured compound containing in T2 cluster of $[Ge_4S_{10}]^{10-}$ connected through hydrated transition metal centres.

Cubic-C_3N_4 lattice

The cubic-C_3N_4 topology is found in the family of compounds UCR-8 [85]. The structure is built by $[M_{12}In_{48}S_{97}]^{26-}$ T4 supertetrahedra (M = Fe, Co, Zn or Cd) which are four-connected through three coordinated S^{2-} bridges (Figure 1.27). The connection between the three supertetrahedra present angles In-S-In closer to the planarity (118.8°~

120°) and the bond distance are consistent with the cations involved following Pauli's electrostatic rule.

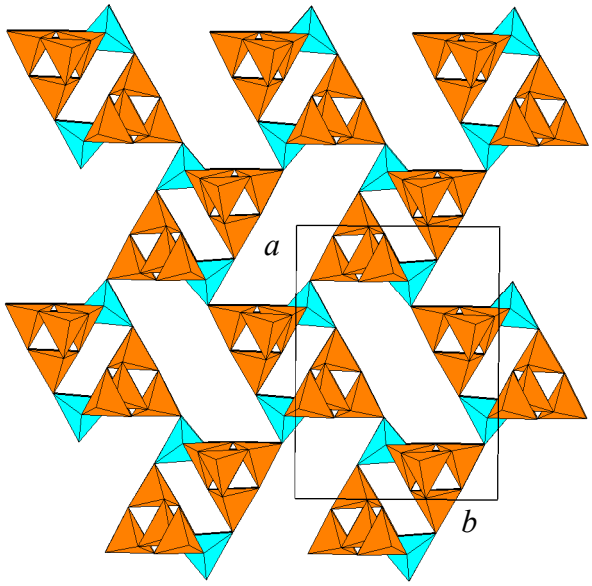

Figure 1.26. Polyhedral representation perpendicular to the (001) plane of $MnGe_4S_{10}$ clusters assembled in the ABW zeolites-type structure. GeS_4 tetrahedra are shown in orange and MnS_4 in blue.

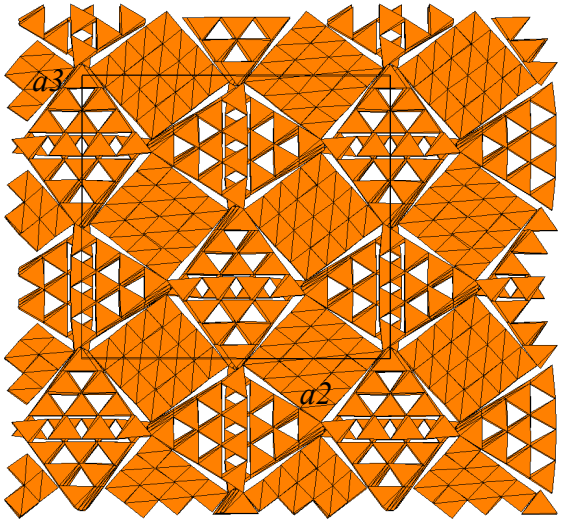

Figure 1.27. Polyhedral representation on the (100) plane for $[M_{12}In_{48}S_{97}]^{26-}$ forming the cubic-C_3N_4 lattice. MS_4 tetrahedra are shown in orange.

Single and double diamond lattice

The crystallisation process in materials formed by SBUs is controlled by the charge density of the template [99]. Additionally, the synthesis of clusters is usually associated with strong reducing conditions and clusters of various types could coexist in a solution

at equilibrium. Therefore, the final composition of a structure is sometimes stabilised by the presence of several types of cluster linked together. That is the case in the first compound containing diamond lattices [100] of transition-metal germanium sulphides. Alternating T2 and T1 clusters form six-membered rings and when represented by nodes the structure resembles the diamond lattice (Figure 1.28).

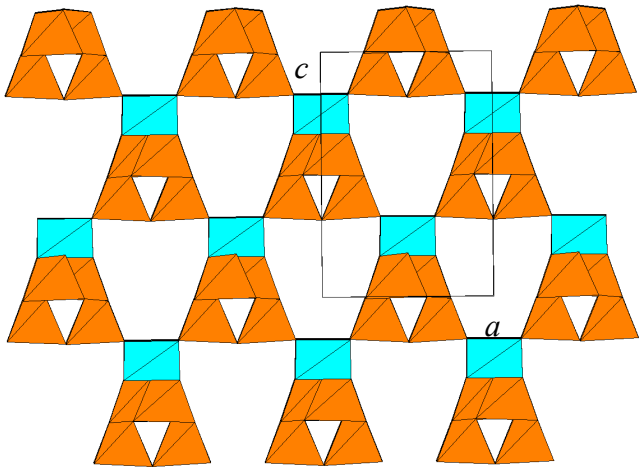

Figure 1.28. Polyhedral structure of a single diamond-type structure of $[MGe_4S_{10}]^{4-}$ on the (010) plane. $[Ge_4S_{10}]^{6-}$ T2 clusters are shown in orange and MnS_4 centres in blue.

Attempts to introduce lower valence metals in order to increase the size of the cluster with this type of lattices were initially carried out by Ozin et *al.* [101]. Feng and co-workers, in their series of experiments to produce metal sulphides simulating conditions of reactions of the synthesis of zeolites [94], reported a few families of this type of structure. The UCR-21 are composed of T2 clusters of composition $[M_4S_{10}]^{10-}$ (M = Ga, In, Sn or Ge and S = S or Se) arranged in a single diamond lattice. By using a different template, the UCR-22 family, which contains T4 coreless supertetrahedra, was also produced. These T4 clusters contain a mixture of M^{3+} and M^{4+} metal cations.

Solvothermal synthesis of indium sulphides has been extensively explored [49,43,71,102]. Materials containing T3 clusters (Figure 1.29), mixtures of T3 and T5 clusters and penta-supertetrahedral clusters have been reported. The structures of all of these compounds consist of interpenetrating double diamond lattices.

Using solvothermal conditions, supertetrahedral gallium-sulphide clusters [103] can be linked by polysulphide bridges in conjunction with the usual S^{2-} bridges. When transition metals are incorporated into the reaction mixture in order to produce T4 clusters, depending on the template and the reaction conditions, structures based on only

T4 clusters or containing alternating T4 and T3 clusters are formed. These adopt a double diamond lattice are found.

As a consequence of the presence of T4 clusters in the structure, materials with large pore sizes are obtained. Despite the interpenetration, it has been shown that these materials exhibit ion-exchange properties [104] and photocatalytic activity [94]. Other compounds adopting the double diamond lattice are built using T5 clusters. Such large units are either hollow clusters of indium chalcogenides or produced by the insertion of Cu^{+} instead of In^{3+} within the supertetrahedral units. To improve the optical properties, selenide frameworks were also produced with In^{3+} and Ga^{3+} [84,102] which can be described as homogeneous diamond lattices formed by T3 clusters.

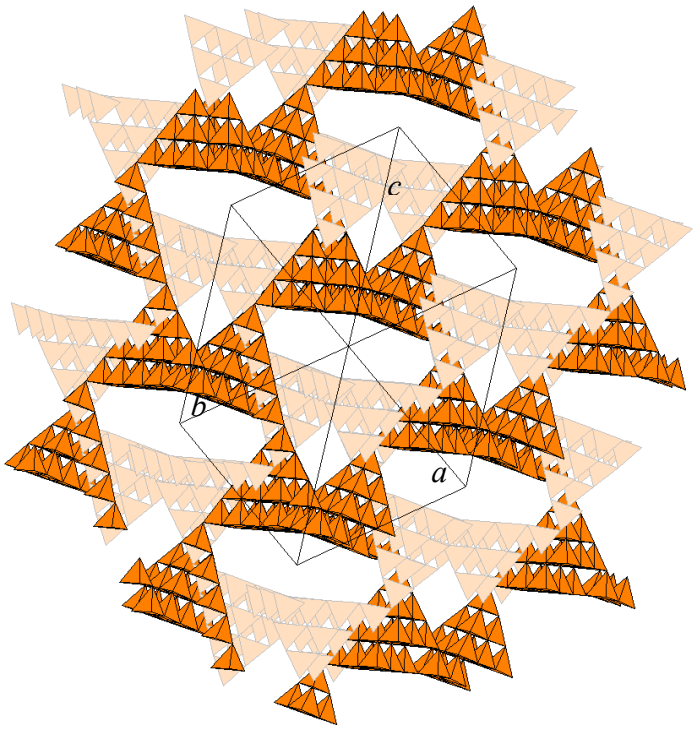

Figure 1.29. Polyhedral representation of a supertetrahedral structure with a double diamond lattice-type structure. View along the [111] direction. MS_4 tetrahedra are shown in orange. The two interpenetrating networks are shown in different shades.

Other lattices

Apart from the topologies outlined above, supertetrahedral clusters are capable of presenting other three-dimensional structures only observed in supertetrahedral materials. Hydrated supertetrahedral chalcogenide compounds were produced using kinetically controlled hydrothermal methods from organic-free aqueous solutions and highly alkaline conditions [105]. These materials are denoted by ICF-m, of which the

subfamilies ICF-24 and ICF-25 are constituted by T2 clusters. In both structures, the T2 units are four-connected through corner-sharing and form three-membered rings. Linkage of these rings results in the formation of larger rings of 20 and 16 members for ICF-24 and ICF-25, respectively (Figure 1.30).

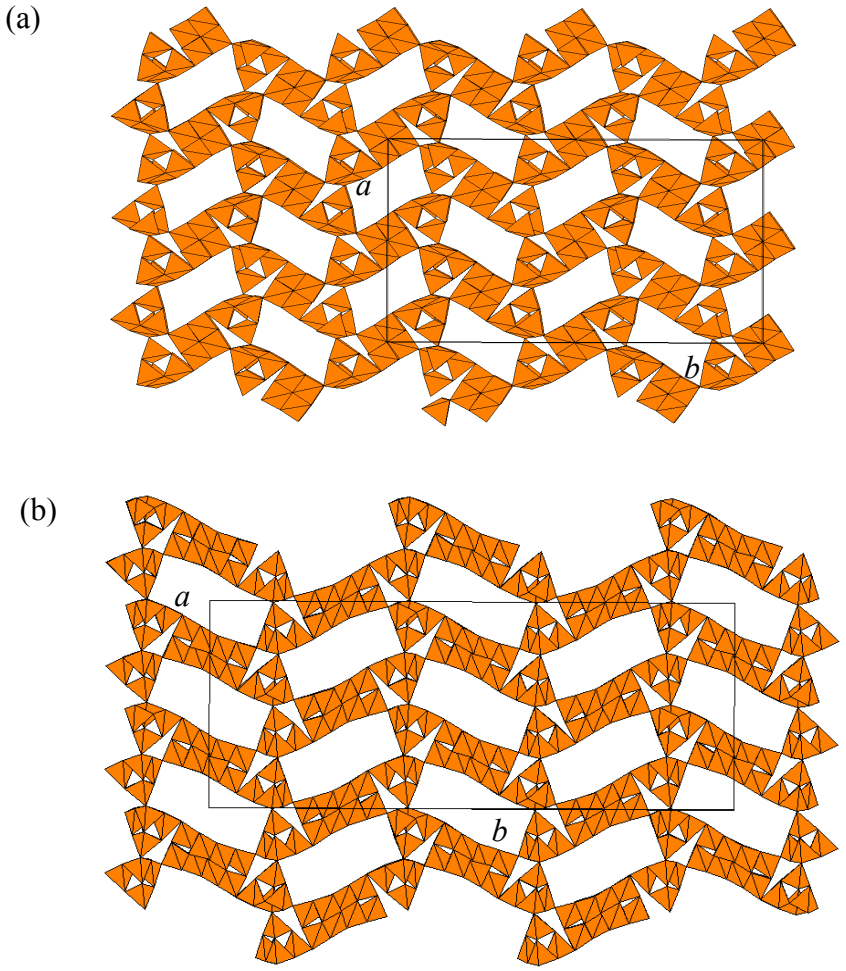

Figure 1.30. Polyhedral representation of: (a) ICF-24 on the (001) plane and (b) ICF-25 on the (001) plane. MS_4 tetrahedra are shown in orange, metallic cations and H_2O molecules located in the cavities are omitted for clarity.

Kanatzidis in collaboration with co-workers produced a series of compounds characterised by excellent stability and exchange capacity. The most representative supertetrahedral structure is $[Zn(H_2O)_4][Zn_2Sn_3Se_9(MeNH_2)]$ [106], which consists of a three-dimensional polar framework formed by chains of $[ZnSn_3Se_{10}]^{2-}$. There are T2 chains running along the *a*-axis. These chains are interconnected through Zn^{2+} cations along the *b*- and *c*-axis. These metal centres are also coordinated to methylamine ligands forming distorted tetrahedra (Figure 1.31). The charge balance is stabilised by $[Zn(H_2O)_4]^{2+}$ aqueous complexes, which are placed filling the pores in the structure.

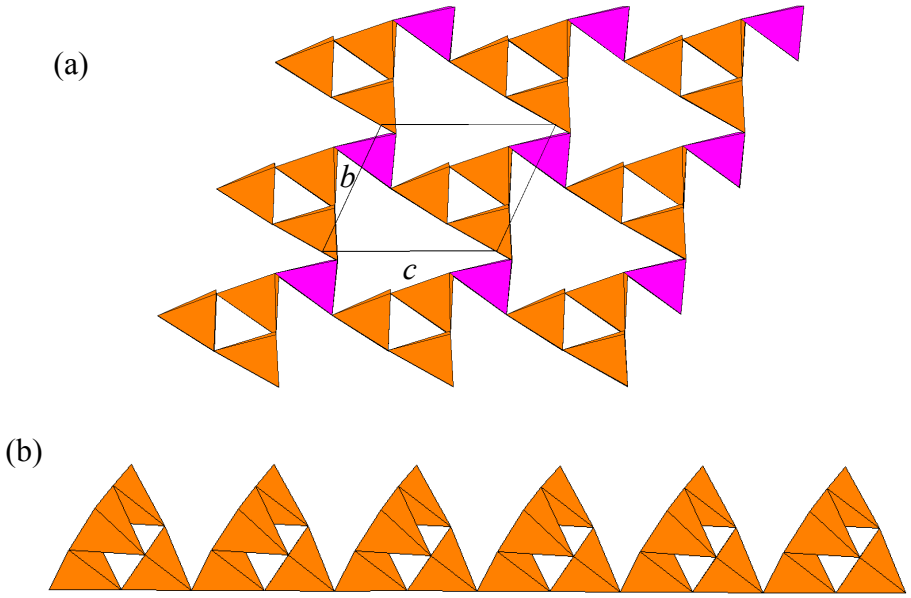

Figure 1.31. (a) View of the inorganic framework $[Zn_2Sn_3Se_9(MeNH_2)]^{2-}$ and (b) T2 chain along the *a*-axis. $SnSe_4$ and $ZnSe_4$ tetrahedra are shown in orange; ZnS_3N in pink. C and H atoms and $[Zn(H_2O)_4]^{2+}$ units were omitted for clarity.

1.3.3. Structures containing hybrid supertetrahedral clusters

The interest in hybrid materials started in the 1990's when it was found that poly-functional organic molecules could be used to bridge metal cations or clusters into extended arrays [11]. The majority of these compounds are based on oxygen bridges from carboxylic, phosphoric or phenolic acids and other types of connections, i.e. N atoms from pyridyl and imidazol ligands. However, in some cases a mixture of different types of ligands is found. Most of the published work involves transition metals and there is a growing body of literature dealing with rare-earth based systems. There has been a certain amount of effort with p-block elements (especially Al, Ga, Sn and Mg) driven by the search for lightweight materials for hydrogen storage and other potential applications [107].

Hybrid supertetrahedral compounds are part of the family of coordination polymers. They are defined as systems that contain extended arrays of inorganic clusters connected through organic ligands. The presence of ligands affects the inorganic structure in two ways, first, poly-functional ligands modify the spatial organization of clusters affecting the dimensionality of the porosity; and secondly, the band gap can be improved by extending the range of UV-Vis light that the semiconductor materials are capable of adsorbing. The synergistic effects resulting from the integration and interaction of inorganic and organic components can

dramatically vary the cluster properties and allow a new level of control over the electronic and optical properties. The first reported discrete hybrid supertetrahedral clusters [50] were produced by taking into account the similarity in coordinating properties between S^{2-} and RS^{-}, which was observed in metal-thiolates [108], and were comparable to materials constituted by bulk metal and terminated by ligands such carbon monoxides [109] and alkoxides [110]. Several authors continued this work and a large diversity of these clusters can be found in the literature, as will be described in the following sections.

Discrete units

The first hybrid tetrahedral discrete units were reported by Dance [50], whose work was focused on the study of the mono-thiolate group (RS^{-}), whose chemistry was poorly developed at the time. This first structure published consists of discrete anions formed from an inorganic core of $[Co_4S_{10}]^{2-}$, (forming a T2 cluster) shielded by phenyl groups (Figure 1.32). The neutrality in the crystal is obtained through charge balance by protonated trimethylammonium cations. A series of analogous compounds with other transition metals from the first row were produced using the same method [51,111]. However, the majority of the reported discrete units are formed by elements of Group 10, such as T3 clusters [51], P1 clusters [104] and capped clusters [58,55] (including Cn,m [103]). The most widely used RS^{-} ligand was thiophenylate and other similar compounds, such as seleno-phenylates [54].

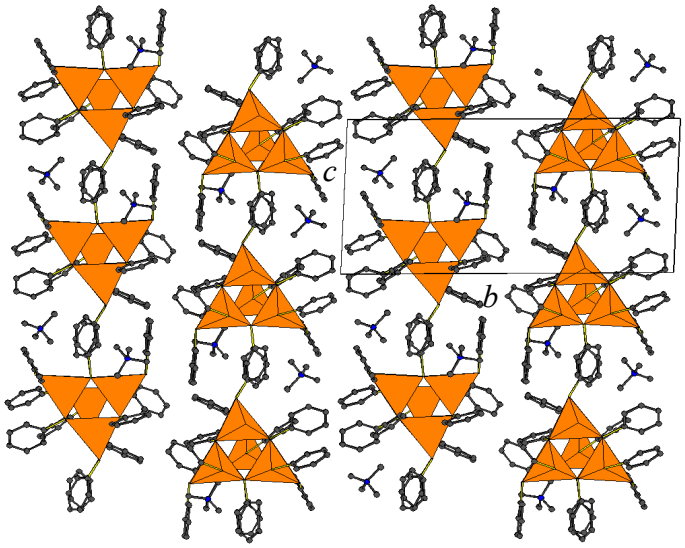

Figure 1.32. View of $[(CH_3)_4N]_2[Co_4(SPh)_{10}]$ on the (100) plane. CoS_4 tetrahedra are shown in orange, C atoms in dark grey and N in blue. H atoms are omitted for clarity.

The buoyant activity in the synthesis of these types of compounds (and the establishment of the conditions in which the clusters were produced) motivated several groups to design hybrid supertetrahedral clusters with improved electrical properties. Some of them present photovoltaic properties. They were based on $CuInE_2$ (E = S, Se) and initially produced by Kanatzidis et *al*. [112]. In conjunction with her colleagues, Shapiro [55] produced a structure formed by hybrid $C_{3,1}$ clusters which are shielded by thiphenylphosphine and alkyl groups (see Section 1.31.). The first hybrid metal-chalcogenide cluster organically unshielded was produced by Schmidbaur and Nogai (see Section 1.3.1) [56].

Extended structures of this type of cluster linked through organic ligands could produce open-frameworks with large cavities. The characteristics of some pyridyl ligands (poor electron donor with bi- or multi-dentate coordination) make them potential ligands for the synthesis of these compounds.

The combination of different ligands (thiolates and pyridyl ligands with two coordination positions), resulted in the formation of the first known hybrid dimeric unit [60]. The structure consists of dimeric molecules of two $[Cd_{17}Se_4(SPh)_{26}]$ supertetrahedral clusters bridged through two bicoordinated dipyridylethane (BPe) ligands (Figure 1.33).

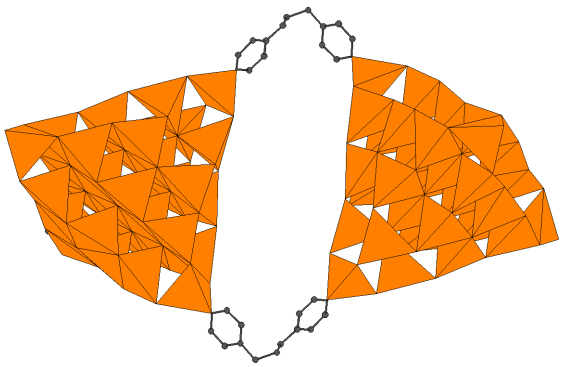

Figure 1.33. Dimeric unit of $Cd_{17}Se_4(SPh)_{26}L_2$. $CdSe_4$ and $CdSe_3N$ tetrahedra are shown in orange and C atoms in dark grey. $(SPh)^-$ ligands and H atoms are omitted for clarity.

Research efforts were focused on the introduction of dyes as templates in the synthesis. As a result, charge transfer salts based on anionic supertetrahedral clusters and methyl viologen cations (MV^{2+}) [104] were produced. Compounds were described as IPCT (Ion Pair Charge-Transfers) [113-115]. The compounds obtained using this template contain hybrid T3 chalcogenide clusters of formula $[Zn_{10}S_4(SPh)_{15}Cl]^{2-}$ or P1

clusters of formula $[Cd_8S(SPh)_{16}]^{2-}$, respectively. Both of them are charge balanced by MV^{2+} cations. The optical properties of the clusters are dramatically affected by the interaction of this type of template when compared to other compounds containing the same cluster units (band gaps are red-shifted).

More recently, a new type of hybrid materials has been described containing discrete T3 clusters where metal complexes are terminating the four corners via covalent bonding with S atoms [79,116].

Infinite chains

Two types of chains are known. The first consists of P1 penta-supertetrahedral clusters connected by cross-linked dipyridyl ligands forming zig-zag chains. This structure has been observed in three analogous compounds produced using different templates [53]. The coordination polymers formulae are $[Zn_8S(SC_6H_5)_{14}L]$ and $[Zn_7CoS(SC_6H_5)_{14}L]$, where L is either 1,2-bis(4-pyridyl)ethylene (DPE) or 1,3-bis(4-pyridyl)propane (BPP). The chains are stacked parallel the plane (100) (Figure 1.34). The difference between the compounds is related to the disorder and staking of the organic components.

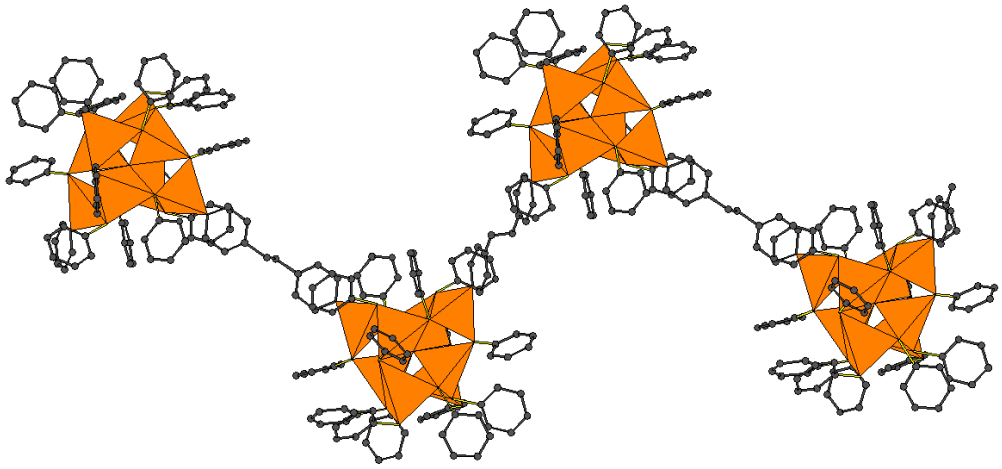

Figure 1.34. View of the one-dimensional zig-zag chain of $[Zn_8S(SC_6H_5)_{14}DPE]$. ZnS_4 and ZnS_3N tetrahedra are shown in orange and C atoms in dark grey. H atoms are omitted for clarity.

The second type of chain consists of clusters connected through quadridentate linkers [104]. One example is TPOM [tetrakis(4-pyridyloxymethylene)methane], which was produced from pentaerythrityl tetrabromide with 4-hydroxylpyridine in N,N'-dimethylformamide. The first compound, denoted by MCOF-9, presents a belt-like structure. It is formed from P1 units of stoichiometry $[Cd_8S(SPh)_{16}]^{2-}$ which are

connected in two positions by two different molecules of TPOM, forming four-membered rings. Additionally, the rings are cross-linked through the remaining coordination positions of TPOM, forming two-membered rings between the former rings. A slight change in reaction conditions produced MCOF-10, which is formed by TPOM molecules cross-linking two $C_{3,1}$ clusters of composition $[Cd_{17}S_4(SPh)_{28}]^{2-}$. The result is one-dimensional infinite chains packed along the *c*-axis (Figure 1.35).

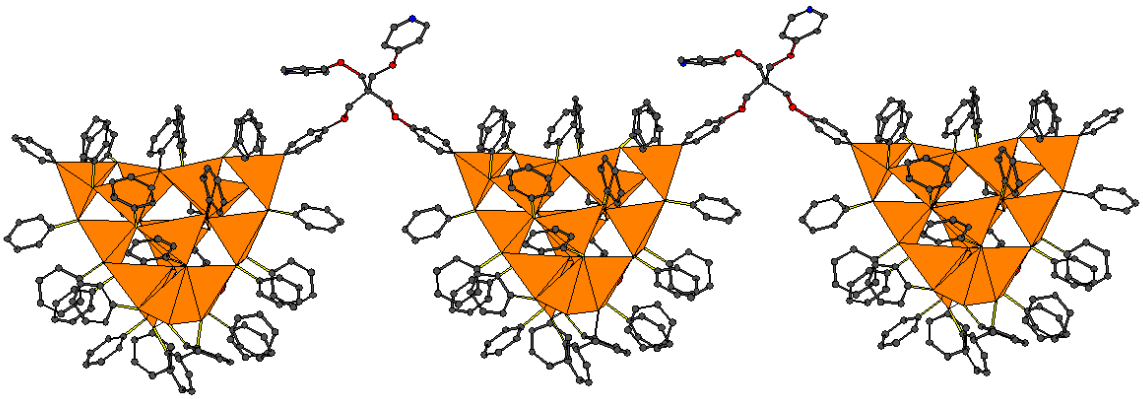

Figure 1.35. Infinite chain of (TMOP) $[Cd_{17}S_4(SPh)_{28}]$. CdS_4 and CdS_3N tetrahedra are shown in orange, C atoms in dark grey and O atoms in red. H atoms are omitted for clarity.

Two-dimensional layers

Only two hybrid compounds present a two-dimensional structure. They are denoted by COV-5 and COV-7 and are obtained under the same conditions with different ligands acting as linkers [60]. The structures are formed by $C_{2,1}$ clusters (which consist of the $[Cd_{32}S_{14}(SPh)_{36}]^{4-}$ units) and are cross-linked through the sharing of two coordination ligands, forming dimeric units. These connect units to other units through two different ligands, resulting in six-membered rings linked in a two-dimensional layer (Figure 1.36). The layers are stacked along the (101) plane, with a compact packing and no cavities because of the interaction between phenyl groups from each cluster.

Recently, the first indium telluride forming two-dimensional layers and constituted of hybrid supertetrahedral clusters has been reported [117]. The layers are formed by alternating $[In_4Te_9(en)]^{6-}$ and $[InTe_3(en)]^{3-}$ clusters sharing three corners through S atoms and creating to six-membered windows. The layers are stacked along the *c*-axis (Figure 1.37) and separated by $[In(en)_3]^{3+}$ metal complexes.

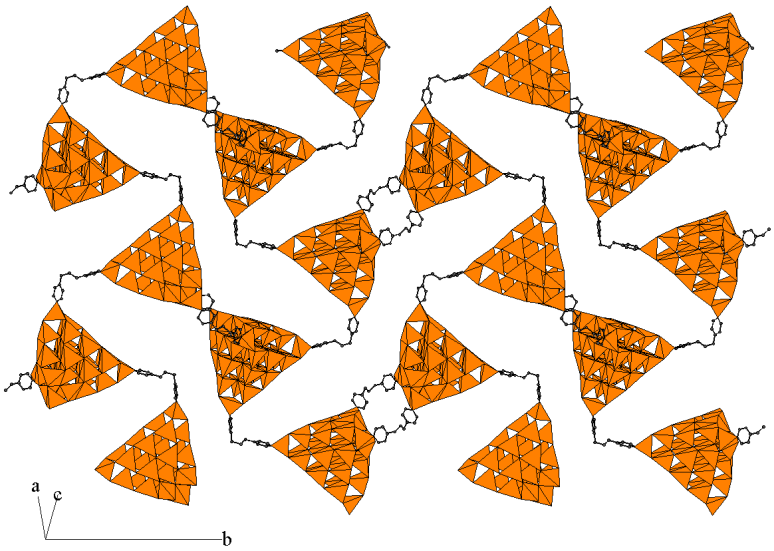

Figure 1.36. Infinite layers of $[Cd_{32}S_{14}(SPh)_{36}]^{4-}$ parallel to the plane (101). CdS_4 and CdS_3N tetrahedra are shown in orange, C atoms in dark grey. H atoms are omitted for clarity.

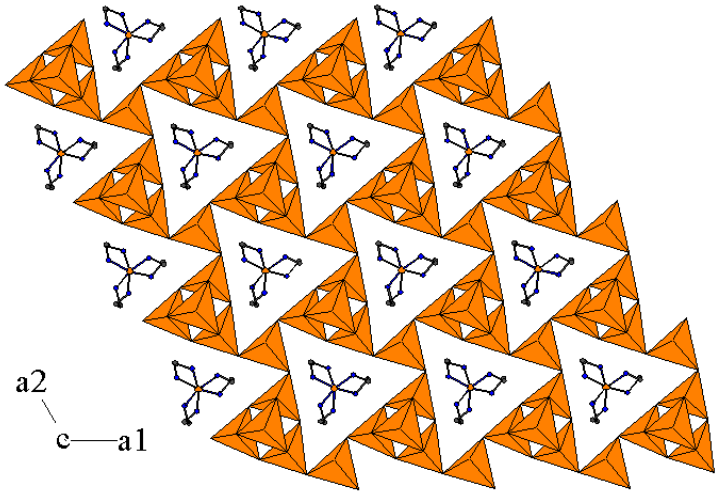

Figure 1.37. View of a single layer $[In(en)_3][In_5Te_9(en)_2]$ within the (001) plane. $InTe_4$ and $InTe_3N$ tetrahedra are shown in orange, In atoms in orange, N in blue and C in dark grey. H atoms and en molecules coordinated to In are omitted for clarity.

Three-dimensional structures

The hybrid three-dimensional structures are based on supertetrahedral clusters and represent the ultimate goal of the study of open-framework materials. They are not very common and only a few examples have been reported. The use of organic ligands as linkers between clusters is limited to two-dimensional structures and therefore, when a higher dimensionality is reached, the inorganic connections between clusters through S^{2-}

bridges are predominant. Nonetheless, the organic moieties are still covalently bonded to the S atoms on the faces of the clusters.

The first structure was reported by Vossmeyer et *al*. [118]. It is based on the C_4 clusters, $[Cd_{17}S_4(SCH_2CH_2OH)_{26}]^{2-}$. These units were earlier described as discrete clusters by Dance and co-workers [58]. The clusters are four connected by sharing sulphur corners, forming two interpenetrating diamond lattices (Figure 1.38).

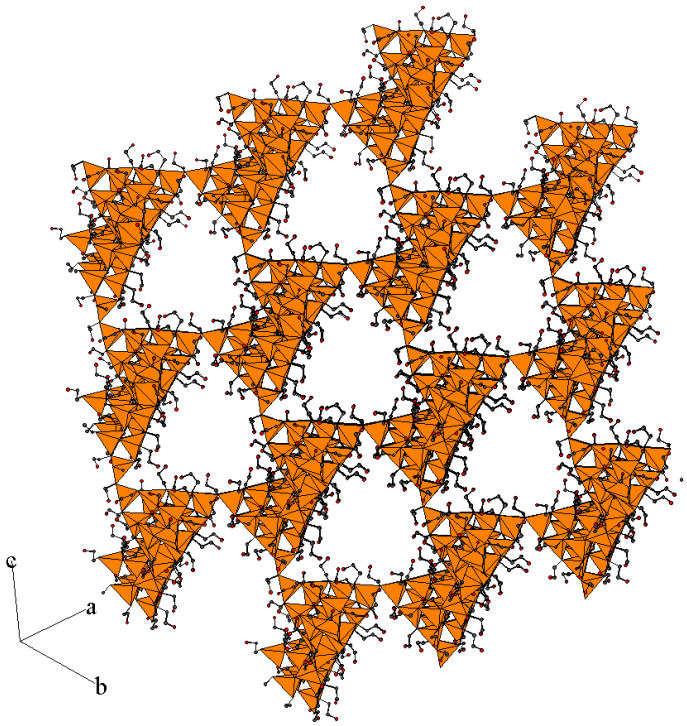

Figure 1.38. Single diamond lattice of $[Cd_{17}S_4(SCH_2CH_2OH)_{26}]^{2-}$. CdS_4 tetrahedra are shown in orange, C atoms in dark grey and O atoms in red. H atoms are omitted for clarity.

Analogous structures with C_2 clusters of composition $[Cd_{32}S_{14}(SPh)_{38}]^{2-}$ were produced, using metal-chelate dyes as templates [119]. Recent works report the preparation of structures with chiral properties not previously observed in inorganic frameworks. The first of these compounds is denoted by CMF-4 [120]. This structure is formed by $[Cd_{17}S_4(SPhMe\text{-}3)_{28}]^{2-}$ units (HSPhMe-3: 3-methylbenzene-thiol) which are C_1 clusters. The units are three- and four-connected through S atoms, forming a covalently bonded framework and results in two interlaced lattices with a boracite-type topology (Figure 1.39). This structure is similar to that found in materials with piezoelectric properties. Other chiral structures are constituted by hybrid cluster assemblies with the topologies of different SiO_2 polymorphs. The compound denoted as CMF-8 was produced in a three-step synthesis [121] using as precursor CMM-5,

which is an ionic compound of formula $[Cd_8(SPhF\text{-}3)_{14}(DMF)_6(NO_3)][NO_3]$. This precursor consists of a hybrid cubic cluster formed by eight metal-sulphide tetrahedra connected, via three of their corners through S atoms. The cluster is shielded by twelve (Ph-F3) ligands distributed around the faces of the cluster. Six cadmium corners are bonded to DMF molecules and $(NO_3)^-$. The remaining corners are bound by two mono-negative charged (SPhF-3) groups.

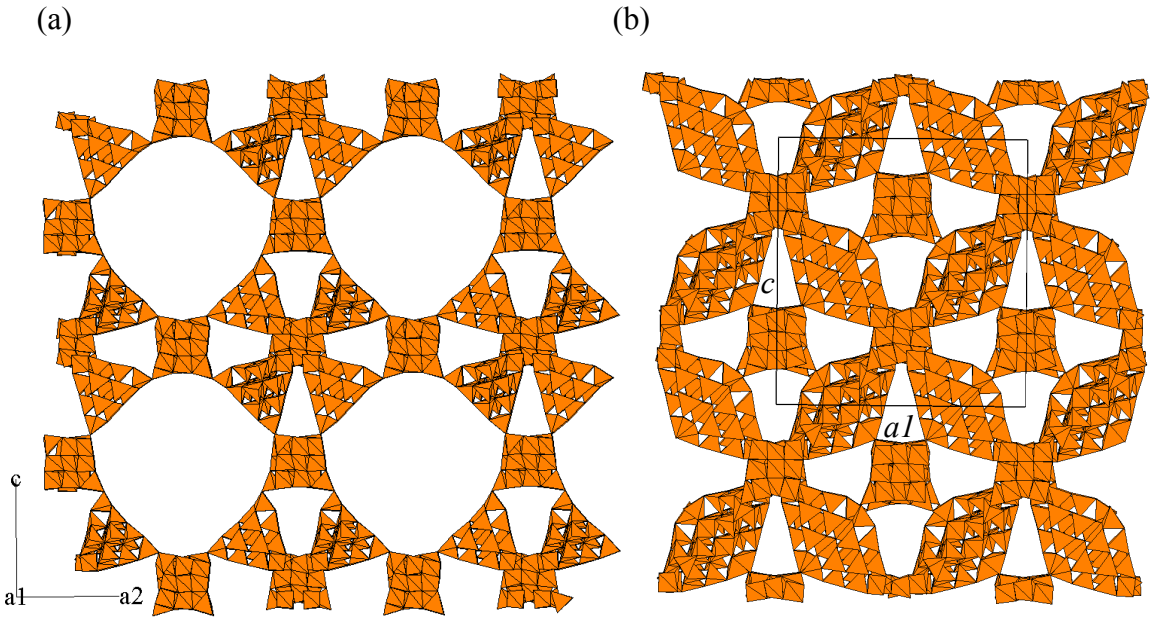

Figure 1.39. View of the structure formed by $[Cd_{17}S_4(SPhMe\text{-}3)_{28}]^{2-}$ on the (010) plane. (a) View of a single boracite net and (b) double interpenetrated boracite networks. CdS_4 tetrahedra are shown in orange. Organic moieties are omitted for clarity.

The three-dimensional structure of CMF-8 consists of P1 clusters with a composition $[Cd_8S(SC_6H_4F\text{-}3)_{12}]^{2+}$, which are four-connected forming alternating three- and six-membered rings and resulting in the α-quartz-type topology. This topology is interesting because (i) α-quartz exhibits enantio-selectivity in the adsorption of aminoacids and (ii) technological applications as a piezoelectric material. Thus, materials with this type of structure could present similar applications. Other lattices, corresponding to different polymorphs of SiO_2 were also reported [122]. Compounds CMF-1, -2 and -5 all have the β-quartz topology. The materials CMF-1 and -5 contain the P1 cluster, $[Cd_8S(SC_6H_4Me\text{-}3)]^{2-}$, CMF-5 differs in the presence of a 6-fold super-cell with ordered S_2^- sites between two adjacent clusters; and CMF-2 is constituted by the C_1 cluster ($[Cd_{17}S_4(SC_6H_4M\text{-}4)_{28}]^{2-}$). The supertetrahedra are four-connected forming three- and six-membered rings (Figure 1.40).

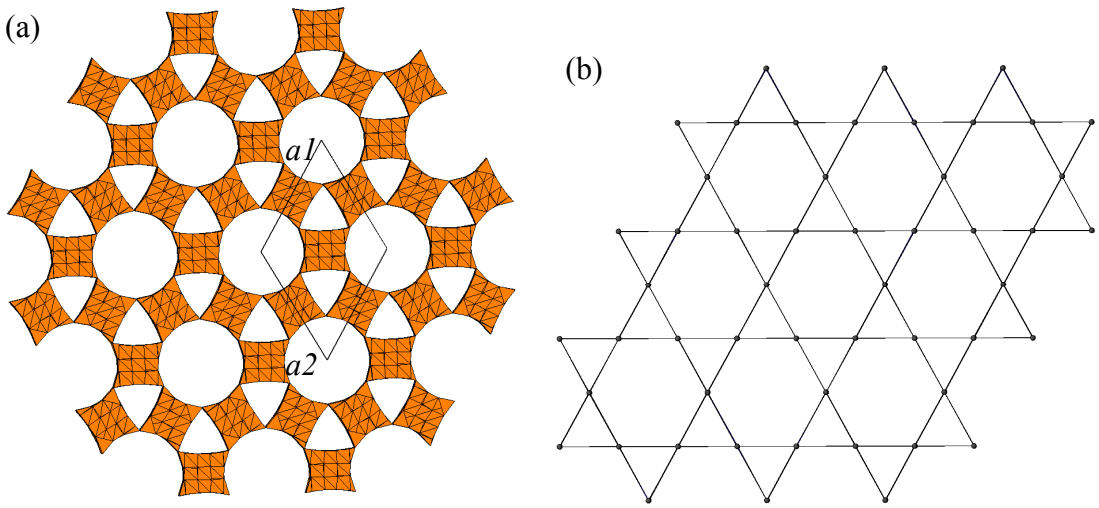

Figure 1.40. View on the (001) plane of compound CMF-1. (a) Polyhedral representation with CdS_4 tetrahedra shown in orange and organic components omitted for clarity. (b) α-quartz lattice.

In addition, the three-dimensional structure of compound CMF-3 has been reported, which is produced from alternating P1 and C1 clusters of $(Cd_8S(SC_6H_4M\text{-}3)_{14}]^{2-}$ and $[Cd_{17}S_4(SC_6H_4M\text{-}3)_{26}]^{2-}$), respectively. The clusters are connected, building a structure analogous to the moganite lattice (a polymorph of SiO_2, which exhibits similarities with the α- and β-quartz) (Figure 1.41).

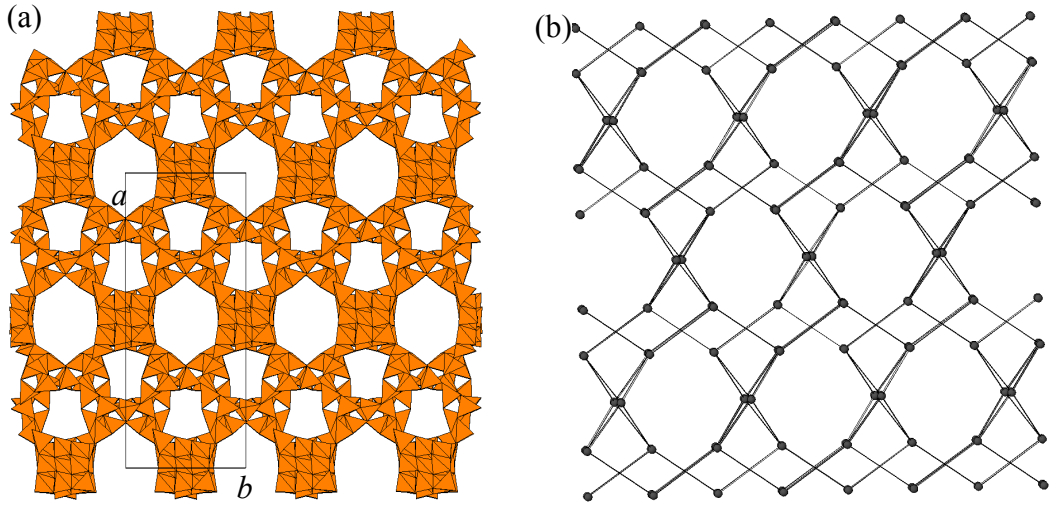

Figure 1.41. (a) View on the (001) plane of the framework CMF-3, CdS_4 tetrahedra are shown in orange and organic components are omitted for clarity. (b) Simplified net diagram of moganite.

1.4. Non-supertetrahedral metal chalcogenide structures of group 13

Elements from groups 10 and 13 are present in a large number of supertetrahedral compounds. However, the assemblies of the tetrahedra are not limited to compounds based on supertetrahedral clusters or condensed phases. Tetrahedra can share corners and edges or a combination of both types of linkage to give different elements such as chains, sheets or arrays of non-supertetrahedral clusters. The solvothermal method is frequently used in the synthesis of these phases, where the use of organic molecules as templates produces other hybrid structures. Recently, a comprehensive review of metal chalcogenides (group 13 and 15) has been published [123], showing the chelating organic amine's role in compounds obtained under solvothermal conditions.

1.4.1. Infinite chains

There are a large number of ternary compounds, based on the group 13 chalcogenides, forming one-dimensional chains. The first type of chain is based on compounds containing the MS_4 tetrahedron (M = In or Ga; Q= S or Se). These tetrahedra are linked together by sharing non-adjacent edges to form one-dimensional $[MQ_2]^-$ chains, similar to those found in SiS_2 [124] and in $KFeS_2$-type compounds [125] (Figure 1.43). Small fragments of this type of chain were reported as $[Ga_6Se_{14}]^{10-}$ units containing six gallium atoms [126]. This type of compound, which contains $[MQ_2]^-$ chains (M = Si, Fe, Ga; Q = S, Se), is produced by edge-sharing MQ_4 tetrahedra. However, they differ significantly in the packing of the chains. Depending on the counter-ion present, it is possible to distinguish between the different types of packing.

Gallium and indium chalcogenides containing inorganic cations (Na^+, K^+, Cs^+ or Rb^+) [127,128] are characterised by chains running parallel to each other and separated by the inorganic cations. A similar packing of the chains is found in the structures of solvothermally prepared chalcogenide chains containing $[M(en)_3]^{2-}$ complex [129] (M = Mn, Co, Ni) as counter cations (Figure 1.44 (a)). These materials demonstrate that the introduction of transition metals in the presence of ethylenediamine can result in the formation of metal complexes. Similar behaviour was also observed in Sb [130] and Ge sulphide compounds prepared solvothermally [131]. Using only organic templates in the synthesis, analogous infinite chains were produced. The chains are separated by protonated organic molecules and neighbouring chains are rotated by *ca.* 45° with respect each other [84,132]. The differences in packing with respect to previous materials might be related to the presence of hydrogen-bond interactions between the chains and the protonated amines (Figure 1.44 (b)).

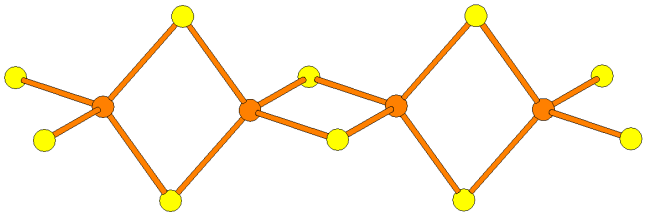

Figure 1.43. View of an infinite one-dimensional chain of tetrahedra sharing edges. Metal centers are shown in orange and chalcogenide atoms in yellow.

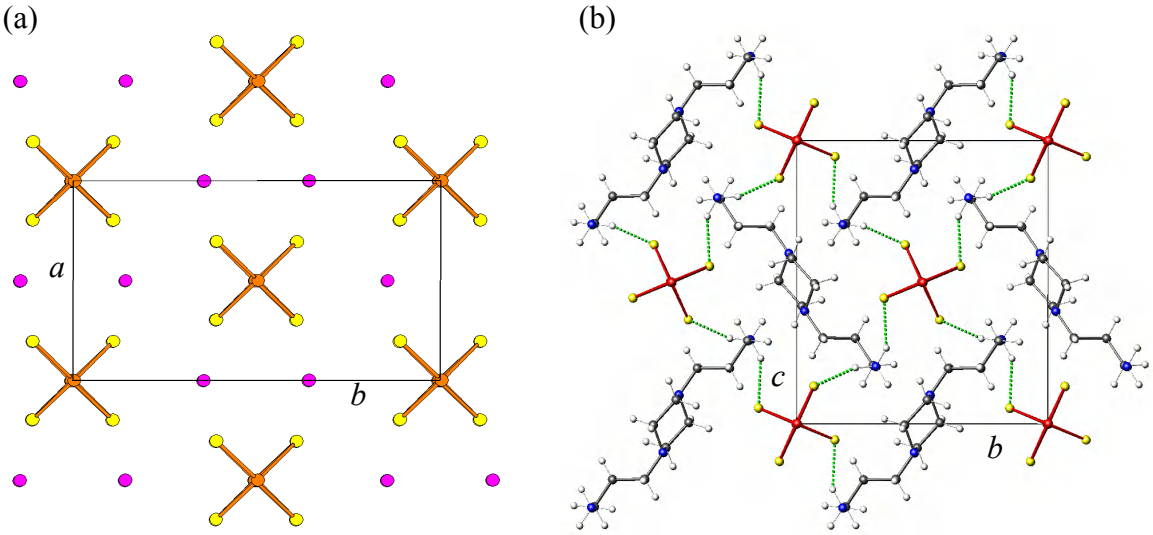

Figure 1.44. (a) View on the (001) plane in $KFeS_2$ and (b) view of [BAPP][GaS_2] on the (100) plane. Metallic atoms are shown in orange, sulphur in yellow, K in pink, C in dark grey and N in blue. Hydrogen bonds are shown in dashed green lines.

The presence of metal complexes in the structure is not uniquely limited to counter-ions. Metal cations can also be coordinated to sulphur atoms in the chains and additionally also act as ligands. Therefore, the complexes form part of the inorganic framework. When the coordination of the metal complex is only coordinated to one S atom (*i.e.* the complex is only coordinated to one chain) a distortion in the chain is observed [133], producing a slight curve. Distorted chains are also produced in the presence of $[Dy_2(en)_6\mu_2\text{-}OH)_2]^{4+}$ [134]. A pair of tetrahedra in the chain acquire a butterfly conformation due to the interactions with the Dy complexes; the chains run parallel along the [011] direction (Figure 1.45). This is the first compound of this type where the presence of a lanthanide complex is observed. Other covalently-bonded complexes were found in other type of chains i.e. $[Ni(Tepa)]_2[In_4S_7(SH)_2]\cdot H_2O$ [135], which consists of arachnid-shaped In_4S_{11} clusters formed by four-connected tetrahedra that are linked by sharing one of the tetrahedral edges.

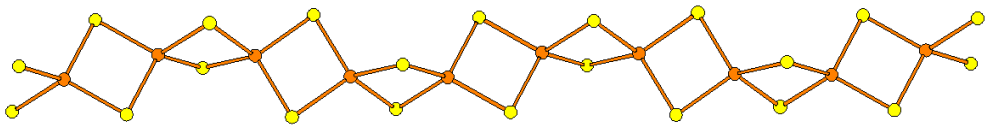

Figure 1.45. View of the $[GaS_2]^-$ chain presenting a butterfly conformation. Ga atoms are shown in orange and S in yellow.

The $[MQ_3]^-$ infinite chains are closely related to the $[MQ_2]^-$ chains. The substitution of one of the chalcogenide atoms by a poly-chalcogenide bridge $[Q_2]^{2-}$ results in the formation of $[MQ(Q_2)]^-$ chains. Some ternary gallium chalcogenides present this type of structure [136,137]. The anionic chains are parallel to each other and each metal is tetrahedrally coordinated to two sulphur atoms and two di-chalcogenide ions (Figure 1.46). These type of compounds are isostructural with reported boron poly-chalcogenides ABS_3 (A= Cs, Rb, Tl) [138,139].

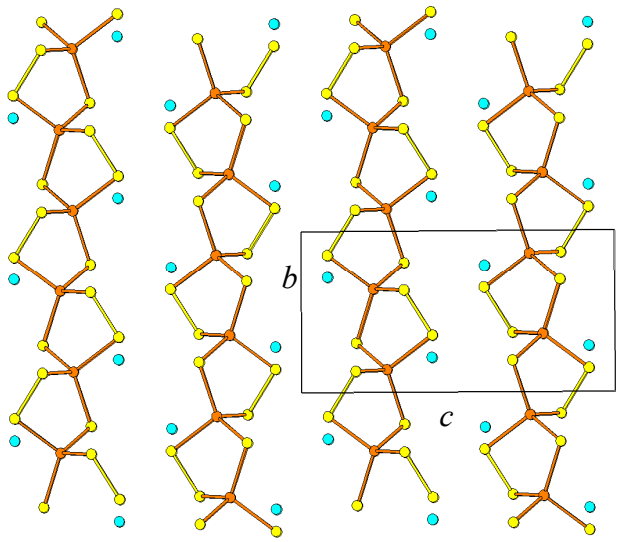

Figure 1.46. View along the (100) plane of $CsGaS_3$. Ga atoms are shown in orange, S in yellow and Cs in blue.

1.4.2. Two-dimensional structures

Many metal chalcogenides solvothermally prepared consist of two-dimensional layers and contain organic template molecules forming weak hydrogen bonds with them. Some, such as antimony sulphides [140,141] contain two-dimensional layers in which protonated amines are placed between the anion layers. However, as described in a previous section, compounds from group 10 and gallium chalcogenides are capable of

stabilising covalently bonded amine groups. The formation of this type of hybrid materials has been found in a small number of hybrid non-cluster chalcogenides such as CdQ*0.5 en (Q = S, Se, Te) [142-144] with only a couple of examples of layered compounds reported to date [129,145]. They are closely related compounds of formula $[Ga_4Se_7(en)_2][enH]_2$ and $[Ga_4S_7(en)_2][enH_2]$ which consist of anionic layers formed by two GaQ_4 and two GaQ_3N tetrahedra, linked by their corners forming a building unit with stoichiometry $[Ga_4Q_7(en)_2]^{2-}$ (Q = S or Se). This unit consists of six-membered Ga_3Q_3 rings in a boat conformation fused to form the final inorganic layer. Therefore, GaQ_4 tetrahedra are connected by their four corners and GaQ_3N by their three corners through the sulphur to three or four other units (respectively), thus forming the layers. The covalently bonded ethylenediamine molecules are orientated pointing towards the neighboured layers on both sides of each layer and constitute an organic-inorganic-organic layer (Figure 1.47). Additionally, protonated ethylenediamine molecules are located between layers to balance the charge in the structure. The difference between both structures is related to the orientation and amount of these ethylenediamine molecules. Layered structures based on supertetrahedral chalcogenide clusters [79,80,82] were based on four-connected building units. In these structures, the coordinated amines act as limiting factors which lead to the production of a supertetrahedral structure.

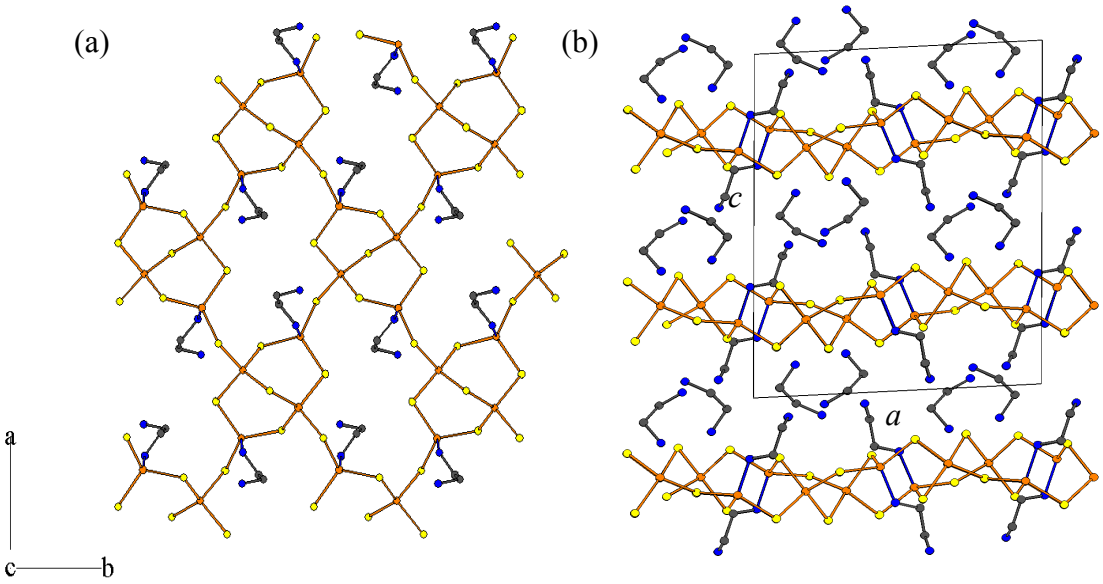

Figure 1.47. $[Ga_4Q_7(en)_2{\cdot}(enH)_2]$: (a) view of a single layer and (b) view of the packing on the (010) plane. Ga atoms are shown in orange, chalcogenide in yellow, C in dark grey and N in blue. H atoms are omitted for clarity.

1.4.3. Three-dimensional structures

Although is possible to design materials with particular desired structures and properties; a slight change in the solvothermal conditions can produce different results. Chalcogenide tetrahedra not only produce supertetrahedral clusters which link together to form frameworks, other types of clusters can also form three-dimensional structures presenting a porous structure (with cavities and channels).

The UCR-2 family of compounds [146] is a series of three-dimensional open frameworks of formula $[In_{33}Q_{56}]^{13-}$ (Q = S, Se, Te). The building units do not have a regular polyhedral shape and the connection between units is produced by sharing corners through common S atoms. The structure can be described as cross-linking helical chains (Figure 1.48).

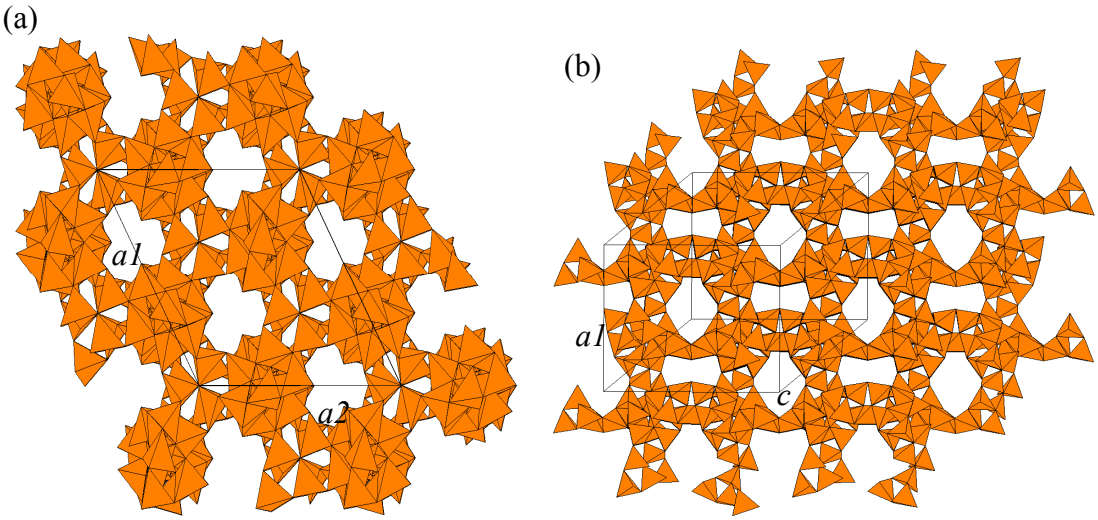

Figure 1.48. Polyhedral representation of $[In_{33}Q_{56}]^{13-}$ presenting a three-dimensional network of intersecting tunnels; (a) view on the (001) plane and (b) view along the [111] direction. Tetrahedra are shown in orange.

Under solvothermal conditions, the first three-dimensional structure of indium selenides based on edge-linked $InSe_4$ tetrahedra was prepared [147]. The structure is described as consisting of individual chains formed by three-membered tetrahedral rings linked by a tri-coordinated Se, which are connected into a three-dimensional honeycomb structure by sharing the terminal Se atoms opposite to the ring with four adjacent chains (Figure 1.49). The structure contains circular channels of *ca.* 6 Å in width running parallel to the *c*-axis. The template (3,5-dimethylpyridine) exhibits high disorder and its presence was confirmed by FTIR.

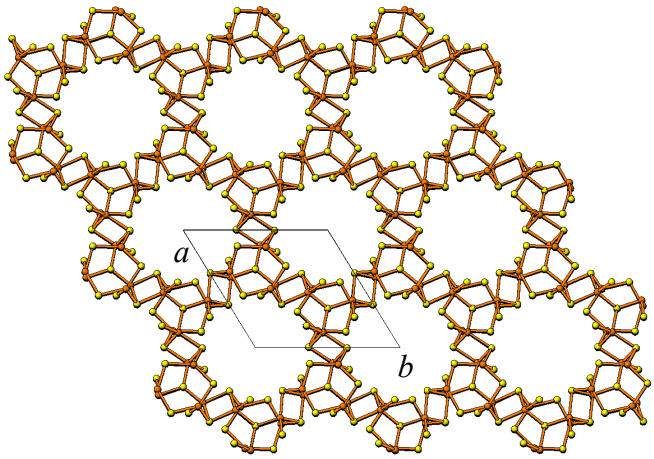

Figure 1.49. View of the $[C_7H_{10}N][In_9Se_{14}]$ structure on (001) plane. In atoms are shown in orange and Se in yellow.

Another interesting material which is formed with different clusters is $Na_5(In_4S)(InS_4)\cdot 6H_2O$ [148] (Figure 1.50). It is denoted as ICF-29 and can be understood as a structure derived from the perovskite ($CaTiO_3$), which contains simultaneous substitutions of all atomic sites by tetrahedral buildings units: Ti^{4+} by $(SIn_4)^{10+}$; O^{2-} by $(InS_4)^{5-}$ and Ca^{2+} by $[Na\cdot 6(H_2O)]^{5+}$. This material contains an unusual $(SIn_4)^{10+}$ unit, in which S is coordinated by four In^{3+}. The building unit hence consists of $[SIn_4(InS_4)_{6/2}]^{5-}$ clusters which are formed by a central SIn_4 tetrahedron surrounded by InS_4 tetrahedra. Each cluster is connected through six peripheral InS_4 tetrahedra of adjacent clusters. These units are linked, forming cavities of eight members, where the Na^+ and its hydrated coordination sphere are located. The three-dimensional quaternary chalcogenide $[Na_5Zn_{3.5}Sn_{3.5}S_{13}]\cdot 6H_2O$ [142] presents an analogous structure.

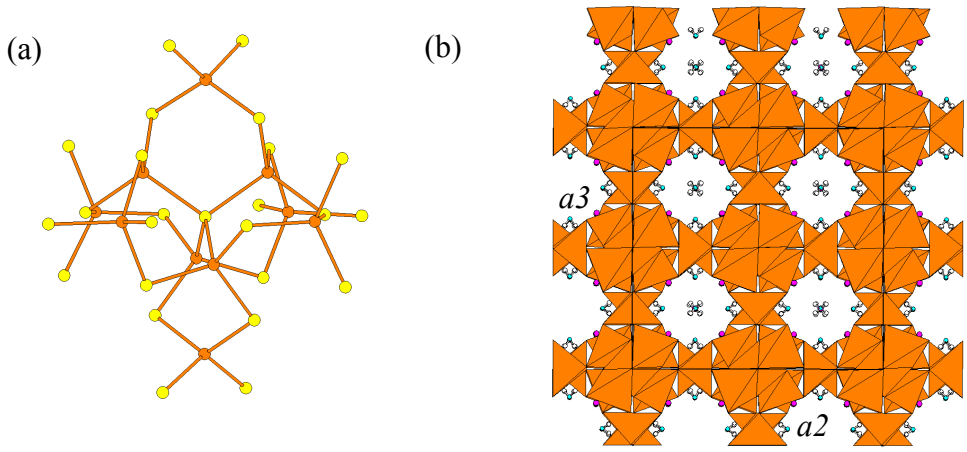

Figure 1.50. ICF-29 (a) $[In_9(\mu\text{-}Se)_4(\mu\text{-}Se)_6Se_{5\times 1/3}]$ unit and (b) view on the (001) plane. In atoms are shown in orange, S in yellow, Na in pink, O in blue, H in white, and InS_4 tetrahedra in orange.

A purely inorganic framework is found in $(NH_4)[In_{12}Se_{20}]$ [149]. The structure is formed by nona-nuclear clusters of $[In_9(\mu\text{-}Se)_4(\mu\text{-}Se)_6Se_{5\times1/3}]$, which are built up by interconnection of tri-nuclear $[In_3Se(Se_{1/2})_6]$ and binuclear $[In_2Se_{1/3}(Se_{1/2})_6]$ units. The former unit consists of three $InSe_4$ tetrahedra with a common corner and the binuclear units consist of two $InSe_4$ tetrahedra also with a common corner. The nona-nuclear clusters are linked to each other by sharing corners between their binuclear units and as results form columns running along the *a*-axis, which are linked. The columns are arranged in a hexagonal fashion resulting in a honey-comb type lattice (Figure 1.51).

Other three-dimensional hybrid structures were produced i.e. $Mn(en)_2Ga_2S_4$ [129]. The structure contain $[GaS_2]^-$ chains which run parallel and are separated by Mn^{2+} centres coordinated by two molecules of ethylenediamine and by two S from different chains; as a consequence, a three dimensional network is produced. A related compound, presenting the same features, was reported based on an indium chalcogenide framework [135].

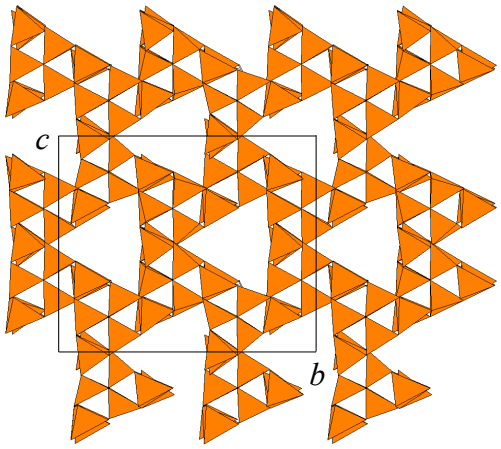

Figure 1.51. View of $[(NH_4)In_{12}Se_{20}]$ along the *a*-axis. InS_4 tetrahedra are shown in orange and NH_4^+ cations are omitted for clarity.

1.5. Applications and Properties

The structure-property relationship is an important factor in the design of new materials. Metal chalcogenides are materials with interesting properties and form a large number of structures. However, there is a special interest in three-dimensional structures because they present cavities which would permit their use for shape- and size-selective catalysts, ion exchangers and adsorbents.

Electronic structure

Supertetrahedral clusters can reach dimensions of up to 2.3 nm and, therefore, this type of crystalline material can be considered as crystals formed by nanoclusters.

Semiconducting nanoclusters are used in detector devices and their properties are related to their size [150]. Three-dimensional supertetrahedral compounds present the properties of arrays of nanoclusters, avoiding dispersion and orientation problems. The electronic structure of the supertetrahedral chalcogenide cluster $[In_{10}S_{18}]^{6-}$ [90], which crystallizes in a cristobalite lattice was modelled [151]. This work demonstrated that the pores can be considered as particle-in-box (PIAB) acceptor 'deep-level' states. The PIAB states decrease rapidly when the angle between the different units which form the cavity increases from an initial value of 109.5º, producing a decrease in the band gap value. Therefore, an array of pores in supertetrahedral chalcogenide frameworks behave as an anti-dot lattice, where electronic states are localised within the holes and the charge is compensated by the counter-ions, needed to stabilise the structure. The band gap value will depend on the nature of the elements forming the structure and the angle between units. Other studies have focused on the band energy-state of isolated clusters [81], concluding that the valence band is dominated by sulphur lone-pair orbitals, which produce a wide band due to their weak bonds. As a consequence, these materials present a sharp intensity band gap suitable for materials employed in efficient lasers and solar cell devices (which require high band gap energies).

Ion-exchange properties

Chalcogenide structures present an affinity for heavy atoms. This property has been studied for its application in the purification and extraction of toxic elements. The effectiveness of one-dimensional metal chalcogenides structures in exchanging cations such as Rb^{+}, Cs^{+}, Fe^{3+} or Cu^{2+} has been proven [152,153]. Ion-exchangeability is among the most common properties of open-framework solids. The capacity of supertetrahedral metal chalcogenide materials to undergo ion-exchange was explore through experiments which indicate that exchange with mono- and divalent cations (Li, Na, K, Rb, Cs, Mg, Ca, Sr, and Ba) takes place. In addition, they present a high selectivity for heavy cations in water solutions, which are comparable with that of mesoporous thio-functionalized silicates [154,155], which are the most efficient adsorbents for heavy-metal cations [149,156] currently available. The efficiency on the exchange of species depends on the nature of the counter-ion and their relationship with the framework. It is known that two-dimensional layers of supertetrahedral clusters combined with surfactants present a high affinity for various alcohols over water [74]. This high affinity means that they have many potential applications in the separation and purification of alcohols.

Surface area and volume distribution

Gas adsorption is commonly used in the characterisation of porous materials, allowing the determination of the specific surface area, pore volume and size distributions. Pores are classified on the basis of their diameter as micropores (below 2 nm), mesopores (between 2 and 50 nm) or macropores (above 50 nm) [157]. In siliceous ordered mesoporous materials [158,159] it is observed that when the isotherms do not reach levels below a relative pressure of 0.1, the material is likely to contain an appreciable amount of micropores. Chalcogenides with structures similar to those who show the type I isotherm characteristic of microporous solids and high capacity of adsorption [94,90]. For compound UCR-20GaGeS-TAEA [94] (with structure analogous to sodalite) exhibit the type I isotherm, the BET surface area is 807 m^2 g^{-1} and the micropore volume of 0.23 cm^3g^{-1}.

Ionic Conductivity

The electrical conductivity of chalcogenides is due to contributions from electronic states of the inorganic frameworks (including discrete clusters and extended structures of clusters and tetrahedra) as well as the interaction with counter ions and solvents. Supertetrahedral chalcogenide structures demonstrate the appropriate characteristics to be used as electrical conductors because they are usually porous three-dimensional structures. The chalcogenide frameworks present a higher polarisability than O^{2-} frameworks and the negative charge is distributed along the structure; which means the interaction with the counter ions is weak and favours the migration of mobile cations. However, the use of solvothermal methods in the synthesis of chalcogenide frameworks implies the use of organic templates which are difficult to remove without collapsing the structure [160].

Three-dimensional hydrated supertetrahedral clusters presenting a high ionic conductivity have been produced [105] and are denoted by the abbreviation ICF (Inorganic Chalcogenide Frameworks). They constitute a family of compounds with several compositions. Their conductivity values increase with temperature. The highest specific conductivity achieved among open frameworks chalcogenides is 0.15 $\Omega^{-1}cm^{-1}$ at 27º C and under 100% relative humidity [98] which is comparable with known crystalline sodium or lithium conductors [160].

Photoluminiscent and Photocatalitic Activity

Another application that has been developed is the synthesis of supertetrahedral chalcogenide structures with band gaps lying in the visible-light region. Several approaches have been carried out such as the insertion of transition metals [86,103] or the combination of chalcogenides within frameworks [161,162]. A porous structure is a potential host for metal complexes or dyes optically active in the visible region. Some examples of these materials are the family of compounds ICF [96] and UCR [94] whose band gaps values lie over the range from 2.0 to 3.6 eV.

Initial exploration of the photo-catalytic activity in supertetrahedral chalcogenides concludes in promising results subject to further studies [163]. For example, the quantum efficiency for ICF-5CuInS-Na was found to be *ca.* 3.7% at 420 nm, higher than in condensed phases such as $CuInS_2$ with the cubic-ZnS structure or $CuIn_5S_8$ with the spinel structure. The quantum yield of $CuIn_5S_8$ with Ag_2S as co-catalyst was reported to be smaller than 0.02 % at 460 nm and 298 K while the efficiency of $CuInS_2$ was even lower [164]. Also ion-exchange experiments demonstrated the incorporation of $[Fe(2,2'\text{-bipydirine})_3]^{2+}$ complexes into the framework of UCR-20GaGeS, which exhibits photo-catalytic activity under the UV light [96].

1.6. Aims

Given the literature review that has been provided in this chapter, the following aims in the synthesis of supertetrahedral gallium sulphides can be proposed:

- To synthesise novel tetrahedral gallium sulphides with semiconductor properties, focusing on the preparation of three-dimensional structures, materials containing large clusters, compounds containing hybrid clusters with improved semiconductor properties and other extended structures.
- To produce a full structural characterisation of the compounds using powder and single X-ray diffraction, elemental analysis, thermogravimetric analysis and FTIR.
- To study physical properties such as optical absorption, using diffuse reflectance of the materials produced. Additionally, ion-exchange properties of three-dimensional gallium-sulphide open-frameworks will be examined by ion-exchange experiments and adsorption/desorption isotherms.

These objectives were met in the work detailed in this thesis. The results presented in this thesis will help in the development of the understanding of gallium sulphides and in the study of their properties.

Chapter 2: Experimental methods

2.1. Synthetic methodology

2.1.1. Solvothermal synthesis

Solvothermal synthesis is employed for the crystallisation of compounds from mild temperature solutions at high vapour pressures which is created by the vaporisation of the solvent. When the solvent is water, it is called hydrothermal synthesis. It was historically applied to the study of geothermal processes, in an attempt to mimic conditions for the synthesis of zeolites [32], and for crystal growth processes such as in the production of quartz [165]. It is extensively used for the production of different type of materials, resulting particularly useful in the synthesis of new open-framework materials such as zeolites, aluminophosphates, recently applied to MOF's [107]. These materials present interesting applications such as molecular sieves or catalyst, and therefore, their synthesis was expanded up to industrial scale [166]. In 1989, Bedard and co-workers [167] extended this method to the synthesis of chalcogenides. The synthesis can be performed using a sealed Teflon vessel contained in stainless steel autoclaves (Figure 2.1).

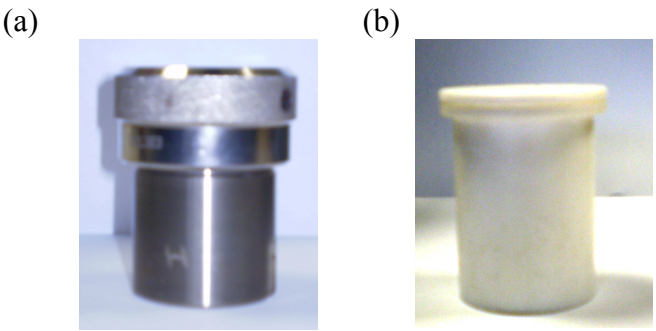

Figure 2.1. (a) Parr acid digestion bomb. (b) Teflon vessel.

At high pressures and temperatures, the solvent within the autoclave is over-heated and can even become a supercritical fluid. These conditions favour an intimate contact between reactants, increasing dramatically their reactivity, producing new materials and/or metastable phases.

The design of open-framework materials is related to the use of a substance called template in the synthesis. The purpose of this molecule is attributed to directing-agent, space filler or counter ion roles, and therefore, there is not a clear function. The template is essential on the reaction. Another important factor in the design of the experiments is that the autoclave does not permit monitoring of the crystal growth or the

evolution in the reaction. However, the condensation mechanisms are sensitive to factors including solvent, temperature, reaction time, reagent ratios and pH. All those can be fixed and controlled in the beginning, favouring oriented synthesis of new materials.

In this work, the synthesis of new materials is carried out under solvothermal conditions, using Parr Acid Digestion Bombs (model 4748) with 23 ml of capacity. At the beginning of each experiment, proper amounts of reagents and solvent are loaded in the Teflon-lined vessel, the mixture is stirred for 10 min, and the pH is measured. The system is then sealed in the stainless steel autoclave. The autoclave is placed inside an oven at room temperature, and heated in the range of 423-473 K at 1 K min^{-1}. Higher temperatures result in deformation of the Teflon vessel. The reaction times between 5 to 20 days were used. After this period, the oven is cooled down to room temperature at 1 K min^{-1}. The bulk product is filtered and washed with methanol, water and acetone, and dried in air at room temperature before analysed. Crystalline products were primarily analysed using single crystal X-ray diffraction and powdered products by power X-ray diffraction. A number of organic amines named in the following chapters are listed in Appendix I containing the systematic names, the acronyms and the structures.

2.1.2. Parallel solvothermal synthesis

Our inability to predict the required reaction conditions, combined with the serial nature of synthetic studies involving individual Teflon-lined stainless steel autoclaves, makes the discovery of new materials a time-consuming process. High-throughput (HT) methods are powerful techniques for the rapid investigation of a large number of reaction parameters in a short time. The development of automated systems and autoclave chambers such as multiple autoclaves [27], multi-reactor autoclave [28] or autoclave blocks [168] has been successfully implemented for hydrothermal synthesis. They contribute to accelerated discovery of new materials and the optimization of synthesis parameters [22]. HT approaches have been successfully applied to the hydrothermal synthesis of zeolites [27], phosphates [169-172] and arsenates [172]. Multiple reactions can be carried out at the same time, reducing the time and cost that the same reactions would require in the Teflon-lined autoclaves. The only possible negative factors are the scalability and reproducibly of the products and cross-contamination issues.

In this work, the parallel methodology employed by Dr R.J.E. Lees for the solvothermal synthesis of antimony sulphides [173] has been applied to gallium sulphides. The method consists of the use of Teflon-FEP (Fluorinate Ethylene Propylene) bags as they are reactor vessels (Figure 2.2). The bags are made from small pieces of Teflon tube which are sealed. The size and properties of this material allows confining of all the bags simultaneously in Teflon-lined autoclaves.

Figure 2.2. Batch of sealed FEP bags ready for reaction.

The initial procedure consists of the preparation of the bags. 4 cm sections of tubing of FEP (Adtech, 19 mm ID x 20 mm OD) were secured at one edge with a large clip and sealed using modified Antex heated pliers, fitted with a thermostat set at 543 K (Figure 2.3); producing a open Teflon bag ready for filling.

(a)

(b)

Figure 2.3. (a) Hot pliers. (b) Thermostat.

Afterwards, the Teflon bags are filled with solid reagents (total mass not higher than 0.3 g) and a maximum volume of 1 ml of solvent. Then, they are secured from the fixed edge and sealed in the top to obtain a hermetic bag. After sealing, each bag is gently squeezed to locate possible leaks. Approximately 18 Teflon bags were placed in a 125 ml Teflon lined steel (Parr Acid Digestion Bomb 4748). In order to balance the

vapour pressure of the solvent within the bags during the reaction, 15-20 ml of solvent is also added to the autoclave before closing. The autoclave is placed in an oven and heated at 423-443 K for 5-10 days. Afterwards, it is cooled down to room temperature at 1 K min^{-1}. The product from each reaction is filtered and washed with water, methanol and acetone, and it allowed to dry in the air at room temperature. Final products are analysed by X-ray diffraction. When a new phase is identified, the reaction was scaled up to three-fold in 23 ml Teflon-lined stainless steel autoclaves in order to obtain enough products for physical and structural characterisation. The optimised reactions are described through the experimental section. A summary of the reactions carried out using parallel synthesis can be checked on Appendix IV. Additionally, information related to unexpected synthesis of compounds under solvothermal synthesis is reviewed in Appendix V.

2.1.3. Ion-Exchange experiments

Ion exchange is the exchange of ions between two electrolytes or between an electrolyte solution and a material. The first time the exchange process was observed in materials was in the early twentieth century by Gans [174], who observed that aluminosilicates were able to soften hard waters.

Typical ion exchanger materials are ion exchange resins, zeolites, clay and soil humus. Depending on the type of ion to exchange there are types of cation exchangers, anion exchangers or amphoteric exchangers. To date, there is large number of applications. The most typical example is preparation of high purity water for power engineering or the production of soft water for laundry purposes or filters. Several techniques were developed such as ion-exchange chromatography which is widely used for chemical analysis in the separation of ions. Ion-exchange processes are also used to separate and purify metals.

Open framework sulphides are usually constituted by an inorganic metal sulphide skeleton, which is charged negatively and is compensated for cationic species. The nature of this bonding makes them potential ion-exchange materials. Supertetrahedral gallium sulphides normally present this kind of structure, where amines compensate the charge balance. The bonding between amines and the inorganic framework is very weak and, consequently, the substitution by inorganic cations is feasible. Appropriate amounts of chalcogenide material (20-100 mg), water and a solid exchange salt are loaded into a 100 ml conical flask which is then sealed with paraffin paper. The mixture is heated at temperatures over the range 300 to 348 K with or without

continuosly stirring for a period between 1 to 7 days. After cooling down, the mixture is filtered and washed with distilled water, methanol and acetone.

2.2. Microscope Examination

The products of the reactions are examined using an optical Meiji microscope to establish the presence of crystals. The optical microscope is also used to pick up pure crystalline phases from the bulk product by handpicking.

2.3. X-ray diffraction

The study of the crystal structure of the new materials is carried out using X-ray diffraction methods. The X-ray presents a wavelength with the same magnitude size as the atoms. X-ray techniques are used in a large number of methods and are the most common techniques to solve structures.

X-rays are produced by bombarding a metal target, often Cu or Mo, with a beam of electrons emitted from a heated filament. The incident electron beam will ionize electrons from the K-shell (1s) of the target atoms, and X-rays are emitted as the resultant vacancies are filled with electrons from the L (2p) or M (3p) levels, which gives rise to the intense K_α and K_β radiation. For the selection of one of these two radiations, a crystal monochromator is usually used. When a crystalline material is irradiated with an X-ray source, it acts as a three-dimensional diffraction grating. This interaction with the atoms produces scattering and interference processes, related with the atomic arrangement.

The scattering effect from an X-ray beam is explained by the Bragg's law (2.1), which defines the relationship between the paths of two X-ray beams to obtain a constructive interference in a set of lattice planes (Figure 2.4).

$$n\lambda = 2d_{hkl} \sin\theta \qquad \textbf{(2.1)}$$

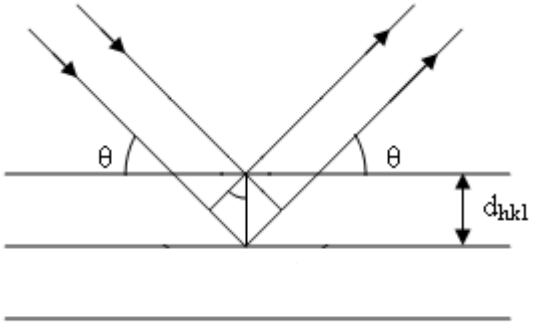

Figure 2.4. Bragg reflection from crystal planes with spacing $d_{hkl.}$

2.3.1. Powder X-ray diffraction

A powder sample will contain an infinite number of randomly oriented crystallites. Each set of lattice planes *hkl* will accordingly scatter at the appropriate *2θ* angle, in agreement with the Bragg equation and, since all possible orientations of crystallite are presented, a cone of scattering beams will be formed (Figure 2.5).

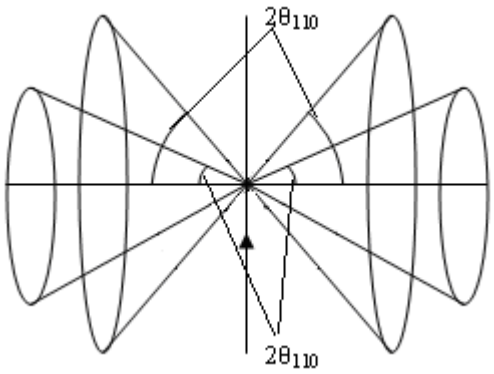

Figure 2.5. Scattering of X-rays into cones by a powder sample.

The diffracted beams may be detected either by surrounding the sample with a strip of film (see Debye-Schrerrer and Guinier focusing method) or by using a movable detector. The result is the diffraction pattern of the substance, which can be considered as a fingerprint of the material, and is directly related with the internal structure.

The powder X-ray diffractograms were recorded with three different instruments, due to the installation of new instruments during the course of this project. Initially a Philips PA2000 powder diffractometer with nickel filtered Cu-$K_{\alpha 1}$ radiation (λ = 1.54056 Å) was used. Samples were mounted on a glass slide and data were collected in over the angular range $4.5 \leq 2\theta/° \leq 50$, counting for 1s at 0.05° increments in 2θ. A D8 Advance Bruker diffractometer fitted with Bruker LynxEye linear detector was employed. It was used for long exposure experiments and single crystal samples. The D8 Advance diffractometer is operating with germanium-monochromated Cu-$K_{\alpha 1}$ radiation (λ = 1.54056 Å) and operated by Bragg-Brentano geometry (reflection). Zero background holders were employed using Vaseline to fix the sample. And a D8 Discover Bruker diffractometer was used for the analysis on the parallel synthesis products and bulk product samples for a short time exposure experiments or small amount of material. The instrument was operated by parallel beam geometry (generated by a Göbel mirror) running Cu-K_{α} radiation (λ = 1.54184 Å) and operated in transmission geometry. A Bruker LynxEye linear detector was employed. A 96 holder

plate was used for the experiment. Data were collected in step-scan mode over the angular range $4.5 \leq 2\theta/° \leq 50$ in 0.02° increments for 39.5 s per step in both cases.

The powder X-ray diffraction patterns from the bulk products were compared to the simulated XRD pattern produced from the crystal structure solution. This was created using the software Powder cell (version 2.4) [175] and TOPAS [176] for crystalline samples containing small single crystals. When possible, phases were identified using the Inorganic Crystal Structural Database (CSD) [177] and Powder Diffraction File Database (PDF) [178].

2.3.2. Single crystal X-ray diffraction

Single crystal X-ray diffraction is based on the same principles of powder diffraction. However, when an X-ray beam is scattered by a single crystal, a three-dimensional diffraction pattern is obtained (Figure 2.6).

(a) 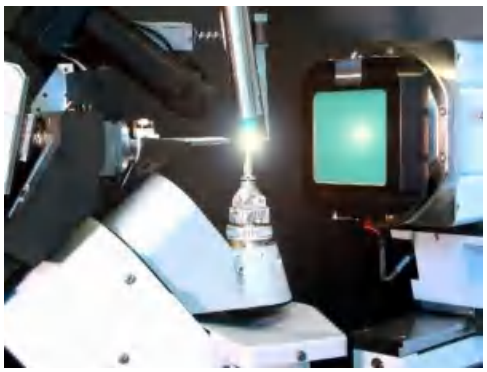 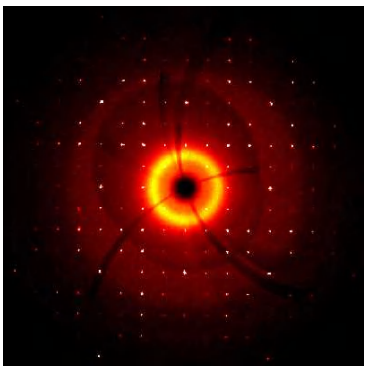 (b)

Figure 2.6. (a) Single crystal diffractometer operating. (b) Typical diffraction frame. Pictures courtesy of X-Ray laboratory, Chemistry Department, Heriot-Watt University.

The X-ray beam is fixed and the crystal is rotated in different positions with reference to four angles φ,χ,ω and 2θ (the latter corresponds to the detector orientation). Once the crystal is positionally defined, a short experiment to determine the unit cell is carried out.

X-rays are treated as a mathematical function corresponding to a wave. This function is characterised by its intensity which is proportional to the square of its amplitude, and its phase. Scattering is proportional to the interaction between X-rays and electron density, so heavy atoms with high atomic number will produce strong scattering. The efficiency of X-ray scattering from an atom is called scattering factor, f_0. It also depends on the wavelength of the radiation and the Bragg angle θ. The dependency on the angle is caused because atoms are discrete and, at high angles, the

beam produce destructive diffraction because interacts with the electron cloud, resulting in a scattering decrease.

The resultant constructive wave from all atoms for a certain *hkl* reflection is called the structure factor, $\mathbf{F_{hkl}}$ (2.2)

$$F_{hkl} = \sum_j f_j e^{2\pi i(hx_j + ky_j + lz_j)} \quad \textbf{(2.2)}$$

Where f_j is the scattering factor of the j^{th} atom, and it can be considered as the amplitude; and (x_j y_j z_j) are its fractional coordinates as the phase of the equation, respectively. This equation can be expressed in terms of sines and cosines, it is known as Fourier series. In a centrosymmetric structures and with n unique atoms in the unit cell (2.2) is simplified as (2.3).

$$F_{hkl} = 2\sum_n f_n \cos 2\pi(hx_n + ky_n + lz_n) \quad \textbf{(2.3)}$$

The electron density distribution within a crystal can be expressed as function of Fourier series in three dimensions (2.4):

$$\rho(x,y,z) = \frac{1}{V}\sum_h \sum_k \sum_j F_{hkl} e^{-2\pi i(hx+ky+lz)} \quad \textbf{(2.4)}$$

Where, $\rho(x,y,z)$ is the electron density at a position (*x y z)* in the unit cell and *V* is the volume of the unit cell. The electron density expression is the Fourier transform, between factors (which are related to the reciprocal space) and density (which is corresponding to real space) and in the other way around

As the intensity for a *hkl* reflection is proportional to the square of the structure factor (2.5),

$$I_{hkl} \propto F_{hkl}^2 \quad \textbf{(2.5)}$$

Because the square root of the intensity is proportional to the modulus of the structure factor, but not its sign; the electron density cannot be calculated, and thus the atomic positions. This is called **the phase problem**.

Before using the data obtained from the diffraction experiment, some corrections have to be made, this is called data reduction:

i) The Lorentz correction, L, corresponding to experiment procedure; the diffraction for some lattice planes is measured for a longer time than for others.

ii) The polarization correction, p, consequence of the X-ray beam being partially polarized on the reflection process.

iii) Absorption correction, related to the crystal size and shape.

After all these considerations, resolution methods are based on reiterative trial phases for the structure factor. Two main types of method are normally employed to determine the crystal structure:

1) Patterson method: this method uses a Fourier summation rather similar to the electron density distribution (2.4), but the intensity data form the coefficients (2.6).

$$p(u,v,w) = \frac{1}{V}\sum_{h}\sum_{k}\sum_{j}\left|F_{hkl}\right|^2 e^{-2\pi i(hu+kv+lw)} \qquad \textbf{(2.6)}$$

The resulting Patterson map looks similar to a Fourier map, but the regions of high electron density correspond to vectors between pairs of atoms. This information helps to find relative positions of heavy atoms, and may suggest the position for others. Fourier methods are then applied to complete the structure determination.

2) Direct methods: they are usually applied when the structure has atoms with similar scattering properties. The method is based on the calculation of the probabilities for the phase values and, thus, an electron map of the unit cell. Once the atoms in the structure are located, a calculated set of structure factors, $\mathbf{F_c}$, is determined for comparison with the $\mathbf{F_{obs}}$ magnitudes. The positions of the atoms are refined using least-squares. In the refinement process, restraints and constraints are applied to minimize thermal motion or adjust isotropic/anisotropic displacement parameters. The residual index, or **R** factor, (2.7) gives a measure of the difference between the observed and calculated structure factors and therefore of how well the structure is refined.

$$R = \frac{\sum\left|\left(\left|F_o\right| - \left|F_c\right|\right)\right|}{\sum\left|F_o\right|} \qquad \textbf{(2.7)}$$

A low R value (0.2-0.7) is usually indicative of a better structure determination. Nevertheless, a low standard deviation on atomic positions and bond length is also reliable on a good solution.

For the preparation of the sample, a single crystal was selected and mounted on a glass fibre using cyanoacrylate, and it was supported with wax on a tip, which was fitted in a goniometer head to place and locate the crystal in the instrument. The crystal was

then centred with the X-ray beam and its dimension measured using a video camera (typical dimension 0.3 x 0.1 x 0.1 mm).

X-ray intensity data were collected at room temperature or 100 K in order to reduce frequent thermal disorder for the organic components in the structure, using a Bruker X2 APEX 2 diffractometer [17] with graphite monochromated Mo K_α radiation (λ= 0.710073 Å).

Good quality crystals were selected collecting frames with 10 to 30 second X-ray exposure, taking into account the shape and intensity of the spots and the resolution. Resolution limit values lower than 0.8 Å produce poor quality data set**.**

Experiments and data were directed and collected using Apex-2 software [179]. The first step was the determination of the unit cell for each crystal. The data were compiled in three matrixes composed by 12 frames which were collected from 10-30 second X-ray exposure, for 60° ω sweeps at φ angles of 0°, 120° and 240° at constant 2θ and χ angles. The reflections were harvested and indexed to a unit cell using direct methods and, finally, refined. The quality of the crystal and the calculated unit cell were determined checking the percentage of spots well fitted with the assigned unit cell (not less than 75%), their residual values (RMS, root mean squares) corresponding to cell dimensions (RMS xyz, not higher than 0.03 mm) and the angle values (RMS angle, not greater than 0.5º).

For each crystal, the data collection strategy was determined in the proposed crystal system with a resolution limit not higher than 0.6 Å, and between 10-30 seconds X-ray exposure per frame. Collections were typically 10-20 hours in length and collected at least 99% completeness of the data and *ca*. 4 redundancy. Data correction was carried out using SADABS software [180]. Before the data were used to solve and refine the crystal structure, it was necessary to convert the information recorded on the frames into a set of integrated intensities and to put all of the measurement data on the same scale. A list of reflections was produced with *hkl*, $|F_o|$ and the standard uncertainty $\sigma(F_o)$. The determination of the space group was performed using XPREP [179]. This software evaluates the systematic absences for all collected reflections, taking into account the intensities and I/σ rations, and proposes space groups compatible with those systematic absences. The structures were solved by direct methods using the SIR92 program [181] and models were refined using CRYSTALS [182]. In some cases, carbon and nitrogen atoms were located using Fourier maps. Hydrogen atoms were placed geometrically, and possible effect of solvent disorder was modelled using

SQUEEZE [183]. The goodness of fit was around 1.00, and the typical residual value was around 0.02-0.07 for a complete model in all the cases.

2.4. FTIR

The presence of organic molecules was confirmed by using FTIR. A small amount of bulk sample (*ca.* 5 mg) was mixed and ground with CsI at room temperature and pressed under vacuum at 10 tones for 5 min, until a 5 mm diameter pellet with 1-2 mm thickness was obtained. Infrared spectra were recorded in the 500-4000 cm^{-1} range on a Perkin Elmer spectrum RXFT-II System.

2.5. Elemental analysis

Elemental analysis was carried out by Mrs Christina Graham at Heriot-Watt University using an Exeter CE-440 Elemental Analyser for C, H and N analysis. An accurate amount of sample in a tin capsule is heated up to 1223 K in a tube oven under oxygen atmosphere. At this temperature, the capsule is combusted to SnO_4, and the temperature is then increased at 2073 K, at which the sample is completely burnt, giving CO_2, N_2, nitrogen oxides, H_2O and other products, that are removed by scrubbing. In a second step, the remaining oxygen is removed and the nitrogen oxides are reduced to N_2. The gases (under the same conditions of temperature and pressure) are transferred to a mixing area and a small proportion is analysed by thermal conductivity cells, to detect and quantify the amount of CO_2, N_2 and H_2O.

2.6. Thermogravimetric Analysis

Thermogravimetric analysis (TGA) is the measurement of the variation of the weight of a substance when subjected to a controlled temperature program. The difference of weight on the sample is plotted against the temperature or time. The final product is analysed by X-ray diffraction powder to identify the residue.

TGA measurements were carried out in a Dupont instrument 951 thermogravimetric analyser. Finely ground single crystal samples (*ca* 7 mg.) were loaded in a quartz crucible. The crucible was placed in the TGA arm balance and heated under a 60 ml/min flowing nitrogen atmosphere at a rate of 2-5 K min^{-1} up to *ca.* 1073 or 1273 K with isothermal hold for 60 min.

2.7. Diffuse Reflectance

The visible and ultraviolet regions correspond to the electron transitions of atoms and molecules. The Beer-Lambert law (2.8) is applied in the study of gases and solutions, because light is usually transmitted by them when irradiated and other processes which involve loss of energy are not significant.

$$I = I_o e^{-kx} \tag{2.8}$$

Where, I and I_o are the observed/original intensities, k is the absorption coefficient and x the distance through the system.

In the solid state, materials are composed of disperse particles, whose sizes are of the same order of magnitude of the radiation wavelengths and this causes reflection and scattering processes. The light is no longer transmitted and is lost inside the material. For that reason, a different instrumental setup is necessary. Diffuse reflectance is the study of the light that has been reflected or scattered (as a function of wavelength) from a solid with a flat surface.

The reflecting power (R), characterised by the scattering coefficient (s in cm^{-1}), is related to the absorbance capacity, and defined by the absorption coefficient (β in cm^{-1}). This relationship is the Kubelka-Munk function [184] (2.9):

$$F\left(R_\infty\right) = \frac{\left(1-R_\infty\right)^2}{2R_\infty} = \frac{K}{S} \tag{2.9}$$

Where the new terms are described as K= (2 β) as total absorption coefficient and S= (2s) as total scattering coefficient. R_∞ is the reflecting power at infinite thickness of a sample. Assuming that:

i) the incident light is monochromatic in nature,

ii) the surface of the sample has an isotropic distribution of particles, which produce the scattering,

iii) the particles are randomly distributed,

iv) the particle size is smaller than the thickness of the sample layer.

The measurement of R_∞ is always related to a white standard (reference) (2.10):

$$R'_\infty = \frac{R_{sample}}{R_{standar}} \tag{2.10}$$

Substances such as $BaSO_4$, MgO, $MgCO_3$, NaCl, SiO_2 or TiO_2 are commonly used as standards, for which it is assumed K = 0 in the region of interest. Diluting the sample on the powdered standard and measuring against the same pure standard gives an accurate result. The representation of $F(R_\infty)$ as function of the wavelength gives the absorption spectrum of the material. However, when the scattering coefficient is independent of the wavelength and if the standard itself has no absorption [184], it is coincident with that measured in transmitted light.

Gallium sulphides present a semiconductor nature. They are characterised by an electronic structure constituted by a filled valence band, which is produced from sulphur atoms 's' and 'p' orbitals, and an empty conduction band attributed to the empty cations orbitals, gallium in this case. The difference in energy between both bands is called band gap, and it usually lies to energies *ca.* 0.05 and 9 eV. The band gap gives rise to an intense absorption edge in the absorption spectrum, which can be determined using diffuse reflectance. The calculation of the band gap is determined as the value corresponding to the interception of the extrapolation of the absorption edge with the base line, corresponding to the experimental data [185]. Diffuse reflectance was successfully applied in sulphides [186]. When the baseline differs from the x-axis, the linear increase in diffuse reflectance is determined by extrapolation of both sides of the curve with a linear regression. The merging point between both lines indicates the value on the x-axis that is taken as the value of the energy band gap of semiconductors [187].

Diffuse reflectance measurements were collected using a Perkin Elmer Lambda 35 UV-Vis Spectrometer. $BaSO_4$ was used as a reference (100% reflectance). Hand-picked single crystals samples (*ca.* 15 mg) were ground and deposited as a smooth thin layer over a diffuse reflectance holder, previously filled and pressed to the top with $BaSO_4$. This was then equivalent to diluting the sample in the standard material. The sample holder is located into the instrument and the sample is scanned between 200-1100 nm (1.2-6.2 eV) in steps of 240 nm min^{-1}, with the slit open at 4 nm.

2.8. BET. Specific surface and pore volume distribution

Ion-exchange properties are considered as one of the several applications of three-dimensional open-frameworks. When ions are exchanged in one material its composition changes and microvolumes are created, depending on the charge and size of the exchanged species. In addition, elemental analysis, X-ray powder diffraction and adsorption/desorption isotherms were performed to determine the specific surface area

and the pore volume distribution. The absorption/desorption isotherm shapes are classified in BDDT system (Brunauer, Deming, Deming and Teller), providing information of the material porosity. Microporous materials usually produce Type-I, characterised by a plateau a low P/P_o. Types-II, -III and –VI are mainly indicative of meso/macroporous, while types-IV and –V suggest the presence of mesoporosity (Figure 2.7).

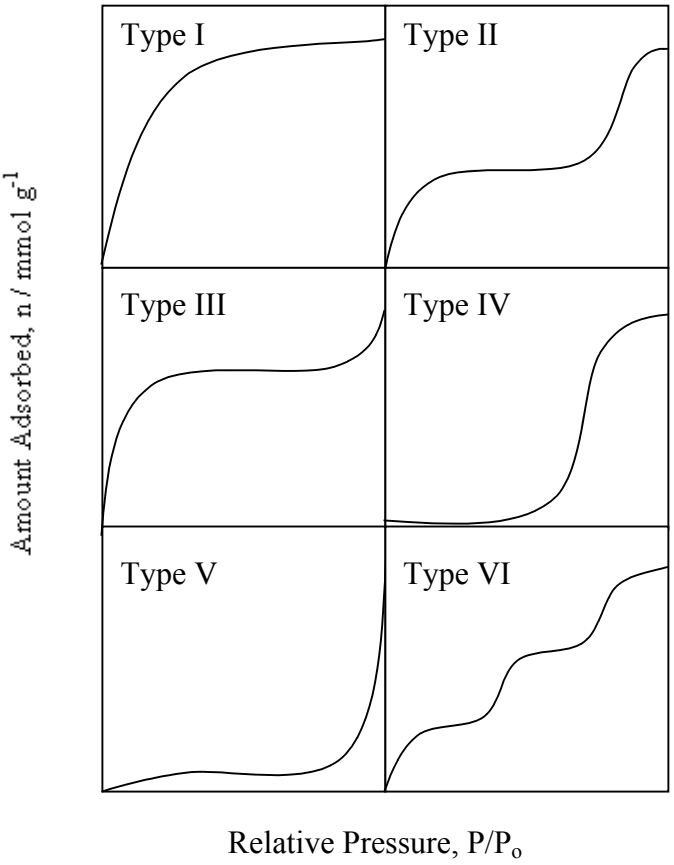

Figure 2.7. Diagrammatic representation of isotherm classification.

BET surface area analysis and pore size distribution were performed by Mr. Santiago Gomez-Quero in the catalysis laboratory (Chemical Engineering) at Heriot-Watt University, using a commercial Micromeritics Flowsorb II 2300. The sample was degassed at room temperature with 3 cycles of adsorption /desorption (in 20 cm^3 min^{-1} dry N_2), producing a flash effect. BET area was obtained in a 30 % v/v N_2/He flow (20 cm^3 min^{-1}) with at least three cycles of N_2 adsorption-desorption using the standard single-point BET method. N_2 adsorption/desorption isotherms were performed over the relative pressure range $0.05 \leq P/P_0 \leq 0.95$, where the total micropore volume and size distribution were obtained according to the method of Dollimore and Heal [188]. The

BET areas and raw pore volume values were reproducible to within ± 4 % and the values quoted in this thesis are the mean.

2.9. Measurement of the magnetic properties

2.9.1. Theory

The magnetic forces are produced by electrically charged moving particles. The matter contains electrons (negatively charged particles), and in consequence, magnetism is an inherent property of matter. Depending on the different behaviour of a substance under an external magnetic field it is possible to classify materials as diamagnetic, paramagnetic, ferromagnetic, anti-ferromagnetic and ferrimagnetic.

Interesting magnetic properties are susceptible to be presented in compounds of transition metals and lanthanides, which usually have unpaired 'd' and 'f' electrons, respectively. The different types of magnetic behaviour are studied with the application of an external magnetic field, and register the magnetic induction. **Susceptibility (κ)** of the sample per unit volume is the degree of magnetization of a material in response to an applied magnetic field and it is usually expressed as the **molar susceptibility (χ)** (2.11)**,**

$$\chi = \frac{\kappa F}{d} \qquad \textbf{(2.11)}$$

Where F is the formula weight and d the density of the sample.

Magnetic materials are also distinguished by their relationship between their molar susceptibility and the temperature. In general, the dependence of the temperature is explained by the grade of order/disorder in the electron alignment. Paramagnetic materials obey the Curie-Weiss law (2.12) where susceptibility is inversely proportional to the temperature:

$$\chi = \frac{C}{T + \theta} \qquad \textbf{(2.12)}$$

Where C is the curie constant and θ is the Weiss constant.

Magnetic properties are also defined in terms of the magnetic moment (μ) which is related with the susceptibility and the number of impaired electrons (2.13):

$$\chi = \frac{N\beta^2\mu^2}{3kT} \qquad \textbf{(2.13)}$$

Where N is Avogadro's number, β is the Bohr magneton and k is the Boltzmann's constant.

Substituting the constants by the corresponding values (2.14):

$$\mu = 2.83\sqrt{\chi T} \qquad \textbf{(2.14)}$$

2.9.2. Magnetic Measurements

The technique to determine magnetic behaviour is using a SQUID (Superconducting Quantum Interference Devices) and consists of an extremely thin electrically resistive junction (called the Josephson junction) between two superconductors. Superconductors are materials which undergo a transition at low temperatures to a state of zero electrical resistance and a near complete exclusion of magnetic fields. The direct mode of operation is performed as follows: the SQUID is first cooled down to its superconducting state; then a current is passed through it while the voltage across the junction is monitored. When the junction senses a magnetic field, the current flow is altered due to interference at the quantum level between two electron wave fronts through the junction, resulting in a change in voltage.

Magnetic susceptibility measurements were carried out on a Quantum Design MPMS-XL SQUID magnetometer located at the University of Edinburgh. Samples consist of handpicked single crystals (15-30 mg) which are loaded into a pre-weighted gelatine capsule. This capsule is placed in the middle of a plastic drinking straw free of magnetic impurities, and secured by internal pieces of straw which form the final sample holder (Figure 2.7). The holder is then attached to the end of the sample stick and lowered into the cryostat (Figure 2.8). The data were collected over the temperature range 5-295 K in 5 K steps in a field of 100 G, after cooling the sample to 5 K under a zero field.

(a)

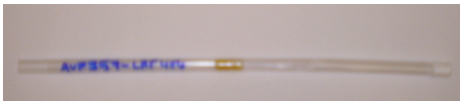

(b)

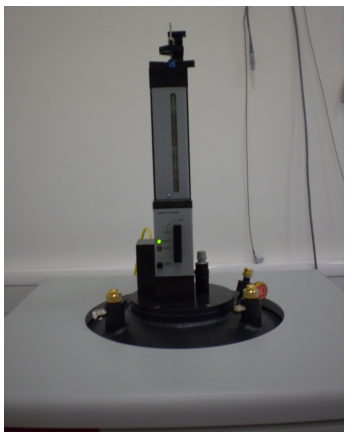

Figure 2.8. (a) Sample holder for SQUID measurements. (b) Sample stick.

The SQUID signal, M_{raw}, is obtained against the temperature. The value obtained is related with the magnetism and the weight of the sample. This value has to be corrected (M_c) (2.15) due to the diamagnetic contribution of the capsule**:**

$$M_{corr} = M_{raw} - M_{cap} \quad \textbf{(2.15)}$$

In order to determine the degree of magnetization of the sample, we have to calculate the molar susceptibility χ_m (2.16), and the final value is corrected (2.17) for the diamagnetic contribution of the ions within the formula unit.

$$\chi_m = \frac{M_{corr}}{F \times H} \quad \textbf{(2.16)}$$

$$\chi_c = \chi_m - \sum \chi_{ions} \quad \textbf{(2.17)}$$

The curvature of the plot χ_c *vs.* temperature will provide the kind of magnetic material. Plotting $1/\chi_c$ *vs.* temperature will serve to obtain magnetic parameters (*C* and θ) and the magnetic transition temperatures. The calculation of the effective magnetic moment (μ_{eff}) made by (2.18):

$$\mu_{eff} = \sqrt{\frac{8 \times C}{n}} \quad \textbf{(2.18)}$$

Where, *C* is Curie-Weiss constant and *n* is the number cations per formula unit.

Chapter 3: Inorganic supertetrahedral gallium-sulphide structures

3.1. Introduction

Supertetrahedral clusters are a frequently observed building unit in microporous chalcogenides. Supertetrahedral metal chalcogenides containing In, Ge or Sn [17,86] have been produced. In particular, a large number of indium-sulphide clusters are known and In and Ga belong to the same group and have similar behaviour. However, a small number of supertetrahedral gallium sulphides have been produced by Feng and co-workers, who applied the solvothermal method for the synthesis of these compounds [103].

In this chapter, supertetrahedral gallium sulphides have been obtained by solvothermal synthesis. Reactions involving gallium, sulphur and DEA resulted in the formation of three-dimensional structures which contain T3 clusters linked by their four vertices. Those reactions in that a transition metal salt was added resulted in the formation of larger building units. These phases consist of alternating T4 and T3 clusters linked by their vertices into a three-dimensional network.

3.2. Gallium-sulphide supertetrahedral structures

3.2.1. Synthesis

$[C_4H_{12}N]_6[Ga_{10}S_{18}]$ **(1)**: a mixture of gallium metal (69.5 mg, 1 mmol) and sulphur (66.3 mg, 2.1 mmol) in diethylamine (DEA) (3.4 ml) was placed in a Teflon-lined 23 ml stainless steel autoclave with an approximate stoichiometry 1:2.1:30, and heated at 443 K for 8 days. The final product consists of colourless crystals (identified as **(1)**), Ga_2S_3 and gallium.

$[C_4H_{12}N]_{12}[Ga_{20}S_{35.5}(S_3)_{0.5}O]$ **(2)**: was prepared from a mixture of gallium metal (139.7 mg, 2 mmol) and sulphur (145.4 mg, 4.5 mmol) in 3.4 ml DEA with a stoichiometry 2:4.5:30, loaded in a 23 ml Teflon-lined stainless steel autoclave, and heated at 463 K for 10 days. The product was constituted of white crystals of **(2)**, unknown white powder and gallium.

Isostructural materials to compound **(2)** were obtained using the similar reaction conditions with tetraethylenepentamine (TEPA) **(2.b)** and 4-aminomorpholine (Amp) **(2.c)**:

$[C_8H_{24}N_5]_6[Ga_{10}\ S_{16.5}(S_3)_{0.5}\ O]$ **(2.b)**: gallium metal (139.7 mg, 2 mmol), sulphur (144 mg, 4.5 mmol), 3.4 ml TEPA and 0.5 ml of methanol with a stoichiometry $2:4.5:30:1.2\times10^{-4}$ were mixed in a 23 ml Teflon-lined stainless steel autoclave, and heated at 473 K for 5 days. The product was formed by white crystals of **(2.b)** and unreacted gallium.

$[C_5H_{12}NO]_6\ [Ga_{10}\ S_{16.5}(S_3)_{0.5}\ O]$ **(2.c)**: gallium metal (139.4 mg, 2 mmol), sulphur (144 mg, 4.5 mmol) and Mmp (3 ml) with a approximate molar composition of 2:4.5:30 were loaded in a 23 ml Teflon-lined stainless steel autoclave and heated at 473 K for 20 days. The final product consisted of white crystals identified as **(2.c)** and unreacted gallium.

3.2.2. Structure description

Crystallographic information and refinement details for compound **(1)** and **(2)** are given in Table 3.1. The non-hydrogen atomic coordinates, bond lengths and angles are summarised in Appendix II. The structures were solved using direct methods, which located the Ga and S atoms. The organic component on the structures presented high disorder and could not be placed. Solvent disorder was modeled using SQUEEZE [183].

For compounds **(2.b)** and **(2.c)**, crystals were identified by powder X-ray diffraction as isostructural to compound **(2)**. Although crystals were too small for a single-crystal X-ray diffraction structural determination it was possible to use them to determine their unit cells, which are given in Table 3.2.

The structures of **(1)** and **(2)** consist of three-dimensional networks of supertetrahedral T3 which are linked by clusters sharing corners. The building units are different for each structure. Compound **(1)** contains $[Ga_{10}S_{20}]^{10-}$ clusters, while compound **(2)** by $[Ga_{10}S_{19}O]^{10-}$ units (Figure 3.1). In both structures, gallium atoms adopt tetrahedral coordination. Gallium-sulphur distances lie in the range of 2.214(6)-2.350(6) Å and 2.214(3)-2.335(2) Å for **(1)** and **(2)** respectively, with the larger distances corresponding to trigonally coordinated sulphur. The gallium-oxygen distance in **(2)** 1.935(4) Å, is significantly shorter than the Ga-S bonds, and similar to the Ga-O distances found in Ga_2O_3 (1.92-2.08 Å) [189].

Table 3.1. Crystallographic data for the structures **(1)** and **(2)**.

Formula	$[C_4H_{12}N]_6[Ga_{10}S_{18}]$ **(1)**	$[C_4H_{12}N]_{12}[Ga_{20}S_{35.5}(S_3)_{0.5}O]$ **(2)**
Mr	1336.44	2596.84
Crystal habit	Colourless plate	Colourless plate
Dimensions/mm^3	0.04 × 0.08 × 0.14	0.06 × 0.06 × 0.12
Crystalline System	Tetragonal	Monoclinic
Space group	*P4$_3$2$_1$2*	*C2/c*
T/K	100	100
a/Å	18.9621(7)	33.8210(11)
b/Å	18.9621(7)	18.4173(6)
c/Å	29.675(2)	20.9778(7)
β/°	-	116.6010(10)
V/Å^3	10669.9(9)	11683.7(7)
Z	8	4
Wavelength/Å Mo K_α	0.71073	0.71073
μ/cm^{-1}	5.67	5.19
Δρ max / Å^{-3}	1.22	2.12
Δρ min / Å^{-3}	-1.12	-1.04
Measured data	51669	58030
Unique data	10907	11909
Observed data ($I > 2\sigma(I)$)	4664	5449
R_{merg}	0.034	0.030
$R(F_o)$[a]	0.041	0.045
$R_w(F_o)$[b]	0.046	0.051

[a] $R(F_o)=\Sigma(|F_o| - |F_o|)/ \Sigma|F_o|$. [b] $R_w(F_o)= [\Sigma w(|F_o|- |F_o|)^2 / \Sigma w|F_o|^2]^{1/2}$

Table 3.2. Unit cell parameters found for compounds **(2.b)** and **(2.c)**.

Unit cell parameters	**(2.b)**	**(2.c)**
a/Å	35.315(6)	34.9(2)
b/Å	18.45(3)	18.28(11)
c/Å	21.01(3)	20.32(11)
β/°	116.28(3)	115.594(8)

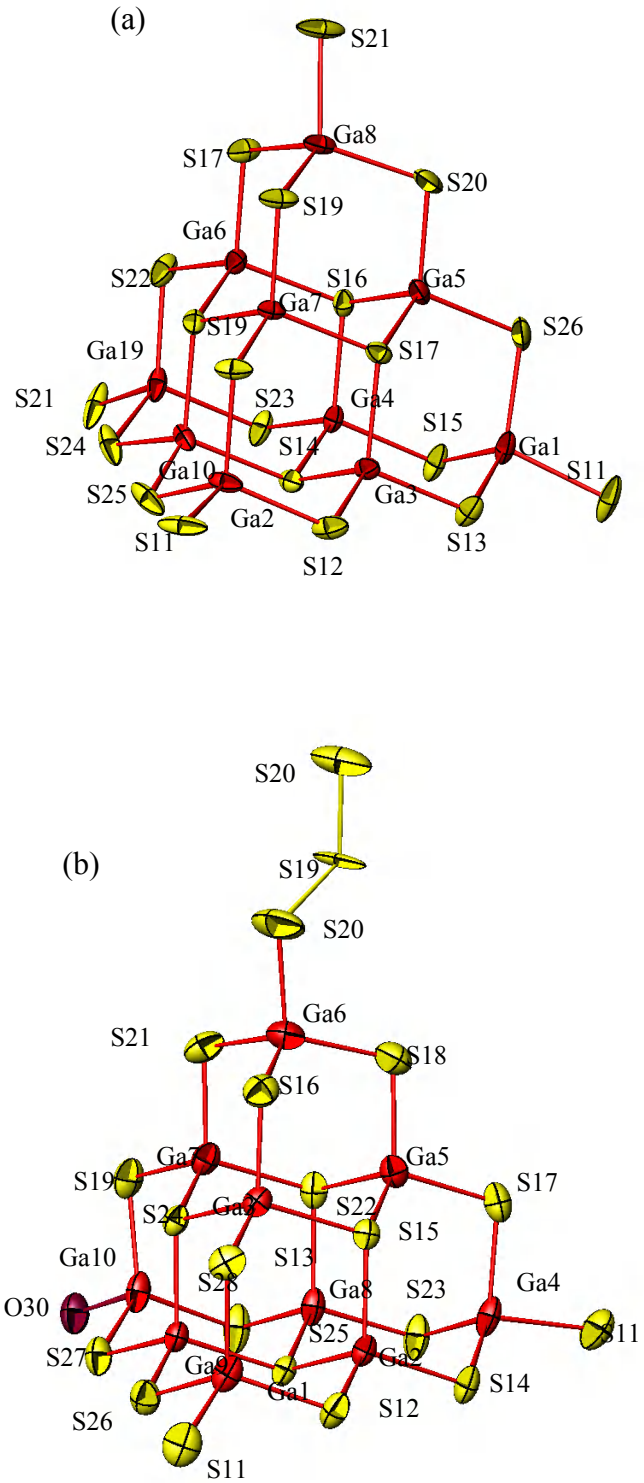

Figure 3.1. Local coordination diagram for (a) compound **(1)** and (b) compound **(2)**, showing the atom labelling scheme and displacement ellipsoids at 50% probability. Ga atoms are shown in red and S in yellow.

In **(1)**, T3 clusters of $[Ga_{10}S_{20}]^{10-}$ (Figure 3.2(a)) are connected by sharing their four sulphur vertices, resulting in an open framework with the composition $[Ga_{10}S_{18}]^{6-}$. In compound **(2)**, the supertetrahedral cluster has one of the terminal sulphurs substituted by oxygen (Figure 3.2(b)). Additionally, one quarter of the connections are formed by polysulphide S_3^{2-} bridge and the resultant structure is an inorganic framework of stoichiometry $[Ga_{20}S_{35.5}(S_3)_{0.5}O]^{12-}$.

Both structures exhibit the same type of framework. The T3 supertetrahedral clusters form six-membered rings (Figure 3.2(a)) by sharing two of the corners from the cluster. This motive constitutes a three-dimensional network which is formed by sharing the remaining vertices of each supertetrahedron connecting rings (Figure 3.2(c)) and the structure is finally formed by two of these identical interpenetrating networks (Figure 3.2(d)). When supertetrahedral clusters are substituted by nodes the single net can be described as a diamond-type lattice (Figure 3.2(e)) and the total structure is viewed as two interpenetrated lattices (Figure 3.2(f)). Taking into account the van der Waals' radii, channels of dimensions 7×2 Å were found for compounds **(1)** and **(2)**. The solvent void space (which was calculated using SOLV routine from PLATON [183]) is *ca.* 50% in both structures. As the inorganic framework is negatively charged, protonated molecules of DEA are believed to be located in the cavities, occupying the empty space.

Analysis of the powder X-ray diffraction data indicates that the bulk product of the reaction contains large amounts of compound **(1)** along with small amounts of a poor crystalline phase. There is a good agreement between the experimental diffraction pattern and the simulation obtained from structural model using Powder Cell [175] (Figure 3.3) for compounds **(1)** and **(2)** and TOPAS for compounds **(2.b)** and **(2.c)** (Figure 3.4). The observed diffraction patterns were fitted using with TOPAS [176] in order to refine the lattice parameters, which are given in Tables 3.3 for compounds **(1)**, **(2)**, **(2.b)** and **(2.c)**, showing a relatively good agreement when compared with lattice parameters obtained by single crystal X-ray diffraction (Table 3.1).

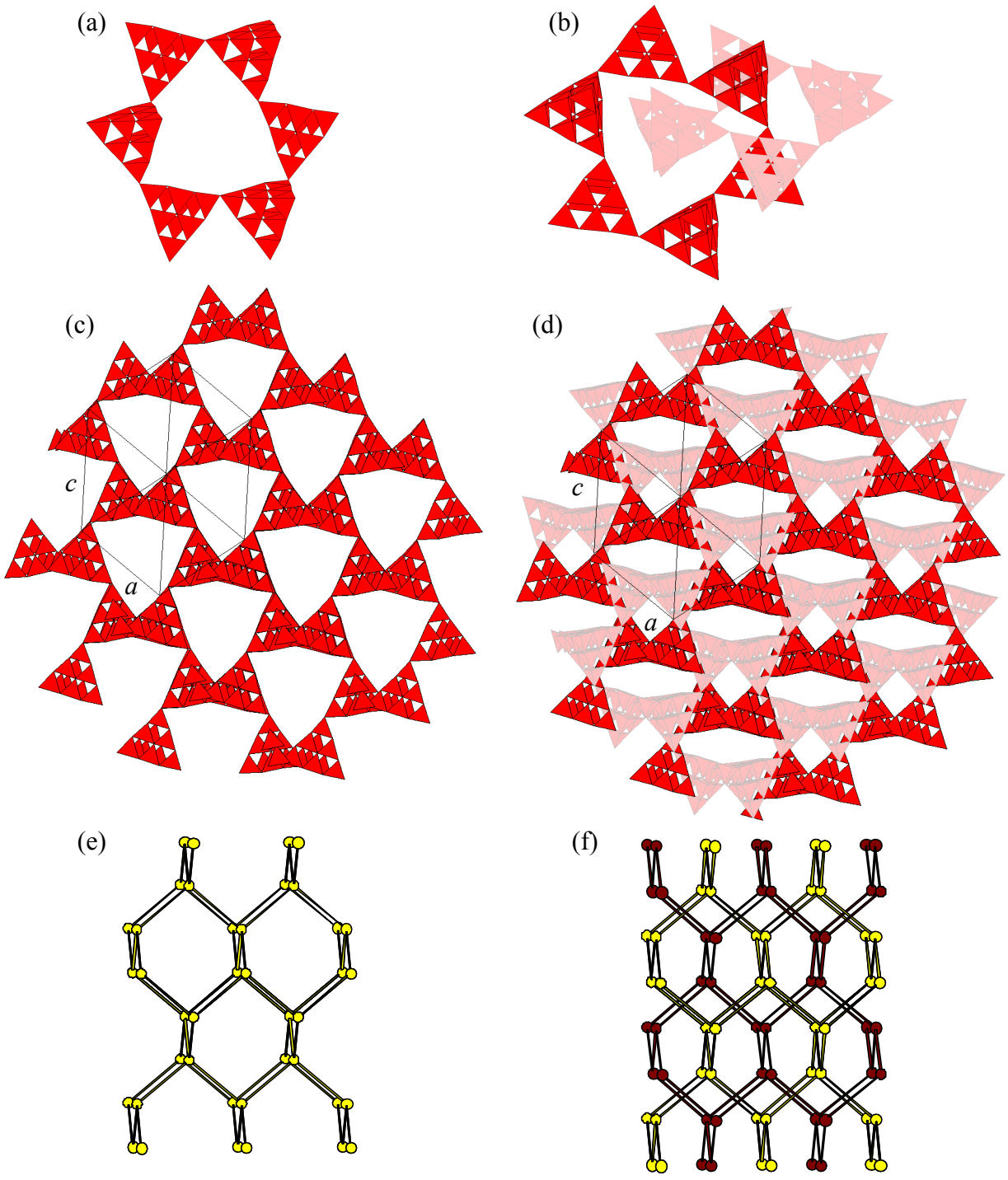

Figure 3.2. Crystal structure of compound **(1)**. (a) Polyhedral representation of a six-membered ring. (b) Two interpenetrating rings. (c) Single network. (d) The two interpenetrating networks shown in lighter and darker shades. Representations of the topology of (e) the single diamond-type lattice and (f) double diamond lattice, GaS_4 tetrahedra are shown in red. In (e) and (f) each supertetrahedral clusters is represented by a node, and the two lattices are shown in yellow and brown.

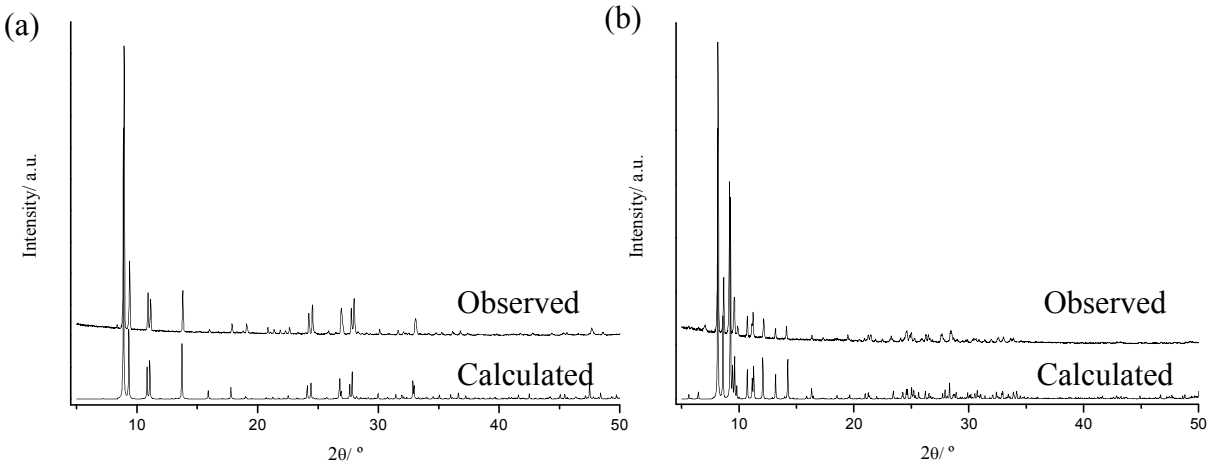

Figure 3.3. Comparison between calculated and experimental powder X-ray diffraction patterns for compounds (a) **(1)** and (b) **(2)**.

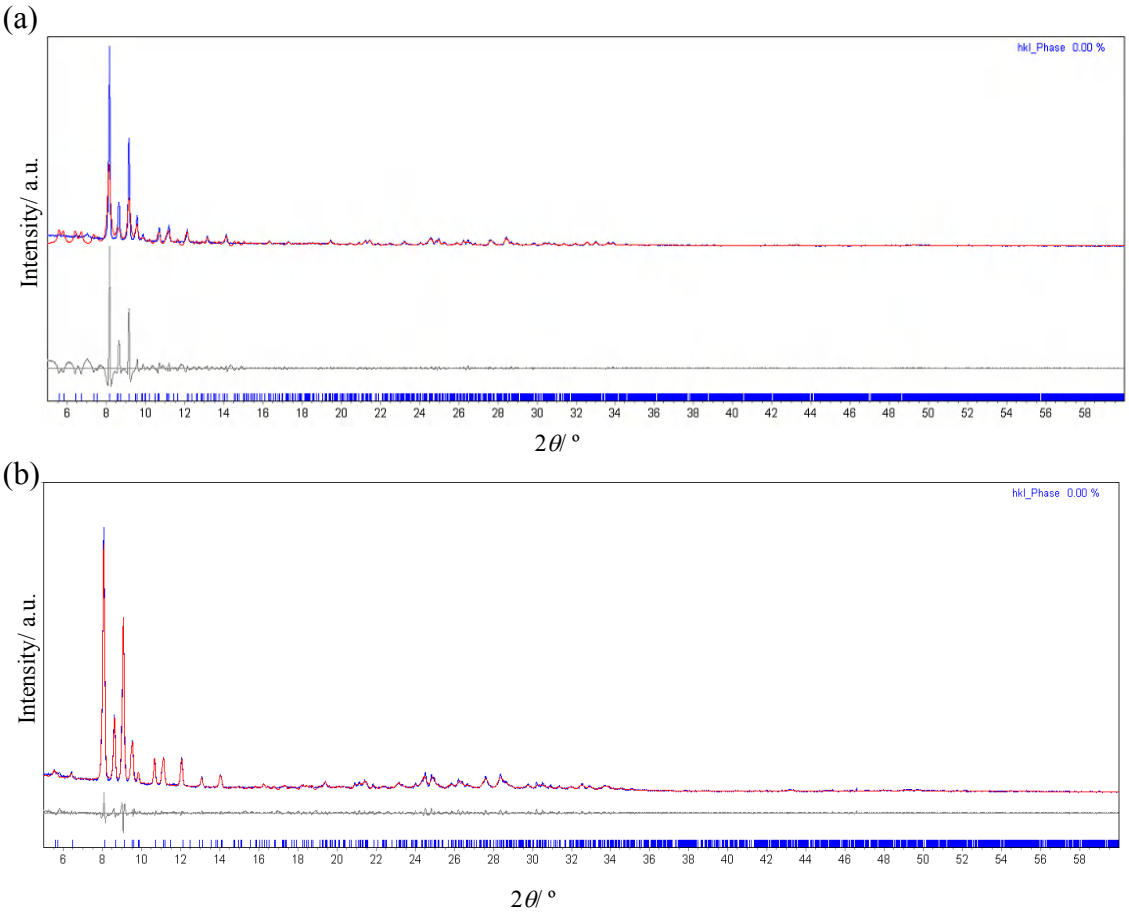

Figure 3.4. Comparison of powder X-ray diffraction pattern using TOPAS refinement for: (a) compound **(2.b)** and (b) compound **(2.c)**. Experimental pattern is shown in blue, calculated pattern in red and difference in grey.

Table 3.3. Lattice parameters for compounds **(1)**, **(2)**, **(2.b)** and **(2.c)** determined using powder X-ray diffraction data.

Unit cell parameters	**(1)**	**(2)**	**(2.b)**	**(2.c)**
a/Å	18.56(2)	33.663(2)	35.334(13)	34.400(1)
b/Å	-	18.383(1)	18.456(7)	18.398(1)
c/Å	29.57(3)	20.989(1)	21.017(8)	20.679(2)
β/°	-	116.258(4)	116.304(15)	116.309(4)

3.2.3. Elemental analysis and TGA

Elemental analysis reveals for compound **(1)** a composition of C: 11.06 %, H: 3.46 %, N: 8.47 %, different to the expected values of C: 16.77%, H: 4.22, N: 4.87%. For compound **(1)** TGA is shown in Figure 3.5(a), the decomposition of the compound occurs in two steps with two gentle slopes, the intermediate phase could not be isolated nor identified. The change of slope is observed at 650 K corresponding to *ca.* 16 % of weight loss. The compound is totally decomposed at *ca.* 900 K. The final weight loss is *ca.* 32 %, higher than the expected value (26%) from the total removal of the organic component. The remaining residue was a pale grey poor crystalline material that could not be identified by powder X-ray diffraction. This difference could be attributed to the partial decomposition of the initial material to amorphous Ga_2S_3. The presence of different steps in the TGA analyses could be assigned to the presence of formation of volatile organo-sulphur species [190], previously observed in supertetrahedral indium sulphides, where similar amines were employed.

For compound **(2)** the experimental composition is: C: 13.01 %, H: 3.83 %, N: 4.44 %; while the theoretical values are: C: 16.54 %, H: 4.16 %, N: 4.82 %. Figure 3.5 (b) shows TGA data for compound **(2)**. The decomposition takes place in one step. The compound is stable up to *ca.* 450 K, and has a total weight loss of *ca.* 24 % at 800 K, close to the theoretical weight loss which corresponds to 26 %. The remaining residue was a pale grey amorphous material that could not be identified by powder X-ray diffraction.

These results are consistent with the presence of organic material within the cavities of the structures. It is remarkable that the volatile material determined by TGA analysis and the percentage of CHN values differ and could be attributed to the partial degradation of the sample after loosing the organic component to Ga_2S_3.

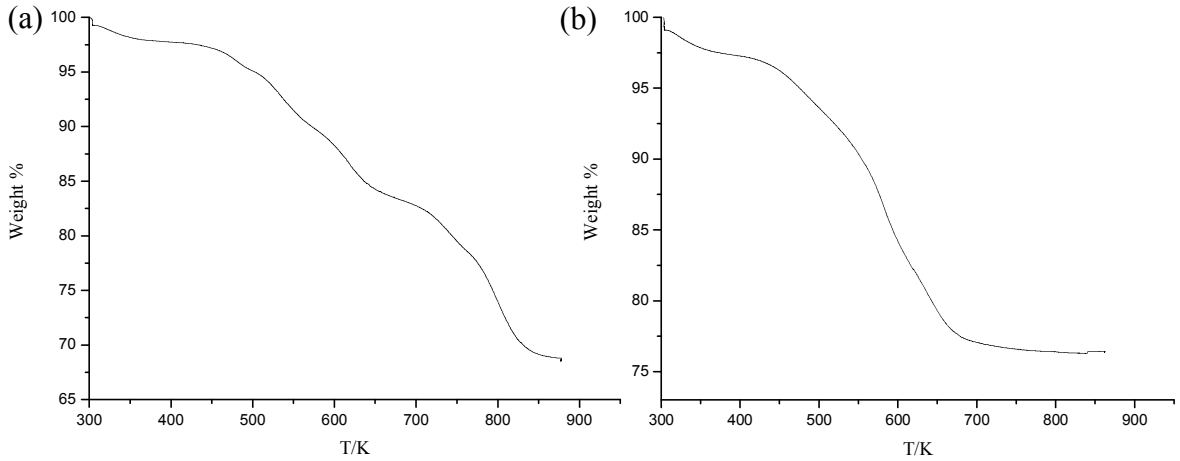

Figure 3.5. TGA for (a) compound **(1)** and (b) compound **(2)**.

3.3.4. FTIR

FTIR data (Appendix III) reveal for both compounds bands corresponding to the vibrations of the DEA molecules. The vibrational modes and their frequencies are given in Table 3.4. Both profiles are characteristic for secondary protonated amines, meaning that DEA is totally protonated, and the results are similar to those found in other related compounds [82,191]. The presence of possible counter-ions that originated from the decomposition of DEA such as $CH_3NH_3^+$ or NH_4^+ was undetermined. However bands in the region corresponding to $-CH_3$ rocking (1100-900 cm^{-1}) differ, which could indicate the presence of other species that maybe contain these functional groups.

Table 3.4. IR selected bands (values in cm^{-1}) for compound **(1)** and **(2)**. υ = stretching, δ = deformation; s = strong, m = medium, w = weak.

Assignment	**(1)**	**(2)**
υ (N-H)	3435.8 (w)	3469.9 (w)
υ (C-H)	2982.3 (w)	2972.2 (w)
υ (N-H)	1617.8 (s)	1691.2 (s)
δ (C-H)	1491.4 (s)	1449.9 (s)
δ (C-H)	1103.6 (w), 1017.9 (w)	1156.1 (w),1053.7 (w), 964.2 (w)

3.3. Metal gallium sulphide supertetrahedral structures

3.3.1. Synthesis

$[C_4H_{12}N]_{16}[Ga_{10}S_{18}Zn_4Ga_{16}S_{33}]$ **(3)**: was obtained from a mixture of gallium metal (142 mg, 2 mmol), sulphur (128.2 mg, 4 mmol) and $ZnCl_2{\cdot}2H_2O$ (135 mg, 1 mmol), in DEA (3.4 ml) with an approximate stoichiometry 2:4:1:3.4, heated in a 23 ml autoclave at 463 K for 5 days. The result of the reaction consisted of white crystals identified as **(3)**, a white powder formed by amorphous material and ZnS.

$[C_4H_{12}N]_{16}[Ga_{10}S_{18}Co_4Ga_{16}S_{33}]$ **(4)**: a mixture of gallium metal (142 mg, 2 mmol), sulphur (128.2 mg, 4 mmol) and $CoCl_2{\cdot}4H_2O$ (135 mg, 1 mmol) in DEA (3.4 ml,) with an approximate stoichiometry 2:4:1:3.4 was heated in a 23 ml autoclave at 463 K for 5 days. The final product was constituted of a mixture of unidentified dark powder and a small yield (*ca.* 15%) of green octahedral crystals of **(4)**.

3.3.2. Structure description

Crystallographic information and refinement details for compound **(3)** and **(4)** are given in Table 3.5. The non- hydrogen atomic coordinates, bond lengths and angles are summarised in Appendix II. The structures were solved using direct methods, which located the Ga and S atoms. The organic component on the structures could not be located. The data were treated with SQUEEZE [183] to correct the effect of the disordered organic cations.

In these compounds, gallium and the metallic atoms are tetrahedrally coordinated (Figure 3.6). Selected bond distances and angles are shown in Tables 3.6 and 3.7. Gallium-sulphur distances lie in the range 2.218(4)-2.327(3) Å and 2.226(5)-2.322(4) Å, respectively. The M-S distances lie in the range of 2.297(3)-2.3179(14) Å and 2.2769(18)-2.286(4) Å for **(3)** and **(4)**, respectively. Co-S distances are shorter than Zn-S distances as was observed in other supertetrahedral metal sulphides [86]. In each T4 cluster, the four M^{2+} cations are placed around the central tetrahedral divalent sulphur atom, which forms four bonds (corresponding to the shortest distances M-S) with a bond valence of ½. These distances are in accordance with Pauling's electrostatic valence rules [42]. The rest of the S bonded to M^{2+} are tri-coordinated.

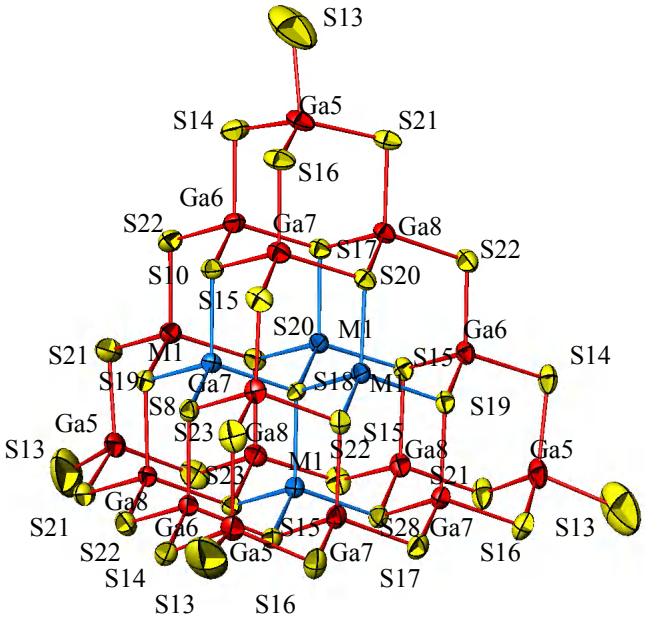

Figure 3.6. Local coordination diagram for $[M_4Ga_{16}S_{35}]^{14-}$ supertetrahedra, showing the atom labelling scheme and displacement ellipsoids at 50% probability. Ga atoms are shown in red, M atoms in blue and S in yellow.

Compounds **(3)** and **(4)** are isostructural. They consist of three-dimensional networks of supertetrahedral T3 and T4 clusters. They contain T3 $[Ga_{10}S_{20}]^{6-}$ similar to those found in compound **(1)** and T4 $[M_4Ga_{16}S_{35}]^{14-}$ supertetrahedral clusters (M= Zn or Co), which are shown in Figure 3.7(a)

The topology of the framework is analogous to that of compounds **(1)** and **(2)**, but T3 and T4 supertetrahedra are now arranged in an alternating fashion, forming six-membered rings (Figure 3.7(b)). The clusters are connected by sharing their corners through a terminal S atom. The crystal structure contains two interpenetrating diamond-type lattices. These structures contain channels with apertures of 10×3 Å. Approximately 50 % of the volume is solvent accessible void space. In consequence, the amines are believed to be placed in these cavities.

Analysis of the powder X-ray diffraction data indicates that there is a good agreement between the experimental diffraction pattern and the simulation obtained from structural model using Powder Cell [175] (Figure 3.8) for compounds **(3)** and **(4)**. Additionally impurities of ZnS were identified in compound **(3)** whereas for compound **(4)** none other crystalline phase was identified in the bulk material. The observed diffraction patterns were fitted using TOPAS program [176] in order to refine the lattice

parameters, which are given in Table 3.8 for both compounds, presenting a relatively good agreement when compared with lattice parameters obtained by single crystal X-ray diffraction (Table 3.5).

Table 3.5. Crystallographic data for the structures **(3)** and **(4)**.

Formula	$[C_4H_{12}N]_{16}$ $[Ga_{10}S_{18}Zn_4Ga_{16}S_{33}]$ **(3)**	$[C_4H_{12}N]_{16}$ $[Ga_{10}S_{18}Co_4Ga_{16}S_{33}]$ **(4)**
Mr	3709.61	3683.82
Crystal habit	White plate	Green octahedron
Dimensions/mm^3	0.10 × 0.12 × 0.14	0.06 × 0.08 × 0.08
Crystalline System	Tetragonal	Tetragonal
Space group	$I4_1/a$	$I4_1/a$
T/K	100	100
a/Å	20.8195(5)	21.0010(7)
b/Å	20.8195(5)	21.0010(7)
c/Å	34.5499(19)	33.997(3)
V/Å^3	14975.7(10)	14994.0(13)
Z	4	4
Wavelength/Å Mo K_α	0.71073	0.71073
μ/cm^{-1}	5.934	5.730
Δρ max / Å^{-3}	0.47	0.68
Δρ min / Å^{-3}	-0.61	-0.78
Measured data	153400	33293
Unique data	7683	7662
Observed data ($I > 2\sigma(I)$)	1994	2269
R_{merg}	0.045	0.041
$R(F_o)$[a]	0.030	0.043
$R_w(F_o)$[b]	0.034	0.047

[a] $R(F_o)=\Sigma(|F_o| - |F_o|)/ \Sigma|F_o|$. [b] $R_w(F_o)= [\Sigma w(|F_o|- |F_o|)^2 / \Sigma w|F_o|^2]^{1/2}$.

Table 3.6. Selected bond lengths (Å) and angles (°) for compound **(3)**.

Bond	Distance	Bond	Angle	Bond	Angle
Zn1-S12	2.297 (3)	S11-Zn1-S15	109.33 (12)	S15-Zn1-S22	110.30 (10)
Zn1-S15	2.297 (3)	S11-Zn1-S16	108.63 (12)	S16-Zn1-S22	109.98 (9)
Zn1-S16	2.298(3)	S15-Zn1-S16	107.79 (13)		
Zn1-S22	2.3179 (14)	S11-Zn1-S22	110.74 (10)		

Table 3.7. Selected bond lengths (Å) and angles (°) for compound **(4)**. Symmetry codes: (i) −y+1/4, x+1/4, −z+5/4; (ii) y−1/4, −x+1/4, −z+5/4.

Bond	Distance	Bond	Angle	Bond	Angle
Co1-S12i	2.286 (4)	S12i-Co1-S11ii	107.09 (15)	S11ii-Co1-S10	107.56 (15)
Co1-S11ii	2.281 (4)	S12i-Co1-S9	111.75 (12)	S9-Co1-S10	110.57 (12)
Co1-S9	2.2769 (18)	S11ii-Co1-S9	111.13 (11)		
Co1-S10	2.281 (4)	S12i-Co1-S	10108.57(15)		

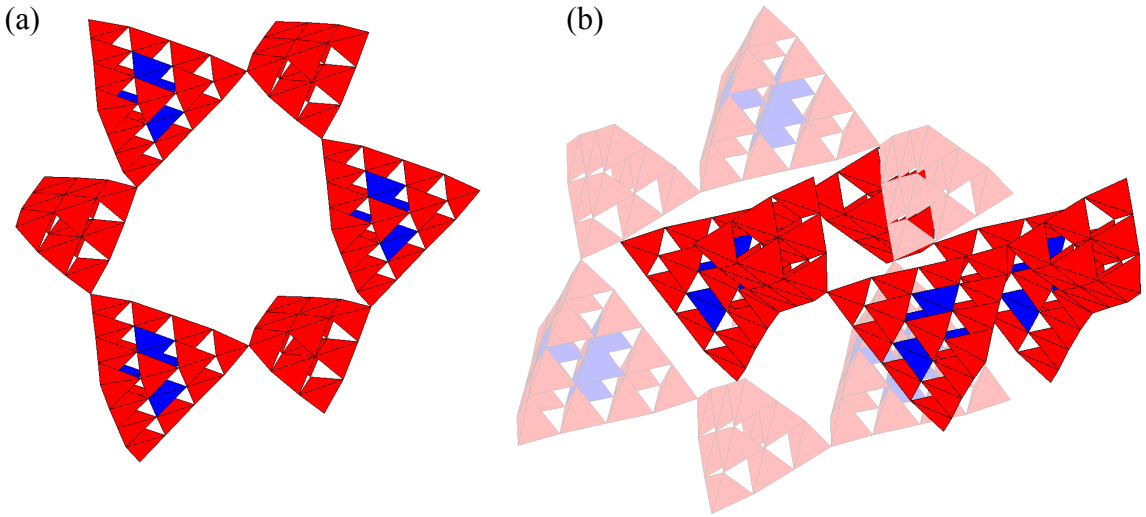

Figure 3.7. Polyhedral representation for compounds **(3)** and **(4)** showing alternating T3 and T4 clusters. (a) Six-membered ring and (b) two interpenetrating rings. GaS_4 tetrahedra are shown in red and MS_4 tetrahedra in blue. Non-connected rings are shown in different shady.

Table 3.8. Lattice parameters for compounds **(3)** and **(4)** determined using powder X-ray diffraction data.

Unit cell parameters	**(3)**	**(4)**
a/Å	20.459(4)	20.58(4)
c/Å	34.515(9)	34.20(8)

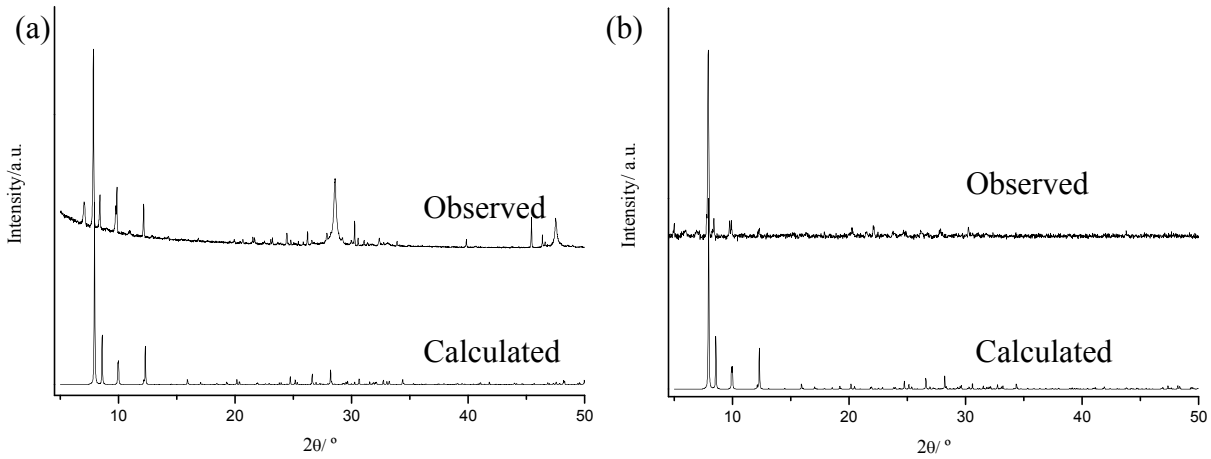

Figure 3.8. Comparison of calculated and experimental powder X-ray diffraction patterns for compounds (a) **(3)** and (b) **(4)**.

3.3.3. Elemental analysis and TGA

Elemental analysis reveals for compound **(3)** a composition of C: 11.58 %, H: 2.87 %, N: 4.24 % different to the expected values of C: 15.7%, H: 3.95, N: 4.24%. The crystals of compound **(3)** were coated with a ZnS powder, making it was impossible to remove this coating prior to analysis and potentially be the cause of the disagreement. TGA data (Figure 3.9) show that the sample was decomposed in two steps. It is stable up to *ca.* 390 K with a gentle weight loss at 773 K, where there is a change of slope with a total weight loss of *ca.* 25% at *ca.* 870 K. The theoretical weight loss is 24 %. The remaining residue after TGA was a pale grey material identified as a mixture of $ZnGa_2O_4$, Ga_2O_3 and ZnO, using X-ray diffraction. This may be a consequence of possible leaks in the system due to the temperature applied. The first weight loss could be adjusted to the percentage of organic material determined by CHN. The second step could be attributed to the decomposition of compound **(3)** to the identified phases. Therefore, the percentage of CHN in both analyses is consistent. The difference with the expected amount could be attributed to the presence of ZnS that could not be separated from the crystals of **(3)** and, consequently, reduced the relative amount of experimental organic material.

Elemental and TGA analysis for compound **(4)** were not carried out due to the small amount of crystals produced. Attempts to increase the reaction yield were not successful.

3.3.4. FTIR

FTIR data for both compounds are similar and consistent with the presence of DEA in the structure (Appendix III). The vibrational modes and their frequencies are given in Table 3.9. Both profiles are characteristic of secondary protonated amines. This suggests that DEA molecules are protonated. These results are similar to those found in other related compounds [82,191].

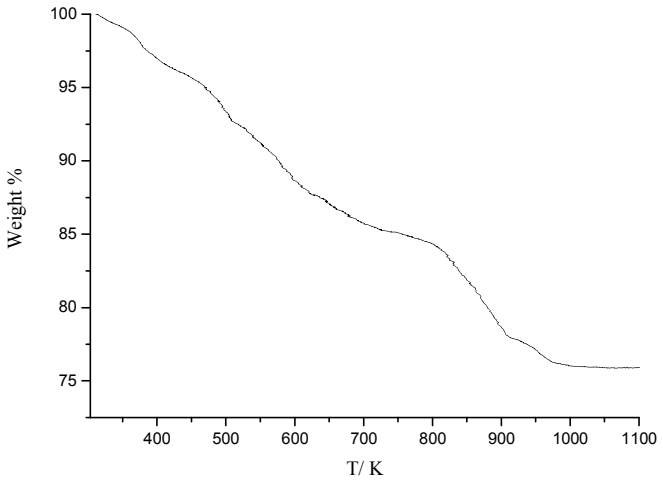

Figure 3.9. Thermogravimetric data for compound **(3)**.

Table 3.9. IR selected bands (values in cm^{-1}) for compound **(3)** and **(4)**. υ = stretching, δ = deformation; s = strong, m = medium, w = weak.

Assignment	**(3)**	**(4)**
υ (N-H)	3435.0 (w)	3317.5 (w)
υ (C-H)	2989.7 (w)	2964.7 (w)
υ (N-H)	1664.3 (s)	1632.5 (s)
δ (C-H)	1453.3 (s)	1453.3 (s)

3.4. Diffuse Reflectance

The optical absorption spectra for compound **(1)** to **(4)** are shown in Figure 3.10. All of them present a sharp adsorption edge corresponding to the band gap value from valence band corresponding to the 'p' orbitals from the S^{2-} and conduction band corresponding to the 'p' orbitals from Ga^{3+}/M^{2+}. The band gap values obtained from the absorption edges are 4.0(1), 4.1(1) 3.5(1) and 3.4(1) eV for each compound, that confirm the semiconducting nature of these materials. The values are blue shifted with respect to the value found for Ga_2S_3 (3.3 eV) [192]. This blue shift, which has also been observed

in solvothermally produced zinc tellurides [193], could be attributed to quantum confinement. For this reason, the generation of porosity in crystalline semiconductors leads to increase the band gap and energy levels of the conduction band. This effect was demonstrated in supertetrahedral indium-sulphides [96]. It is also possible to consider each cluster as an independent nanodot and therefore, the three-dimensional arrangement gives rise to physical interaction between clusters such as inter-dot coupling. The 'density of state' of this type of compound was studied by Li et *al.* [81] and Sankey and co-workers [151], explain the characteristics of the absorption band and potential application of these compounds in efficient laser and solar devices.

It is worth noticing that compound **(4)** also presents a pronounced band of low intensity at 1.6 eV, attributed to the presence of tetrahedrally coordinated Co^{2+} and corresponding to the transition from the energy states $^4A_2(F) \rightarrow {}^4T_1(P)$. This type of transition has been previously detected in the absorption spectrum of sphalerites containing Co^{2+} impurities [194]. For compound **(3)**, a small shoulder at the end of the absorption edge can be observed, similar to those previously observed for supertetrahedral zinc gallium selenides [84].

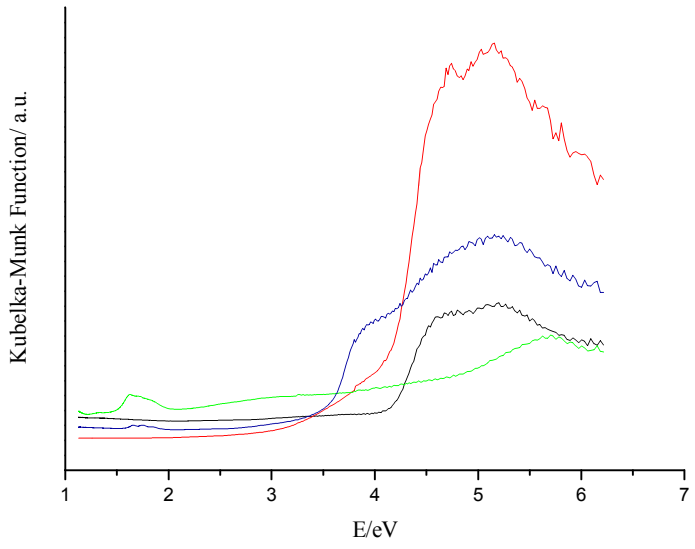

Figure 3.10. Diffuse reflectance for compounds **(1)**, **(2)**, **(3)** and **(4)** are shown in black, red, green and blue lines, respectively.

The incorporation of divalent transition metals has a dramatic effect on the band gap. There is a red shift of band gap values in comparison with supertetrahedral gallium sulphides which do not contain such metals (compounds **(1)** and **(2)**). The different electronic configurations between M^{2+} and Ga^{3+} result in low energy levels in the

conduction band. In consequence, M^{2+} could be considered as a positive dopant substance in the band gap of supertetrahedral chalcogenide clusters.

3.5. Ion-Exchange experiments

To perform ion-exchange experiments, attempts to optimise the yield of the different products were carried out. After several tests, compound $[TEPAH^+]_6$ $[Ga_{10}S_{16.5}(S_3)_{0.5}O]$ **(2.b)** was chosen owing to its high yield and purity. The resultant product from the reaction of Ga: S: TEPA: MeOH contains small white crystals identified as **(2.b)** and a small amount of unreacted gallium (which was removed before ion-exchange experiments), with a yield of *ca*. 90%. The compound was fully characterised by powder X-ray diffraction, infrared, thermogravimetric analysis and diffuse reflectance. This material is isostructural to compound **(2)**.

Different masses of sample were exposed to saturated aqueous salt solutions containing monovalent cations (NH_4^+, K^+, Na^+ and Cs^+) at different conditions (Table 3.10). The amount of organic material exchanged was determined by elemental analysis of the final product. Possible structural changes were investigated using powder X-ray diffraction (Figure 3.11). Patterns do not show impurity phase and refinement of them using TOPAS were carried out exhibiting small changes in the unit cell parameters (Table 3.11). The exchange of the amine for species of different size within the cavities should produce small changes in the framework.

Table 3.10. Ion-Exchange conditions and percentage of amine removed for exchange of monovalent cations when no-evident changes in the structure were found after the experiment.

Cation Exchanged	Time/days	T/ K	% Amine Exchanged
NH_4^+	3	348	63
K^+	3	348	31
Na^+	10	RT	20
Cs^+	7	RT	33

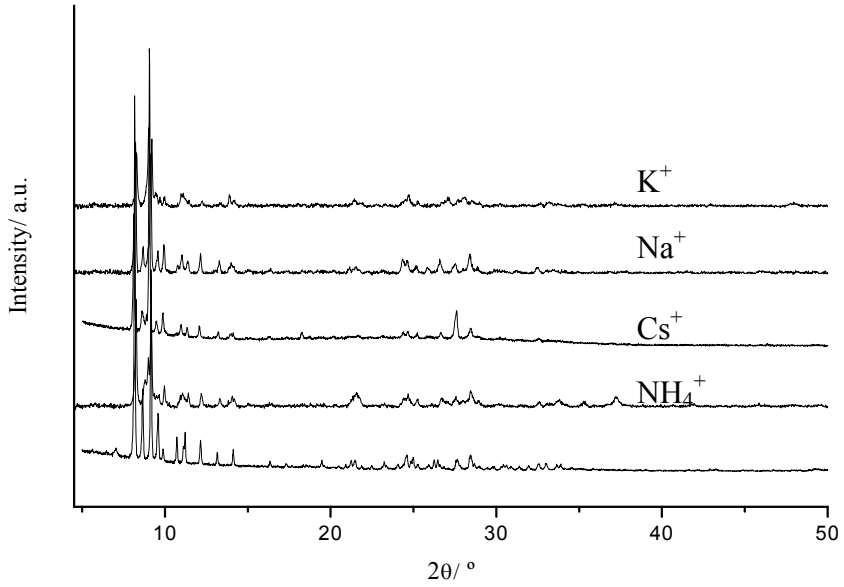

Figure 3.11. Comparison of powder X-ray diffraction patterns for compound **(2.b)** before and after ion-exchange with different cations.

Table 3.11. Lattice parameters for compounds for material exchanged determined using powder X-ray diffraction data.

Unit cell parameters	(NH_4^+)	Cs^+	Na^+	K^+
a/Å	34.03(4)	33.797(2)	33.97(3)	34.42(2)
b/Å	18.43(2)	18.396(1)	18.40(2)	18.333(9)
c/Å	20.79(3)	20.100(1)	20.95(2)	20.89(1)
β/°	117.05(6)	117.01(4)	116.74(5)	117.76(2)

3.5.1. Exchangeability of extra-framework amine

The maximum exchange value obtained was for a sample immersed in a saturated solution of ammonium iodide with no stirring at *ca.* 348 K for 3 days, for which 66% of the organic material was exchanged. These values are pretty similar to those found for UCR-7GaS-TETA [103], which is isostructural to compound **(1)**, when ion-exchange is carried out with a 2M NH_4Cl solution. Elemental analysis shows that there is still organic material in the structure: CHN experimental values C: 4.74 %, H: 1.59 %, N: 3.16 %; and calculated values for the total exchange of the organic material (C: 0%, H: 2.22, N: 7.72%). This suggests the material was partially exchanged and that a distribution of counter ions (protonated amines and NH_4^+ cations) it likely occurs.

After a fivefold increase in the amount of the sample prepared, infrared, UV-Vis diffuse reflectance, thermogravimetric and BET surface analysis were carried out. All the partial ion-exchanges do not present evidence of new phases. However, at high temperatures or for a long exchange times, decomposition of the structure took place to give a material analogous to compound **(1)**. This may suggests that the polysulphide bridge is the weaker part of the structure. More aggressive experiments yielded traces of Ga_2S_3.

Analysis of the porosity was carried out using the CAVITIES routine in ATOMS [195] (Figure 3.12). The cavities are communicated with each other through narrow necked regions, forming a three-dimensional network. The void space (setting particle radius to zero to obtain the true porosity) was 60 %. The large channels predicted in this structure (7×3 Å) match with the three-dimensional cavity network experimentally found.

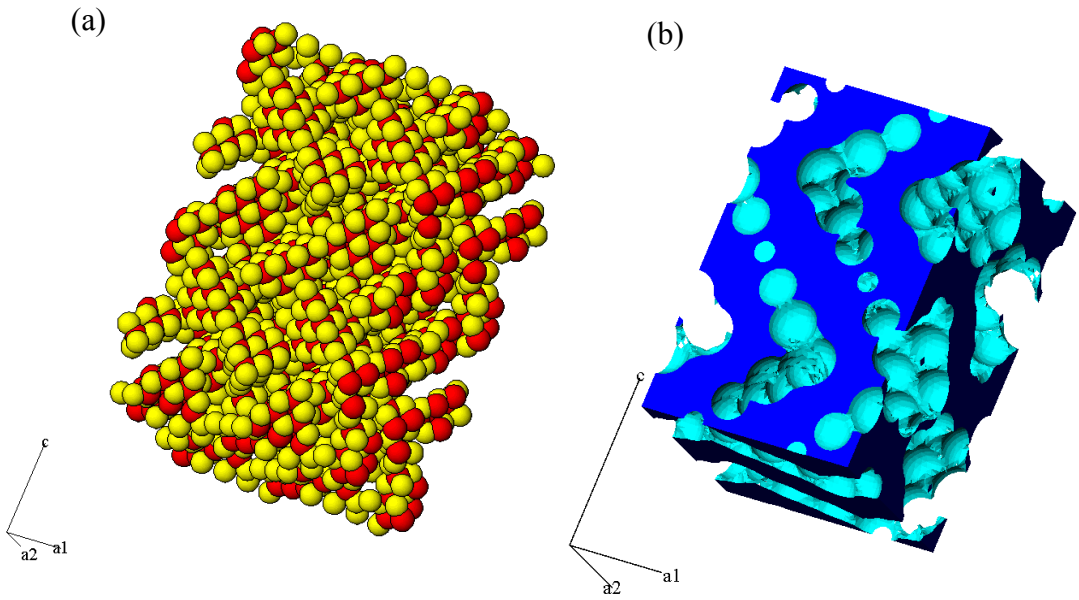

Figure 3.12. Comparison between (a) space-filling representation of structure of **(2)** (Ga atoms are shown in red and S in yellow) and (b) the three-dimensional representation of the cavities, where dark blue indicates the exterior surface of the cavities and the light blue shows surfaces where the cavities cross the unit-cell faces.

3.5.2. Analytical data

Figure 3.13 shows thermogravimetric and diffuse reflectance data of compound **(2.b)** before and after ion-exchange. Thermogravimetric analysis shows for the initial sample weight loss with several slopes. The first weight loss of *ca.* 20 % occurs at *ca.* 630 K and is followed by a gentle weight loss of *ca.* 38.31 % at *ca.* 900 K. The final residue

was identified as Ga_2S_3. TGA data for the ion-exchange sample show a similar profile with two steps. The total weight loss is *ca.* 30 % and differs by *ca.* 20 % from that of the initial sample.

The optical absorption spectrum of the exchange sample is similar to that of the initial sample. The band gap remains 4.1(1) eV and this may indicate that the band gap is totally dominated by the inorganic framework and extra-framework cations do not affect in any way the absorption process.

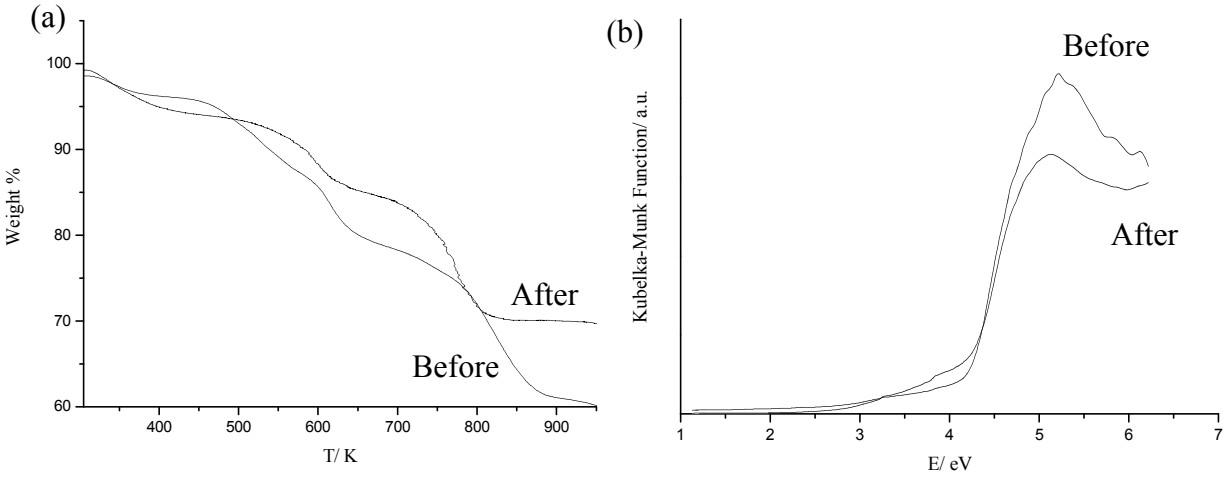

Figure 3.13. (a) Thermogravimetric and (b) UV-Vis diffuse reflectance data of **(2.b)** sample before and after ion-exchange process.

FTIR data (Appendix III) (Table 3.12) for both samples demonstrated the presence of TEPA, but at lower intensity for the sample after the exchange. There is a broad band in the region 3000-3500 cm^{-1} and it is difficult to identify stretching bands corresponding to NH_4^+ cations. However, the band at *ca.* 1440 cm^{-1} presents several peaks that may be indicative of NH_4^+ bending. This data is similar to the effect produced in the FTIR data of $[In_{10}S_{18}(C_6H_{12}NH_2)_6(C_6H_{12}NH)(H_2O)_5$ (ASU-34) after the exchange of monovalent and divalent cation [90].

3.5.3. Adsorption/desorption isotherms

To study the sorption within the pores, N_2 adsorption/desorption isotherms for the initial sample and the exchanged product were collected. All recorded isotherms are a combination of type IV and VI (Figure 3.14). The hysteretic adsorption is associated with mesoporosity, where capillarity condensation gives rise to a hysteresis loop. The presence of a plateau at $P/P_0 < 0.5$, and the subsequent progression in several steps with gentle slopes suggests the formation of monomolecular layers indicating complete

filling of the pores. This behaviour is attributed to weak adsorbate-adsorbent interactions and is indicative of microporous or mesoporous solids [196,197].

Table 3.12. IR selected bands (values in cm^{-1}) for compound **(2.b)** before and after of the ion exchange with NH_4^+. υ = stretching, δ = deformation; s = strong, m = medium, w = weak.

Assignment	Before	After
υ (N-H)	3452.8 (w)	3438.8 (w)
υ (C-H)	2924.5 (w)	2985.4 (w)
υ (N-H)	1678.6 (s)	1614.1 (s)
δ (C-H)	1448.7 (s)	1463.6 (s)
δ (N-H)	-	1439.0 (s)
δ (C-H)	1113.7 (w)	1105.0 (w)

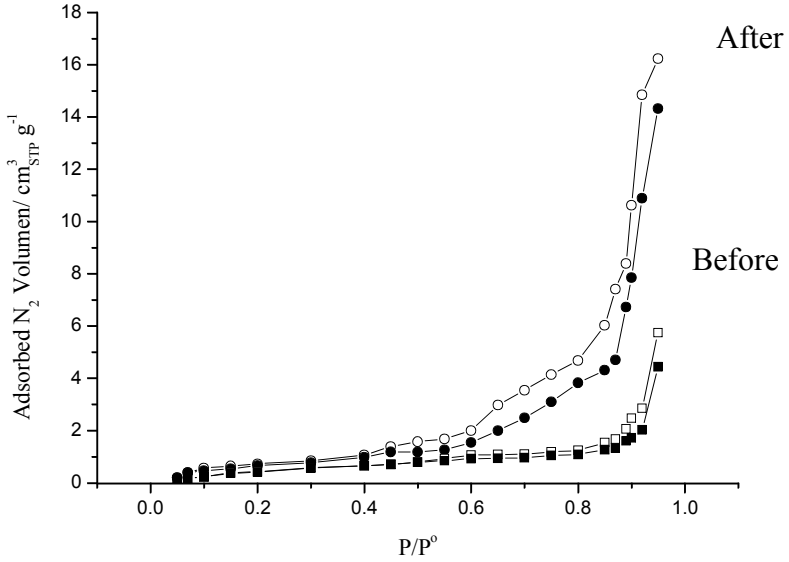

Figure 3.14. Adsorption/desorption Isotherms of compound **(2.b)** before and after ion-exchange with NH_4^+.

The pore size distribution (Figure 3.15) shows for the initial sample a high percentage of micropores (75%) (micropore: < 2nm, mesopore: 2-50 nm and macropore: >50 nm [198]). After ion-exchange the proportion of meso- and macropores has increased dramatically in detriment with the proportion of micropores. In addition, the total pore volume increases from 0.007 to 0.022 cm^3g^{-1}, suggesting that the substitution of large volume counter-ions by species of lower size. An increment in

the free volume space of 68 % is produced. These differences are related to the ion-exchange mechanism.

In both cases, the BET surface area is constant (2 m^2g^{-1}) in both samples, which confirms small structural changes have been produced after the exchange. However, the BET surface area value is very low in comparison which values found in other supertetrahedral chalcogenides closer to zeolites [41]. It is worth noticing that compound **(2.b)** presents a double interpenetrating diamond lattice and hence, the value expected should be much lower than those found for more open structures. As a result, the pore distribution and specific surface is much similar to the vast majority of solids than microporous materials. In any case, the capacity of the framework to increase the free volume pore (without any evidence of contraction in the structure) is exceptional, as well as, its flexibility.

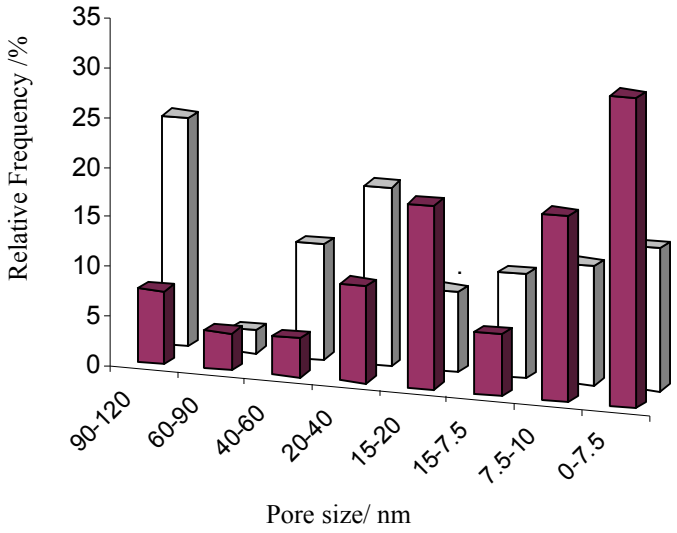

Figure 3.15. Pore size distribution before (solid bars) and after (open bars) ion-exchange with NH_4^+ for compound **(2.b)**.

3.6. Discussion

The double interpenetrating diamond type lattice is one of the most common topological types found for structures containing T3 supertetrahedral clusters. Analogous structures to compound **(1)** have been reported for supertetrahedral metal chalcogenides such as $[In_{10}Se_{18}]^{6-}$ using 2-(2-aminoethylaminoethanol) (AEAE) and 3-dimethyl aminopropylamine (DMAPA) [12], $[In_{10}S_{18}]^{6-}$ using dimethylamine (DMA) and DEA as templates [190]. The isostructural gallium-sulphides $[Ga_{10}S_{18}]^{6-}$, prepared using triethylenetriamine (TETA) and tris-(2-aminoethyl)amine (AEP) [103] were also described.

The geometry and charge distribution of organic molecules are important factors in the synthesis of structures containing supertetrahedral clusters. In the present four structures, the same amine was employed in the synthesis and frameworks with the same topology were obtained in each case. The same double diamond lattice has been obtained using a large variety of amines in related compounds (Figure 3.16).

Compound **(2)** is the first supertetrahedral three-dimensional structure presenting three different types of assembly between clusters. The supertetrahedral clusters are four-coordinated through S^{2-} bridges, O^{2-} bridges and $(S_3)^{2-}$ polysulphide bridges. The first one is the frequent linker between tetrahedral clusters and supertetrahedral structures in which one fourth of the connections are made through polysulphide bridge are also reported [103,46]. Feng's group [103] proposed that the formation of a polysulphide bridge in supertetrahedral open-framework compounds is related to the shape of the amine employed. The synthesis of compounds **(1)** and **(2)** demonstrates that the same amine can produce different types of units by changing slightly the reaction conditions. Similar observations were reported by Cahill and Parise for supertetrahedral indium sulphides [71].

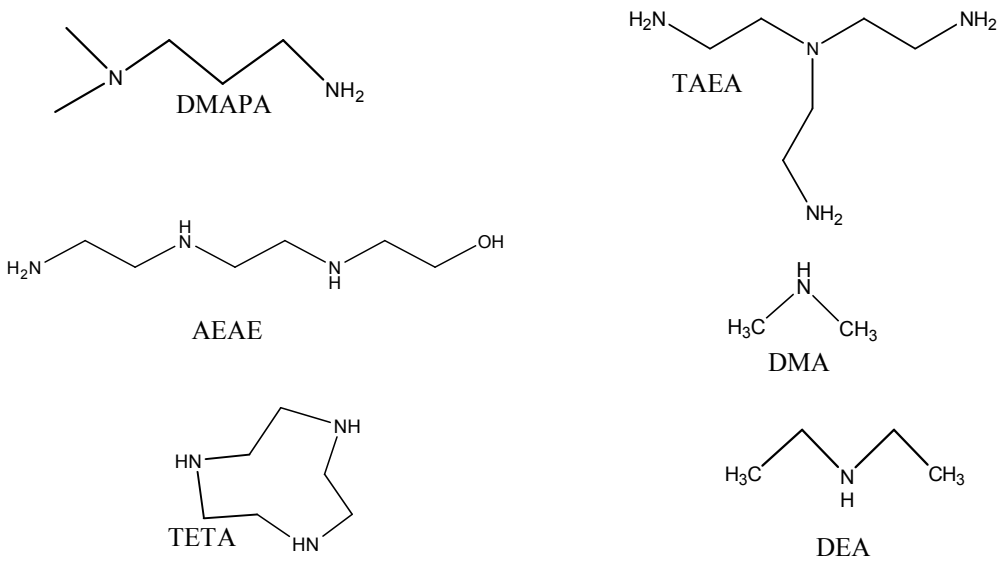

Figure 3.16. Different kinds of amines used as template able to form the same structure.

However, O atoms acting as linkers between clusters have not been reported before in inorganic three-dimensional supertetrahedral structures. In oxide-based silicates, linkages present angles between 120-180° [12], whereas M-S-M bridges between tetrahedra exhibit much narrower typical range (90-115°) [61,39] in inorganic

frameworks. Compounds containing a mixture of chalcogenide ions (X = S, Se or Te) were obtained by Feng and co-workers [43], presenting similar ranges to sulphur frameworks.

The similarity between S, Se and Te increases the probability of producing mixed-ion supertetrahedral clusters in comparison with S and O [162,161]. The insertion of O atoms within supertetrahedral structures should not be desirable in the first instance for the search of electrical properties (due to its high electronegativity). However, the location of O atoms in the structure could be limited to bridge position and therefore they could act as linkers between supertetrahedral clusters (as it is observed for compound **(1)**). Therefore, the range of angles present between clusters could be larger than for structures based only on O and S, increasing flexibility of the structure and the possibility of producing large cavities which could improve ion-exchange properties.

The diversity of supertetrahedral chalcogenide units could be enormous, tuning supertetrahedra by the insertion of metal cations [81,85,105]. Two examples of this trend are compounds **(3)** and **(4)**, which contain two different types of clusters. The most common situation for clusters of the same size is to crystallise into a uniform super-lattice. For frameworks containing different types of clusters, crystallisation will involve a homogeneous distribution of the clusters through the structure. Super-lattices containing different sizes of supertetrahedra are known such as (DEA-H)$In_{11}S_{21}H_2$ [82] (which is constituted of alternating T3 and T1 indium sulphide clusters forming layers) and three-dimensional structures such as $[C_{11}H_{24}N_2]_6[In_{20}S_{18}In_{34}S_{53}]$ [43] (built of T3 and pseudo-T5 clusters and forming a double diamond lattice). Alternating T3 and T4 clusters were found in $[C_6H_{22}N_4]_4[Ga_{10}S_{18}Zn_4Ga_{16}S_{33}]$ [103], which is isostructural to compounds **(3)** and **(4)**.

The formation of clusters larger than T3 generally requires the presence of a mixture of tetravalent or trivalent cations and divalent or monovalent cations. The cation's valence is considered to be an important factor affecting the size of the supertetrahedral cluster, as was discussed in great detail in [199]. The internal charge balance between metal sites and chalcogenide sites has to be maintained according to Pauling's electrostatic valence rule. The formation of large clusters with the same type of cation usually results in missing cations in tetrahedral positions or in the formation of 'pseudo-clusters' such as pseudo-T5 [43]. Generally, the incorporation of first row transition metals in supertetrahedral indium sulphides [86] produces T4 clusters, where the metallic M^{2+} position is tetrahedrally coordinated by sulphur atoms in the centre of the cluster. T4 are four-connected forming four and eight membered rings [9].

Supertetrahedral gallium sulphides were the first family of supertetrahedral compounds presenting structures formed exclusively of T4 clusters [103] and compounds with alternating T3 and T4 clusters. It is worth noticing that compound **(4)** is the first compound in the series which contains Co.

Findings on supertetrahedral gallium-sulphide structures to date are: (i) structures reported so far contain usually T3 and/or T4 clusters (when the insertion of transition metals happen), (ii) the topology of these compounds is restricted to interpenetrating networks and (iii) the reaction is in the majority of the cases only possible in non-aqueous media. However, the synthesis of gallium-sulphide supertetrahedra in the presence of water has been reported [79].

The exchange capacity of one of these supertetrahedral structures was investigated by elemental analysis. It was found that there is a higher ion-exchange activity for NH_4^+ than for the rest of monovalent cations. NH_4^+ and K^+ have a similar hydration sphere diameter (*ca.* 3 Å) and the same charge, so they could be expected to have the same behaviour, but this is not the case. This phenomenon could be attributed to a higher NH_4^+ diffusion coefficient. Cs^+ that has larger atomic radii but small hydration sphere diameter should be comparable to exchange percentage of NH^+_4 and K^+ and indeed it shows the similar exchange values than K^+ (see Table 3.10). Na^+ ions have a large hydration sphere which prevents them from entering inside the framework [200]. In consequence, after considering these factors, cations can only access specific cavities and they cannot diffuse within the structure with as much facility as NH_4^+. The movement inside the cavities is expected to be restricted to those neck points and the total or partial exchange could be only possible when the specie is able to access to the internal chambers; as observed in other metal sulphide structures [149] and in other rigid exchange materials as zeolites [201]. The flexibility of the structure allows to readjust and compensate the effect of the exchange by structural transformations which have been described as stretching, rotational, 'breathing' and scissoring mechanisms [202,203]. The mechanism of diffusion in compound **(2.b)** can be understood as the cations are first relocated in those cavities close to the surface, creating free volume when displacing the organic template. The movement within the structure can be more difficult due to the connections between chambers and therefore, cations could not have access to the more internal pores. The structure has then to adjust to a mixture of cations (NH_4^+ and protonated TEPA cations). That is why the increment of mesopores and macropores is appreciated.

Chapter 4: Hybrid supertetrahedral gallium-sulphide structures

4.1. Introduction

Supertetrahedral gallium sulphides are part of the family of supertetrahedral chalcogenides, but only a small number of structures have been reported [103]. Inorganic three-dimensional structures based on these materials can be produced using primary and secondary amines as templates (see Chapter 3). In comparison with the main-group metals (In, Ge), Ga is capable of coordinating amines through Ga-N covalent bonding [56] forming hybrid structures.

Hybrid tetrahedral clusters are well-known. They are mostly based on metal sulphides and a large number of structures have been reported with Cd and Zn (see Section 1.3.3), but to date, the hybrid tetrahedral gallium-sulphide family has not been explored in detail.

The feasibility of preparing organically-functionalised gallium-sulphide supertetrahedral clusters, via a solvothermal method, is demonstrated in this chapter. Isolated T3-type clusters can be obtained using pyridine derivatives, such as 3,5-dimethylpyridine (lutidine) and 4-methylyridine (4-picoline). Hybrid supertetrahedral clusters are connected using ditopic linkers resulting in the preparation of dimeric units, one-dimensional chains and two-dimensional extended structures. Observations suggest that the gallium-sulphide phases prepared to date are the first representatives of a large family of hybrid supertetrahedra-based materials.

4.2. Discrete hybrid clusters

4.2.1. Structures containing lutidine as a ligand

Synthesis

$[C_7H_{10}N]_2[Ga_{10}S_{16}(NC_7H_9)_4]$ **(5)**: was obtained from a mixture of gallium metal (139.44 mg, 2 mmol) and sulphur (128 mg, 4 mmol) in lutidine (2.5 ml). The mixture was placed in a 23 ml Teflon-lined stainless steel autoclave with an approximate stoichiometry 2:4:22. The autoclave was located in an oven and heated at 443 K for 10 days. The resultant product was a mixture of pale brown crystals identified as **(5)** and gallium.

$[C_4H_{12}N_2][C_7H_{10}N]_2[Ga_{10}S_{16}(NC_7H_9)_4]$ **(6)**: gallium metal (139.44 mg, 2 mmol), sulphur (128 mg, 4 mmol), lutidine (3 ml) and additionally, piperazine (Pp) (50 mg, 6×10^{-4} mmol) were located in a 23 ml Teflon-lined stainless steel autoclave. The

stoichiometry of the mixture was 2:4:26: 6×10^{-4}. The autoclave was heated at 443 K for 10 days. The final product consist of a mixture of small brown crystals identified as **(6)**, brown amorphous powder and unreacted gallium.

Table 4.1. Crystallographic data for the structures **(5)** and **(6)**.

Formula	$[C_7H_{10}N]_2$ $[Ga_{10}S_{18}(NC_7H_9)_4]$ **(5)**	$[C_4H_{12}N_2][C_7H_{10}N]_2$ $[Ga_{10}S_{18}(NC_7H_9)_4]$ **(6)**
Mr	1835.05	1941.34
Crystal habit	Colourless plate	Pale brown needle
Dimensions/mm^3	0.40 × 0.40 × 0.50	0.07 × 0.10 × 0.30
Crystalline System	Orthorhombic	Monoclinic
Space group	*Fddd*	*C2/c*
T/K	100	293
a/Å	15.4885(10)	23.5945(16)
b/Å	26.9605(17)	17.9036(11)
c/Å	35.320(2)	20.6686(15)
β/°	-	104.897(3)
V/Å^3	14748.9(16)	8337.5(10)
Z	8	4
Wavelength/Å Mo K_α	0.71073	0.71073
μ/cm^{-1}	4.08	3.57
Δρ max / Å^{-3}	1.17	0.93
Δρ min / Å^{-3}	-0.40	-0.84
Measured data	64594	47785
Unique data	6974	10933
Observed data ($I > 3\sigma(I)$)	2490	3341
R_{merg}	0.027	0.089
$R(F_o)$[a]	0.045	0.062
$R_w(F_o)$[b]	0.054	0.063

[a] $R(F_o)= \Sigma(|F_o| - |F_o|)/ \Sigma|F_o|$. [b] $R_w(F_o)= [\Sigma w(|F_o|- |F_o|)^2 / \Sigma w|F_o|^2]^{1/2}$.

Structure description

Crystallographic information and refinement details for compound **(5)** and **(6)** are given in Table 4.1. The atomic coordinates (excluding H atoms), bond lengths and angles are summarised in Appendix II. The structures were solved using direct methods which located the Ga and S atoms. The amine C and N atoms were placed using Fourier maps and modelled isotropically. H atoms were placed geometrically on the C and N atoms after each cycle of refinement (Figure 4.1).

The structures of **(5)** and **(6)** consist of $[Ga_{10}S_{16}(NC_7H_9)_4]^{2-}$ isolated supertetrahedral clusters (Figure 4.1) and organic moieties. Gallium is tetrahedrally coordinated to S and N, forming GaS_4 and GaS_3N tetrahedra. Tetrahedra are connected sharing corners, forming the supertetrahedral unit. The GaS_3N tetrahedra are placed in the vertices of the supertetrahedron connecting the organic molecules with the inorganic cluster. The distances Ga-S lie between 2.2271(15)-2.3225(14) for **(5)** Å and 2.218(5)-2.336(4) Å for **(6)**, where the larger distances correspond to trigonally coordinated sulphur. The Ga-N distances lie between 2.045(5) Å and 2.052(16)-2.060(15) Å for both compounds, respectively. These distances are similar to those found in gallium sulphides containing covalently-bonded amines [56,145,129]. As a consequence of the shorter Ga-N bonds, GaS_3N tetrahedra are significantly more distorted than GaS_4.

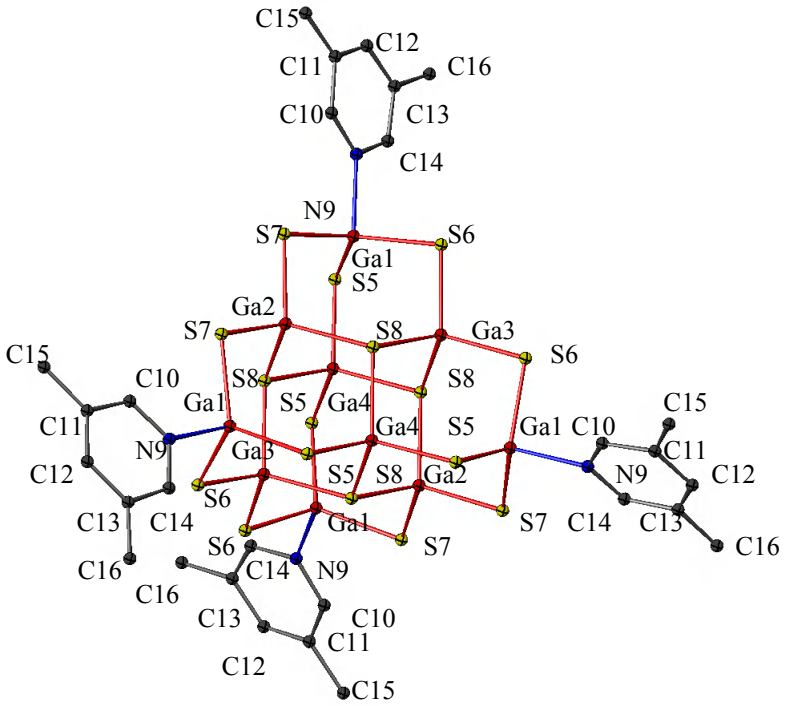

Figure 4.1. Local coordination diagram for $[Ga_{10}S_{16}(NC_7H_9)_4]^{2-}$ cluster of compound **(6)** showing the atom labelling scheme and displacement ellipsoids at 50% probability. Ga atoms are shown in red, S in yellow, C in grey and N in blue. H atoms were omitted for clarity.

Isolated clusters are separated by monoprotonated amine cations to achieve charge balance. In compound **(5)** (Figure 4.2 (a)), clusters are alternatively oriented, showing interactions between the organic ligands in the clusters and the lutidinium cations. As a consequence, a sandwich-type structure is observed along the *c*-axis (Figure 4.2 (b)), in which organic and inorganic layers alternate. In **(6)**, the supertetrahedral units are also arranged in layers parallel to the (010) plane. However, while the lutidinium cations are placed between the lutidine ligands and piperazinium cations are located between the faces of neighboring clusters (Figure 4.3). The packing is also maintained in both structures by π- π stacking interactions of the coordinated pyridine molecules to neighboring clusters. These stacking interactions have average inter-ring distances of 3.46 Å for **(5)** and 3.71 Å for **(6).** This is consistent with the range of observed distances for these type of interactions in metal complexes (contacts between two parallel pyridine ligands have been counted from slightly below 3.4 Å, which is approximately the sum of van der Waals' radii of two carbon atoms [204], up to *ca.* 3.8 Å. Higher distance values observed for very weak interactions not providing stability to the structures studied. Shorter distances were found for T-stacking interactions [205]). Additional H bonding interactions between counter cations and with the framework were found in compound **(6)**, they were calculated using PLATON [183] and are summarised in Table 4.2.

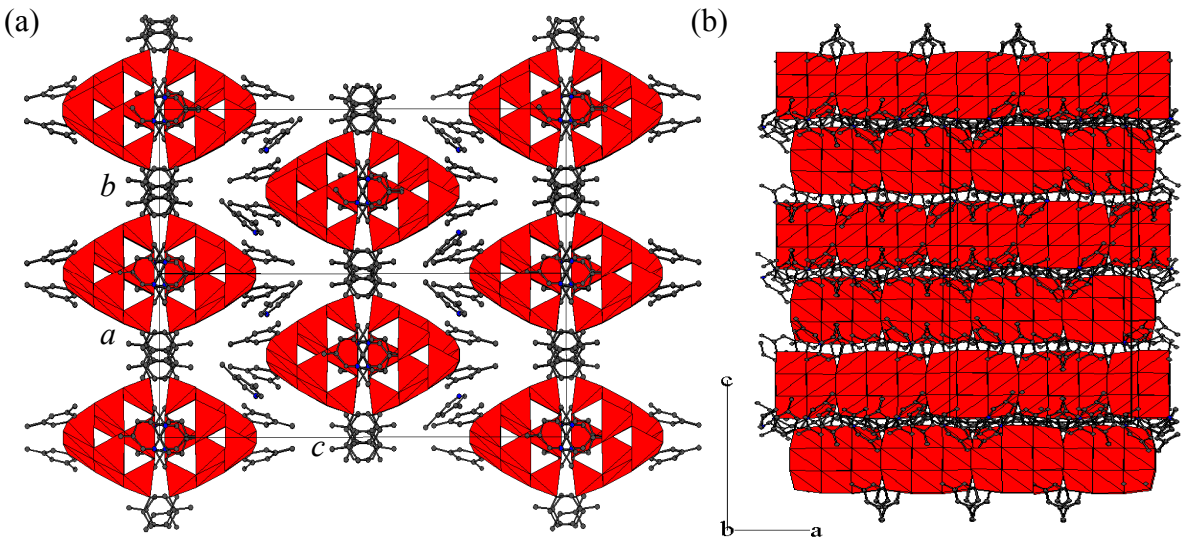

Figure 4.2. Polyhedral representation of compound **(5)**. (a) View along the [111] direction and (b) view on the (010) plane. GaS_4 and GaS_3N polyhedral clusters are shown in red, C in dark grey, and N in blue. H atoms are omitted for clarity.

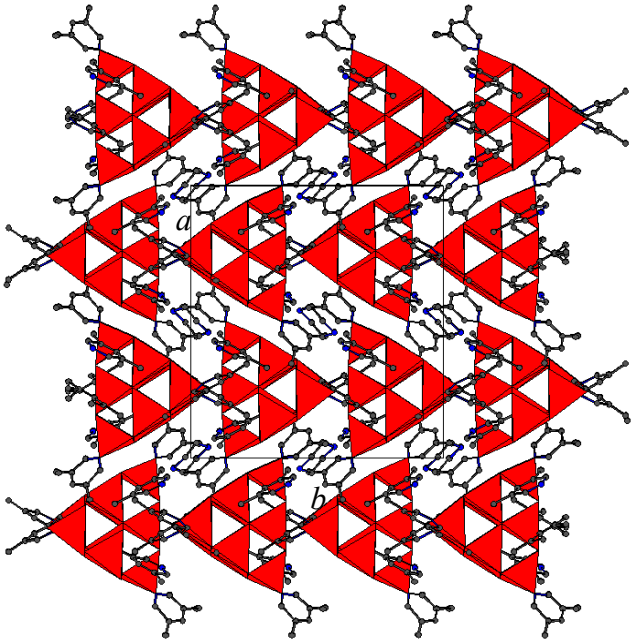

Figure 4.3. Polyhedral representation on the (001) plane of compound **(6)**. GaS_4 and GaS_3N polyhedral clusters are shown in red, C in dark grey, and N in blue. H atoms are omitted for clarity.

Table 4.2. Hydrogen bonds for **(6)**. Atoms code: D = donor, A= acceptor.

D—H…A	D—H /Å	H…A /Å	D—H…A/Å	Angle/°
N17—H171...N18	1.0300	1.6600	2.68(3)	167.00
N18—H182…S13	1.0200	2.7900	3.467(19)	124.00
N18–H182...S14	1.0200	2.5500	3.442(19)	147.00

Experimental powder X-ray diffraction patterns of **(5)** and **(6)** are in reasonable agreement with the simulated powder X-ray diffraction patterns, calculated using Powder Cell [175] (Figure 4.4). The observed diffraction patterns were fitted using TOPAS [176] in order to refine the lattice parameters (which are given in Table 4.3) and show a relatively good agreement with the unit cell parameters obtained by single crystal X-ray diffraction (Table 4.1).

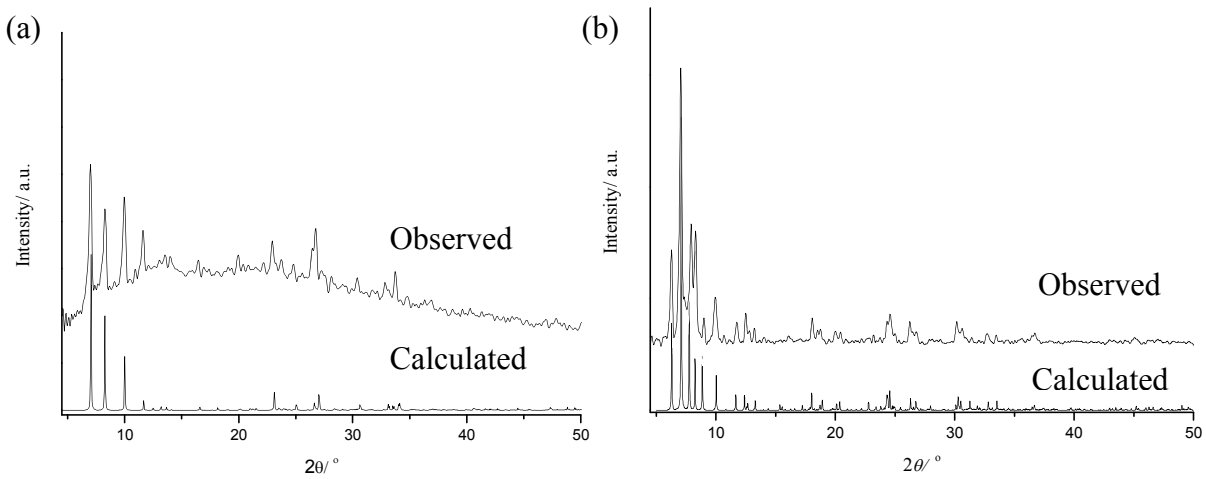

Figure 4.4. Comparison between calculated and experimental powder X-ray diffraction patterns for compounds (a) **(5)** and (b) **(6)**.

Table 4.3. Lattice parameters for compounds **(5)** and **(6)** determined using powder X-ray diffraction data.

Unit cell parameters	**(5)**	**(6)**
a/Å	15.495(1)	23.28(5)
b/Å	26.970(3)	17.93(2)
c/Å	35.243(3)	20.46(5)
β/°	-	105.8(1)

Elemental analysis and TGA

Elemental analysis for compound **(5)** reveals a composition of C: 26.50 %, H: 3.59 %, N: 4.40 %, in agreement with the calculated values deduced from the proposed formula C: 27.19 %, H: 3.04, N: 4.53%. Thermogravimetric analysis of compound **(5)** (Figure 4.5 (a)) reveals the material is stable up to *ca*. 573 K. The decomposition takes place in a single step and the total amount of weight loss is *ca.* 33%, corresponding to the total removal of the organic cations (calculated, 35 %). The final residue is a poorly crystalline grey material that could not be identified by powder X-ray diffration.

For compound **(6)** the elemental analysis composition was: C: 24.91 %, H: 3.12 %, N: 4.94 %; while the theoretical values were: C: 28.43 %, H: 3.53 %, N: 5.77 %. This disagreement could be consequence of the amorphous powder coating the crystals, which increments the amount of inorganic component and, therefore, the percentage of the organic matter is reduced. Compound **(6)** is stable up to *ca.* 450 K (Figure 4.5 (b)) and the decomposition occurs in two steps. The fist step reveals a weight loss of *ca.* 22 % at *ca.* 870 K and can be associated with the removal of the organic cations and partial

organic component of the clusters, producing an amorphous metastable phase. Finally, the total decomposition stops at *ca.* 1100 K, resulting in an amorphous grey residue. The total weight loss was *ca.* 35 %, while the calculated from the formula was 37.8%. These results are consistent with those from CHN.

FTIR

Infrared data (Appendix III) are consistent with the presence of aromatic and amine functional groups in both compounds. The vibrational modes and their frequencies are given in Table 4.4. Similar spectra were previously observed in materials containing lutidine molecules [147,206]. The presence of piperazine in compound **(6)** is almost imperceptible. However, there are differences in the shape of the spectra in the region of 2900-3500 cm^{-1}, corresponding to N-H stretching and C-H stretching in the ring, which may attributed the presence of protonated secondary amine (piperazine) in the structure [191]

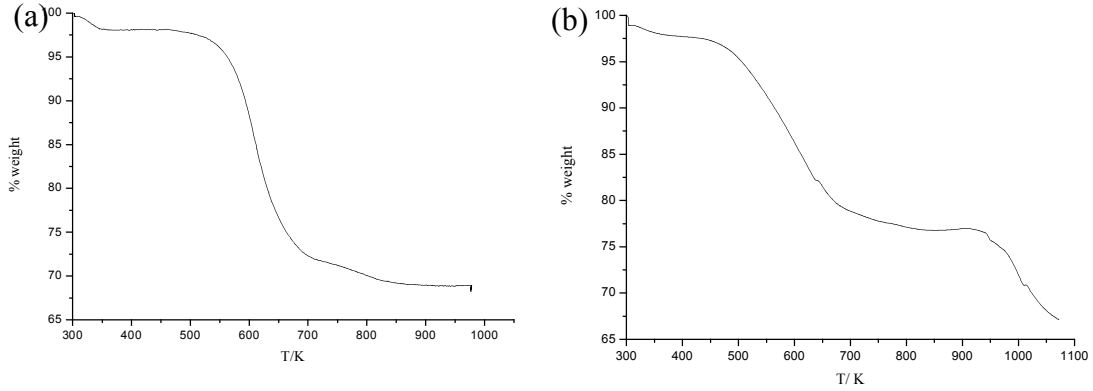

Figure 4.5. Thermogravimetric analyses for (a) compound **(5)** and (b) compound **(6)**.

Table 4.4. IR selected bands (values in cm^{-1}) for compounds **(5)** and **(6)**. υ = stretching, δ = deformation in the plane, γ = deformation out of the plane; s = strong, m = medium, w = weak.

Assignment	**(5)**	**(6)**
υ (N-H)	3476.2 (w)	3484.0 (w)
υ (C-H)	3034.7 (w)	3021.9 (w)
δ (C=C)	1609.9 (s)	1610.0 (s)
γ (C-C)	1462.7 (s)	1466.6 (s)
δ (C-H)	1149.9 (m)	1156.6 (s)
γ (C-H)	780.1 (s)	781.7 (m)

4.2.2. Structures containing picoline as ligand

$[C_{12}H_{10}N_2]_2[C_{12}H_{12}N_2]_2[C_6H_8N]_6[Ga_{10}S_{16}(NC_6H_7)_4]_4$ **(7)**: compound **(7)** was produced by mixing gallium metal (139.44 mg, 2 mmol) and sulphur (224 mg, 7 mmol) in 4-methylpyridine (4-picoline) (3 ml) in a 23 ml Teflon-lined stainless steel autoclave. The mixture had an approximate stoichiometry 2:7:30. The autoclave was placed in an oven and heated at 443 K for 5 days. The final product was formed by red needles of compound **(7)** and unreacted gallium.

$[C_6H_{7.5}N]_2[Ga_{10}S_{16}(NC_6H_7)_4]$ **(8)**: gallium metal (139.44 mg, 2 mmol), sulphur (144 mg, 4.5 mmol), 1,2-diaminocyclohexane (DACH) (114 mg, 1 mmol) and 4-picoline (3 ml) were mixed in a 23 ml Teflon-lined stainless steel autoclave with a approximate stoichiometry 2:4.5:1:30. The mixture was heated at 463 K for 10 days in an oven. The reaction product was constituted by white crystals of **(8)** and pale brown amorphous material.

Additionally, other reactions containing a different second template produced compounds identified as **(8)** by single crystal X-ray diffraction (Table 4.5).

Table 4.5. Conditions of reaction producing compound **(8)**.

Reaction Components	Ratio	T/K	Time/days
Ga:S:DAB:4-Pic	2:4:1:30	443	5
Ga:S:TPA:4-Pic	2:4.5:1:30	443	5
Ga:S:TPA:4-Pic	2:4:1:30	473	5
Ga:S:BIAL:4-Pic	2:4:1:30	443	5

$[C_{24}H_{20}P][C_6H_8N][Ga_{10}S_{16}(NC_6H_7)_4]$ **(9)**: was prepared from a mixture of gallium metal (139.7 mg, 2 mmol), sulphur (160 mg, 5 mmol), 4,4'-trimethylenedipyridine (TMPyr) (160 mg, 0.8 mmol) and tetraphenyl phosphonium bromide (TPPB) (111 mg, 0.26 mmol) in 3 ml of 4-picoline, with an approximate stoichiometry 2:5:0.8:0.26:30. The mixture was loaded in a 23 ml Teflon-lined stainless steel autoclave and heated at 463 K for 10 days. The product was constituted of orange crystals of **(9)**, orange crystalline powder (which could not be identified) and gallium.

Table 4.6. Crystallographic data for the structures **(7)**, **(8)** and **(9)**.

Formula	$[C_{12}H_{12}N_2]_2[C_{12}H_{14}N_2]_2[C_6H_7N]_6[Ga_{10}S_{16}(NC_6H_7)_4]_4$ **(7)**	$[C_6H_8N]_2[Ga_{10}S_{16}(NC_6H_7)_4]$ **(8)**	$[C_{24}H_{20}P][C_6H_8N][Ga_{10}S_{16}(NC_6H_7)_4]$ **(9)**
Mr	3814.41	1769.03	3938.47
Crystal habit	Orange plate	Pale yellow octahedron	Yellow plate
Dimensions/mm^3	0.08×0.12×0.17	0.05×0.10×0.10	0.05×0.10×0.22
Crystalline System	Triclinic	Triclinic	Monoclinic
Space group	$P\bar{1}$	$P\bar{1}$	*C2/c*
T/K	100	100	100
a/Å	20.3237 (9)	13.0962 (8)	34.5912(14)
b/Å	20.7115 (10)	14.2096 (9)	24.2839(9)
c/Å	21.4951(17)	21.0272 (13)	24.9524(10)
α/°	108.993 (4)	91.742 (3)	-
β/°	113.111 (3)	104.921 (4)	130.377(2)
γ/°	101.139 (3)	111.757 (4)	-
V/Å^3	7313.4(9)	3477.9 (4)	15967.5(12)
Z	1	2	4
Wavelength/Å Mo K_α	0.71073	0.71073	0.71073
μ/cm^{-1}	4.11	4.32	3.79
Δρ max / Å^{-3}	1.34	1.25	0.83
Δρ min / Å^{-3}	-0.79	-0.74	-1.35
Measured data	29242	20960	24315
Unique data	12723	7474	24315
Observed data ($I > 3\sigma(I)$)	15049	7474	9626
R_{merg}	0.055	0.030	0.30
$R(F_o)$[a]	0.059	0.042	0.039
$R_w(F_o)$[b]	0.064	0.047	0.042

[a] $R(F_o)=\Sigma(|F_o| - |F_o|)/ \Sigma|F_o|$. [b] $R_w(F_o)= [\Sigma w(|F_o|- |F_o|)^2 / \Sigma w|F_o|^2]^{1/2}$.

Structure description

Crystallographic information and refinement details for compound **(7)**, **(8)** and **(9)** are given in Table 4.6. The atomic coordinates (excluding hydrogen atoms), bond lengths and angles, are summarised in Appendix II. The structures were solved using direct methods, which located the Ga and S atoms. The amine C and N atoms were placed using Fourier maps and modelled isotropically for the three structures. H atoms were placed geometrically on the C and N atoms after each cycle of refinement. In compound **(7)**, distances and angles for C and N were also restrained. In compounds (7) and **(9)**, SQUEEZE [183] was also applied to reduce the effect of the solvent.

The structures of **(7)**, **(8)** and **(9)** are constituted of $[Ga_{10}S_{16}(NC_6H_7)_4]^{2-}$ isolated hybrid supertetrahedral clusters (Figure 4.6) and organic moieties. This supertetrahedral cluster is similar to those found in compound **(5)** and **(6)**. The difference is in this case that the amine is 4-picoline, which is coordinating the corner positions in the tetrahedron. The distances Ga-S lie in the 2.222(3)-2.340(2) Å range, with the larger distances corresponding to trigonally coordinated sulphur. Ga-N distances lie between 2.022(6)-2.054(8) Å, similar to those found of **(5)** and **(6)**, as expected.

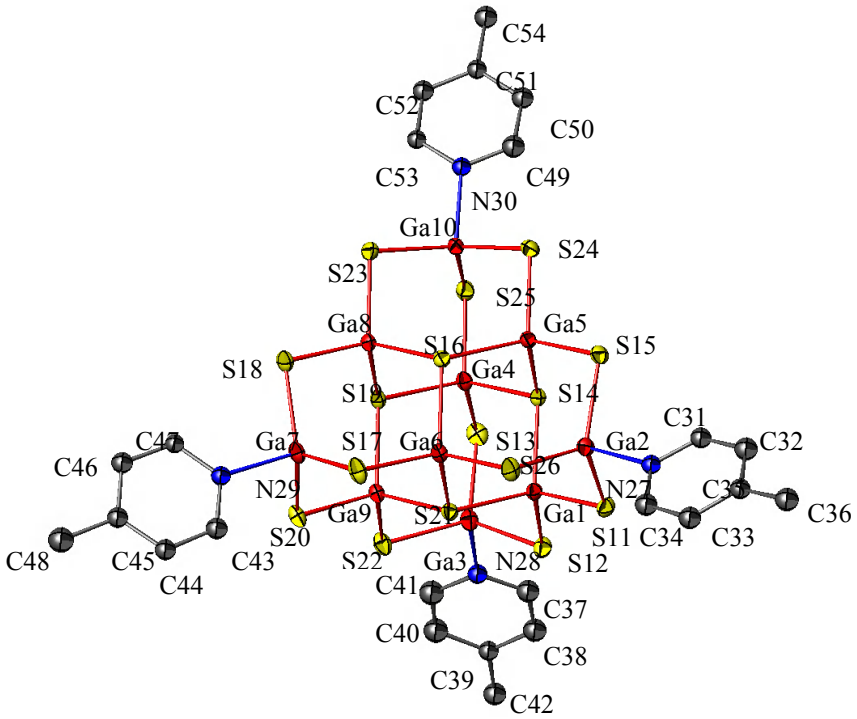

Figure 4.6. Local coordination diagram for $[Ga_{10}S_{16}(NC_6H_7)_4]^{2-}$ cluster of compound **(7)** showing the atom labelling scheme and displacement ellipsoids at 50% probability. Ga atoms are shown in red, S in yellow, C in grey and N in blue. H atoms were omitted for clarity.

The packing of clusters in compounds **(7)** and **(9)** is similar. In both compounds, the arrangement of clusters in the crystal structure results in the formation of large channels (*ca.* 5×16 Å and 5×20 Å, respectively), which are surrounded by six supertetrahedra. For **(7)** (Figure 4.7), channels run perpendicular to the (110) plane. 4-picoline and dipyridyl molecules (Dp) are found together within the cavities. The latter is a consequence of the dimerisation of 4-picoline under the conditions employed in the reaction [207]. Meanwhile in compound **(9),** the channels are filled with protonated 4-picoline and tetraphenyl phosphonium (TPP) cations. The interactions between clusters are caused by the arrangement of the pyridyl rings through π–π stacking. For compound **(7)**, there are observed slipped stacking interactions between 4-picoline ligands, 4-picolinium and Dp cations with an average interring distance of 3.52 Å and T-stacking interactions with a distance of 2.86(5) Å. In compound **(9)** (Figure 4.8), slipped stacking interactions are observed between TPP cations and 4-picoline ligands with a interring distance of 3.81(5) Å and T-stacking interactions with 4-picoline cations 2.42(6) Å.

In compound **(7)**, a portion of these organic moieties are protonated to achieve the charge balance in the structure and interactions between organic moieties are observed. H bonds were calculated using Platon [183] and summarised in Table 4.7.

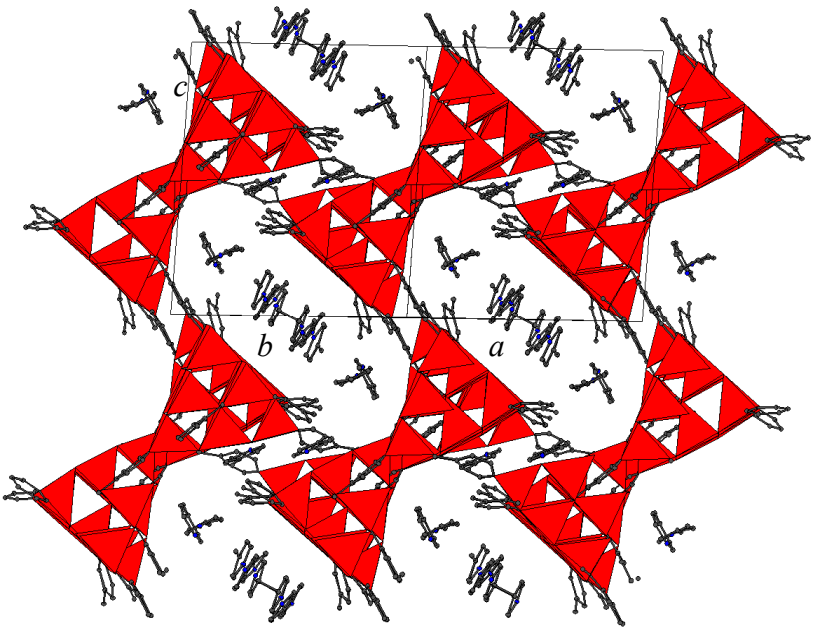

Figure 4.7. Polyhedral representation on the (111) plane of compound **(7)**. GaS_4 and GaS_3N polyhedra are shown in red, C in dark grey, and N in blue. H atoms are omitted for clarity.

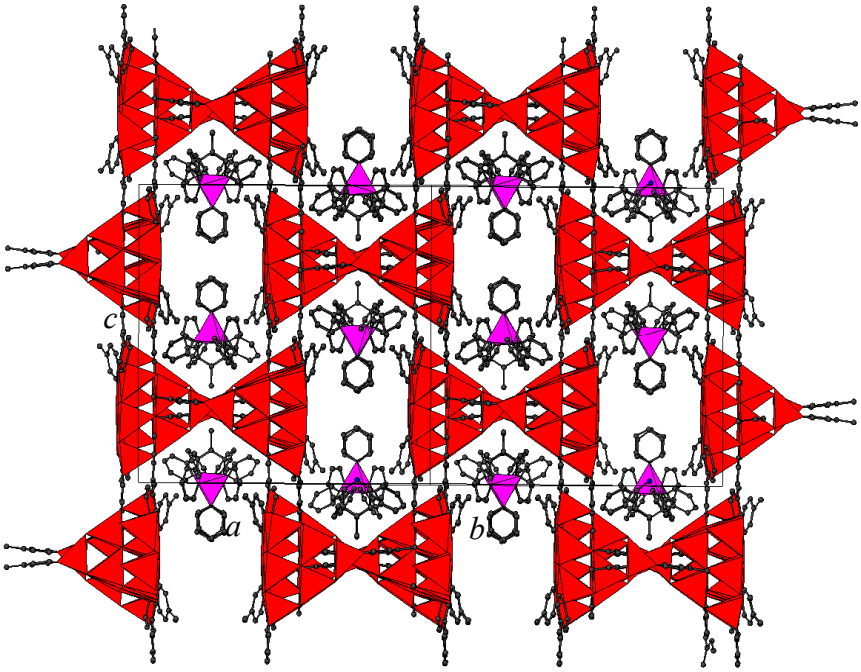

Figure 4.8. Polyhedral representation on the (111) plane of compound **(9)**. GaS_4 and GaS_3N polyhedra are shown in red, PC_4 polyhedra in pink, C in dark grey, and N in blue. H atoms are omitted for clarity.

Table 4.7. Hydrogen bonds for **(7)**. Atoms code: D = donor, A= acceptor. Symmetry codes: (ii) $-x+1, -y, -z+1$.

D—H…A	D—H /Å	H…A /Å	D—H…A/Å	Angle/°
N64——H641...N61	1.05	1.55	2.60(4)	176
N67—H671…N62	1.00	1.45	2.44(4)	168

In compound **(8)** (Figure 4.9), the supertetrahedral units form a zig-zag distribution which run parallel to the *c*-axis. Zig-zag lines of supertetrahedra are aligned in parallel sheets along the (010) plane. This configuration is consequence the presence of π–π interactions between 4-picoline ligands. The interring distance found was 3.74(1) Å. 4-picoline cations are placed between the zig-zag supertetrahedral distributions, stabilising the crystal structure through electrostatic interactions. Interactions between the organic moieties are also observed and are summarised in Table 4.8.

Table 4.8. Hydrogen bonds for **(7)**. Atoms code: D = donor, A= acceptor.

D—H…A	D—H /Å	H…A /Å	D—H…A/Å	Angle/°
N62—H641...N55	1.00	1.61	2.611(16)	179

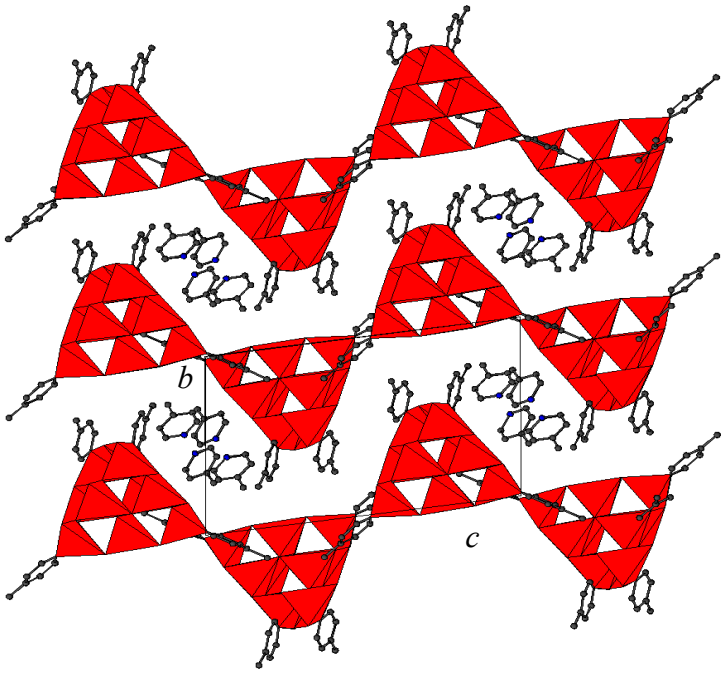

Figure 4.9. Polyhedral representation along the (011) plane of compound **(8)**. GaS_4 and GaS_3N polyhedra are shown in red, C in dark grey, and N in blue. H atoms are omitted for clarity.

The simulated powder X-ray diffraction patterns (using Powder Cell [175]) for the three structures are in good agreement with the experimental powder X-ray diffraction patterns obtained from the bulk samples (Figure 4.10). Some differences on the intensities are observed when the X-ray pattern are compared may be caused by preferred orientations of the crystals. The observed diffraction patterns were fitted using TOPAS [176] in order to refine the lattice parameters, which are given in Table 4.9, and show a reasonable agreement when compared with the cell parameters obtained using single crystal diffraction (Table 4.6).

Table 4.9. Lattice parameters for compounds **(7)**, **(8)** and **(9)** determined using powder X-ray diffraction data.

Unit cell parameters	**(7)**	**(8)**	**(9)**
a/Å	20.31(1)	13.066(3)	34.61(1)
b/Å	20.66(1)	14.185(3)	24.28(1)
c/Å	22.56(2)	20.976(5)	24.98(1)
α/°	110.06(4)	91.71(1)	-
β/°	115.62(2)	104.97(1)	130.42(2)
γ/°	101.18(4)	111.82(1)	-

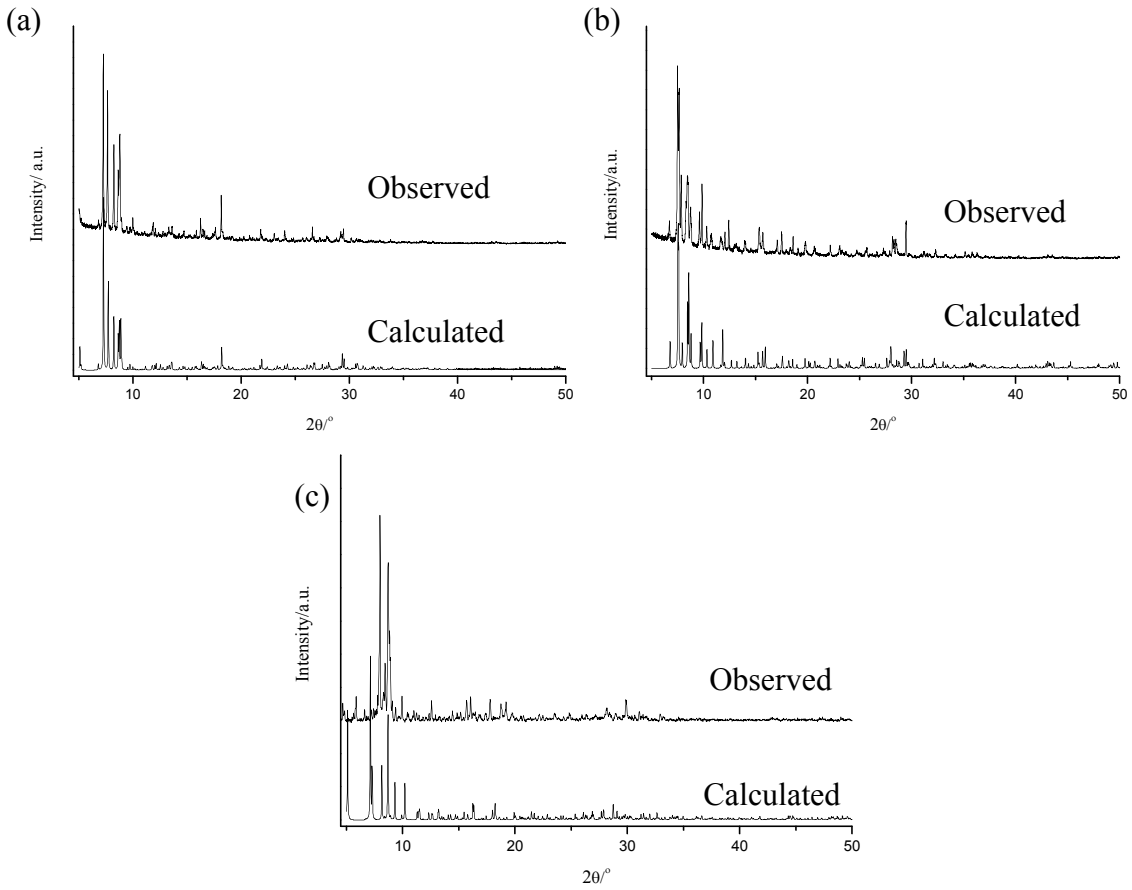

Figure 4.10. Comparison between calculated and experimental diffraction patterns for compounds (a) **(7)**, (b) **(8)** and (c) **(9)**.

Elemental analysis and TGA

For compound **(7)**, elemental analysis shows a good agreement with the calculated data (experimental: C: 27.2, H: 2.6, N: 5.1%; calculated: C: 28.3, H: 2.7, N: 5.5%). Thermogravimetric analysis of compound **(7)** (Figure 4.11 (a)) indicates the compound is stable up to *ca*. 393 K. The decomposition occurs in two steps. The first weight loss corresponds to *ca.* 22 %, which may be attributed to the lost of organic matter not forming part of the clusters. The total weight loss was *ca*. 53 % at *ca.* 1200 K. This result differs from the expected weight loss value from the formula (35 %). As the remaining product was identified as Ga_2O_3 by powder X-ray diffraction, the second step could be associated to the lost of the remaining organic matter (*ca.* 10 %) and the decomposition of the sample to Ga_2O_3. The formation of Ga_2O_3 is probably associated to leaks in the system at that temperature or to the reaction of impurities (O_2) in the N_2 flow (purity 99%) which react with the sample at those temperatures. Attempts to identify the intermediate product or stop the decomposition before the formation of Ga_2O_3 were unsuccessful.

Compound **(8)**: elemental analysis is in fair agreement with the proposed formula (experimental C: 25.6, H: 2.8, N: 5.7%; calculated: C: 24.4, H: 2.4, N: 4.8%). Compound **(8)** presents similar stability of that of compound **(7)** up to *ca.* 393 K (Figure 4.11 (b)). The degradation takes place in two steps. The first step corresponds to a weight loss of *ca.* 30 % at *ca*. 700 K (calculated value 32 %). This intermediate could not be identified by powder X-ray diffraction. The second step finishes at *ca.*1200 K and is associated with the decomposition of the material to Ga_2O_3, which was identified by powder X-ray diffraction.

In compound **(9)**, the content of organic component is inferior to the calculated one, this disagreement may be caused by crystals coated with the second phase present in the sample (experimental C: 27.88 H: 2.67 N: 2.65; calculated C: 32.17, H: 2.8, N: 3.46). **(9)** is stable up to *ca.* 450 K, analogous to compounds containing hybrid lutidine gallium-sulphide clusters. The decomposition takes place with two dramatic changes of slope (Figure 4.11(b)). The first weight loss of *ca.* 28 % occurs between 450 and 800 K and is consistent with weight loss calculated from CHN analysis (32%). The second weight loss finishes at 1200 K. The remaining residue was identified as Ga_2O_3.

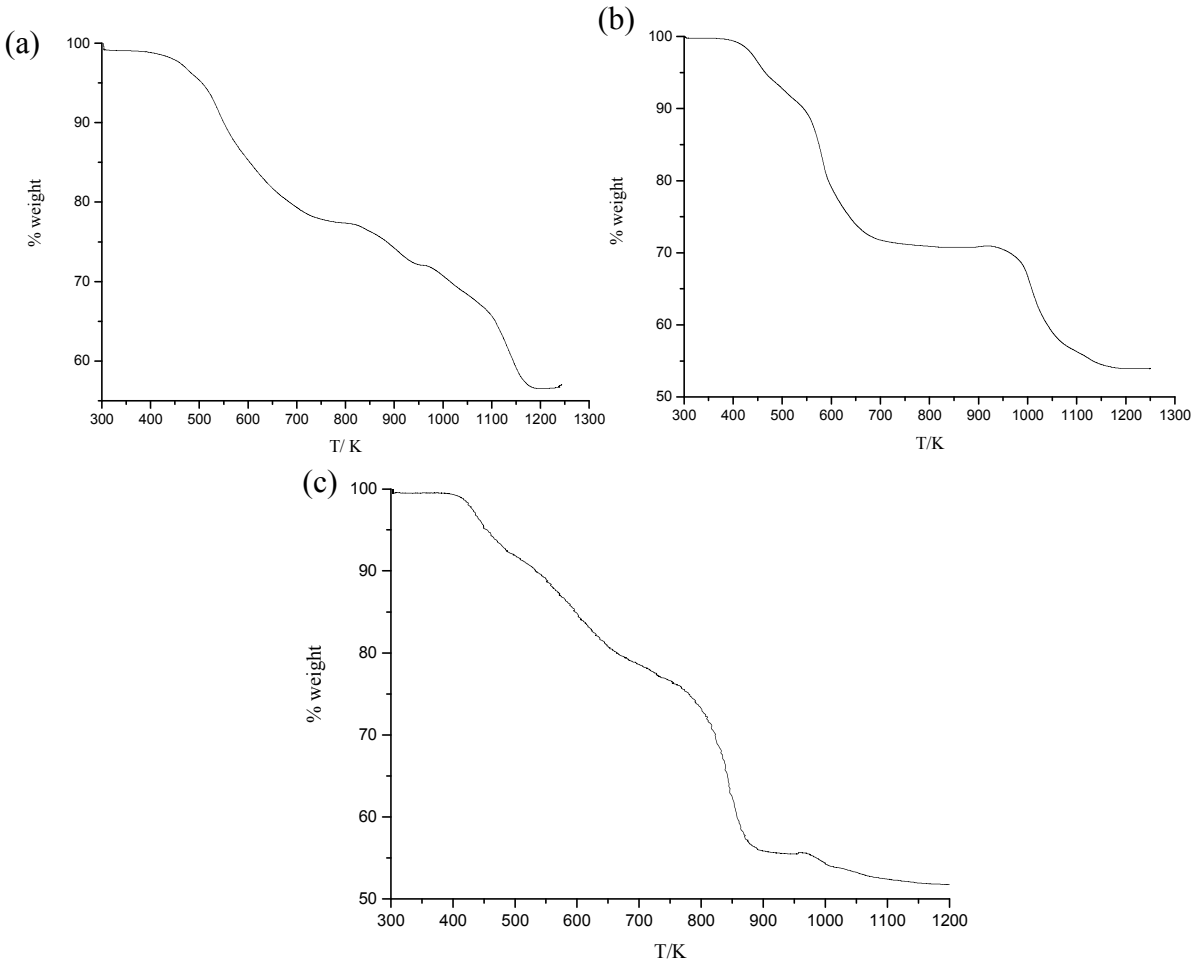

Figure 4.11. TGA data corresponding to compounds (a) **(7)**, (b) **(8)** and (c) **(9)**.

FTIR

Compounds **(7)**, **(8)** and **(9)** present similar infrared spectra (Appendix III). The vibrational modes and their frequencies are given in Table 4.10. They are consistent with the presence of aromatic and amine functional groups, and the presence of 4-picoline. In compound **(7)**, the presence of Dp is masked because both amines present the same functional group. In compound **(8)**, the presence of 4-picoline is observed, and any sign of secondary amine is not observed. In compound **(9)**, the presence of tetraphenyl phosphonium cations is corroborated by the presence of a deformation band C-H at 1109 cm^{-1}, assigned to the phenyl vibrations in the ring and weak stretching band (P-ϕ) at 760.0 cm^{-1} [208].

Table 4.10. IR selected bands (values in cm^{-1}) for compound **(7)**, **(8)** and **(9)**. υ = stretching, δ = deformation in the plane, γ = deformation out of the plane; s = strong, m = medium, w = weak.

Assignment	**(7)**	**(8)**	**(9)**
υ (N-H)	3449.6 (m)	3466.8 (m)	3568.0 (w)
υ (C-H)	3040.4 (w)	3035.9 (w)	3058.1 (w)
υ (C=C)	1621.0 (s)	1629.5 (s)	1618.8 (s)
γ (C-C)	1439.8 (s)	1439.6 (s)	1438.3 (s)
δ (C-H)	1037.6 (s)	1037.4 (s)	1037.5 (s)
γ (C-H)	815.8 (s)	816.8 (s)	816.6 (s)
δ (C-H)	-	-	1109.0 (w)
υ (P- ϕ)	-	-	760.0 (w)

Diffuse Reflectance

The optical absorption spectra for compounds from **(5)** to **(9)** are shown in Figure 4.12. Band gap values are summarised in Table 4.11 and indicate that these materials exhibit semiconducting behaviour. There is a red shift of the absorption edge when compared with extended frameworks containing T3 clusters (see Section 3.4; E = 4.0(1) eV). For compound **(7)**, an extra band is observed at *ca*. 2.9(2) eV (425 nm). This band may be attributed to differences on the band gap caused by non-equivalent supertetrahedral clusters. In this compound, the presence of different type of counter-cations interacting in a different grade which each cluster. Therefore, the positions of the supertrahedra are

non-equivalent. The band gap that is a contribution of the energy levels from all the supertetrahedral cluster is not regular then and the linearity in the band gap which is assumed for homogeneous material is broken. This phenomenon is also reflected in a low symmetry for compound **(7)**. This compound exhibits also an incipient band at *ca.* 2 eV (*ca.* 620 nm) and raises up to 1.2 eV (*ca.* 1000 nm) that could be associated to the red colour of the crystal. This bands may be attributed to relaxation process of a ion-pair charge-transfer [209], which can take place between the organic moieties contained within the structure and with the hybrid clusters. For compound **(9) (*)** the low band gap value is clearly associated to an ion-pair charge-transfer between the clusters and the tetraphenyl phosphonium cations [209], that may be mask the band gap corresponding to the gallium-sulphide supertetrahedral cluster.

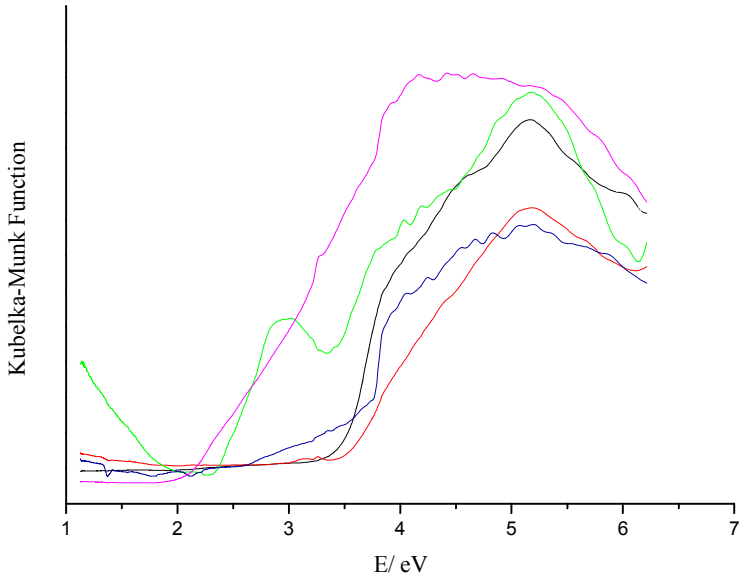

Figure 4.12. Optical absorption spectra for compounds **(5)** to **(9)**. Compounds are represented by red, blue, green, black and magenta lines, respectively.

Table 4.11. Band gap values for compound **(5)** to **(9)**.

Compound	Band Gap/ eV
(5)	3.3(1)
(6)	3.5(1)
(7)	2.9(1)
(8)	3.4(2)
(9)	2.0(3)*

4.2.3. Structures containing dimeric units

Synthesis

$[C_7H_{10}N]_6[Ga_{20}S_{34}H_2(NC_7H_9)_4(N_2C_{12}H_{10})]$ **(10)**: gallium metal (139.4 mg, 2 mmol), sulphur (144 mg, 4.5 mmol), 1,2-di(4-pyridyl)ethylene (DPE) (182 mg, 1 mmol), $FeCl_2 \cdot 4H_2O$ (59.6 mg, 0.29 mmol) and lutidine (3 ml) were mixed in a 23 ml Teflon-lined stainless steel autoclave. The molar ratio of the mixture was 2:4.5:1:0.29:26. After the vessel was sealed, the reaction mixture was heated at 473 K for 10 days and then allowed to cool to room temperature at 1 K min^{-1}. The product consisted of a mixture of white crystals identified as **(10)** and a dark grey polycrystalline powder.

$[C_6H_8N]_2[Ga_{20}S_{32}(N_2C_{12}H_{12})(N_2C_{12}H_{13})_2(NC_6H_7)_4]$ **(11)**: gallium metal (139.4 mg, 2 mmol), sulphur (144 mg, 4.5 mmol), DPE (182 mg, 1 mmol), TPPB (111 mg, 0.26 mmol) and 4-picoline (3 ml) with an approximate stoichiometry 2:4.5:1:0.26:31 were loaded in a 23 ml Teflon-lined stainless steel autoclave and heated at 473 K for 20 days. The final product consisted of a mixture of yellow crystals of **(11)**, yellow powder and unreacted gallium.

$[C_7H_{10}N]_6[Ga_{10}S_{16}(NC_7H_9)(N_2C_{10}H_8)_3][Ga_{20}S_{32}(NH_3)_2(NC_6H_7)_4(N_2C_{10}H_8)]$ **(12)**: a mixture of gallium metal (139.44 mg, 2 mmol), sulphur (144 mg, 4.5 mmol), Dp (156 mg, 1mmol) and lutidine (3 ml) was located in a 23 ml Teflon-lined stainless steel autoclave. The stoichiometry of the mixture was 2:4.5:1:26. The autoclave was heated at 473 K for 20 days. The reaction product contained orange needles identified as **(12)** and a small amount of unreacted gallium.

Structure description

Crystallographic information and refinement details for compounds **(10)** to **(12)** are given in Table 4.12. The atomic coordinates, excluding hydrogen atoms, bond lengths and angles, are summarised in Appendix II. The structures were solved using direct methods, which located the Ga and S atoms. The amine C and N atoms were placed using Fourier maps. In compounds **(11)** and **(12)**, C and N atoms were modeled isotropically because the presence of large thermal parameters may indicate certain degree of disorder. The data in both cases were treated with SQUEEZE [183] to correct the effect of the disordered organic cations not located. H atoms were placed geometrically on the C and N atoms after each cycle of refinement. For compound **(12)**, H atoms placed and the positions refined with riding constraints.

Table 4.12. Crystallographic data for the structures **(10)**, **(11)** and **(12)**.

Formula	$[C_7H_{10}N]_6$ $[Ga_{20}S_{34}H_2(NC_7H_9)_4$ $(N_2C_{12}H_{10})]$ **(10)**	$[C_6H_8N]_2$ $[Ga_{20}S_{32}(N_2C_{12}H_{12})$ $(NC_{12}H_{13}N)_2$ $(NC_6H_7)_4]$ **(11)**	$[C_7H_{10}N]_6$ $[Ga_{10}S_{16}(NC_7H_9)$ $(N_2C_{10}H_8)_3]$ $[Ga_{20}S_{32}(NH_3)_2$ $(NC_6H_7)_4(N_2C_{10}H_8)]$ **(12)**
Mr	3746.48	3440.89	5201.90
Crystal habit	Colourless plate	Yellow plate	Orange plate
Dimensions/mm^3	0.08 × 0.40 × 0.46	0.15 × 0.20 × 0.25	0.12 × 0.20 × 0.30
Crystalline System	Triclinic	Monoclinic	Monoclinic
Space group	$P\bar{1}$	$P2_1/n$	$P2_1/m$
T/K	100	100	100
a/Å	12.0720 (6)	13.7338 (5)	14.8534(6)
b/Å	12.2402 (7)	19.8894 (7)	34.1528(15)
c/Å	22.7189 (12)	47.2955 (16)	21.0321(9)
α/°	89.774 (3)	-	-
β/°	80.018 (3)	94.340 (2)	91.630(3)
γ/°	76.112 (3)	-	-
V/Å^3	3207.1 (3)	12882.1(8)	10665.0(8)
Z	1	4	2
Wavelength/Å Mo K_α	0.71073	0.71073	0.71073
μ/cm^{-1}	4.72	4.66	4.22
$\Delta\rho$ max / Å^{-3}	0.61	1.27	1.31
$\Delta\rho$ min / Å^{-3}	-0.66	−0.80	-0.75
Measured data	85265	39791	32644
Unique data	19455	10814	32644
Observed data ($I > 3\sigma(I)$)	11777	13997	10626
R_{merg}	0.27	0.051	0.042
$R(F_o)$[a]	0.024	0.053	0.043
$R_w(F_o)$[b]	0.027	0.066	0.048

[a] $R(F_o)=\Sigma(|F_o| - |F_o|)/ \Sigma|F_o|$. [b] $R_w(F_o)= [\Sigma w(|F_o|- |F_o|)^2 / \Sigma w|F_o|^2]^{1/2}$.

Compound **(10)** contains clusters of stoichiometry $[Ga_{10}S_{17}H(NC_7H_9)_2(N_2C_{12}H_{10})_{1/2}]^{3-}$ (Figure 4.13), which are connected by a DPE molecule forming dimeric units of stoichiometry $[Ga_{20}S_{34}H_2(NC_7H_9)_4(N_2C_{12}H_{10})]^{6-}$ (Figure 4.14). The remaining vertexes of each supertetrahedral cluster are terminated by two lutidine molecules and in the fourth vertex SH groups were found. The average Ga-N distance has been found to be 2.042 Å, significantly shorter than the Ga-SH distance, 2.2680(7) Å, which is comparable with the Ga-S distances within the cluster, (between 2.2107(7)-2.3513(7) Å). The longer Ga-S distances correspond to the tri-coordinated S located in the center of the faces.

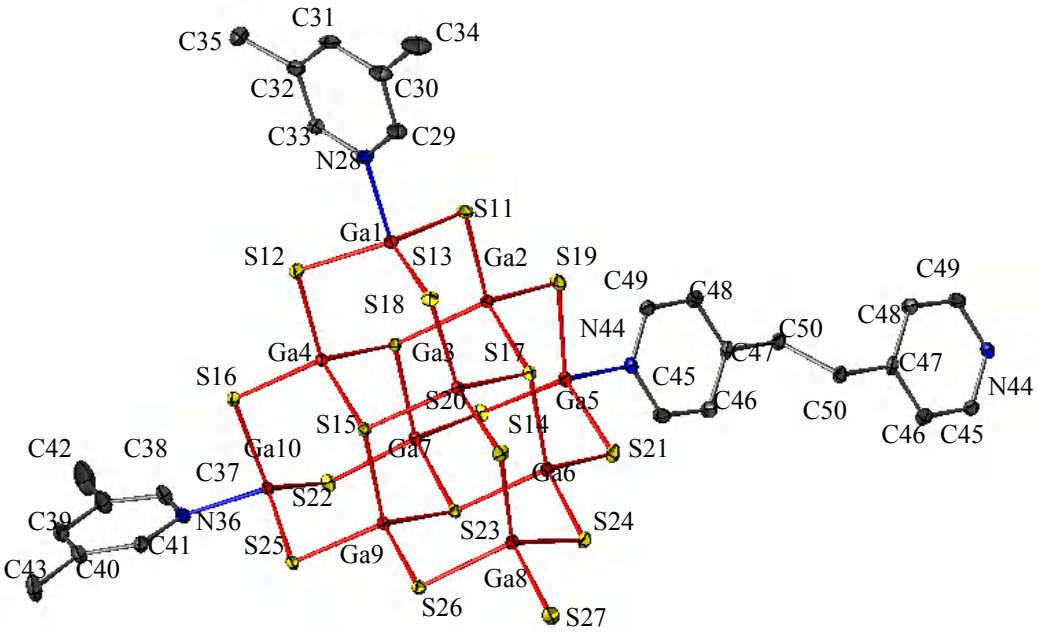

Figure 4.13. Local coordination diagram for $[Ga_{10}S_{17}H(NC_7H_9)_2(N_2C_{12}H_{10})]^{3-}$ showing the atom labelling scheme and displacement ellipsoids at 50% probability. Ga atoms are shown in red, S in yellow, C in grey and N in blue. H atoms were omitted for clarity.

The dimeric supertetrahedral clusters are arranged in sheets parallel to the plane *ab* and separated by protonated lutidine cations (Figure 4.15). The structure is stabilised by hydrogen bonding between the anionic clusters and the protonated amines. Hydrogen bonding distances were obtained using PLATON [183] and are summarised in Table 4.13. Slipped parallel stacking interactions between pyridyl rings of neighbouring dimers are also observed along the [-110] direction, with an approximate interaction distance of 3.56(0) Å. Parallel stacking of pairs of organic cations are observed at 3.51(9) Å.

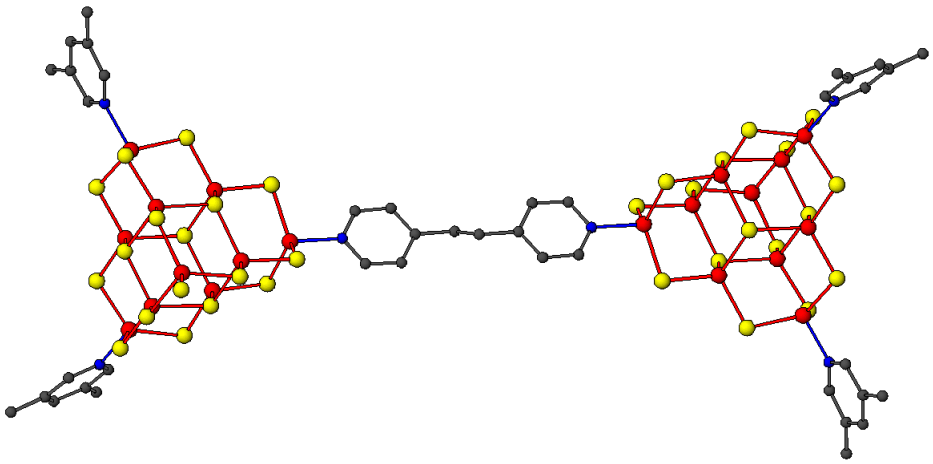

Figure 4.14. The discrete unit $[Ga_{20}S_{34}H_2(NC_7H_9)_4(N_2C_{12}H_{10})]^{6-}$ found in compound **(10)**. Ga atoms are shown in red, S in yellow, N in blue and C in dark grey. H atoms have been omitted for clarity.

Table 4.13. Hydrogen bonds for **(10)**. Atoms code: D = donor, A= acceptor.

D—H…A	D—H /Å	H…A /Å	D—H…A/Å	Angle/°
N90—H901…S34	1.0000	2.610(0)	3.426(4)	138.00

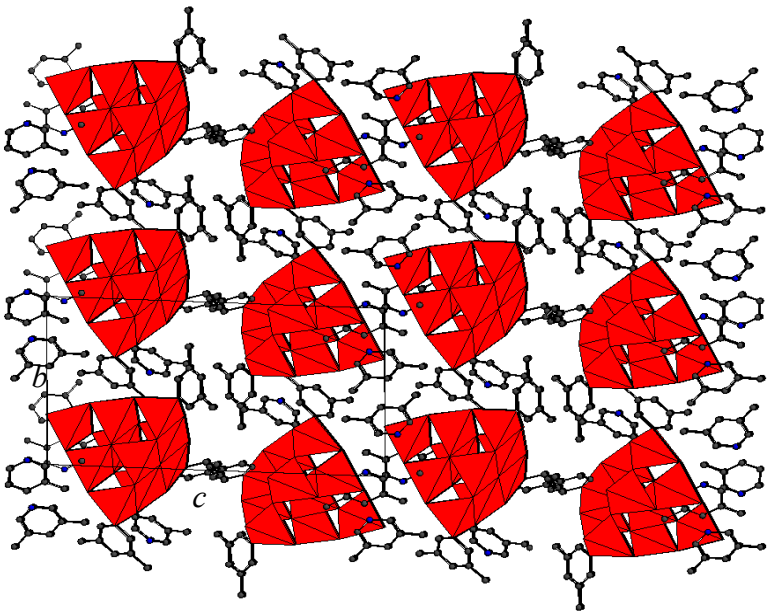

Figure 4.15. Polyhedral representation on (100) plane of compound **(10)**. GaS_4 and GaS_3N tetrahedra are shown in red, C atoms in dark grey and N in blue. H atoms are omitted for clarity.

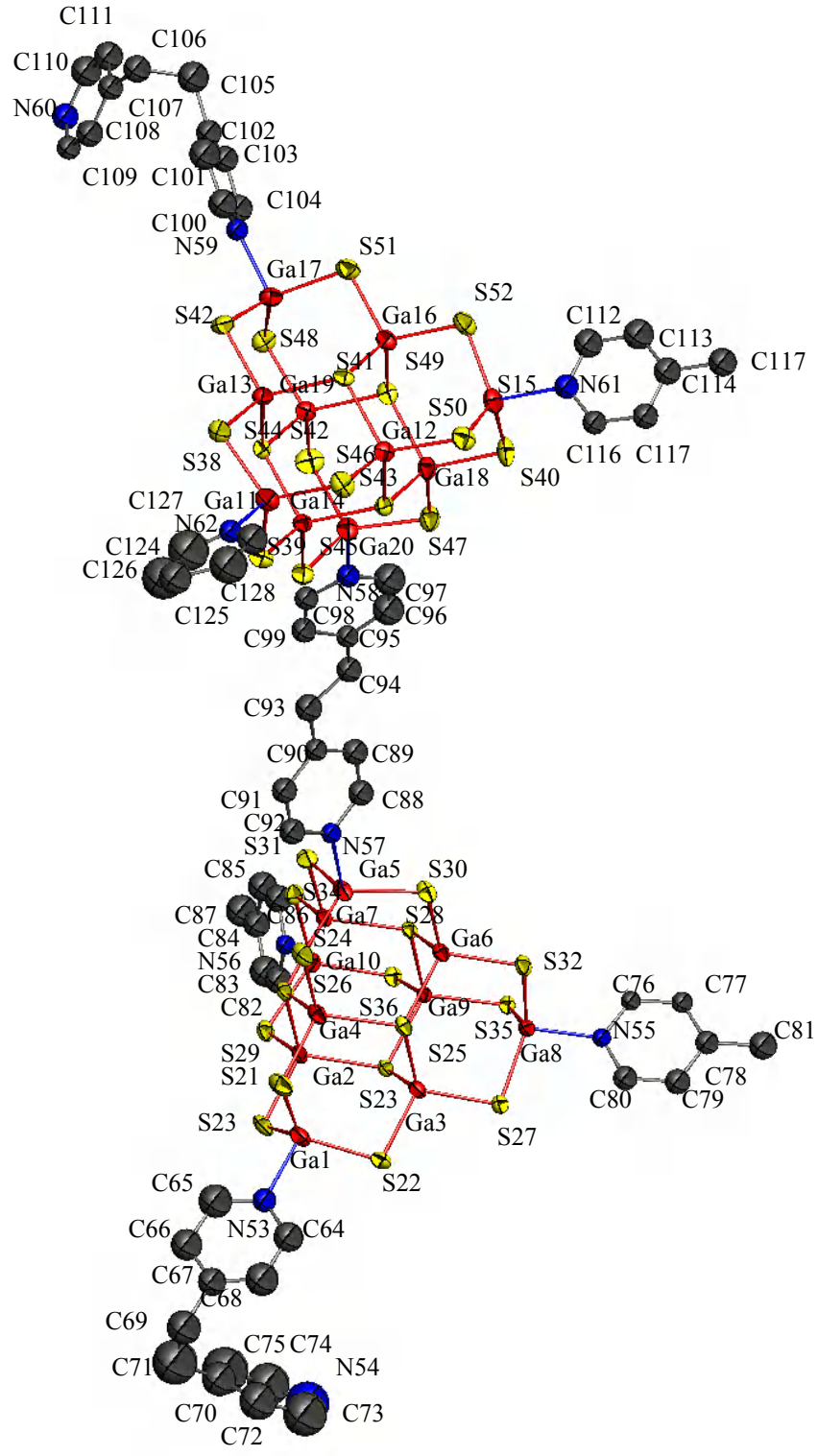

Figure 4.16. Local coordination diagram for $[Ga_{20}S_{32}(N_2C_{12}H_{12})(NC_{12}H_{13}N)_2(NC_6H_7)_3(NC_5H_5)]^{4-}$ showing the atom labelling scheme and displacement ellipsoids at 50% probability. Ga atoms are shown in red, S in yellow, C in dark grey and N in blue. H atoms were omitted for clarity.

The $[Ga_{20}S_{32}(N_2C_{12}H_{12})(NC_{12}H_{13}N)_2(NC_6H_7)_3(NC_5H_5)]^{2-}$ dimeric unit found in compound **(11)** (Figure 4.16) consists of two supertetrahedral hybrid clusters connected

through a 1,2-di(4-pyridyl)ethane (BPe) ligand. The presence of 1,2-di-(4-pyridyl)ethane (BPe) is consequence of the hydrogenation of the double bond that separates pyridine rings in the initial 1,2-di-(4-pyridyl)ethylene (DPE). The remaining corners in both clusters are coordinated by one DPE ligand (which is not coordinated to other clusters), 4-picoline and pyridine molecules. Ga-S distance lie in the range 2.223(3)-2.326(2) Å and the mean value of the Ga-N distance is 2.032 Å. Both are comparable with previous supertetrahedral hybrid gallium-sulphides.

The structure of **(11)** may be described as dimeric units of supertetrahedral clusters with the same orientation ordered forming layers parallel to the (100) plane, which are packed following an ABCD sequence (Figure 4.17). Charge balancing is achieved through incorporation of protonated 4-picoline cations. Only one molecule of 4-picoline per formula unit which is located between the layers, was found in the Fourier maps. Given charge balancing requirements together with the large amount of void space (2401.4 $Å^3$) (which was calculated with PLATON [183]), it is likely that the structure contains a second disordered 4-picoline cation. This assumption is in agreement with the analytical data.

Only interactions through hydrogen bonding are observed between ligands and protonated amines. Distances were obtained using PLATON [183] and are summarised in Table 4.14.

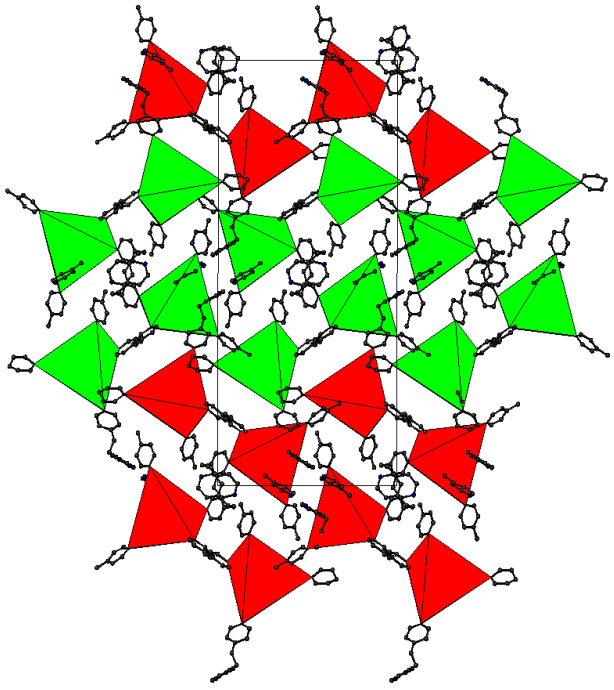

Figure 4.17. Polyhedral representation of the structure of the compound **(11)** within the (100) plane. Supertetrahedra with different orientated layers are shown in red and green, respectively. C atoms are shown in dark grey and N in blue. H atoms are omitted for clarity.

Table 4.14. Hydrogen bonds for **(11)**. Atoms code: D = donor, A= acceptor. Symmetry codes: (iii) $-x+3/2, y-1/2, -z+3/2$; (iv) $-x+3/2, y+1/2, -z+3/2$.

D—H…A	D—H /Å	H…A /Å	D—H…A/Å	Angle/°
N60—H140...N63iii	0.9	1.95	2.67(3)	141
N63—H159...N60iv	0.9	1.82	2.67(3)	168

In compound **(12)**, $[Ga_{20}S_{32}(NH_3)_2(NC_6H_7)_4(N_2C_{10}H_8)]^{4-}$ dimers (Figure 4.18) and $[Ga_{10}S_{16}(NC_7H_9)(N_2C_{10}H_8)_3]^{2-}$ discrete clusters (Figure 4.19) co-exist as anionic species (Figure 4.20). The dimers are formed by two supertetrahedral hybrid clusters connected by a Dp molecule. The terminal S^{2-} anions are replaced in each cluster by 4-picoline, pyridine and NH_3. The isolated hybrid cluster has three of its terminal gallium coordinated to molecules of Dp and the fourth corner is substituted by a lutidine molecule.

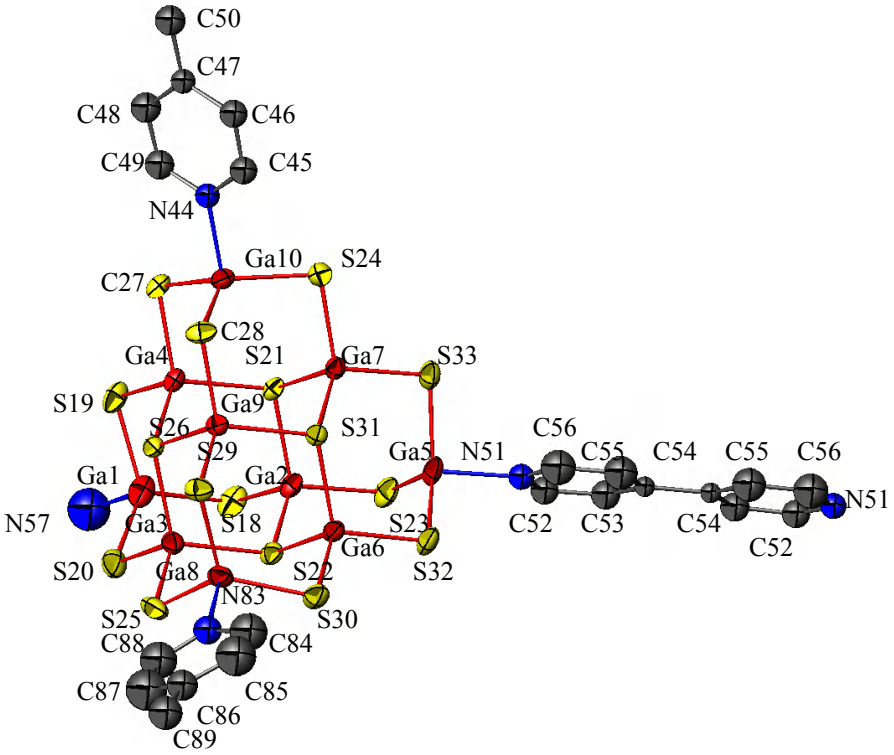

Figure 4.18. Local coordination diagram for the supertetrahedral unit in the dimer $[Ga_{10}S_{16}(NH_3)(NC_6H_7)_2(N_2C_{10}H_8)]^{2-}$ showing the atom labelling scheme and displacement ellipsoids at 50% probability. Ga atoms are shown in red, S in yellow, C in grey and N in blue. H atoms were omitted for clarity.

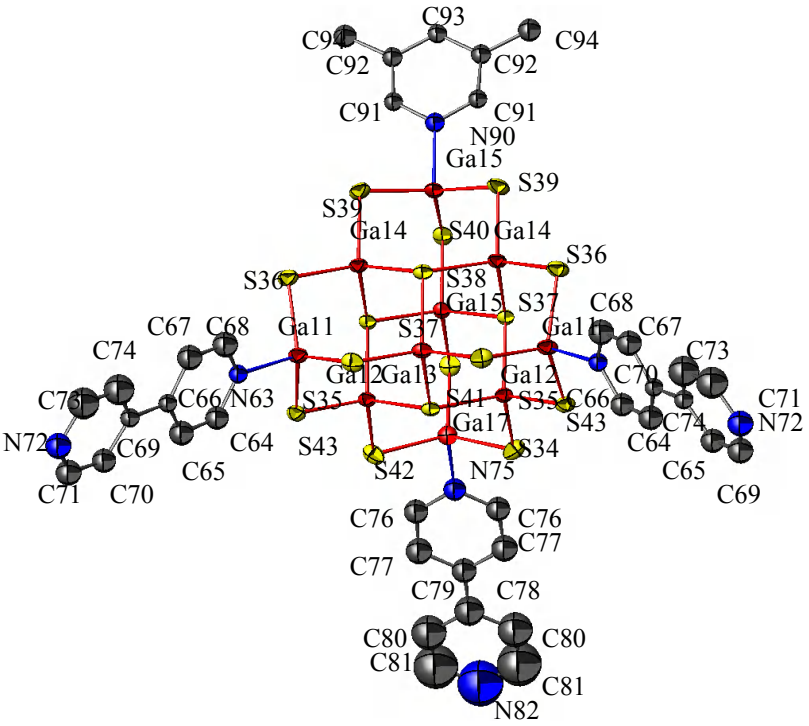

Figure 4.19. Local coordination diagram for $[Ga_{10}S_{16}(NC_7H_9)(N_2C_{10}H_8)_3]^{2-}$ discrete cluster showing the atom labelling scheme and displacement ellipsoids at 50% probability. Ga atoms are shown in red, S in yellow, C in grey and N in blue. H atoms were omitted for clarity.

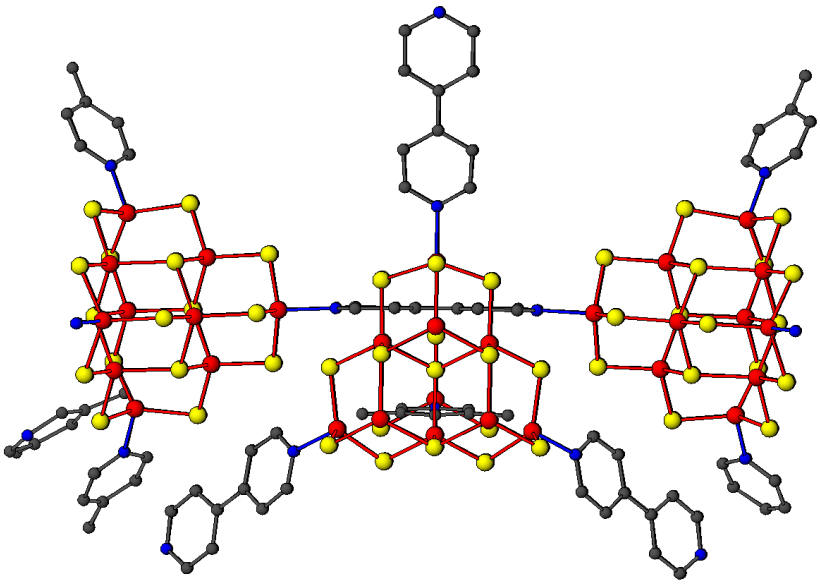

Figure 4.20. View of the anionic building units in compound **(12)**. Ga atoms are shown in red, S in yellow, N in blue and C in dark grey. H atoms have been omitted for clarity.

The structure of **(12)** consists of dimeric units and isolated clusters arranged in an alternating fashion in layers parallel to the (100) plane (Figure 4.21). Protonated lutidine cations are placed between the anions, some of them present a high disorder and could not be found in the Fourier maps, but were added in the formula to stabilise the charge and are consistent with the analytical data. Parallel stacking of pairs of pyridyl rings are observed between neighbouring pyridyl ring clusters and lutidine cations and organically-functionalised clusters, showing an average interaction distance of 3.74 Å.

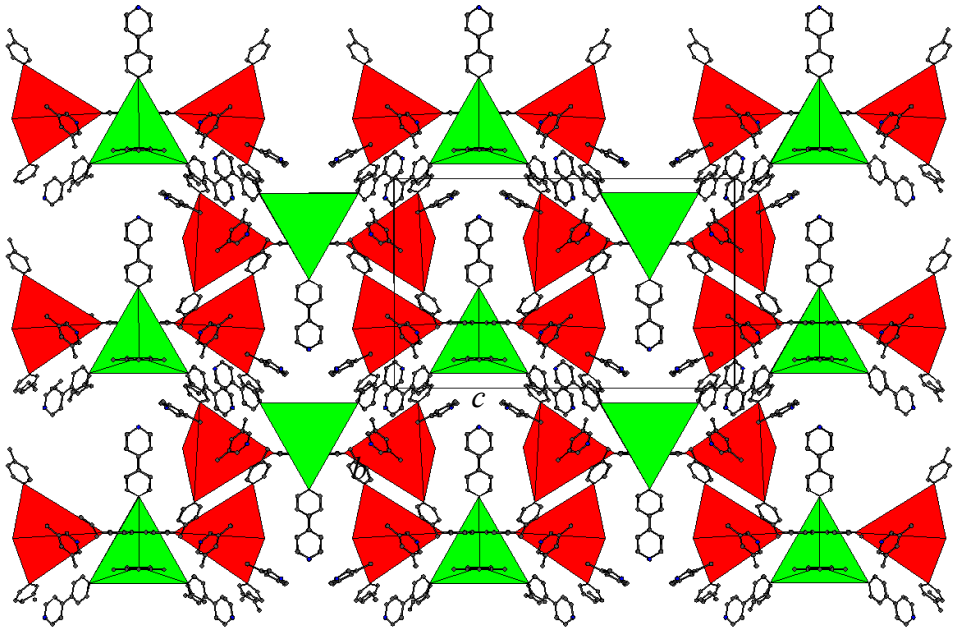

Figure 4.21. View on the (100) plane of compound **(12)**. Clusters from dimeric anions are shown in red, anionic isolated supertetrahedral clusters are in green. C atoms are shown in dark grey and N in blue. H atoms are omitted for clarity.

There is good agreement between the experimental and calculated (Powder Cell [175]) powder X-ray diffraction patterns for **(10)** and **(12)** (Figure 4.22). However, intensity differences are observed in the case of compound **(10)**, and those may be attributed to the presence of a second unidentified phase, consisting of a dark grey polycrystalline powder. Attempts to produce a single phase were unsuccessful and similar problems have been previously mentioned by other authors [71]. The observed diffraction patterns were fitted using TOPAS [176] in order to refine the lattice parameters which are given in Table 4.15 for compounds **(10)** to **(12)**. These values show a reasonable agreement with those obtained using single crystal X-ray diffraction (Table 4.12).

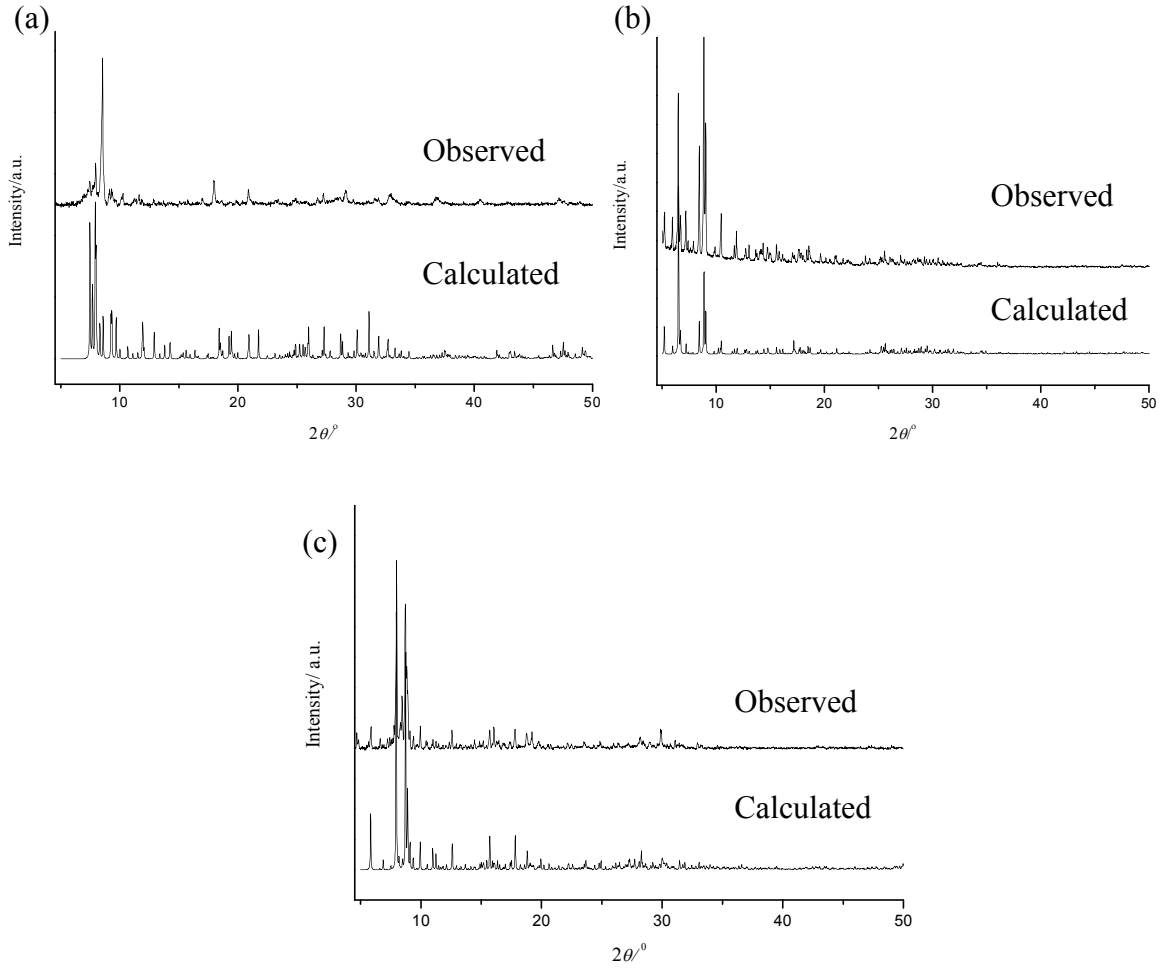

Figure 4.22. Comparison between calculated and experimental powder X-ray diffraction patterns for compounds (a) **(10)**, (b) **(11)** and (c) **(12)**.

Table 4.15. Lattice parameters for compounds **(10)**, **(11)** and **(12)** determined using powder X-ray diffraction data.

Unit cell parameters	**(10)**	**(11)**	**(12)**
a/Å	12.03(2)	13.72(1)	14.910(1)
b/Å	12.23(2)	19.89(1)	34.100(3)
c/Å	22.54(3)	47.26(3)	21.064(7)
α/°	89.7(1)	-	-
β/°	80.0(1)	94.46(5)	91.754(7)
γ/°	75.9(1)	-	-

Elemental analysis and TGA

Elemental analysis for compound **(10)** presents a good agreement with the calculated values from the proposed formula (calculated: C: 26.3%; H: 2.9%: N: 4.5%; experimental: C: 25.9%; H: 2.8%; N: 4.6%). Thermogravimetric analysis (Figure 4.23

(a)) indicates it is stable up to *ca.* 473 K under a N_2 atmosphere. The decomposition takes places in two steps. The first step presents slight changes in its slope and is followed by small step. The percentage of volatile component in compound **(10)** (*ca.* 46%) is superior to the expected value (33.3%) calculated from the percentage of C, H and N. The remaining product was identified as Ga_2O_3 and this explains the disagreement with the expected value.

Elemental analysis for compound **(11)** is in good agreement with the calculated value from the proposed formula (calculated: C: 24.5%; H: 2.3%; N: 4.7%, experimental: C: 24.2%; H: 2.6%; N: 4.6%). This material is stable up to *ca.* 473 K (Figure 4.23 (b)) and its decomposition takes place in two steps. The first step occurs at *ca.* 900 K follow by a small step. The residue was identified as Ga_2O_3. The expected weight loss was 31.5 % and the total weight loss (*ca.* 42%) is consistent with the content of CHN and the degradation of the sample to Ga_2O_3.

The experimentally determined carbon content of compound **(12)** is slightly higher than the calculated value (calculated: C: 25.05%; H: 2.5%; N: 5.4%; experimental: C: 27.1%; H: 2.9%: N, 5.7%). This compound is stable up to *ca.* 500 K (Figure 4.23 (c)). The decomposition occurs in two steps. The first weight loss (*ca.* 26%) at *ca.* 900 K may be associated with the partial decomposition of the organic component. The decomposition (*ca.* 48 %) finishes at *ca.* 1200 K and the expected loss weight was *ca.* 33 %. The final residue was identified as Ga_2O_3, which is consistent with the difference between volatile found in TGA and CHN.

FTIR

Compounds **(10)** to **(12)** present similar infrared spectra (Appendix III). The vibrational modes and their frequencies are given in Table 4.16. The spectra are consistent with the presence of aromatic and amine functional groups. In compound **(10)**, the band assigned to N-H stretching vibrations at *ca.* 3500 cm^{-1} is very weak and almost imperceptible. Additionally in this spectrum, a weak band at *ca.* 2500 cm^{-1} is observed and characteristic of S-H stretching vibrations. This confirms the presence of SH^- anions, since that hydrogen atoms could not be located in the Fourier maps.

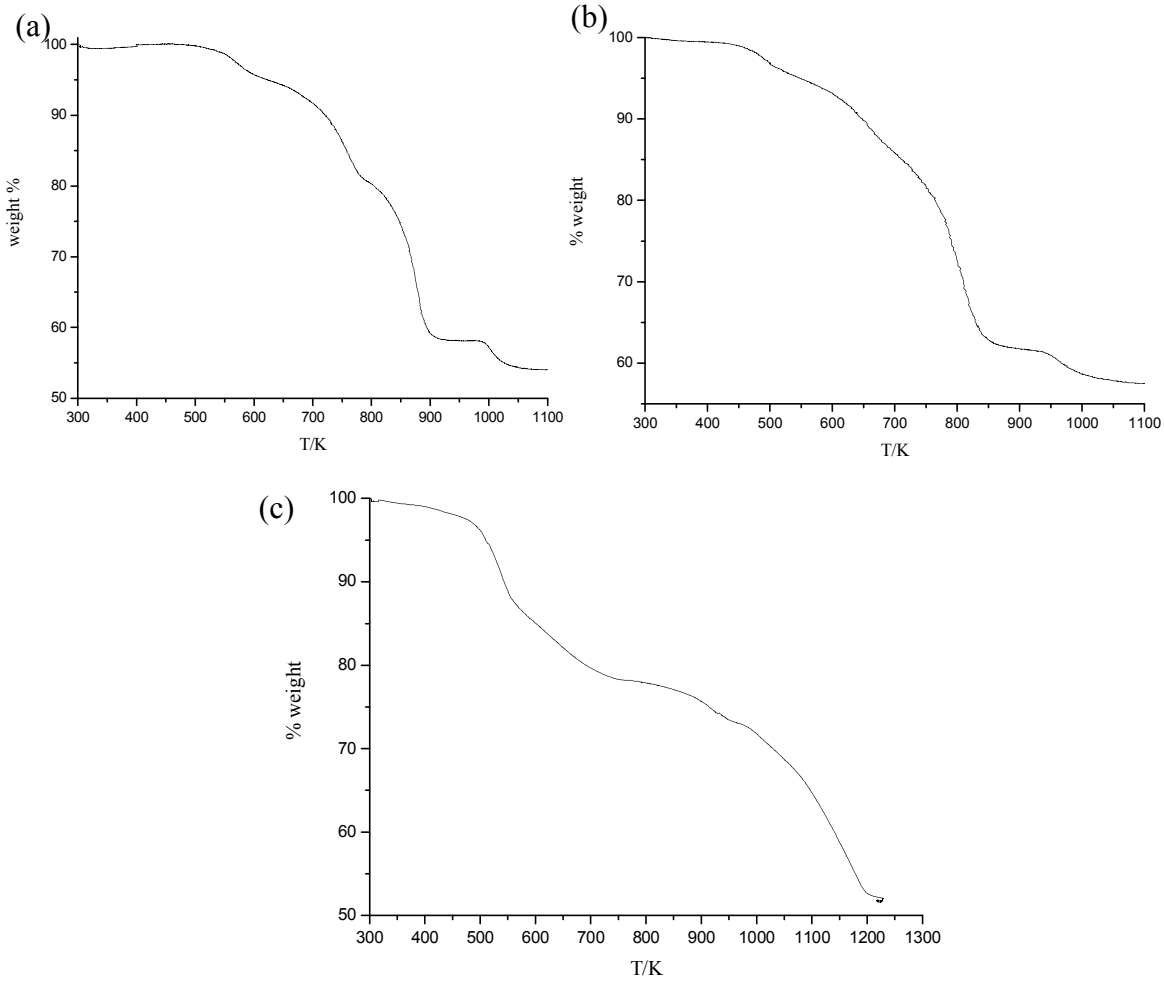

Figure 4.23. Thermogravimetric analysis corresponding to compounds: (a) (**10**), (b) **(11)** and (c) **(12)**.

Table 4.16. IR selected bands (values in cm^{-1}) for compound **(10)**, **(11)** and **(12)**. υ = stretching, δ = deformation in the plane, γ = deformation out of the plane; s = strong, m = medium, w = weak.

Assignment	**(10)**	**(11)**	**(12)**
υ (N-H)	-	3445.2 (m)	3436.6 (m)
υ (C-H)	3025.6 (w)	3082.0 (m)	3059.0 (m)
υ (C=C)	1619.1 (s)	1617.4 (s)	1618.8 (s)
γ (C-C)	1433.2 (s)	1404.7 (s)	1438.0 (s)
δ (C-H)	1068.0 (m)	1057.1 (m)	1037.6 (m)
γ (C-H)	832.2 (m)	808.7 (m)	815.4 (m)
υ (S-H)	2502.4 (w)	-	-

Diffuse Reflectance

The optical absorption spectra for compounds from **(10)** to **(12)** are shown in Figure 4.24. Band gap values are 3.4(2), 3.1(4), 2.6(1) eV, respectively. These values indicate that these compounds exhibit semiconducting behaviour and are similar to those found in isolated hybrid clusters of gallium-sulphide. Additionally, they are also consistent with the colour of each compound. Compound **(10)** exhibits an absorption band close to the low energy area in the spectra similar to that found in compound **(9)**. For compound **(11)** and **(12)** the same arguments can be applied than for compound **(7)** to explain the red-shifting in the band gap in comparison with compound **(10)**. These compounds contain a large amount of organic moieties that create different chemical environment for each cluster and therefore, variations in the band gap, which is formed by the contribution of each cluster. Additionally for compound **(12)**, the presence of two types of clusters (dimeric units and discrete clusters) supports this argument. Also the different grade by π–π stacking could affect those values through charge-transfer process. The stacking interactions have been also related to luminiscence, fluororescence and magnetic properties in metal complexes [210-213].

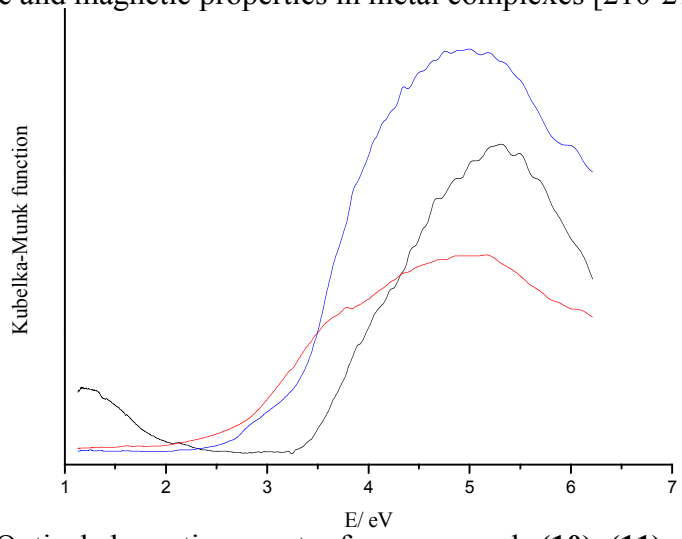

Figure 4.24. Optical absorption spectra for compounds **(10)**, **(11)** and **(12)**. Compounds are represented by black, blue and red lines, respectively.

4.3. Extended structures

4.3.1. One-dimensional chains

Synthesis

$[C_6H_8N]_2[Ga_{10}S_{16}(NC_6H_7)_2(N_2C_{12}H_{12})]$ **(13)**: a mixture of gallium metal (139.44 mg, 2 mmol), sulphur (144 mg, 4.5 mmol), DPE (182 mg, 1 mmol) and 4-picoline (3 ml) was loaded in a 23 ml Teflon-lined stainless steel autoclave with an approximate stoichiometry of 2:4.5:1:30. The vessel was sealed and heated at 443 K for 5 days. The

product contained white crystals identified as **(13),** amorphous powder and unreacted gallium.

$[C_2H_8N]_2[Ga_{10}S_{16}(N_2C_{12}H_{12})(NC_2H_7)_2]$ **(14)**: gallium metal (139.44 mg, 2 mmol), sulphur (144 mg, 4.5 mmol), DPE (182 mg, 1 mmol), TPPB (111 mg, 0.26 mmol) and pyridine (3 ml) were located in a 23 ml Teflon-lined stainless steel autoclave. The mixture contains an approximate stoichiometry 2:4.5:1:0.26:37. The autoclave was heated at 473 K for 20 days in an oven. The resulting product was formed by white crystals identified as **(14)** and white amorphous powder.

$[C_5H_6N]_2[C_6H_8N]_2[Ga_{10}S_{16}(NC_6H_7)_2(N_2C_{12}H_{10})][Ga_{10}S_{16}(N_2C_{12}H_{10})_{1/2}(NC_6H_7)_3]$ **(15)**: gallium metal (139.4 mg, 2 mmol), sulphur (128 mg, 4 mmol), 1,3-Benzodiazole (BIAL) (118.14 mg, 1 mmol) and 4-picoline (3 ml) were mixed in a 23 ml Teflon-lined stainless steel autoclave. The molar ratio of the mixture was 2:4:1:30. After the vessel was sealed; the reaction mixture was heated at 473 K for 5 days and then allowed to cool to room temperature at 1 K min^{-1}. The product consists of orange crystals of **(15)** and unreacted gallium.

Structure description

Crystallographic information and refinement details for compound **(13)** to **(15)** are given in Table 4.17. The atomic coordinates (excluding H atoms), bond lengths and angles are summarised in Appendix II. The structures were solved using direct methods, which located the Ga and S atoms. The amine C and N atoms were placed using Fourier maps. In compound **(13)** and **(15)**, the organic component is disordered, and therefore C-C and C-N distances were constrained and the thermal parameters of those atoms modeled isotropically. Additionally, in compound **(13)** data was treated with SQUEEZE [183] to reduce the effect of the disordered solvent. H atoms were placed geometrically on the C and N atoms after each cycle of refinement.

The structure of **(13)** contains of organically functionalised T3 supertetrahedra (Figure 4.25) by two 4-picoline and the remaining vertexes are connected by two 1,2-di-(4-pyridyl)ethane ligands (BPe) forming one-dimensional zig-zag chains (Figure 4.26). The ligands are consequence of the hydrogenation of DPE molecules, as it was observed in compound **(11)**. The average Ga-N distance has been found to be 2.03 Å and Ga-S distances between 2.2229(2) - 2.333(2) Å, similar to those found in isolated hybrid gallium-sulphide supertetrahedral clusters (see Section 4.2).

Table 4.17. Crystallographic data for the structures **(13)**, **(14)** and **(15)**.

Formula	$[C_6H_8N]_2$ $[Ga_{10}S_{16}(NC_6H_7)_2$ $(N_2C_{12}H_{12})]$ **(13)**	$[C_2H_8N]_2$ $[Ga_{10}S_{16}(N_2C_{12}H_{12})$ $(NC_2H_7)_2]$ **(14)**	$[C_5H_6N]_4[C_6H_8N]_4$ $[Ga_{10}S_{16}(NC_6H_7)_2$ $(N_2C_{12}H_{12})]$ $[Ga_{10}S_{16}(N_2C_{12}H_{10})_{1/2}$ $(NC_6H_7)_3]$ **(15)**
Mr	1580.75	1576.85	2717.61
Crystal habit	White plate	Colourless plate	Orange plate
Dimensions/mm^3	0.05 × 0.10 × 0.10	0.15 × 0.20 × 0.30	0.05 × 0.10 × 0.15
Crystalline System	Orthorhombic	Trigonal	Monoclinic
Space group	*Pcca*	$P3_221$	*C2/c*
T/K	100	100	100
a/Å	37.4329(14)	18.2994(3)	46.4671(14)
b/Å	19.7762(8)	18.2994(3)	17.0824(6)
c/Å	18.5622(7)	13.4631(5)	29.5682(10)
β/°	-	-	109.823 (2)
γ/°	-	120	-
V/Å^3	13741.2(9)	3904.36(17)	22079.6(13)
Z	8	3	8
Wavelength/Å Mo K_α	0.71073	0.71073	0.71073
μ/cm^{-1}	4.36	5.75	4.08
Δρ max / Å^{-3}	1.19	0.77	1.30
Δρ min / Å^{-3}	−1.05	−0.46	−0.60
Measured data	156171	5231	22624
Unique data	20783	3686	22624
Observed data ($I > 2\sigma(I)$)	6921	4093	7191
R_{merg}	0.051	0.050	0.052
$R(F_o)$[a]	0.042	0.024	0.049
$R_w(F_o)$[b]	0.045	0.025	0.051

[a] $R(F_o)=\Sigma(|F_o| - |F_o|)/ \Sigma|F_o|$. [b] $R_w(F_o)= [\Sigma w(|F_o|- |F_o|)^2 / \Sigma w|F_o|^2]^{1/2}$.

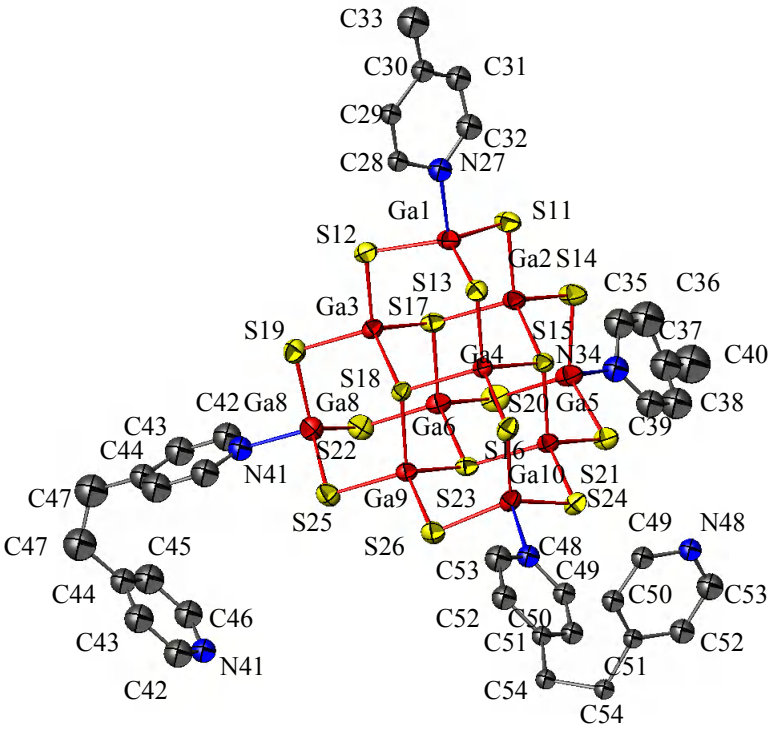

Figure 4.25. Local coordination diagram for $[Ga_{10}S_{16}(NC_6H_7)_2(N_2C_{12}H_{12})_2]^{2-}$ tetrahedral unit showing the atom labelling scheme and displacement ellipsoids at 50% probability. Ga atoms are shown in red, S in yellow, C in grey and N in blue. H atoms were omitted for clarity.

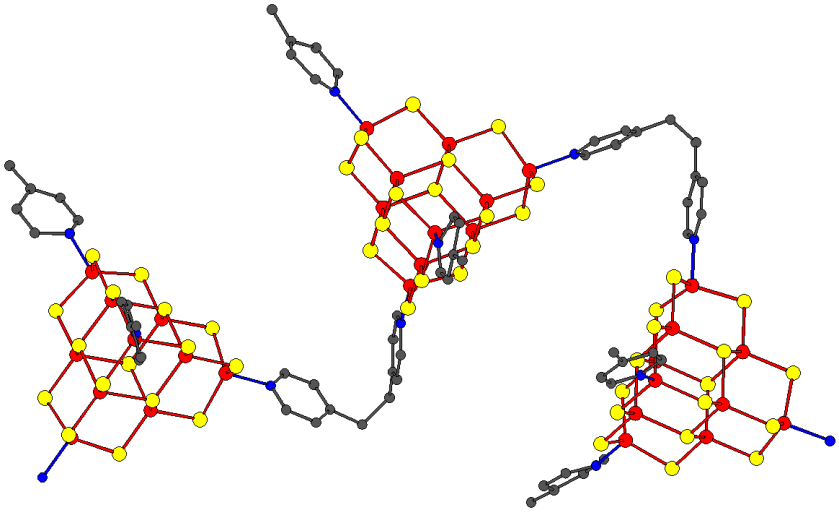

Figure 4.26. Fragment of anionic chain in compound **(13)**. Ga atoms are shown in red, S in yellow, N in blue and C in dark grey. H atoms have been omitted for clarity.

The single bond contained in BPe enable the relative rotation of the pyridine rings, which exhibits a torsion angle of 46.47(1) º. This results in chains which adopt a zig-zag conformation (Figure 4.27). Chains are packed in layers parallel to the (010) plane.

The monodentate ligands are oriented towards the outer part of the layers (Figure 4.28). The structure contains *ca.* 39% of void space [183]. Taking into account charge balance requirements, it is proposed that protonated 4-picoline cations are placed within the crystal structure cavities and is consistent with the analytical data obtained form CHN.

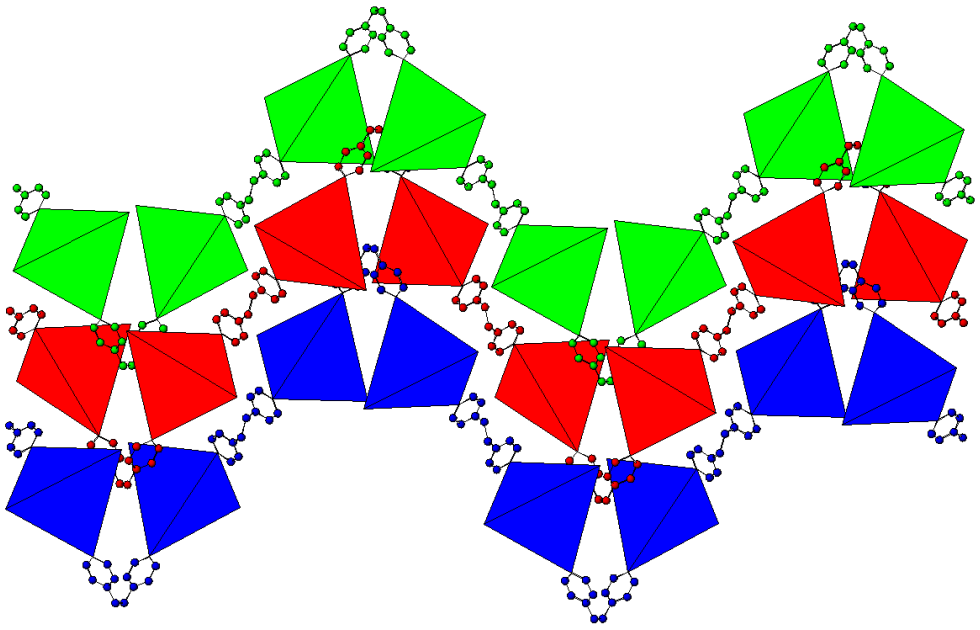

Figure 4.27. Polyhedral representation of the chains in **(13)**. Zig-zag chains are stacked with respect to each other filling the major part of the space in the structure**.** $[Ga_{10}S_{16}N_4]$ supertetrahedral units are replaced by tetrahedra for clarity. Tetrahedra and DPE linkers are shown in blue, red and green for each different chain, respectively. H atoms and 4-picoline molecules are omitted for clarity.

Compound **(14)** contains wavy chains formed by hybrid T3 supertetrahedral (Figure 4.29) unit connected through BPe ligands to two other supertetrahedra (Figure 4.30). The unlinked vertexes of the supertetrahedra are covalently bonded to two ethylamine moieties by Ga-N connections. The ethylamine ligands are believed to be produced in a side reaction in the vessel, in which pyridine molecules are hydrogenated and cracked. To the best of my knowledge, this behaviour has not been observed previously in solvothermal reactions. The BPe ligands were produced by the hydrogenation of DPE molecules, as previously observed for **(11)** and **(13)**. The Ga-N distances exhibit two slightly different values: 2.021(9) Å for the pyridine rings and 2.006(4) Å for the primary amine. This distance is similar to those found in hybrid gallium sulphides structures containing primary amines [145,129]. Ga-S distances lie between 2.2118(12)-2.3331(12) Å, similar to those found in isolated hybrid gallium sulphide supertetrahedral clusters (Section 4.2).

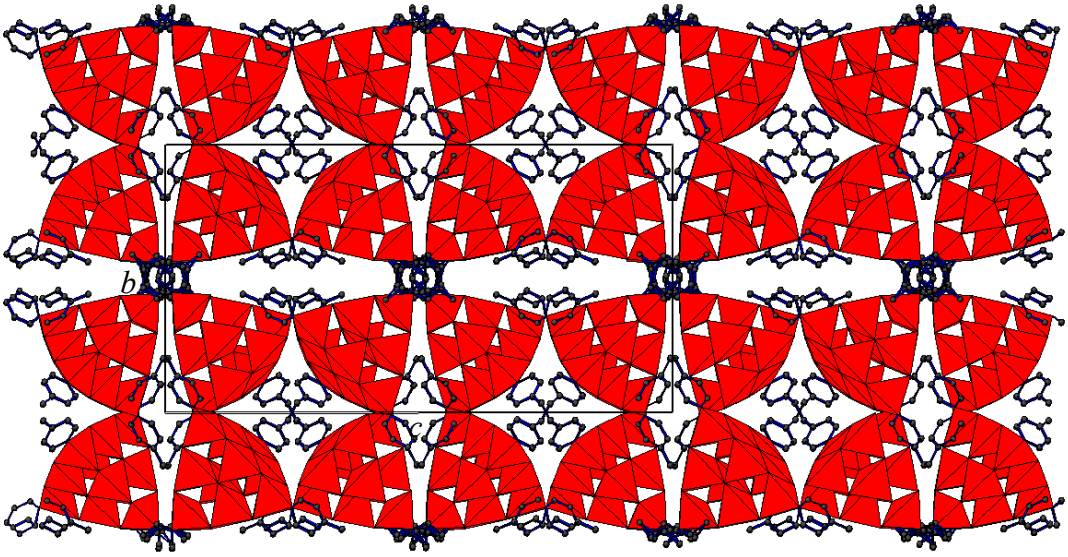

Figure 4.28. View of **(13)** on the (100) plane. Cavities are located between layers of chains forming tunnels along the *a*-axis. GaS_4 tetrahedra are shown in red and C atoms in dark grey. H atoms are omitted for clarity.

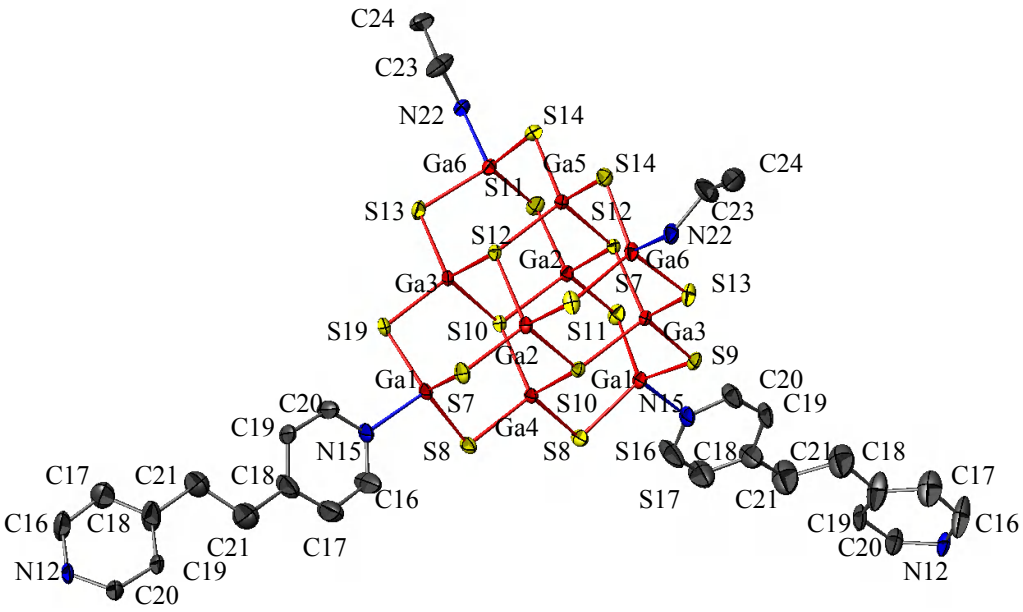

Figure 4.29. Local coordination diagram for $[Ga_{10}S_{16}(N_2C_{12}H_{12})_2(NC_6H_7)_2]^{2-}$ showing the atom labelling scheme and displacement ellipsoids at 50% probability. Ga atoms are shown in red, S in yellow, C in dark grey and N in blue. H atoms were omitted for clarity.

Four helical left-handed chains are spiralling parallel along the [001] direction forming a triangular shaped superchain. Only a few cases of quadruple stranded helices

are known in coordination chemistry [214]. The vertexes connected to ethylamine are pointing towards neighbouring superchains (Figure 4.31 (a), (b)). Superchains run parallel to the *c*-axis (Figure 4.32). Protonated ethylammonium cations are found separating superchains to compensate the charge balance. Ethylammonium cations are believed to have the same origin to the ethylamine ligands.

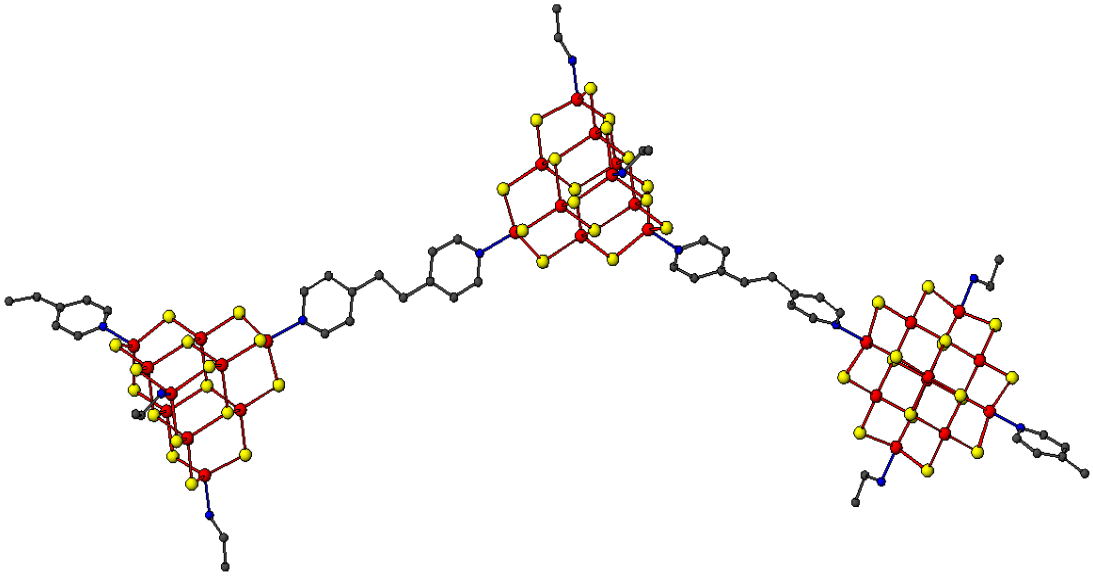

Figure 4.30. Fragment of $[Ga_{10}S_{16}(^1N_2C_{10}H_{12})(^1NC_2H_7)]^-$ chain contained in compound **(14)**. Ga atoms are shown in red, S in yellow, N in blue and C in dark grey. H atoms have been omitted for clarity.

The quadruplet helices are characterised by long face-to-face interactions with an inter-ring distance of 4.66(8) Å. Similar distances were found in other type of structures containing helices [214-216]. The model presents a refined Flack parameter of 0.001(9) that confirms this compound exhibits the absolute structure. The structure is finally stabilised by hydrogen bonding between the anionic clusters and the protonated amines which are acting as counter cations. Hydrogen bond distances were obtained using PLATON [183] and are summarised in Table 4.18.

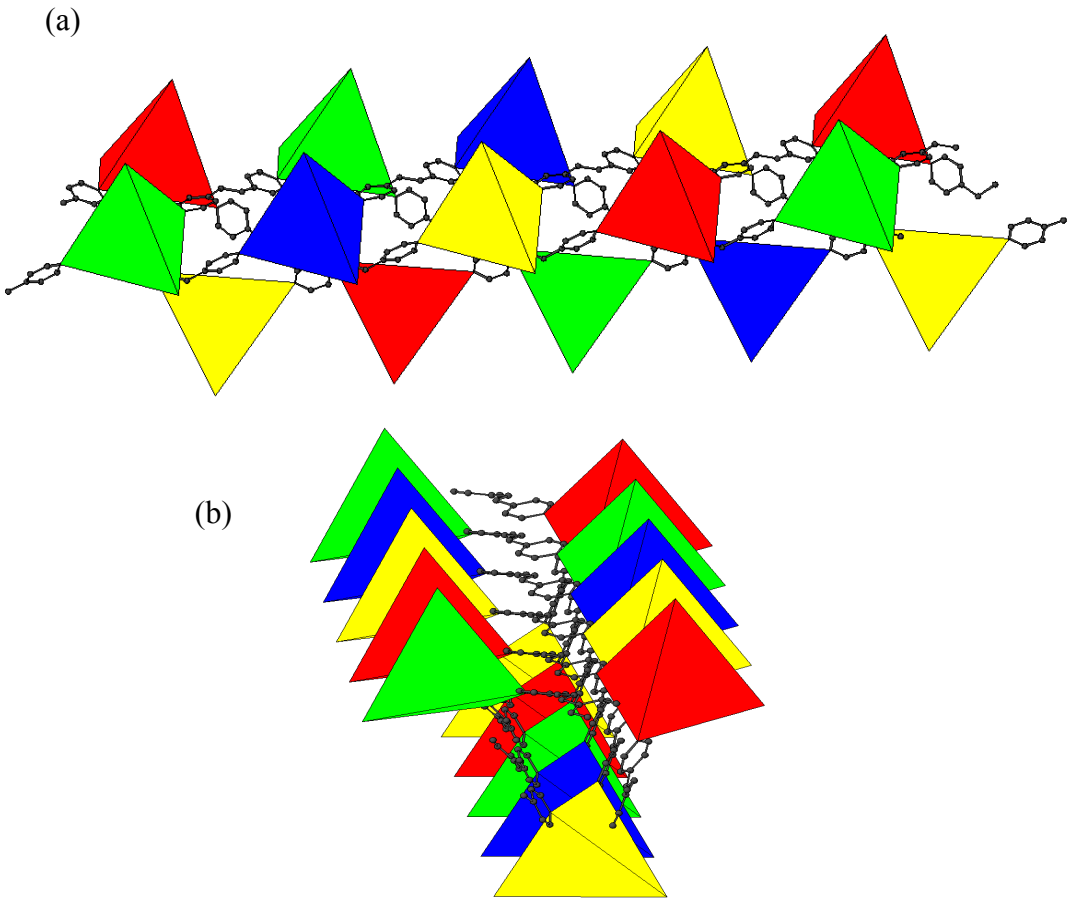

Figure 4.31. View of the superchain found in compound **(14)**: (a) on the *c*-axis and (b) view along the [001] direction showing its trigonal shape. Each chain is represented by tetrahedra in different colours (red, blue, green and yellow, respectively) and C atoms are shown in dark grey. H atoms are omitted for clarity.

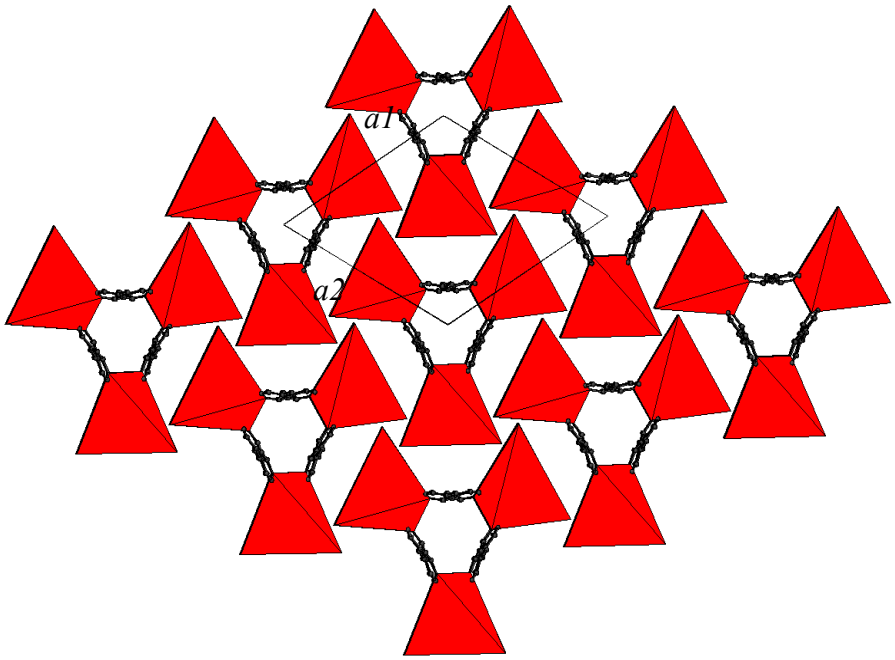

Figure 4.32. Packing of compound **(14)** on the (001) plane. $[Ga_{10}S_{16}(N_2C_{10}H_{12})(NC_2H_7]$ are shown in red and C atoms in dark grey. H atoms, ethylamine ligands and cations are omitted for clarity.

Table 4.18. Hydrogen bonds for **(14)**. Atoms code: D = donor, A= acceptor.

D—H…A	D—H /Å	H…A /Å	D—H…A/Å	Angle/°
N22—H221…S11	1.0000	2.5000	3.462(6)	161.00
N22—H222…S13	1.0000	2.4300	3.407(4)	163.00
N25—H251…S14	1.0000	2.7300	3.482(6)	132.00
N25—H252…S12	1.0000	2.4800	3.331(8)	143.00
N25—H253…S11	0.9900	2.4700	3.410(7)	159.00

In compound **(15)**, chains and dimers co-exist as anionic species. The dimeric anions are formed by two hybrid T3 gallium sulphide clusters (Figure 4.33) linked by a DPE molecule. The remaining corners of the supertetrahedra are coordinated by three 4-picoline molecules in each cluster. The chains are constituted by T3 gallium sulphide clusters (Figure 4.34) connected by two Dp molecules forming zig-zag chains. The Dp molecule adopts *trans*- conformation and the supertetrahedral units are located in the nodes of the chain (Figure 4.35). The remaining vertexes are substituted by two 4-picoline molecules. The average Ga-N distance has been found to be 2.03 Å and Ga-S distances between 2.209(4)-2.335(3) Å, as established in Section 4.2.

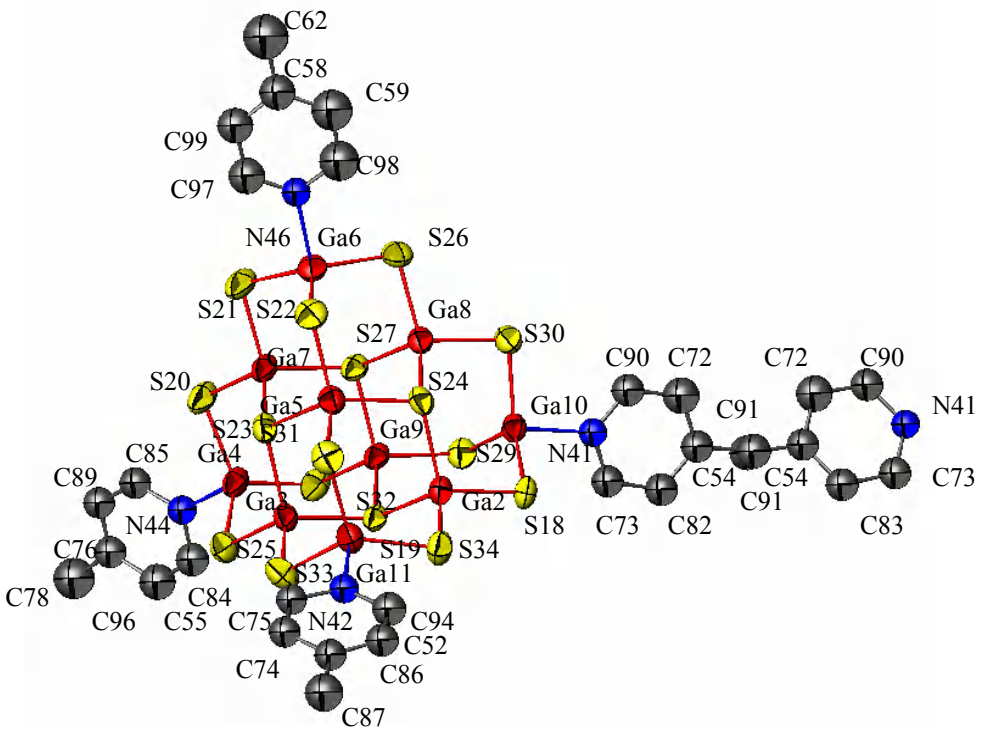

Figure 4.33. Local coordination diagram for $[Ga_{10}S_{16}(N_2C_{12}H_{12})(NC_6H_7)_3]^{2-}$ tetrahedral unit showing the atom labelling scheme and displacement ellipsoids at 50% probability. Ga atoms are shown in red, S in yellow, C in dark grey and N in blue. H atoms were omitted for clarity.

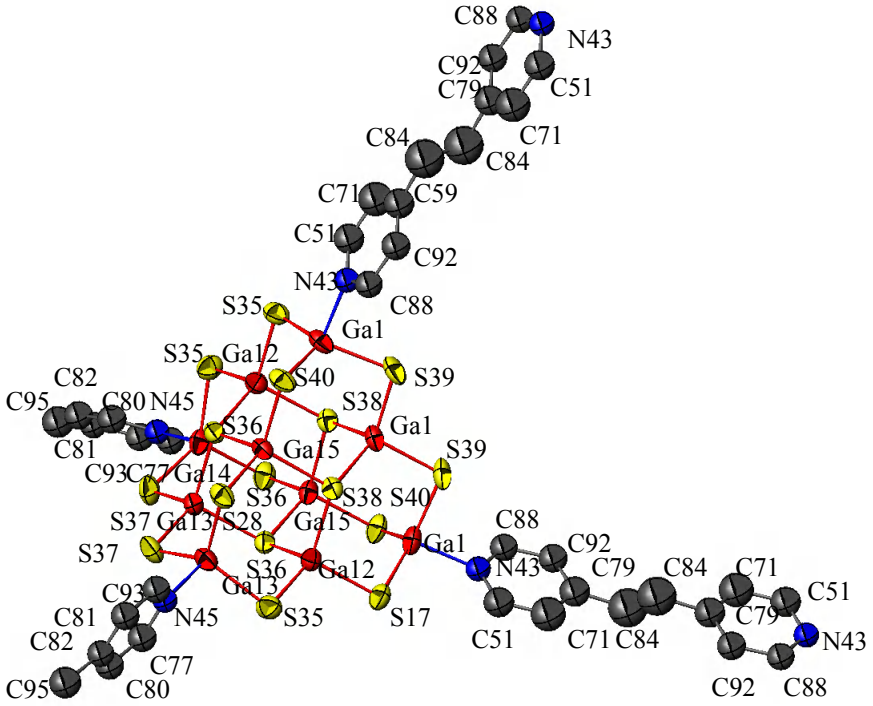

Figure 4.34. Local coordination diagram for $[Ga_{10}S_{16}(NC_6H_7)_2(N_2C_{12}H_{10})]^{2-}$ showing the atom labelling scheme and displacement ellipsoids at 50% probability. Ga atoms are shown in red, S in yellow, C in dark grey and N in blue. H atoms were omitted for clarity.

Chains run along the *c*-axis and are distributed in layers parallel to the (100) plane. Dimeric units are perpendicular to the layers of chains, separating them (Figure 4.36). In addition, protonated 4-picoline and pyridine molecules are located within the layers separating the clusters. A 20 % void space has been calculated using PLATON [183]. This space should be occupied by two protonated 4-picolinium cations. Although, these were not found in the Fourier maps, their presence is required to achieve charge balance. The layers are packed in a staggered fashion, following an ABCD sequence (Figure 4.36). The structure is stabilised then by electrostatic interactions between the anionic clusters and protonated amines; and by H bond interactions between protonated amines, which are summarised in Table 4.19. Additionally, the structure is stabilised by parallel stacking interactions between pyridine rings linked to the supertetrahedral units and the 4-picoline moieties presenting an average inter-ring distance of 3.78 Å.

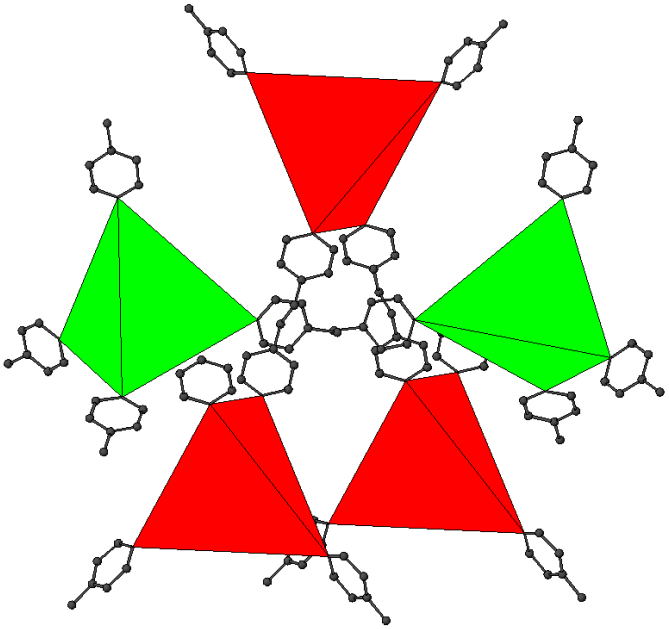

Figure 4.35. Anionic species in compound **(15)**, $[Ga_{20}S_{32}(N_2C_{12}H_{10})(NC_6H_7)_6]^{4-}$ dimeric unit and $[Ga_{30}S_{48}(NC_6H_7)_6(N_2C_{12}H_{10})_3]^{6-}$ fragment of the chain. Tetrahedral units from the dimer are shown in green, tetrahedral units of the chain in red and C atoms in dark grey. H atoms have been omitted for clarity.

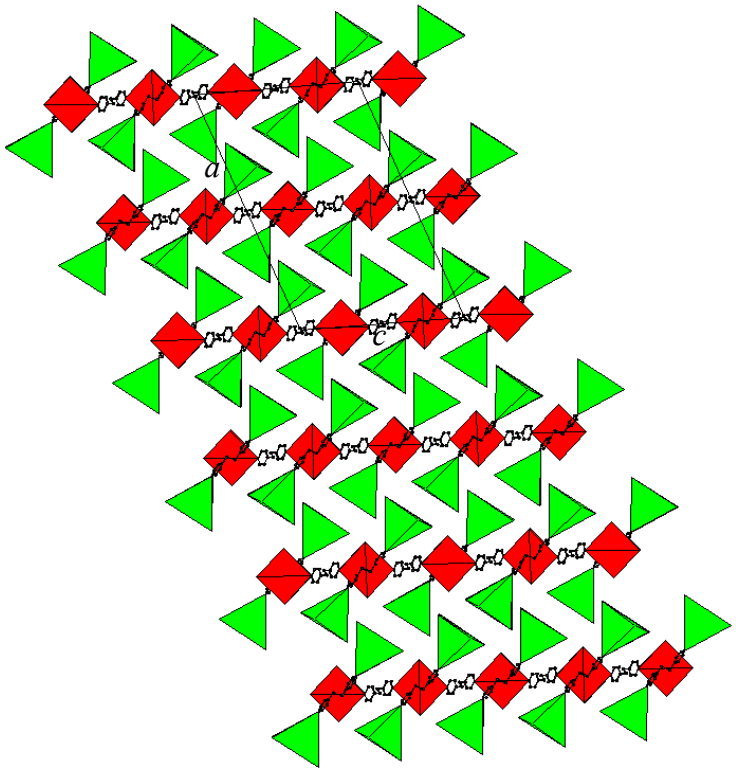

Figure 4.36. Polyhedral representation along the [010] direction of compound **(15)**. $[Ga_{20}S_{32}(N_2C_{12}H_{12})(NC_6H_7)_6]^{4-}$ dimeric units are shown in green, $[Ga_{10}S_{16}(NC_6H_7)_2(N_2C_{12}H_{10})]^{2-}$ tetrahedral units of the chains are shown in red and C atoms in dark grey. 4-picoline ligands, organic moieties and H are omitted for clarity.

Table 4.19. Hydrogen bonds for **(15)**. Atoms code: D = donor, A= acceptor.

D—H…A	D—H /Å	H…A /Å	D—H…A .Å	Angle /°
N47—H471…N495	1.0100	1.6700	2.66(3)	168
N47—H471…C64	1.0100	2.4900	3.35(3)	144

Experimental and calculated (using Powder Cell [175]) powder X-ray diffraction patterns are in good agreement (Figure 4.37). However, differences of intensity are observed for compound **(13)**, and may be attributed to a preferred orientation in the sample. The observed diffraction patterns were fitted using TOPAS [176] in order to refine the lattice parameters which are given in Tables 4.20 for compounds **(13)**, **(14)** and **(15)**. They show a fair agreement when compared with the lattice parameters obtained using single crystal X-ray diffraction (Table 4.17).

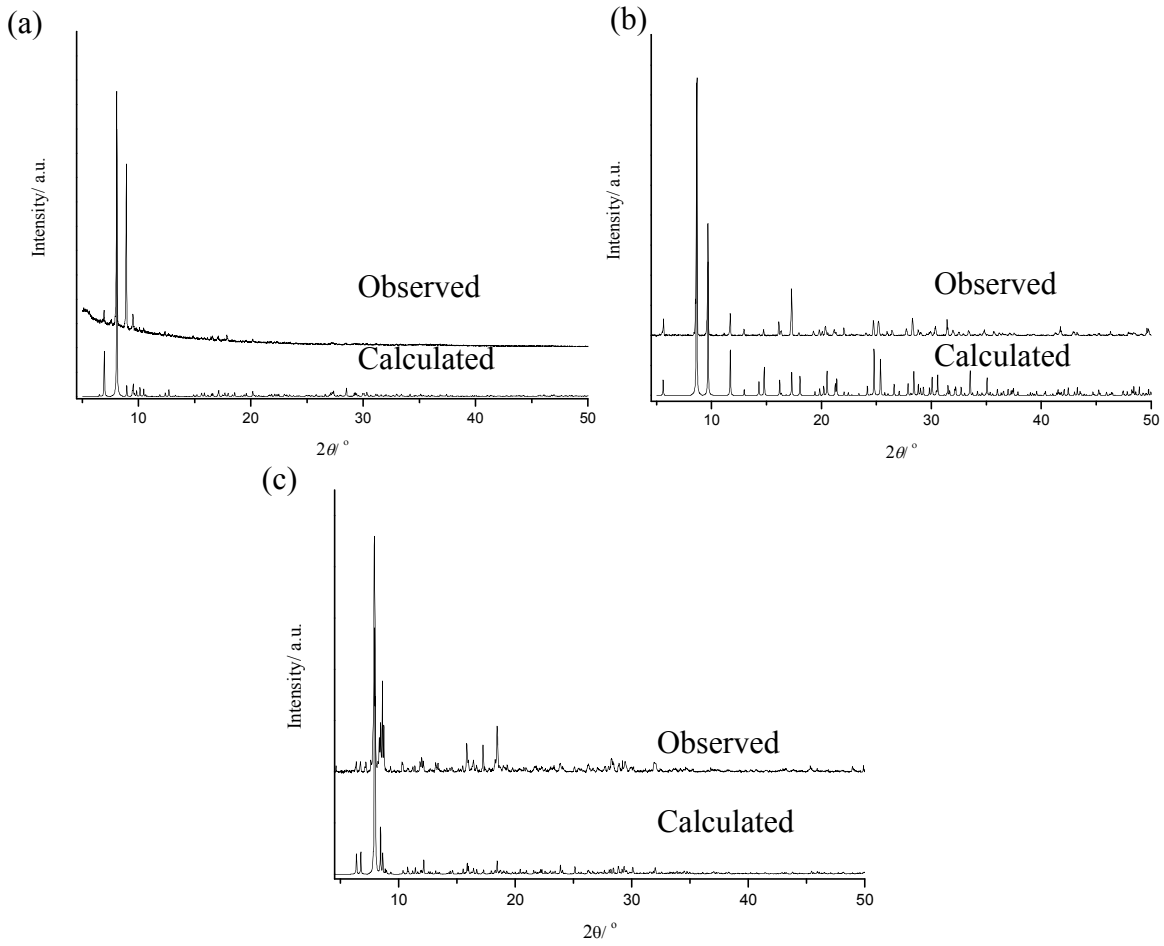

Figure 4.37. Comparison between calculated and experimental powder X-ray diffraction patterns for compounds: (a) **(13)**, (b) **(14)** and (c) **(15)**.

Table 4.20. Lattice parameters for compounds **(13)**, **(14)** and **(15)** determined using powder X-ray diffraction data.

Unit cell parameters	**(13)**	**(14)**	**(15)**
a/Å	37.412(9)	18.499(1)	46.445(17)
b/Å	19.746(5)	18.499(1)	17.106(6)
c/Å	18.526(5)	13.503(1)	29.473(12)
β/°	-	-	109.88(2)
γ/°	-	120	-

Elemental analysis and TGA

Elemental analysis for compound **(13)** is in good agreement with the values calculated from the proposed formula (calculated: C: 24.4%; H: 2.4%: N: 4.7%; experimental: C: 23.9%; H: 2.9%; N: 5.4%). Thermogravimetric analysis indicates that this compound is stable up to *ca.* 550 K (Figure 4.38 (a)). The composition takes place in two steps. The first step with a percentage of weight loss of *ca.* 17 % finishes at *ca.* 750 K, and may be attributed to the loss of protonated amines and the decomposition of the DPE molecules forming the linkage between clusters. The intermediate compound is an amorphous material. The second weight loss may be attributed to the decomposition of the 4-picoline ligands. The total weight loss is *ca.* 36 % at 1000 K slightly superior to the expected value (31.5 %). The remaining product was amorphous and could not be identified by powder X-ray diffraction.

For compound **(14)**, the elemental analysis is slightly inferior to the proposed formula (calculated: C: 15.2%; H: 2.6%: N: 5.3%; experimental: C: 12.6%; H: 2.2%; N: 5.2%) that could be attributed to the presence of an amorphous inorganic sample not identified in the bulk sample. This material exhibits higher thermal stability under N_2 when compared to the other two compounds described in this section (Figure 4.38 (b)). The structure is stable up to *ca.* 600 K. The decomposition occurs in two steps, finishing at *ca.* 1100 K with *ca.* 36 % of the weight loss (calculated weight loss for the formula compound *ca*. 20%). This difference is attributed to the decomposition of the sample to Ga_2O_3 (expected value, *ca.* 15%), identified in the residue after the experiment.

In compound **(15)**, there is a fair agreement between CHN analysis and the values estimated from the proposed formula (calculated: C: 28.6%; H: 2.8%; N: 5.8%; experimental: C: 29.81%; H: 2.79%; N: 6.04%). The decomposition occurs in several steps with gentle slopes (Figure 4.38 (c)) ending with a weight loss of *ca.* 50 % at *ca.*

1300 K and the expected weight loss was 37.2%. The final residue was identified as Ga_2O_3 consistent with this final weight loss.

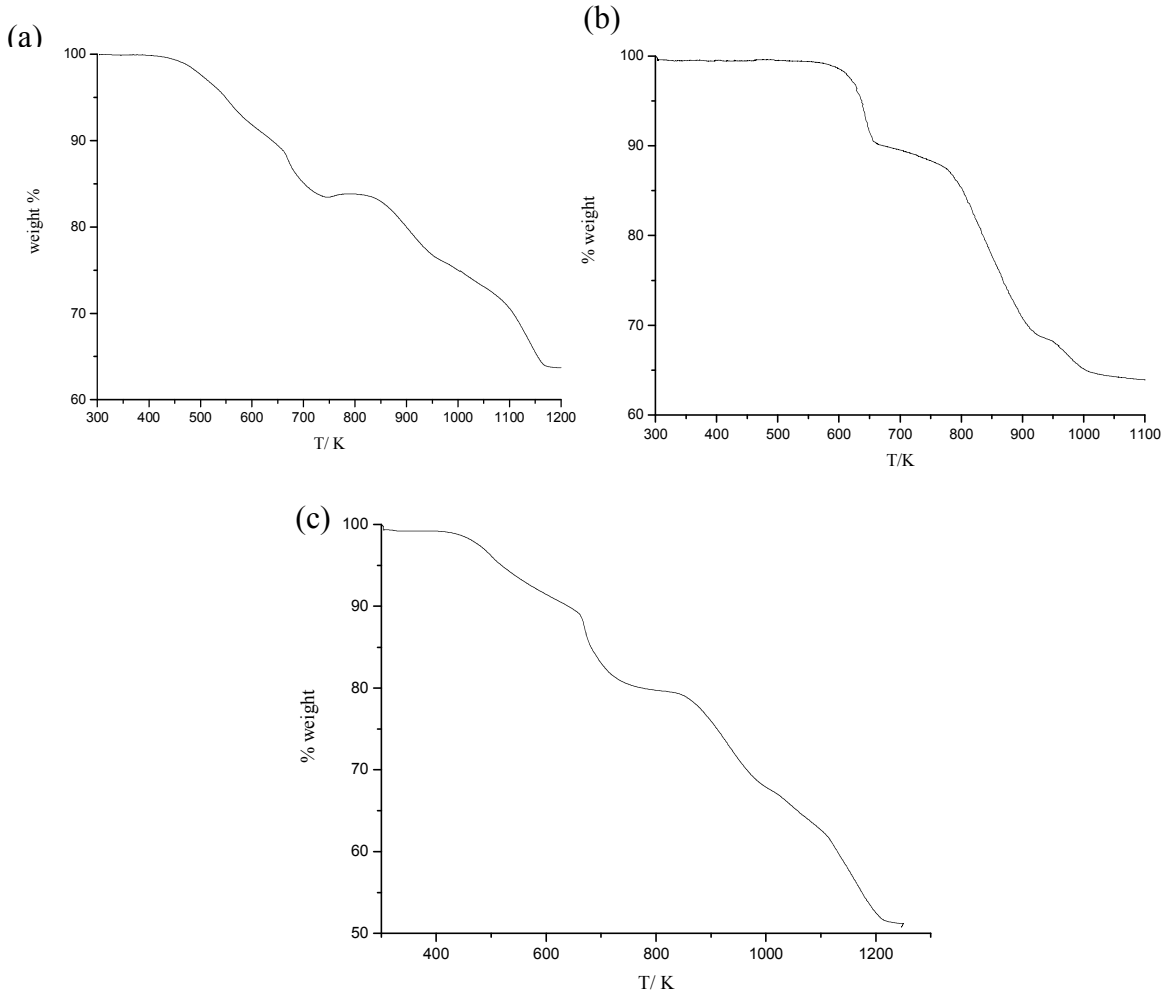

Figure 4.38. Thermogravimetric analysis corresponding to compounds (a) **(13)**, (b) **(14)** and (c) **(15)**.

FTIR

Infrared data spectra for compounds **(13)** to **(15)** (Appendix III) are consistent with the presence of aromatic and amine functional groups. The vibrational modes and their frequencies are given in Table 4.21. It is worth noticing in compound **(14)**, the presence of a sharp band at 3200.0 cm^{-1} and the shape in the range 3200-3000 cm^{-1} may be attributed to N-H stretching frequencies corresponding to the asymmetric and symmetrical N-H stretching vibration, attributed to a protonated primary amine [206,217].

Table 4.21. IR selected bands (values in cm^{-1}) for compound **(13)**, **(14)** and **(15)**. υ = stretching, δ = deformation in the plane, γ = deformation out of the plane; s = strong, m = medium, w = weak.

Assignment	**(13)**	**(14)**	**(15)**
υ (N-H)	3500.0 (w)	3502.3 (w)	3499.9 (w)
υ (N-H)	-	3200.0 (m)	-
υ (C-H)	3035.7 (w)	3102.9 (w)	3059.0 (w)
υ (C=C)	1618.7 (s)	1621.1 (s)	1618.6 (s)
γ (C-C)	1434.5 (s)	1436.1 (s)	1434.3 (s)
δ (C-H)	1065.9 (s)	1070.5 (s)	1068.1 (s)
γ (C-H)	814.6 (m)	818.6 (m)	816.6 (m)

Diffuse Reflectance

The optical absorption spectra for compounds from **(13)** to **(15)** are shown in Figure 4.39. Band gap values are 4.3(1), 3.6(2) and 3.5(1) eV, respectively. These values indicate that these materials exhibit semiconducting behaviour. The optical behaviour is comparable to that previously hybrid structures. It is remarkable in compound **(15)**, the presence of a shoulder at *ca.* 2.7(6) eV (450 nm), it could be associated to the presence of two different types of anions (dimeric and isolated cluster) which are chemically non-identical and contribute to the band gap of the compound with small difference in the energy levels as it has been observed in compound **(12)**.

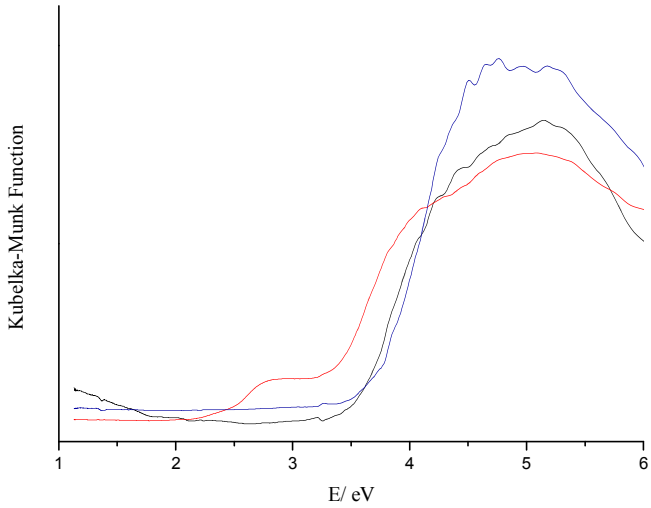

Figure 4.39. Optical absorption spectra for compounds: **(13)**, **(14)** and **(15)** which are represented by a black, blue and red line, respectively.

4.3.2. Two-dimensional structures

$[C_7H_{10}N]_2[Ga_{10}S_{16}(NC_7H_9)(N_2C_{12}H_{10})_{3/2}]$ **(16)**: a mixture of gallium (139.4 mg, 2 mmol), sulphur (128 mg, 4 mmol) and DPE (182 mg. 1 mmol) in 3 ml of lutidine was loaded in a 23 ml Teflon lined stainless autoclave. The approximate molar composition was 2:4.5:1:26. The autoclave was placed in an oven and heated at 473 K for 20 days. The product was formed by yellow crystals identified as **(16)**, amorphous material and unreacted gallium.

$[C_5H_6N]_3[Ga_{10}S_{16}(OH)(N_2C_{13}H_{14})]$ **(17)**: gallium (139.4 mg, 2 mmol), sulphur (144 mg, 4.5 mmol), 4,4'-trimethylenedipyridine (TMPyr) (160 mg, 0.81 mmol), TPPB (111 mg, 0.26 mmol) and 3 ml of pyridine were placed in a 23 ml Teflon lined stainless autoclave. The approximate stoichiometry was 2:4.5:0.81:0.26:37. The system was heated at 473 K for 20 days. The reaction product was small white crystals of **(17)**.

Structure description

Crystallographic information and refinement details for compound **(16)** and **(17)** are summarised in Table 4.22. The atomic coordinates (excluding H atoms), bond lengths and angles, are given in Appendix II. The structures were solved using direct methods, which located the Ga and S atoms. The amine C and N atoms were placed using Fourier maps. In compound **(16)** and **(17)**, C and N atoms corresponding to the different amines present disorder; in consequence, distances were restrained and the position modeled isotropically. H atoms were placed geometrically on the C and N atoms after each cycle of refinement. The data were treated using SQUEEZE tool from PLATON [183] to reduce the effect of the disordered organic molecules which could not be placed.

Compound **(16)** is constituted by organically functionalised T3 supertetrahedral clusters (Figure 4.40), in which the terminal S atoms at the corners are substituted by three 1,2-di-(4-pyridyl)ethylene (BPe) ligands and one lutidine ligand (Figure 4.34). Ga-S distances lie between 2.2251(19) to 2.3275(18) Å and the average Ga-N distance (2.054 Å) is similar to those previously found organically-functionalised gallium-sulphide clusters.

Table 4.22. Crystallographic data for the structures **(16)** and **(17)**.

Formula	$[C_7H_{10}N]_2$ $[Ga_{10}S_{16}(NC_7H_9)(N_2C_{12}H_{10})_{3/2}]$ **(16)**	$[C_5H_6N]_3$ $[Ga_{10}S_{16}(OH)(N_2C_{13}H_{14})]$ **(17)**
Mr	1590.75	1504.63
Crystal habit	Yellow plate	White plate
Dimensions/mm^3	0.16 × 0.36 × 0.70	0.10 × 0.15 × 0.23
Crystalline System	Triclinic	Orthorhombic
Space group	$P\bar{1}$	*Pbcm*
T/K	100	100
a/Å	12.4678(12)	16.9354(8)
b/Å	13.6806(13)	18.6642(9)
c/Å	20.385(2)	19.1575(11)
α/°	81.599(6)	-
β/°	88.542(6)	-
γ/°	82.967(5)	-
V/Å^3	3413.8(6)	6055.4(5)
Z	2	4
Wavelength/Å Mo K_α	0.7073	0.7073
μ/cm^{-1}	4.39	4.94
Δρ max / Å^{-3}	1.88	1.15
Δρ min / Å^{-3}	-1.41	-0.88
Measured data	89986	6379
Unique data	20798	6379
Observed data ($I > 2\sigma(I)$)	11508	2615
R_{merg}	0.034	0.039
$R(F_o)$[a]	0.064	0.054
$R_w(F_o)$[b]	0.079	0.058

[a] $R(F_o)=\Sigma(|F_o| - |F_o|)/ \Sigma|F_o|$. [b] $R_w(F_o)= [\Sigma w(|F_o|- |F_o|)^2 / \Sigma w|F_o|^2]^{1/2}$.

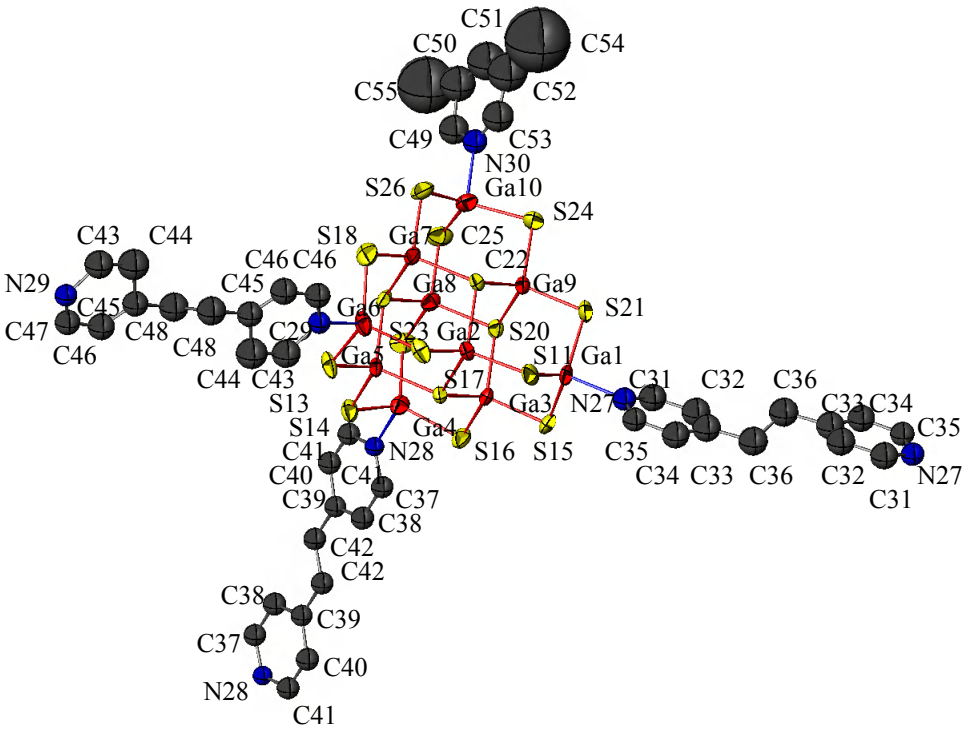

Figure 4.40. Local coordination diagram for $[Ga_{10}S_{16}(NC_7H_9)(N_2C_{12}H_{10})_3]^{2-}$ tetrahedral unit showing the atom labelling scheme and displacement ellipsoids at 50% probability. Ga atoms are shown in red, S in yellow, C in dark grey and N in blue. H atoms were omitted for clarity.

Supertetrahedral clusters are connected by sharing three BPe molecules and form corrugated honeycomb-type layers of six-membered rings (Figure 4.41 (a) and (b)), containing cavities with an approximate pore diameter of 30 Å. Layers are stacked parallel to the (135) plane with the lutidine ligands pointing towards neighbouring layers and partially filling the pores of neighbouring sheets (Figure 4.42). As a consequence, a network of channels of *ca.* 3-4 Å diameter is created, running parallel to the *a*- and *b*-axis (Figure 4.43). After calculations using PLATON [183], a 37% of empty space is observed which is believed to be filled by two protonated 4-picoline molecules to compensate the charge balance in the structure, which is consistent with the analytical data. This structure resembles the grey arsenic and was previously observed in other metal chalcogenide structures [218].

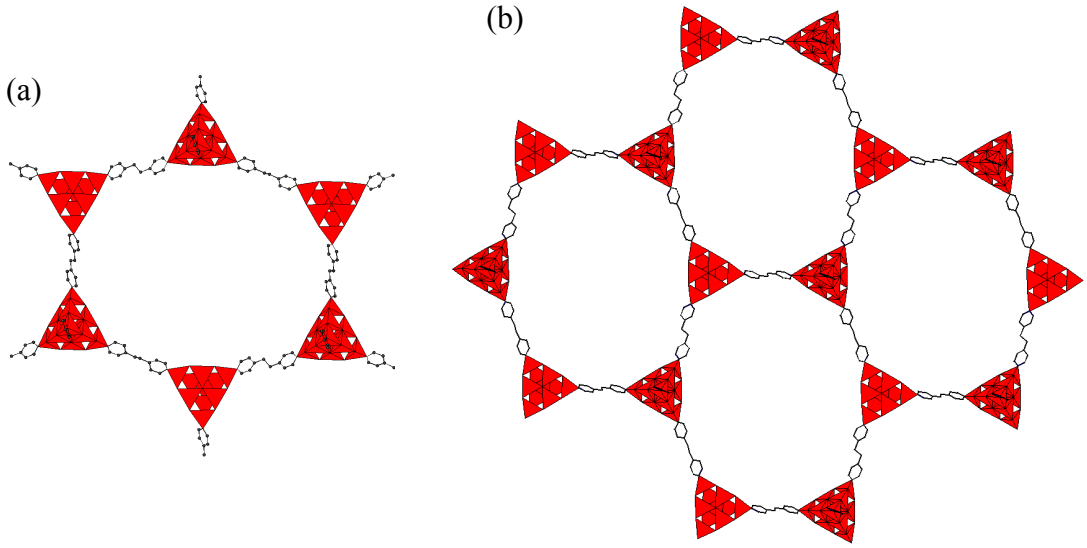

Figure 4.41. Compound **(16)**: (a) supertetrahedral six-membered ring and (b) honeycomb-type layer. GaS_4 and GaS_3N tetrahedra are shown in red and C atoms in dark grey. H atoms are omitted for clarity.

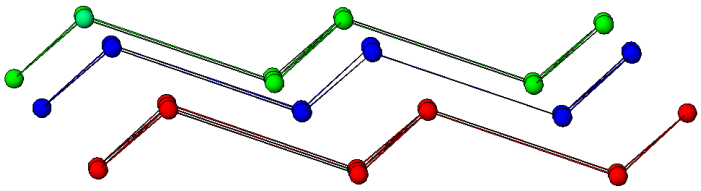

Figure 4.42. View of layer topology in compound **(16)**. Supertetrahedra are substituted by nodes and organic linkers omitted for clarity. Each layer is shown in different colour (red, blue or green).

Compound **(17)** is formed by hybrid T3 gallium-sulphide supertetrahedral clusters (Figure 4.44) in which two of the terminal sulphur atoms are replaced by OH groups and two TMPyr molecules. Ga-S distances lie between 2.223(3) to 2.324(3) Å and the Ga-O distances have average of 1.889 Å, similar to those found in compound **(2)** (see Section 3.2). Ga-N distances are 2.058(13) Å, similar to those found in previous organically-functionalised gallium-sulphide clusters.

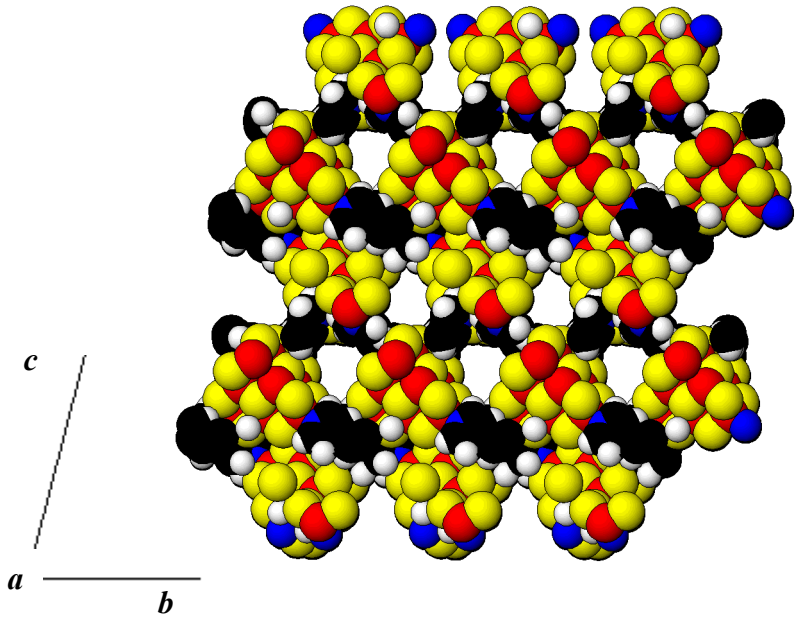

Figure 4.43. Space filling representation of compound **(16)** along the [100] direction. Atoms are represented using their Van der Waals radii. Ga atoms are shown in red, S in yellow, C in black, N in blue and H in white.

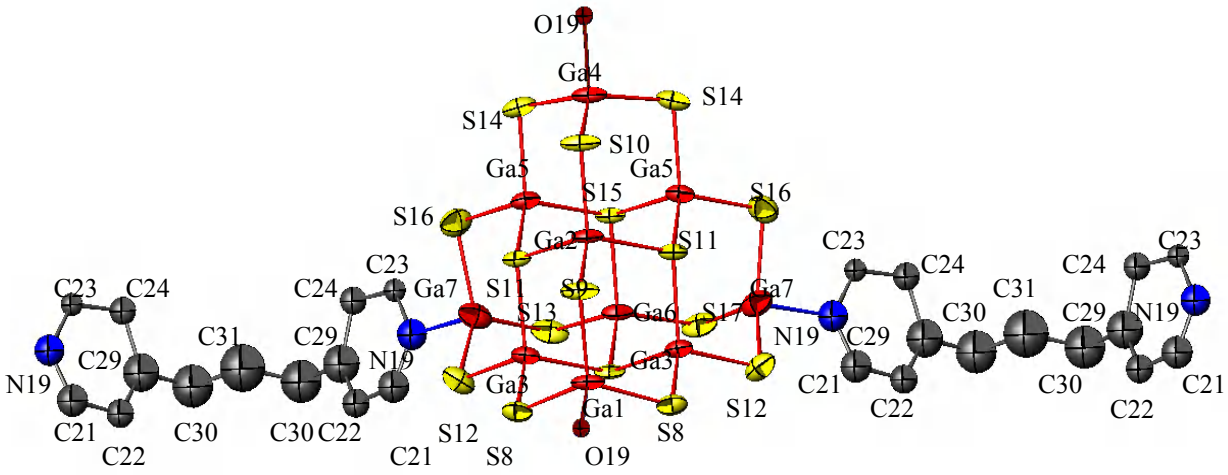

Figure 4.44. . Local coordination diagram for $[Ga_{10}S_{16}(OH)_2(N_2C_{13}H_{14})_2]^{4-}$ tetrahedral unit showing the atom labelling scheme and displacement ellipsoids at 50% probability. Ga atoms are shown in red, S in yellow, C in dark grey and N in blue. H atoms have been omitted for clarity.

Supertetrahedral units are connected by sharing two OH^- anions, and form supertetrahedral inorganic chains along the *b*-axis. These chains are linked through TMPyr ligands forming a corrugated two-dimensional layer with square grid topology, which contains pores of an approximate diameter of 6 × 9 Å (Figure 4.45 (a)). The cavities are partially occupied by an identical layer, forming a composite layer

containing two interpenetrated networks (Figure 4.45 (b)). The TMPyr molecules present a GG conformation from the four possible (TT, TG, GG and GG') [219,220] with observed angle between pyridine rings of 134.5(5)°. As a result, the TMPyr molecules are found on the sides of the double layers, favouring van der Waals' interactions (Figure 4.45 (c)).

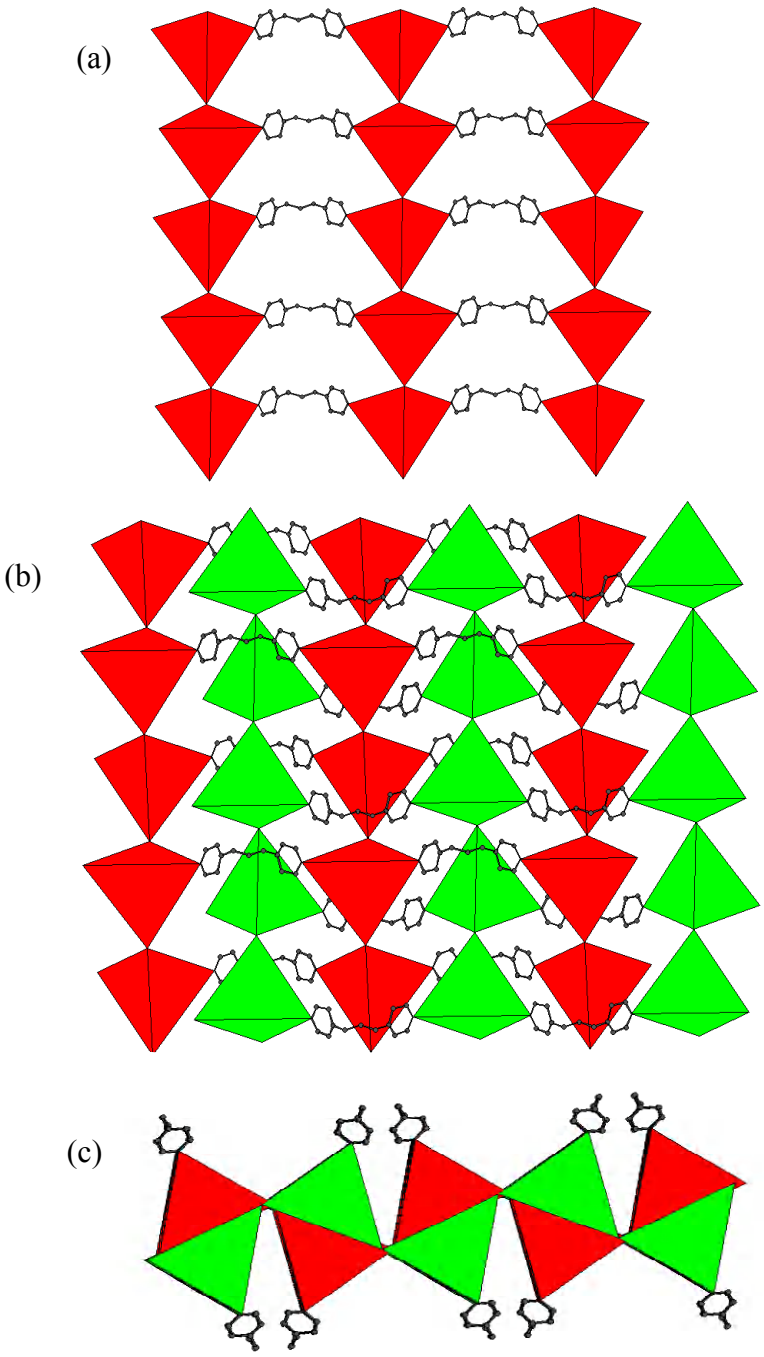

Figure 4.45. View of compound **(17)**: (a) of single square grid layer; (b) along the *a*-axis of the double layer and (c) along the *b*-axis of the double layer.
Different layers are represented by red and green tetrahedra, C atoms are shown in dark grey. H atoms are omitted for clarity.

The crystal structure consists of the double layers stacked in an AA sequence along the *a*-axis and separated by disordered pyridinium cations (Figure 4.46). Given that the composite layers contain OH^-, their overall composition is $[Ga_{10}S_{16}(OH)(N_2C_{13}H_{14})]^{3-}$, and therefore three protonated pyridinium cations would be required for charge balance. Only one pyridinium cation per formula unit was located in the Fourier maps, but given that the structure contains *ca.* 45 % of solvent accessible void space, it is likely that two additional disordered pyridinium cations are present. This is confirmed by the elemental analysis results.

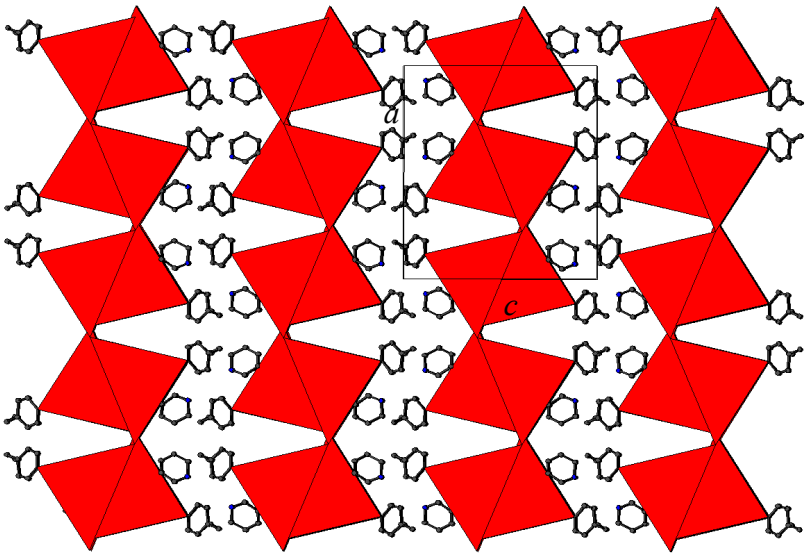

Figure 4.46. View along the *a*-axis of compound **(17)**. Supertetrahedra are shown in red, C atoms are shown in dark grey and N in blue. H atoms are omitted for clarity.

Experimental and calculated (using Powder Cell [175]) powder X-ray diffraction experimental patterns present a fair agreement (Figure 4.47). The observed diffraction patterns were fitted using TOPAS [176] in order to refine the lattice parameters (which are given in Table 4.23 for compounds **(16)** and **(17)**) showing a relatively good agreement when compared with values obtained using single crystal X-ray diffraction (Table 4.22).

Elemental analysis and TGA

Elemental analysis for compound **(16)** is in good agreement with the values calculated from the proposed formula (calculated: C: 25.9%; H: 2.4%: N: 4.6%; experimental: C: 25.70%; H: 2.87%; N: 5.86%). Thermogravimetric analysis (Figure 4.48 (a)) indicates that compound is stable up to *ca.* 673 K. The decomposition takes place in two main

steps. The total weight loss is *ca.* 30% at 1250 K and is slightly lower than the calculated weight loss from the proposed formula and experimental CHN results (34%). The residue consists of an amorphous material that could not be identified by powder X-ray diffraction. The difference of volatile fraction can be associated to the presence of inorganic impurities stacked on the crystals that could not be separated.

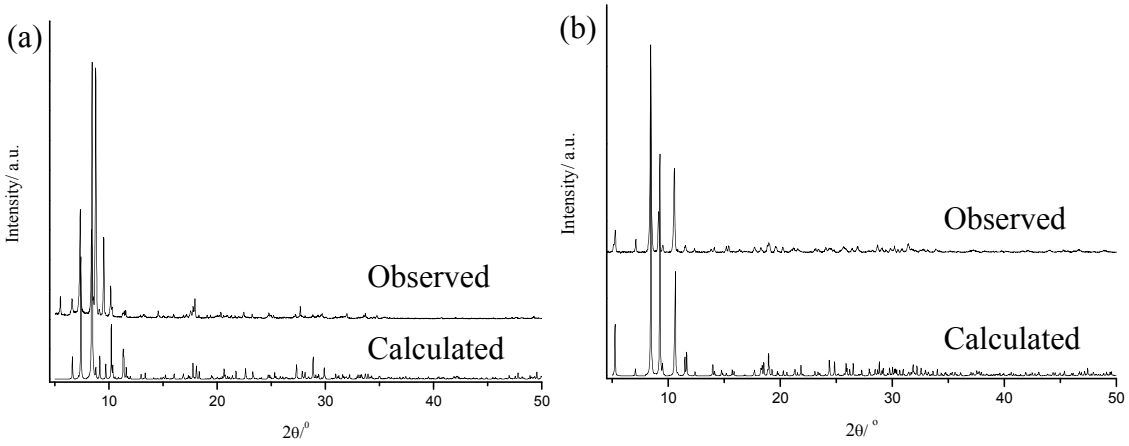

Figure 4.47. Comparison of calculated and experimental powder X-ray diffraction patterns for (a) **(16)** and (b) **(17)**.

Table 4.23. Lattice parameters for compounds **(16)** and **(17)** determined using powder X-ray diffraction data.

Unit cell parameters	**(16)**	**(17)**
a/Å	12.453(4)	16.999(3)
b/Å	13.687(4)	18.713(3)
c/Å	20.382(7)	19.539(3)
α/°	81.29(1)	-
β/°	88.48(1)	-
γ/°	83.01(1)	-

For compound **(17)**, elemental analysis is in fair agreement with the expected data (calculated: C: 18.17%; H: 1.93%: N: 5.19%; experimental: C: 19.37%; H: 3.17%; N: 4.28%) which include the addition of extra organic cations. Thermogravimetric analysis (Figure 4.48 (b)) shows that the decomposition occurs in several steps, from which it was not possible to identify and intermediate phase. **(17)** is stable up to *ca.* 450 K and has a total weight loss *ca.* 55% at 1200 K. The remaining residue was identified

as Ga_2O_3 by powder X-ray diffraction, which is consistent with the difference between the total removal of the organic matter (25.29 %) and the weight loss in TGA.

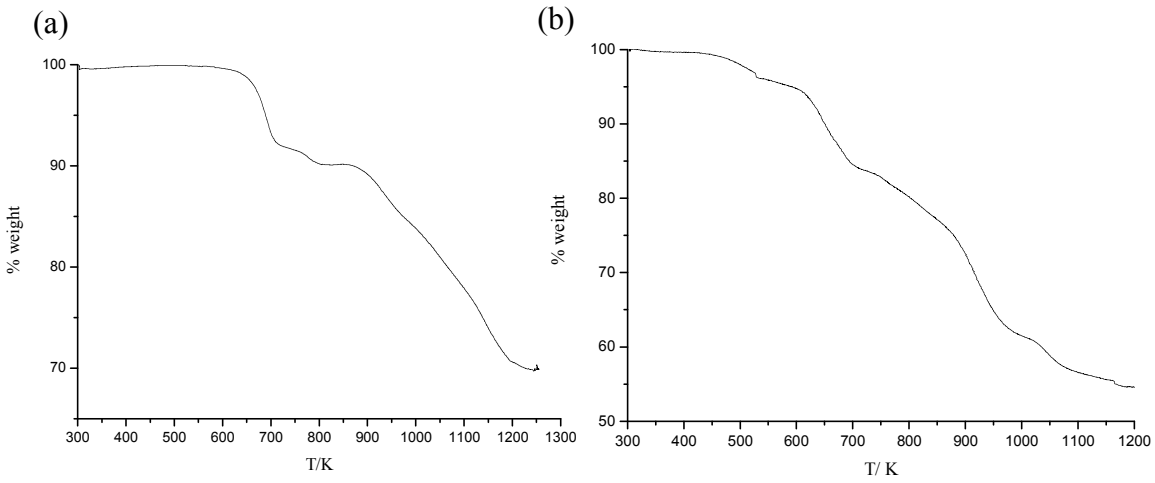

Figure 4.48. Thermogravimetric analyses for: (a) **(16)** and (b) **(17)**.

FTIR

Infrared data spectra for compounds **(16)** and **(17)** (Appendix III) are consistent with the presence of aromatic and amine functional groups. The vibrational modes and their frequencies are given in Table 4.24 [217].

Table 4.24. IR selected bands (values in cm^{-1}) for compounds **(16)** and **(17)**. υ = stretching, δ = deformation in the plane, γ = deformation out of the plane; s = strong, m = medium, w = weak.

Assignment	**(16)**	**(17)**
υ (N-H)	3424.5 (w)	3448.2 (w)
υ (C-H)	3011.7 (w)	3086.8 (w)
υ (C=C)	2981.6 (w)	3040.5 (w)
δ (C-C)	1648.6 (s)	1616.7 (s)
δ (C-H)	1404.7(s)	1436.6 (s)
γ (C-H)	1036.4 (m)	1036.4 (m)

Diffuse Reflectance

The optical absorption spectra for compounds **(16)** and **(17)** are shown in Figure 4.49. Band gap values were estimated as 3.7(1) and 3.4(2) for **(16)** and **(17)**, respectively. These values indicate that these materials exhibit semiconducting behaviour.

Compound **(17)** is slightly blue-shifted respect to **(16)** and that could be attributed to the different ligands coordinating the supertetrahedral clusters in each compound.

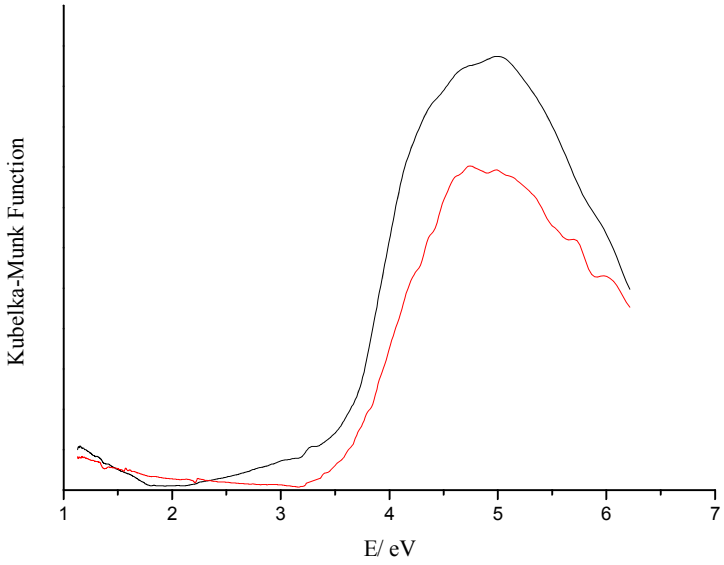

Figure 4.49. Optical absorption spectra for compounds: **(16)** and **(17)** which are represented by a black and red line, respectively.

4.4. Discussion

Isolated clusters of gallium sulphide, $[Ga_{10}S_{16}L_4]^{2-}$, are part of the supertetrahedral cluster family. They maintain the basic structure of a T3 inorganic cluster $[Ga_{10}S_{20}]^{10-}$. However, the terminal S atoms in the corners are substituted by coordinated ligands. Metal thiolate supertetrahedral units such as $[Cd_{10}S_4(SPh)_{16}]^{4-}$ [51] , which are also part of the hybrid tetrahedral cluster family, can be described as an inorganic Tn cluster where the S atoms at the faces and/or the vertices of the cluster are covalently bonded to organic molecules. Within this category, several types of inorganic cores such as penta-supertetrahedral and capped tetrahedral clusters are also known [58]. Under the appropriate reaction conditions, transition-metal thiolate clusters formed extended structures through additional covalently bonded organic ligands [60,53]. However, three-dimensional structures formed by hybrid clusters and inorganic clusters are linked by S bridges [103,120,122] (see Section 1.3.3). In comparison with them, the $[Ga_{10}S_{16}L_4]^{2-}$ units described in this chapter are potential building units to develop a new family of compounds. This family had not been explored before and has been developed during the course of the work reported here. Supertetrahedra are exclusively coordinated by organic ligands in the four corners of the supertetrahedral clusters and, in consequence, structures can present more void space. Additionally, the use of

thiolates is suppressed because supertetrahedral gallium sulphides only require elemental S in their synthesis.

Previously to this work, only one member of this family was reported. This material consisted of discrete T2 molecular clusters $[Ga_4S_6(NC_9H_{15}N_2)_4]$ which crystallised with solvent under refluxing conditions [56]. In this chapter, it has been demonstrated that solvothermal conditions are an effective method of synthesis for functionalised T3 gallium-sulphide clusters. Gallium has a higher hard acid character when compared with other elements from the *p*-block [221], which favour the coordination of organic ligands and produce hybrid supertetrahedral chalcogenide clusters. The ability of primary amines to coordinate to Ga^{3+} cations under solvothermal conditions, resulting in the formation of two-dimensional chalcogenide structures, is also known [145,129].

The first attempts in the design of functionalised clusters resulted in structures containing hybrid clusters coordinated by lutidine (compound **(5)**). A number of pyridine derivates were tested as potential ligands (Figure 4.50). Unfortunately, of the monodentate ligands tested, only 4-picoline proved to be in an effective ligand. It was established that effective ligands are produced at pH ≈ 8 in the mixture previous to the reaction, while the rest of derivates produce mixtures with similar values of pH than secondary amines (pH ≈ 10).

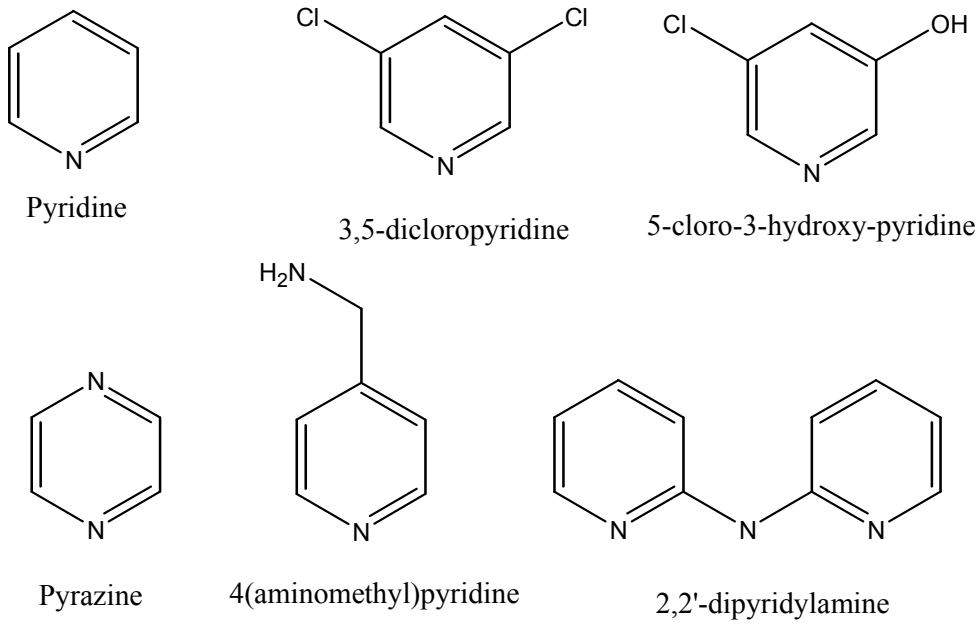

Figure 4.50. Pyridine derivates tested as potential templates in the synthesis of functionalised supertetrahedral gallium sulphides.

This behaviour can be attributed to the substituents in the pyridine ring, which can contribute to the reactivity of the pyridine ring by two factors; (i) the electronegativity of the groups and the inductive effect over the cloud of π electrons, attracting or repelling the lone pair of electrons in the N atom, and (ii) the position of the heteroatom in the ring. That explains the slightly higher reactivity of 4-picoline compared with 3,5-lutidine, because in the former the methyl group is directly pointing to the N atom and the unreactivity of the ligand tested whose groups favour the participation of the lone pair of electrons of the N to maintain the aromaticity in the ring [222]. A guide to choose effective ligands can be the pK_a value (Table 4.25) [223]. Effective ligands exhibit pK_a values around 6. Additionally, the steric impediment of the substituents should be taken into account.

Table 4.25. pK_a value for the ligand tested.

Ligand	**pK_a**
Pyridine	5.25
3,5-lutidine	6.02
4-picoline	6.15
Pirazine	0.65
3,5-dichloropyridine	0.67
5-chloro-3-hydroypyridine	6.81
4-aminomethyl pyridine	8.34
2,2'-dipyridylamine	6.20

Hybrid gallium-sulphide supertetrahedral clusters have been produced only as T2 [56] and T3 units (see sections 4.2 and 4.3). Attempts were carried out to produce larger hybrid clusters. In inorganic metal chalcogenide clusters it has been found that the insertion of transition metals with lower valence produced large clusters [160]. However, under the reaction conditions employed in the work described here, the transition metals tend to be coordinated with the ligands and form coordination polymers (see Appendix V), rather than being incorporated into supertetrahedral clusters.

Monodentate ligands limit the synthesis of functionalised gallium-sulphide clusters to the preparation of discrete cluster anions. The insertion in the synthesis of polytopic ligands (containing two or more pyridine rings) was then expected to produce extended structures similar to those in MOF's. However, those ligands are generally

solids with melting points close to the temperature employed in the solvothermal methods. Reactions without solvent were carried out unsuccessfully and it was concluded that a solvent was required. Pyridine derivates (lutidine, 4-picoline and pyridine) were used as solvents because of their structural similarity. However, these molecules usually compete with the polytopic ligands to produce multi-functionalised supertetrahedra and depending on the reaction conditions either monodentate or bidentate ligands are favoured to coordinate clusters.

Initially, dimeric units were produced and consisted of two supertetrahedral clusters connected through a bidentate ligand. The hybrid tetrahedral compound $[Cd_{17}Se_4(SPh)_{26}(TMPyr)_2]$ was also constituted by dimeric units [60], although, in that compound, clusters were connected via the coordination of two TMPyr molecules forming rings. Few examples of thiolate clusters are known in which supertetrahedra are connected through organic ligands to form covalent structures [53,60,224]. Organic assemblies introduce flexibility in the framework and additional structural units can be produced when compared to inorganic frameworks. They also contribute to the structure stability through $\pi-\pi$ stacking and van der Waals' interactions, in addition to the ionic interactions and hydrogen bonding observed in inorganic solvothemally prepared supertetrahedral compounds (see Chapter 1).

It is worth noticing that in extended structures of hybrid gallium-sulphide supertetrahedra, structural elements such as chains and two-dimensional layers can crystallise forming supra-structures. Compound **(14)** is constituted of super-chains consisting of supertetrahedral one-dimensional chains and the structure of compound **(17)** is based on two interpenetrating square grid layers. These types of associations were not reported in hybrid supertetrahedral compounds to date.

Additionally to reactions containing mixtures of pyridyl ligands, some reactions were carried out to study the influence of a second template. Primary, secondary amines and TPPB were used as second templates. Primary amines such as ethylenediamine (en) were previously used to produce hybrid gallium-sulphide materials (see Section 1.4.3). For that reason, it was thought that the addition of a different template could produce different hybrid supertetrahedral compounds. The employment of the second templates (which were mentioned above) results in compounds **(6)**, **(8)** and **(9).** These structures contain discrete supertetrahedral clusters and organic cations. Generally, the insertions of these second templates produce a variation in the pH. The second template can act as a counter-ion (compounds **(6)** and **(9)**), and affect the packing of the clusters, introducing H bonding interactions between

counter-ions or between counter-ions. It also can interact with the clusters improving optical properties. In contrast to the use of mixture of pyridine ligands, the ditopic ligand is exclusively coordinating the supertetrahedra and the monotopic ligand is acting as a monodentate ligand and counter cation. The supertetrahedral clusters readjust their distribution in function of the size of the second template, that is the case of **(5)** and **(6)**. In other occasions, the second template takes part in the reaction, but its presence is not observed in the structure (compound **(8)**). Analogous structures to compound **(8)** were also obtained using different conditions and templates which are summarised in Table 4.5. This type of behaviour was previously observed in the synthesis of inorganic indium-sulphide frameworks based on supertetrahedral clusters [83], where the main template is usually present in the structure as a counter-ion, and there was no evidence of the second template. However, it was established that the reaction cannot take place without the presence of the second template (see Section 4.2.2).

The presence of other organic species in addition to the ligand could favour the formation of three-dimensional structures with large cavities. As it was studied in inorganic supertetrahedral system, interpenetration tends to take place in porous materials when the cavities are too large to avoid the emptiness and maximise the packing. If a large entity is filling the pores then there will not be a need for interpenetration.

The reducing conditions of the solvothermal synthesis give place to parallel reactions, which may affect the products of the reactions. In compounds **(11)** and **(12)** hydrogenation of Dpe has resulted in the formation of 1,2-di(4-pyridyl)ethane, which favours the linkage of the clusters into hybrid structures. Sometimes, side reactions involving organic templates occur producing new organic moieties and even organic linkers (compounds **(7)** and **(15)**). It was also found that slight changes in the reaction conditions could favour the synthesis of different structures. This is the case of compounds **(11)** and **(14)**, which differ in the solvent (4-picoline for **(11)** and pyridine for **(14)**). Additionally, it is suggested that there are different supertetrahedral monomers and oligomers coexisting into solution under solvothermal conditions. Examples include compounds **(12)** and **(15)** in which monomers and dimers, or dimers and chains, coexist. However, the species presented in the structures produced in this project, exhibit the same cluster dimensionality and vary in the functionalised groups coordinating each cluster; in contrast to inorganic clusters structures, where is possible to find different size clusters.

Materials based on hybrid gallium-sulphide supertetrahedra exhibit semiconducting properties. The band gap is a consequence of the interaction between the 'p' orbitals from Ga (which control the conduction band) and 'p' orbitals of S atoms (which control the valence band). Additionally, the substitution of S by pyridine derivates through Ga-N bonds introduces an extra level in the valence band. However, this usually corresponds to energy levels close to the ultraviolet [50].

Taking into account that the compounds presented in this chapter contain clusters of the same size (T3) and contain only Ga^{3+} as metal, the differences observed in the band gaps can be attributed to the chemical equivalence of the supertetrahedral clusters. The different chemical equivalence is associated with the interaction of each cluster with the ligands, counter cations and the packing in each structure. In materials based in isolated clusters, supertetrahedra coordinated with different type of ligands, exhibit variations in their band gap when are compared, as for example compounds **(5)** and **(7)**. The crystallisation of different species of clusters (as seen in compounds **(12)** and **(15))** shows more obvious cases of non-equivalent clusters. Considering that the band gap is a contribution of the different clusters in each compound, ideally it should be understood as a contribution of the supertetrahedra energy levels. When supertetrahedra are not chemically equivalent, their energy levels differ. Therefore, the continuity of the band gap for the whole material is no longer achieved. The combination of these different energy levels produce shifts in the ideal band gap value for each compound studied.

The presence of the pyridine rings also contribute in stacking interactions that stabilise the structure and allows the appearance of charge-transfer processes. These can shift band gap values to lower values in the UV-Vis region in comparison with the bulk material [50,209,57] and in a certain way mask the band gap corresponding to gallium-sulphide supertetrahedra. The insertion of optically active species (as dyes) was proved by other authors as an effective strategy to produce hybrid material with electronic or optical properties [119]. Therefore, the presence of a large number of aromatic species and/or their interaction could produce a bathochromic shift in the optical spectra of hybrid supertetrahedral cluster materials.

Chapter 5: Non-Supertetrahedral gallium sulphide structures

5.1. Introduction

Initial work on to the solvothermal synthesis of gallium sulphides revealed that the vast majority of structures obtained are based on supertetrahedral clusters, as described in Chapters 1, 3 and 4. However, the unpredictability of solvothermal reactions has resulted in the preparation of a small number of gallium sulphides containing other building units. These structures are also based on simple GaS_4 tetrahedra, which can be connected by sharing edges and corners. In this chapter, two types of structure are described: one-dimensional structures, in which GaS_4 tetrahedra share edges to form infinite $[GaS_2]^-$ chains, and a two-dimensional structure, in which gallium is covalently-bonded to the amine.

5.2. Structure containing infinite $[GaS_2]^-$ chains

5.2.1. Synthesis of $[C_4H_{11}N_2][GaS_2]$ and $[C_6H_{16}N_2][GaS_2]_2$

$[C_4H_{11}N_2][GaS_2]$ **(18)**:A mixture of Ga_2S_3 (136.8 mg; 0.58 mmol), sulphur (148.5 mg, 4.64 mmol) and piperazine (1.290 g, 15 mmol) was loaded into a 23 ml Teflon-lined stainless steel autoclave. 3 ml of methanol were added to form a mixture with an approximate molar composition Ga_2S_3:S:piperazine:methanol of stoichiometry 0.58:4.64:15:74. The container was closed and heated at 443 K for 10 days. The product contained a large number of colourless single crystals, identified by single crystal X-ray diffraction as **(18)** and agglomerates of crystals and a powder, identified by powder X-ray diffraction as Ga_2S_3.

$[C_6H_{16}N_2][GaS_2]_2$ **(19)**: a mixture of gallium (139.44 mg; 2 mmol), sulphur (128 mg, 4 mmol), 1,4-diaminocyclohexane (1,4-DACH) (1.290 g, 15 mmol) and 1,2-diaminocyclohexane (1,2-DACH) (3 ml) were loaded into a 23 ml Teflon-lined stainless steel autoclave with 0.5 ml of methanol. The mixture had a molar composition of *ca.* Ga:S:1,4-DACH:1,2-DACH:methanol of stoichiometry 2:4:1:30:12.3. The autoclave was placed in an oven and heated at 443 K for 10 days. The product contained a large number of crystals, which range from colourless to pale pink depending on their dimensions. These crystals were identified as **(19)** by single crystal X-ray diffraction.

Table 5.1. Crystallographic data for the structures **(18)** and **(19)**.

Formula	$[C_4H_{11}N_2][GaS_2]$ **(18)**	$[C_6H_{16}N_2][GaS_2]_2$ **(19)**
Mr	221.00	383.91
Crystal habit	Colourless block	Colourless plate
Dimensions/mm^3	0.08 × 0.12 × 0.20	0.05 × 0.08 × 0.20
Crystalline System	Monoclinic	Monoclinic
Space group	*P2$_1$/c*	*C2/m*
T/K	298	100
a/Å	6.0798(5)	11.5011(7)
b/Å	16.2655(13)	10.4634(7)
c/Å	8.3611(8)	6.0351(3)
β/°	104.827(5)	115.788(3)
V/Å^3	799.31(12)	653.84(7)
Z	4	2
Wavelength/Å Mo K_α	0.71073	0.71073
μ/cm^{-1}	3.88	4.724
Δρ max / Å^{-3}	0.55	2.26
Δρ min / Å^{-3}	-0.61	-0.70
Measured data	11588	4453
Unique data	2644	1039
Observed data ($I > 2\sigma(I)$)	1772	890
R_{merg}	0.025	0.030
$R(F_o)$[a]	0.022	0.026
$R_w(F_o)$[b]	0.026	0.029

[a] $R(F_o)=\Sigma(|F_o| - |F_o|)/ \Sigma|F_o|$. [b] $R_w(F_o)= [\Sigma w(|F_o|- |F_o|)^2 / \Sigma w|F_o|^2]^{1/2}$.

5.2.2. Structure description

Crystallographic information and refinement details for compound **(18)** and **(19)** are given in Table 5.1. The atomic coordinates excluding H atoms, bond lengths and angles are summarised in Appendix II. The structures were solved using direct methods, which located the Ga and S atoms. The C and N atoms of the amine were found using

difference Fourier maps. H atoms were placed geometrically on the C and N atoms after each cycle of refinement in compound **(18)** (Figure 5.1). The amine was modeled as disordered over two positions with site occupancies fixed at 0.5 for **(19)**, and the H atoms were also placed geometrically with site occupancies fixed at 0.5 (Figure 5.2).

In both compounds, Ga presents tetrahedral coordination, forming elongated GaS_4 tetrahedra which can be observed in Figure 5.3 and 5.4 for compound **(18)** and **(19)**, respectively. Tetrahedra are linked by sharing non-adjacent edges to form one-dimensional $[GaS_2]^-$ chains (Figure 5.3).

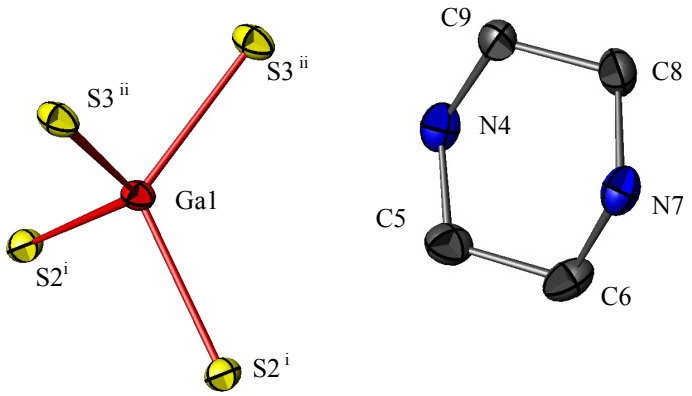

Figure 5.1. Local coordination diagram for **(18)** showing the atom labelling scheme and displacement ellipsoids at 50% probability. Ga atoms are shown in red, S in yellow, C in grey and N in blue. H atoms were omitted for clarity. Symmetry codes: (i) $-x+2$, $-y+1$, $-z+2$; (ii) $-x+3$, $-y+1$, $-z+2$.

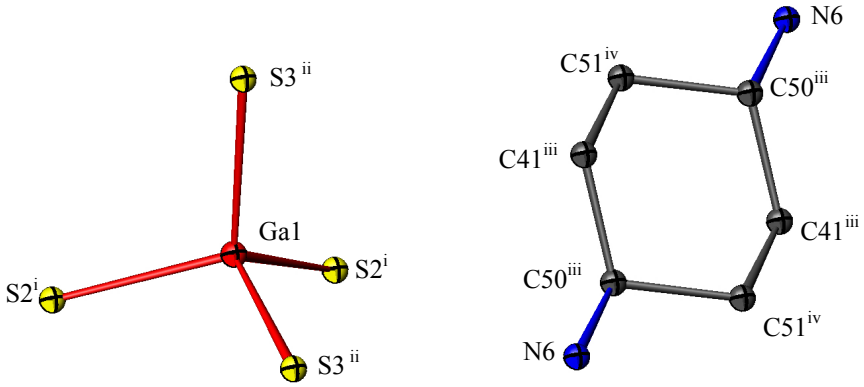

Figure 5.2. Local coordination diagram for **(19)** showing the atom labelling scheme and displacement ellipsoids at 50% probability. Only one of the disordered 1, 2-DACH molecules is shown for clarity. Ga atoms are shown in red, S in yellow, C in dark grey and N in blue. H atoms were omitted for clarity. Symmetry codes: (i) $-x+1$, $-y+1$, $-z$; (ii) $-x+1$, $-y+1$, $-z+1$; (iii) x, $-y$, z; (iv) $-x+1$, y, $-z$.

Selected bond distances and angles are shown in Tables 5.2 and 5.3. The Ga-S distances lie between 2.2771(5) -2.3078(5) Å and 2.2791(6)-2.2958(5), while the Ga-Ga distances are 3.0765(6) and 3.0006(3) Å for **(18)** and **(19)**, respectively. The latter values are indicative of non-metallic interaction between Ga atoms within the chain. These values are similar to those reported for other gallium sulphide chains [129,132]. In comparison with compounds containing tetrahedra which share corners to form structures such as layers [129] and tetrahedral clusters [103] (for which S-M-S angles lie between 102-110°); the $[GaS_2]^-$ chains described here are distorted tetrahedra with S-M-S angles over the ranges 96.215(16)-116.89(2)° and 82.96(2)-117.111(12)° for **(18)** and **(19)**, respectively.

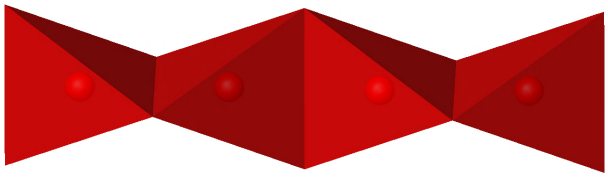

Figure 5.3. Polyhedral representation of $[GaS_2]^-$ chains.

Table 5.2. Selected bond lengths (Å) and angles (°) for compound **(18)**. Symmetry codes: (i) −x, −y+1, −z+2; (ii) −x+1, −y+1, −z+2.

Bond	Distance	Bond	Angle	Bond	Angle
Ga1-S2i	2.3078 (5)	S2i-Ga1-S3ii	112.84 (2)	S3ii-Ga1-S2	115.89 (2)
Ga1-S2	2.2984 (5)	S2i-Ga1-S3	118.656 (19)	S2-Ga1-S3	116.89 (2)
Ga1-S3ii	2.2877 (5)	S2i-Ga1-S2	96.215 (17)		
Ga1-S3	2.2771 (5)	S3ii-Ga1-S3	97.608 (17)		

Table 5.3. Selected bond lengths (Å) and angles (°) for compound **(19)**. Symmetry codes: (i) −x+1, −y+1, −z+1; (ii) −x+1, −y+1, −z.

Bond	Distance	Bond	Angle	Bond	Angle
Ga1-$S2^{I}$	2.2905(5)	$S2^{I}$-Ga1-$S3^{II}$	117.111(12)	$S2^{I}$-Ga1-S2	97.04 (2)
Ga1-$S3^{II}$	2.2785(7)	$S3^{II}$-Ga1-S3	97.96(2)	$S3^{II}$-Ga1-S2	117.111(12)
Ga1-S3	2.2959(6)	S2-Ga1-S3	114.393(12)		
Ga1-S2	2.2905(5)	$S2^{I}$-Ga1-S3	114.393(12)		

In compound **(18)**, chains run parallel to the *a*-axis and are separated by monoprotonated piperazinium cations (Figure 5.4). The structure is stabilised by hydrogen-bonding interactions between the piperazinium cations forming zig-zag chains along the *c*-axis and the sulphur atoms in the $[GaS_2]^-$ chains, as well as, with other

surrounding piperazinium cations (Figure 5.5), forming a three-dimensional network. Hydrogen distances were obtained using PLATON [183], and are summarised in Table 5.4.

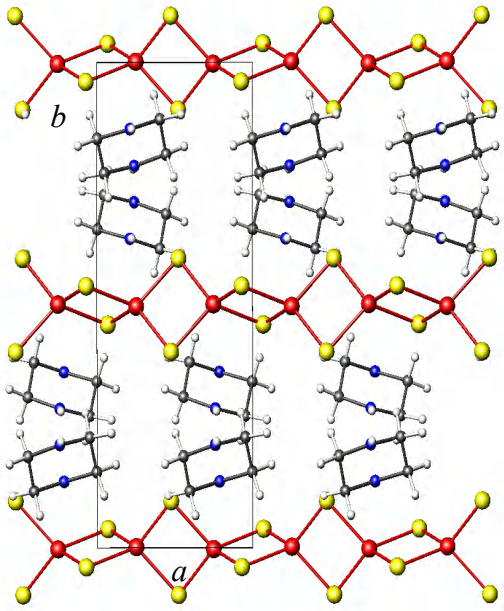

Figure 5.4. View along the [001] direction of compound **(18)**. Ga atoms are shown in red, S in yellow, C in dark grey, N in blue and H in white.

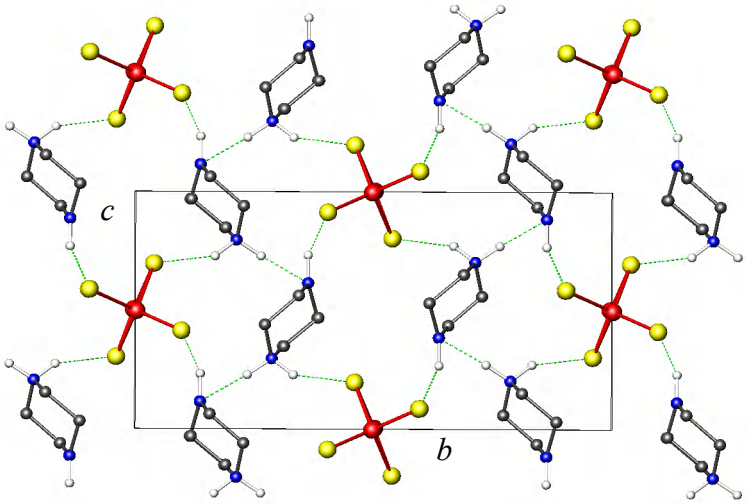

Figure 5.5. Packing of compound **(18)** on the (011) plane. Ga atoms are shown in red, S in yellow, C in dark grey, N in blue and H in white. Non-interacting H atoms are omitted for clarity. Hydrogen-bonding is shown in dashed green lines.

In compound **(19)**, the $[GaS_2]^-$ chains run parallel to the *c*-axis (Figure 5.6). However, 1,4-DACH cations are located in two crystallographically equivalent positions between the chains. As before, hydrogen-bonding interactions between the

diprotonated amines and S atoms in the chains stabilise the structure (Figure 5.6). Hydrogen-bonding interactions between disordered molecular cations are observed. The interactions are oriented in two possible perpendicular directions to the *b*-axis with in a 1:1 ratio due to the disorder. In consequence, the structure can be understood as parallel square grid sheets of amines stacked along the [105] direction which are crossed by $[GaS_2]^-$ chains. Hydrogen distances obtained from PLATON [183] are given in Table 5.5.

Table 5.4. Hydrogen bonds for **(18)**. Atoms code: D = donor, A= acceptor. Symmetry codes: (iii) x, −y+3/2, z+1/2; (iv) −x, −y+1, −z+1.

D—H...A	D—H /Å	H...A /Å	D—H...A/Å	Angle/°
N4—H41...N7(iii)	1.0000	1.9500	2.898(2)	158.00
N4—H42...S2	1.0000	2.7100	3.6072(19)	150.00
N7—H71...S2(iv)	1.0000	2.3200	3.2842(18)	162.00

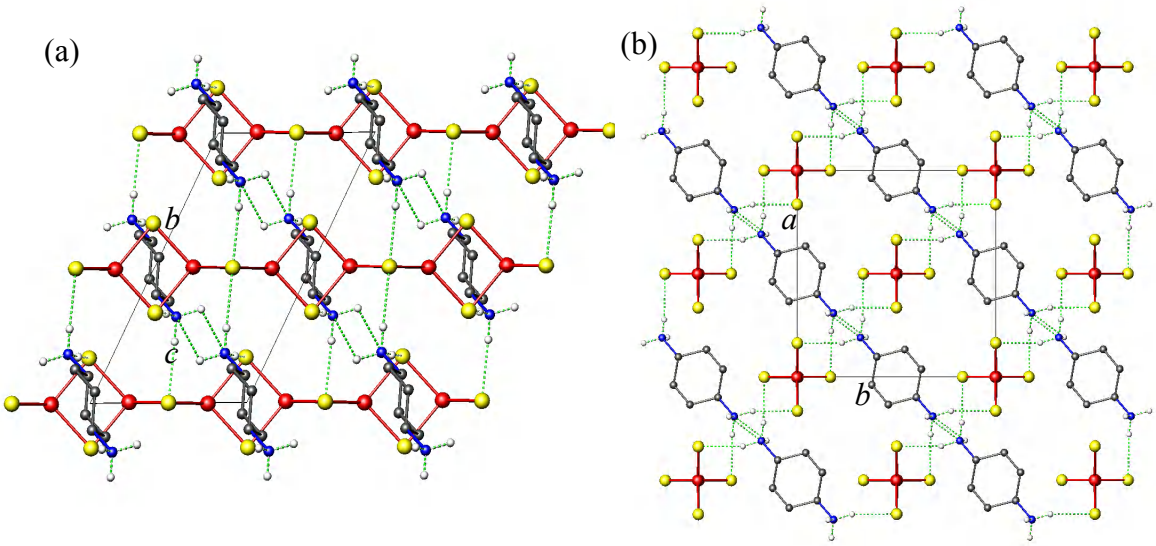

Figure 5.6. Compound **(19)**. (a) View along the [011] direction. (b) View on the (001) plane. DACH cations are shown in one of the possible directions. Ga atoms are shown in red, S in yellow, C in dark grey, N in blue and H in white. Hydrogen bonds are shown in dashed green lines.

Figure 5.7 presents a comparison of experimental powder X-ray diffraction pattern and calculated pattern obtained from the proposed model using Powder Cell [175] for both compounds. For compound **(18)**, crystalline impurities were identified as Ga_2S_3. Compound **(19)** presents a good agreement between both patterns. The

observed diffraction patterns were fitted using the predicted peak positions with TOPAS software [176] in order to refine the lattice parameters. Refined lattice parameters are given in Table 5.6 for both compounds. Refined and calculated unit cell parameters show a relative good agreement when compared with the unit cell parameters obtained from single crystal X-ray diffraction (Table 5.1).

Table 5.5. Hydrogen bonds for **(19)**. Atoms code: D = donor, A= acceptor. Symmetry codes: (v), x,-1+y, z; (vi), 1-x,-y,-z; (vii), 1/2-x,-1/2+y,-z.

D—H...A	D—H /Å	H...A /Å	D—H...A/Å	Angle/°
N6—H61...S(v)	1.0000	2.3500	3.338(3)	166.00
N6—H62...S(vi)	1.0000	2.5200	3.257(3)	131.00
N6—H63...S(vii)	1.0000	2.3500	3.322(3)	164.00

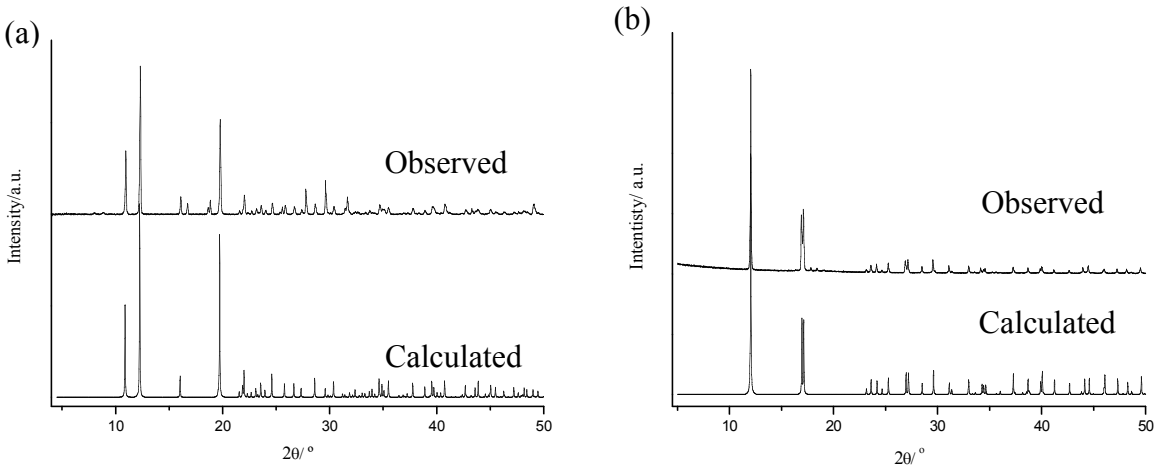

Figure 5.7. Comparison between observed and calculated powder X-ray diffraction patterns for (a) compound **(18)** and (b) compound **(19)**.

Table 5.6. Lattice parameters for compounds **(18)** and **(19)** determined using powder X-ray diffraction data.

Unit cell parameters	**(18)**	**(19)**
a/Å	6.0813(6)	11.5339(3)
b/Å	16.250(2)	10.5116(2)
c/Å	8.357(1)	6.0373(1)
β/°	104.742(8)	115.728(2)

5.2.3. Elemental analysis and TGA

CHN analysis for compound **(18)** reveals a composition of C: 17.58%, H: 4.11%, N: 10.03 %, which differs from the theoretical values C: 21.74%, H: 5.02%, N: 12.68 %. This disagreement could be attributed to the fact that the material under analysis consists primarily of agglomerates of crystals of compound **(18)** coated with Ga_2S_3 powder. Attempts to separate single crystals from this powder were unsuccessful. Thermogravimetric analysis for compound **(18)** (Figure 5.8(a)) indicates that the decomposition occurs in two steps. This compound is stable up to *ca.* 600 K. There is a change of slope at *ca.* 650 K. However, this intermediate present at this stage could not be isolated and identified. The total decomposition takes place at *ca.* 800 K with a weight loss of *ca.* 37 % producing an amorphous material. The expected weight loss derived from the formula was *ca.* 39.9 %. This difference is consistent with crystals coated with Ga_2S_3 that was found as impurity.

CHN analysis for compound **(19)** shows a good agreement between the calculated values (C: 18.77%, H: 4.2%, N: 7.36 %), and the experimental values (C: 18.51%, H: 4.13%, N: 7.14 %). TGA analysis for compound **(19)** is shown in Figure 5.8 (b). **(19)** is stable up to *ca.* 670 K and the decomposition occurs in one step up to *ca.*700 K. The total weight loss is *ca.* 32 % slightly superior to the percentage of organic component calculated from the proposed formula (30.6%). The final residue was identified as amorphous material after analysis with powder X-ray diffraction.

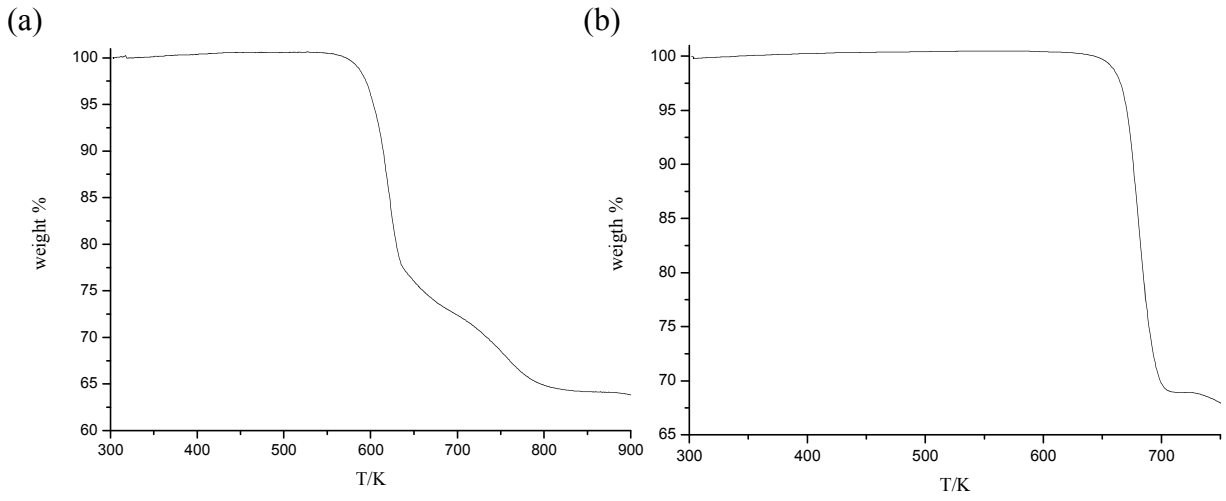

Figure 5.8. Thermogravimetric analyses for (a) compound **(18)** and (b) compound **(19)**.

5.2.4. FTIR.

Infrared data (Appendix III) exhibit bands corresponding to the vibrations of 1, 4-DACH and monoprotonated Pp cations. The vibrational modes and their frequencies are given in Table 5.7. Bands at high frequency and in the 1600-1550 cm^{-1} region can be attributed to primary and secondary protonated amines, respectively. The presence of the vibrational modes of the protonated organic molecules are in agreement with the structural data found in other related compounds [225,226,191].

Table 5.7. IR selected bands (values in cm^{-1}) for compound **(18)** and **(19)**.
υ = stretching, δ = deformation; s = strong, m = medium, w = weak.

Assignment	**(18)**	**(19)**
υ (N-H)	-	3210.2 (s)
υ (N-H)	3266.7 (w)	-
υ (C-H)	2849.5 (m)	2951.9 (m)
υ (N-H)	1581.6 (s)	1595.5 (s)
δ (C-H)	1511.1 (w),1400.0 (w)	1438.6 (m)

5.2.5. Diffuse Reflectance

Optical absorption spectra (Figure 5.9) resulted in identical band gap values of 4.2(1) eV for compounds **(18)** and **(19)**. These values are indicative of their semiconductor behaviour. Although, there are not many studies of the optical properties of one-dimensional gallium sulphides, the values found here are similar to $[Dy_2(en)_6(\mu_2\text{-}OH)_2]Ga_4S_8$ (4.21 eV) [134], which contains a lanthanide counter cation. These values are also slightly higher than those previously found for three-dimensional gallium sulphides (4.0 eV) (Section 3.4). However, there is a significant blue shift when compared with bulk Ga_2S_3 (3.31 eV) [192]. The strong absorption bands found at 5.01 eV (207 nm) and 5.95 eV (246 nm) might be assigned to electronic excitations located at the polymeric anions, similar to those found in $[InS_2]^-$ chain compounds [135]. A low intensity band can be observed for compound **(19)** at 2.5 eV (500 nm). A similar band was found in the two-dimensional $[In_{12}S_{24}H_2]^{10-}$ structure [83], but its origin is unclear.

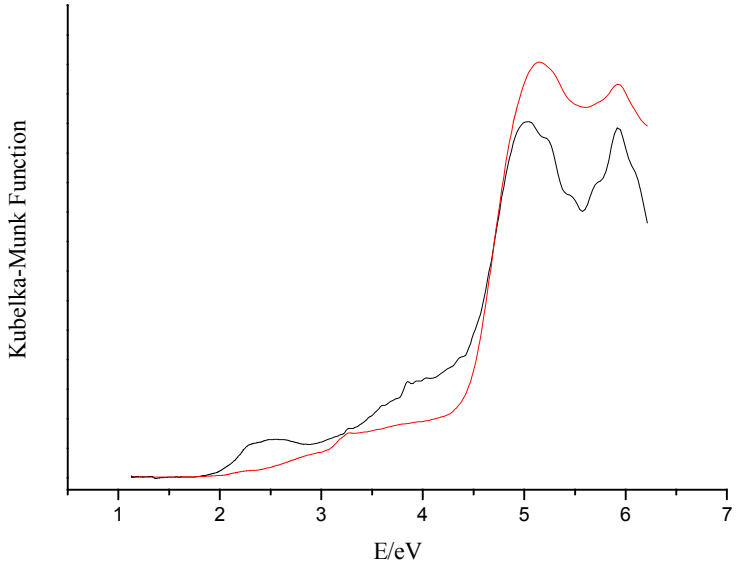

Figure 5.9. Diffuse reflectance for compound **(18)** and **(19),** which is represented by a black and red line, respectively.

5.2.6. Discussion

Compound **(18)** is isostructural to $[(C_4H_{11}N_2)[GaSe_2]]_n$, previously reported by Feng et *al.* [8]. Using alkali solutions and high temperatures, similar compounds containing $[GaS_2]^-$ chains were produced. They follow the general stoichiometry $MGaS_2$ (M= Li, Na, K, Rb, Cs) [128,127,227], where M is an alkali cation which fulfils the charge balance requirements instead of a protonated amine. Analogous chains have been reported as gallium selenides [126]. Compounds containing fragments of the $[GaS_2]^-$ chains with formula $[Ga_2S_6]^-$ and alkali cations [228,75] have also been reported. Other types of chain found in ternary gallium-sulphides are the infinite $[GaS_3]^-$ chains, formed by corner-sharing GaS_4 tetrahedra [137] and $Na_4[Ga_2S_5]$, the latter consists of a fragment of chains in which GaS_4 tetrahedra share vertexes and edges [229]. However, these compounds were not synthesised by solvothermal methods (Figure 5.10).

In solvothermally-prepared materials containing one-dimensional $[GaS_2]^-$ chains, charge balance is achieved via incorporation of counter-ions. In some cases, the charge balance is achieved by the amines [132] and in others, the amine has a chelating effect with the transition metal ions producing transition metal complexes $[M(en)_3]^{2+}$ (M= Mn, Co, Ni; en= ethylenediamine) [129], responsible for giving neutrality. The chain prototype in these materials is isostructural to the SiS_2 structure. However, chains can present several orientations and different types of packing have been found. Compounds **(18)** and **(19)** illustrate two of these (see models of anionic chains in Chapter 1).

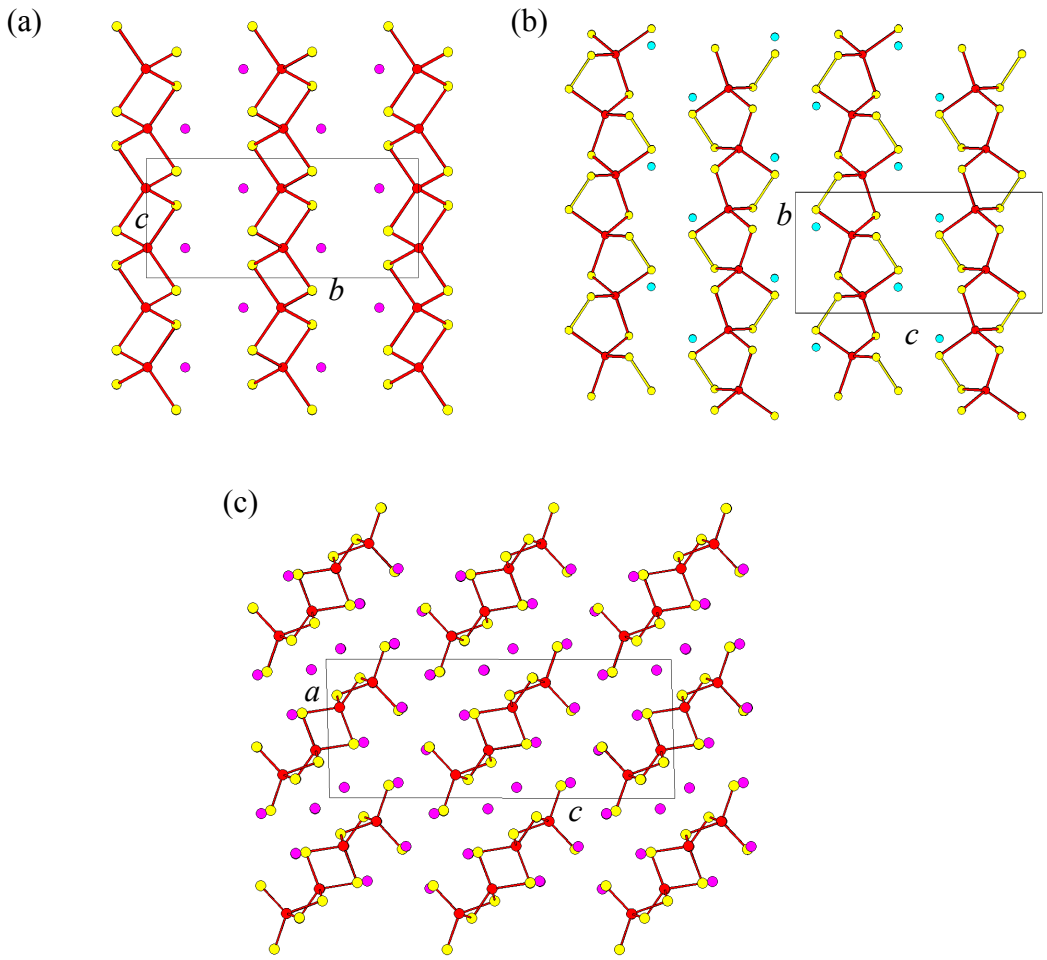

Figure 5.10. Different types of one-dimensional gallium sulphides. (a) View of $NaGaS_2$ along the (001) plane. (b) View of compound $K[GaS_3]$ along the [100] direction. (c) View of $Na_4[Ga_2S_5]$ within the (001) plane. Ga atoms are shown in red, S in yellow, Na in pink and K in blue.

The type of chain may be related to the counter cations contained in the structures. Dai and co-workers compared gallium-sulphide chains containing metal complexes as counter cations, and proposed that the weak interaction together with the shape and size of complex cations play an important role in the conformation of the chains [134]. $[Dy_2(en)_6(\mu\text{-}OH)_2][Ga_4S_8]$ [134] containing $[Dy_2(en)_6(\mu\text{-}OH)_2]^{2+}$ complexes which interact through N-H…S and O-H…S bonds with the chains producing a butterfly conformation $[GaS_2]^-$ chain. Meanwhile, compounds $[M(en)_3]_{0.5}[GaS_2]$ containing $[M(en)_3]^{2+}$ (M= Mn, Co, Ni) complexes [129] present weak interactions, which are reflected in disordered en ligands in the complexes and therefore, straight chains are observed. A similar approach could be applied for

compounds **(18)** and **(19)**, but in this case it is related to the orientation of the H bonding interaction. Both compounds present the same type of H bonding (N-H...S). However in compound **(18)**, piperazinium cations interact through H bonding forming zig-zag chains along the *c*-axis. As a consequence, the N-H…S interactions have preferred orientations along the chain and as a result chains are rotated with respect to their neighbours. In contrast to compound **(19)**, cations can be placed in two different positions with 50% probability. The possible N-H…S interactions have the same probability in orientation and the $[GaS_2]^-$ chains are analogous. This different stability is reflected when TGA analyses are compared. Compound **(19)** exhibits a slightly higher stability than compound **(18)**.

5.3. Layered structure

5.3.1. Synthesis of $[Ga_6S_9(N_2C_6H_{14})_2(NC_6H_{14}N)_2]$

$[Ga_6S_9(N_2C_6H_{14})_2(NC_6H_{14}N)_2]$ **(20)**: was prepared from a mixture of gallium (209.16 mg; 3 mmol), sulphur (128 mg; 4 mmol), $CoCl_2{\cdot}4H_2O$ (63 mg; 0.5 mmol) and a mixture of 1,2-DACH isomers (3.5 ml; 27.2 mmol), with approximate molecular stoichiometry of 3:4:0.5:27.2, which was heated at 463 K for 10 days. The final product was composed of amorphous dark blue powder and colourless crystals of **(20)**.

Heating an identical reaction mixture at a lower temperature (443 K) produced the side product trans-1,2-diaminium cyclohexane sulphide, which was previously reported [230] and obtained by neutralization of (±) 1,2-DACH with H_2SO_4 in H_2O (see Appendix V).

5.3.2. Structure description

Crystallographic information and refinement details for compound **(20)** are given in Table 5.8. The atomic coordinates excluding H atoms, bond lengths and angles are given in Appendix II. The structure was solved using direct methods, which located the Ga and S atoms. The C and N atoms of the amine were found using Fourier maps. Distances and displacement parameters were restrained to model the disorder. H atoms were placed geometrically on the C and N atoms after each cycle of refinement, and refined with riding constraints.

Table 5.8. Crystallographic data for the structure **(20)**.

Formula	$[Ga_6S_9(N_2C_6H_{14})_2(NC_6H_{14}N)_2]$ **(20)**
Mr	1157.63
Crystal habit	White plate
Dimensions/mm^3	0.10× 0.12 × 0.22
Crystalline System	Orthorhombic
Space group	*Pnna*
T/K	100
a/Å	10.7480(5)
b/Å	18.7764(8)
c/Å	21.0644(10)
V/Å^3	4251.0(3)
Z	4
Wavelength/Å Mo K_α	0.71073
μ/cm^{-1}	4.156
$\Delta\rho$ max / Å^{-3}	3.20
$\Delta\rho$ min / Å^{-3}	-1.73
Measured data	36766
Unique data	8136
Observed data ($I > 3\sigma(I)$)	2735
R_{merg}	0.030
$R(F_o)$[a]	0.037
$R_w(F_o)$[b]	0.067

[a] $R(F_o)=\Sigma(||F_o| - |F_o||)/ \Sigma|F_o|$. [b] $R_w(F_o)= [\Sigma w(|F_o|- |F_o|)^2 / \Sigma w|F_o|^2]^{1/2}$.

The structure of **(20)** is formed by neutral layers of tetrahedra with one and two vertices in common. Sulphur is bi-coordinated to gallium, while Ga is tetrahedrally coordinated to S or S and N, resulting in GaS_4, GaS_3N and GaS_2N_2 tetrahedra (Figure 5.11). This means that gallium is coordinated to exclusive *trans*-DACH via N and the amine is acting either as a monodentate or bidentate ligand. The asymmetric unit is a chain of vertex-linked Ga-centered tetrahedra, in which GaS_4 units alternate with GaS_3N and GaS_2N_2 (Figures 5.11).

Selected bond distances and angles are summarised in Table 5.9. The Ga-S distances lie between 2.189(2)-2.298(2) Å and Ga-N between 2.000(11)-2.030(6) Å. The Ga-Ga distances lie between 3.541(2)-3.697(9) Å, comparable to Ga-N distances found in other layered gallium sulphides [129,145]. The presence of Ga-N bonding results in distorted tetrahedra. However, GaS_2N_2 tetrahedra present slightly longer Ga-N lengths than in GaS_3N tetrahedra, while the N-Ga-N angle is shorter than that expected for tetrahedral coordination (*ca.* 109.27 º).

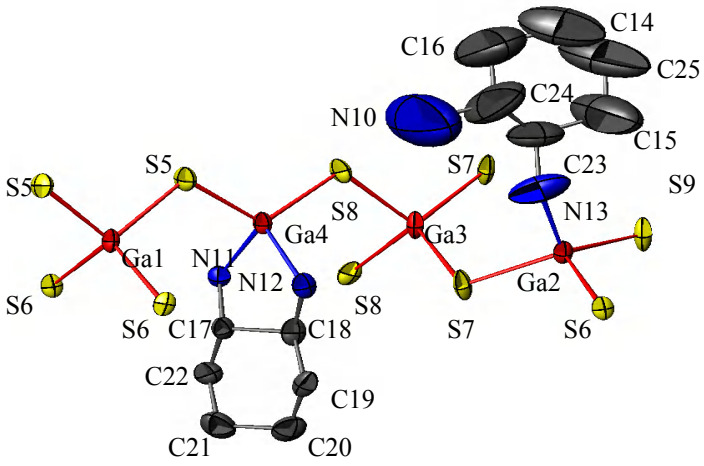

Figure 5.11. Local coordination diagram for **(20)** showing the atom labelling scheme and displacement ellipsoids at 50% probability. Ga atoms are shown in red, S in yellow, N in blue and C in dark grey. (H atoms from *trans*-DACH molecules have been omitted for clarity).

The layers in compound **(20)** are constituted by cross-linked chains, forming square units containing eight-membered rings and smaller three-membered rings of tetrahedra. The latter are Ga_3S_3 rings in half-chair conformation, arising from the corner linkage of one GaS_4 and two GaS_2N_2 tetrahedra (Figure 5.12). These layers are parallel to the (110) plane and are stacked along the *c*-axis in an AB type sequence (Figure 5.13). The interaction between layers is likely to be governed by van der Waals' forces between *trans*-DACH located on opposite sides of consecutive layers. The reaction is exclusively produced with *trans*-DACH, and the *cis*- form was not observed in the structure.

Table 5.9. Selected bond lengths (Å) and angles (°) for compound **(20)**. Symmetry codes: (i) −*x*+3/2, −*y*+1, *z*; (ii) *x*, −*y*+1/2, −*z*+1/2; (iii) −*x*+5/2, −*y*+1, *z*.

Bond	Distance	Bond	Angle	Bond	Angle
Ga1-S5(i)	2.283 (2)	S5(i)-Ga1-S6(i)	113.13 (7)	S9-Ga2-N13	111.4 (4)
Ga1-S6(i)	2.2752 (19)	S5(i)-Ga1-S5	97.08 (12)	S8(ii) -Ga3-S7(ii)	111.29 (8)
Ga1-S5	2.283 (2)	S6(i) -Ga1-S5	115.00 (7)	S8(ii) -Ga3-S7	104.16 (8)
Ga1-S6	2.2752 (19)	S5(i)-Ga1-S6	115.00 (7)	S7(ii) -Ga3-S7	118.44 (10)
Ga2-S6	2.2528 (19)	S6(i)-Ga1-S6	103.98 (11)	S8(ii) -Ga3-S8	107.16 (10)
Ga2-S7	2.238 (2)	S5-Ga1-S6	113.13 (7)	S7-Ga3-S8	111.29 (8)
Ga2-S9	2.2490 (16)	S6-Ga2-S7	106.42 (8)		
Ga2-N13	2.000 (11)	S6-Ga2-S9	112.26 (7)		
Ga3-S8(ii)	2.298 (2)	S7-Ga2-S9	116.70 (8)		
Ga3-S7(ii)	2.257 (2)	S6-Ga2-N13	102.7 (3)		
Ga3-S7	2.257 (2)	S7-Ga2-N13	106.2 (4)		
Ga3-S8	2.298 (2)	S5(iii) -Ga4-S8	111.44 (9)		
Ga4-S5(iii)	2.189 (2)	S5(iii) -Ga4-N11	112.44 (18)		
Ga4-S8	2.2084 (19)	S8-Ga4-N11	116.17 (18)		
Ga4-N11	2.030 (6)	S5(iii) -Ga4-N12	116.0 (2)		
Ga4-N12	2.025 (7)	S8-Ga4-N12	113.41 (19)		

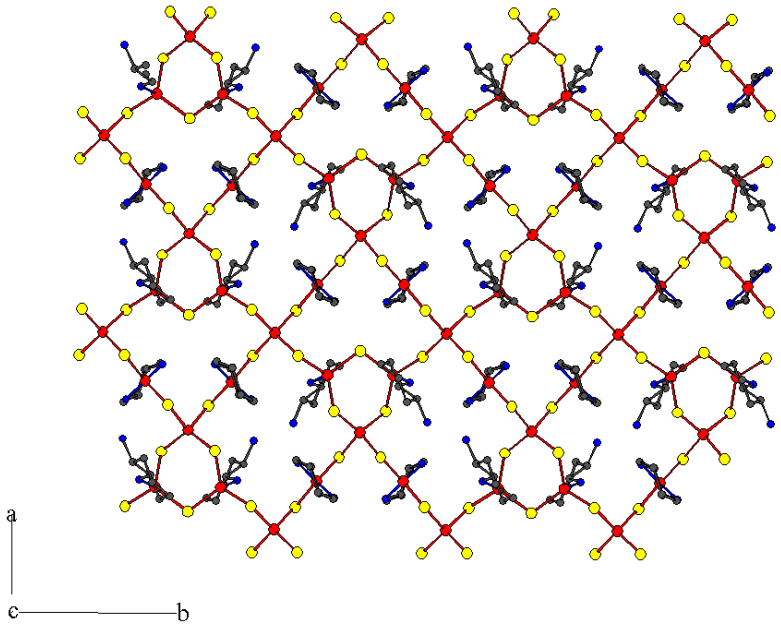

Figure 5.12. Tetrahedral representation of the layers contained in compound **(20)** on the (010) plane. Ga atoms are shown in red, S in yellow, N in blue and C in dark grey. H atoms are omitted for clarity.

A comparison between calculated (on the basis of the single-crystal structure determination using Powder Cell [175]) and observed diffractograms is shown in Figure 5.14. There are small mismatches between calculated and observed reflections, these peaks were fitted with the presence of $[(C_6H_{16}N_2)SO_4]$ (see Appendix V).

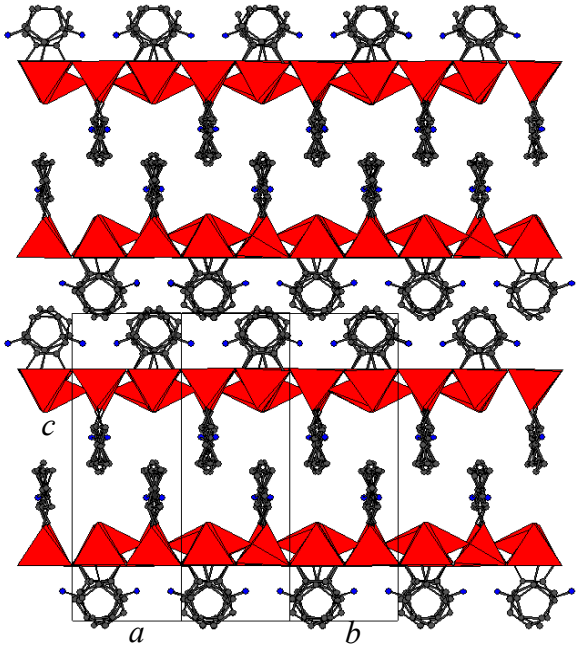

Figure 5.13. View along the [212] direction of compound **(20)**. Ga atoms are shown in red, S in yellow, C in grey and N in blue. H atoms are omitted for clarity.

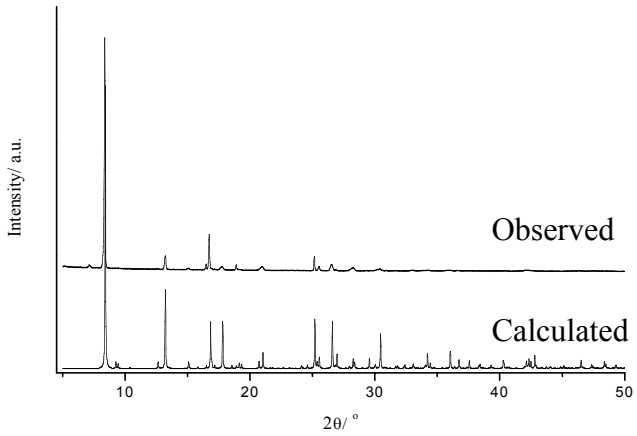

Figure 5.14. Comparison between calculated and observed powder diffraction patterns for **(20)**.

Attempts to index the powder X-ray diffraction data using TOPAS [176] have been carried out using a data collection from D8 Advance diffractometer in step-scan mode over the angular range $5 \leq 2\theta/° \leq 85$ in 0.02° increments for 39.5 s per step. However, obvious differences were not found in the simulated pattern (Figure 5.15). Refined lattice parameters are given in Table 5.10. Additional, precession images were taken from the single crystal X-ray data set to check evidence of diffuse scattering in the crystals of compound **(20)** (Figure 5.16).

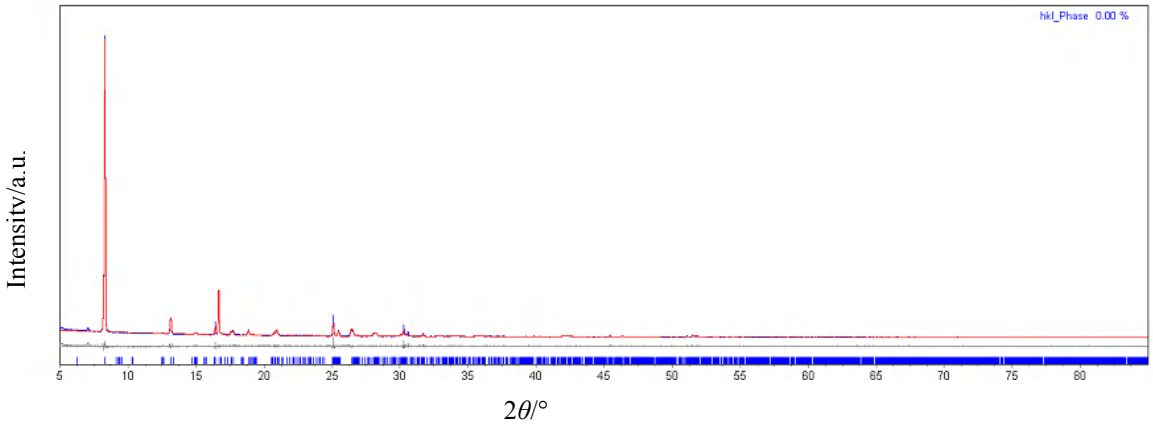

Figure 5.15. Compared experimental diffraction pattern (blue line) and cell parameters refinement pattern (red line) for compound **(20)**.

Table 5.10. Lattice parameters for compound **(20)** determined using powder X-ray diffraction data.

Unit cell parameters	**(20)**
a/Å	10.790(1)
b/Å	18.821(2)
c/Å	21.255(1)

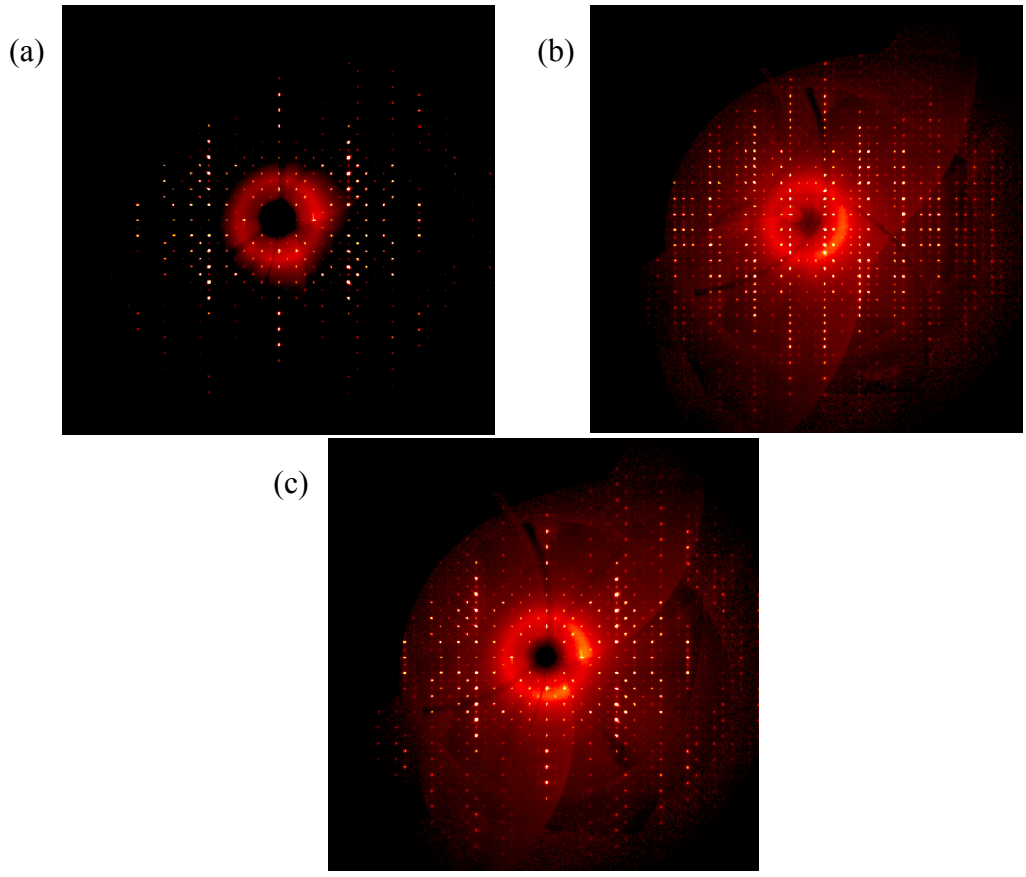

Figure 5.16. Precession images for data set of compound **(20)**: (a) (000) plane, (b) (100) plane and (c) (010) plane.

5.3.3. Elemental analysis and TGA

CHN analysis indicates a composition of: C: 26.55%, H: 5.50%, N: 9.95%, which is in reasonable agreement with theoretical values (C: 24.90%, H: 4.35%, N: 9.68%). Thermogravimetric data (Figure 5.17) indicates that the decomposition takes place in one step. The compound is stable up to *ca.* 650 K, with a steep loss of weight up to *ca.* 700 K followed by a gentler loss of weight up to 900 K. At this final temperature the compound has a total weight loss of *ca.* 40.97%, which is slightly different to the expected value the removal of organic material (*ca.* 38.93 %). Powder X-ray diffraction analysis indicated that the compound became amorphous after the decomposition.

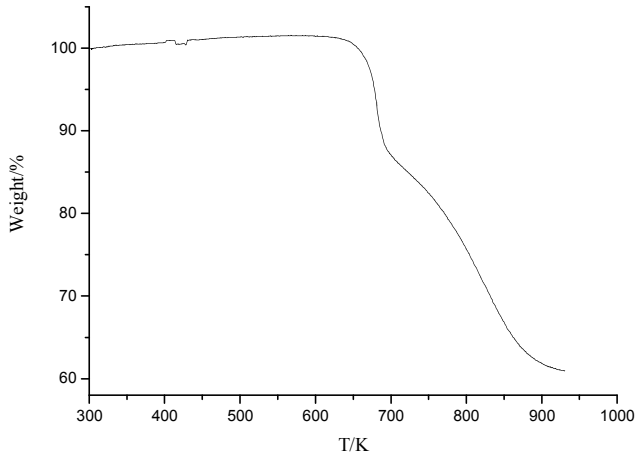

Figure 5.17. Thermogravimetric analysis of compound **(20)**.

5.3.4. FTIR.

Infrared data (Appendix III) exhibit bands corresponding to the vibrations of 1,2-DACH molecules. The vibrational modes and their frequencies are given in Table 5.11. Characteristic bands for protonated primary amines can be observed here. These results are similar to those found in other related compounds [226,191].

Table 5.11. Selected bands (values in cm^{-1}) for compound **(20)**. υ = stretching, δ = deformation; s = strong, m = medium, w = weak.

Assignment	**(20)**
υ (N-H)	3188.0 (s)
υ (C-H)	2937.9 (m)
υ (N-H)	1555.6 (s)-1449.5 (m)
δ (C-H)	1144.3 (m)-1050.6 (w)

5.3.5. Diffuse Reflectance

Analysis of the UV-VIS diffuse reflectance data (Figure 5.18) for **(20)** resulted in a band gap value of 4.4(1) eV, revealing its semiconducting nature. This value is higher than the values obtained for three-dimensional gallium-sulphides (4.0 eV) (see Section 3.4) Ga_2S_3 (3.31 eV) [192] and it is consistent with an expected blue shift due to quantum confinement effects observed in metal chalcogenides containing inorganic layers and organic components [231,232].

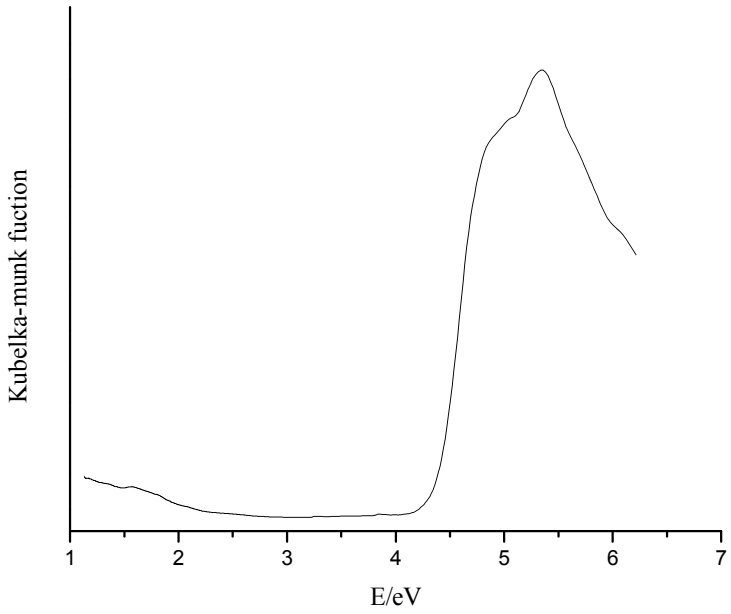

Figure 5.18. Diffuse reflectance for **(20)**.

5.3.6. Discussion

The space group determination for the data set of compound **(20)** using XPREP [179] did not provide an effective space group to obtain a significant crystal structure model. Analysis of the systematic absences (Table 5.12) and Friedel opposites were combined before calculating R(sym) manually. Therefore, the space group was input manually. There were two possible space groups (*Pnn2* and *Pnna*), which present the lowest CSD frequency and the higher number of reflection merged. Additionally, attempts were carried out to solve the crystal structure in *Pbca* and the lower symmetry monoclinic $P2_1/n$ space groups but these gave poor quality solutions (R>30 %). Only by applying the symmetry operations of *Pnna* was a chemically meaningful structure model with acceptable *R* values obtained. However, a detailed examination of these data revealed a large number of intense (*0kl*) and (*h0l*) reflections, which violate the $k+l$=2n and $h+l$=2n conditions for the *n* glide plane of this space group.

Table 5.12. Systematic absences exceptions which violate the translational symmetry element for diffraction symmetry *mmm* in the data set of compound **(20)**.

	b--	c--	n--	2_1--	-c-	-a-	-n-	-2_1-	--a	--b	--n	--2_1
N	2802	2796	2810	37	1517	1530	1557	78	1271	1265	1258	110
N I>3S	1092	1180	360	1	520	503	21	0	289	522	522	1
<I>	4.2	4.5	0.8	0.2	5.1	5.0	0.3	0.1	1.2	4.4	4.4	0.4
<I/S>	4.9	5.4	1.5	0.7	6.1	5.9	0.6	0.5	2.3	6.2	6.3	0.8

High thermal displacement parameters for the amine molecules mono-coordinated to Ga were found in the model. Constraints and restraints were applied to model the disorder and Fourier maps were checked for potential disordered positions but modelling there made no further improvement.

Consideration of twinning using Cell_now and Saint Plus [179] did not improve the model. Taking into account that compound **(20)** presents a layered structure; stacking faults were considered responsible for the violation of systematic absences described above. This phenomenon takes place when laminar structures present a lack of order in the stacking sequence of each layer. There are usually two or more geometrically and energetically comparable ways in which the packing can take place. As a consequence, the possible planes in which the layers are oriented produce an incoherent sum of the diffraction patterns and the presence of systematic absences that do not correspond to any of the 230 crystallographic space groups are common in the final diffraction data set. To study this phenomenon diffuse scattering experiments are required and several methods are applicable in the literature to calculate the diffraction intensities for crystals with planar faults [233]. Such studies were carried out on two-dimensional supertetrahedral gallium chalcogenides [26], using the summed series formula of Cowley [234-236]. For example, it was determined the stacking fault in $KGaTe_2$ by 0.25 (a-b) or 0.25 (a+b) relative to the ideal position. However, synthetic precession images of the data set do not present evidence of diffuse scattering or streaking spots (Figure 5.16).

Efforts were then focused on indexing of the experimental powder X-ray diffraction pattern to determine a different unit cell. However, no alternative space group or cell parameters were suggested. Refinement of the proposed cell parameters was carried out and only slight differences were found, which were not sufficiently significant to indicate an alternative unit cell (Figure 5.15, Table 5.10).

These unsuccessful attempts point out to a possible distortion of the structure which cannot be identified through the available equipment and software. Alternative

options to obtain a better structural model would consist on the use of synchrotron radiation, that could help to increase the quality of the data and identify reflections of low intensity and therefore, to determine the real unit cell and give a better model.

Inorganic metal-chalcogenide compounds are frequently found as two-dimensional structures. Layered structures such [(trans-1,4-$C_6N_2H_{15}$)Sb_3S_5] [144], [$(C_6N_2H_{18})_{0.5}Cu_2SbS_3$] or [$(C_4N_3H_{14})Cu_3Sb_2S_5$] [141], [$(H_3N(CH_2)_4NH_3)Sb_4S_7$] [237], produced under solvothermal conditions and using amines as templates, have been described. These structures consist of sandwich-like stacks of a single inorganic layer of antimony sulphide or cupper antimony sulphide and organic layer formed by protonated amines. This topology is common to phyllosilicates such as micas where the layers are compensated by inorganic cations. Compounds containing corner-sharing adamantine units [76] are also well known where counter cations are separated by inorganic layers.

However, gallium chalcogenides are capable of building hybrid two-dimensional structures based on tetrahedral units. To date, two compounds have been reported. They present analogous layers $[Ga_4Q_7(en)_2]^{2-}$ (Q= S or Se) [129,145] (see section 1.4.2). Ethylenediamine (en) molecules act as ligands by coordinating one of the N atoms to Ga and as also counter cations. Layers are constituted of alternating GaQ_4 and GaQ_3N tetrahedra, which share corners forming sheets constituted of eight-member and three-member rings of tetrahedra. Additionally, the layers are negatively charged and the balance is compensated by protonated en cations placed between the layers. The structure of compound **(20)** is similar to those. However, the layers contained in this structure are neutral and there are not separate organic moieties between the sheets. To the best of my knowledge this is a feature which has never been reported before for solvothermally-prepared gallium-sulphides.

The amine is incorporated via covalent bonding instead of as a counter-ion, and only van der Waals' interactions between 1, 2-DACH molecules stabilize the structure. Previously, a neutral discrete hybrid supertetrahedral cluster was published [$Ga_4S_6(NC_9H_{15}N_2)$] [56], but this is the first time that a neutral hybrid 2-dimensional gallium sulphide open framework has been described.

The chelating effect of the template, such as pyridine derivatives in supertetrahedral structures (see section 1.3.1) and primary amines, with gallium in chalcogenide compounds represents a new approach in inorganic-organic framework materials, which are usually based on the coordination properties of transition and rare earth metals [107]. The template assumes as new function in addition to the role of

template frequently associated with these species [41]. Now it has been shown to function as a ligand which has potential for developing novel materials.

Metal chalcogenide layers are potential materials for optoelectronic and optical devices (visible region) [238-241] and possible starting precursors for the production of nanomaterials. The insertion of divalent transition metals in the preparation of **(20)** was carried out in an attempt to improve optical and electrical properties and to study the influence of divalent metals on the synthesis. In supertetrahedral gallium-sulphide synthesis (see section 3.3), the insertion of divalent transition metals resulted in the production of T4 clusters and a decrease of their band gap values with respect to compounds without divalent metals. A related layered compound to those reported by Vaqueiro [129] and Dong [145] was obtained with Zn^{2+} and Sn^{4+} [242]. The insertion of divalent cations (such as Zn^{2+}) and tetravalent cations (such as Sn^{4+}) could produce equivalent structures than those formed by trivalent cations (such as Ga^{3+}) with lower band gaps depending on the nature of the cations employed. Therefore, it could be possible to tune metal-chalcogenides by the mixture of other cations with different valences. Changing the composition of these types of structures, it would improve the optical properties.

Experiments adding transition metals such as Co and Ni in the reaction that produces compound **(20)** show that these transition metals improve the crystal growth and the yield reaction. However, analogous structures containing those metals or mixed of cations were not produced so far.

Chapter 6: Conclusions and Further work

6.1. Conclusions

In this thesis the chemistry of gallium-sulphide compounds, which were relatively unexplored, has been developed. Gallium-sulphides are mainly produced as modular solids under solvothermal conditions, in a similar manner to other reported metal chalcogenides from the *p*-block such as Ge, In and Sn; which exhibit supertetrahedral clusters. These clusters are secondary building units and tend to build up extended structures such as three-dimensional frameworks which exhibit microporosity. To date, only a few three-dimensional supertetrahedral gallium-sulphide structures have been reported [103].

Three-dimensional inorganic gallium-sulphide supertetrahedral frameworks produced as part of this work are summarised in Chapter 3. These frameworks are analogous to previously reported structures [103]. The synthesis consisted of combining elemental gallium and sulphur with different primary and secondary amines employed as solvent/template. Diethylamine (DEA) proved an effective solvent/template capable of producing structures containing different units using the same reagents, but under different reaction conditions (see compounds $[C_4H_{12}N]_6[Ga_{10}S_{18}]$ **(1)** and $[C_4H_{12}N]_{12}[Ga_{20}S_{35.5}(S_3)_{0.5}O]$ **(2)**. When transition metals are inserted in the synthesis, it is feasible to produce structures containing larger clusters (T4 clusters) (see compounds $[C_4H_{12}N]_{16}[Ga_{10}S_{18}Zn_4Ga_{16}S_{33}]$ **(3)** and $[C_4H_{12}N]_{16}[Ga_{10}S_{18}Co_4Ga_{16}S_{33}]$ **(4)**). The incorporation of other chalcogenides is also possible as it is shown in compound **(2)**, where T3 clusters are connected sharing O atoms. Additionally, it is observed that disulphur bridges can act as linkers between clusters.

The double diamond lattice was found to be the most common framework in this type of material. Optical investigations reveal the semiconducting nature of those materials, a consequence of the interactions between Ga and S orbitals. The insertion of transition metals into gallium-sulphide clusters introduces extra band levels and the band gaps corresponding to these materials (compounds **(3)** and **(4)**), are red-shifted in comparison with pure supertetrahedral clusters containing only gallium and sulphur, compounds **(1)** and **(2)**. Ion-exchange experiments were carried out in an analogous structure of **(2),** $[TEPAH^+]_6$ $[Ga_{10}S_{16.5}(S_3)_{0.5}O]$ **(2.b)**. The results indicate that this type of structure shows an extraordinary flexibility and the framework exhibits a high

selectivity in the exchange for NH_4^+ when compared to alkali metal cations such as K^+, Cs^+ or Na^+.

Hybrid supertetrahedral clusters were extensively produced with metal chalcogenides from group 12 metals (Zn and Cd). The materials were synthesised using thiolates as the ligand agent and source of sulphur, and resulted in tetrahedral clusters being formed by an inorganic core of the metal chalcogenide shielded by the organic ligands. Additionally, other hybrid materials were produced combining thiolates and polydentate pyridine ligands, which successfully produced extended structures where pyridine ligands were coordinated on the vertices of the tetrahedral clusters connecting with other tetrahedral clusters. The only supertetrahedral gallium-sulphide known to date consisted of a T2 cluster, where the four sulphur atoms in the vertexes were substituted by pyridine ligands [56] and the clusters co-crystallised with the solvent forming a covalent crystal. The development of hybrid material based on clusters covalently bonded to amines has been explored for the first time for gallium-sulphides in this work and summarised in Chapter 4. These materials could combine inorganic and organic properties. The Ga-S-Ga angles in extended structures are usually more rigid than other inorganic compounds. As a consequence, the number of inorganic structures is constrained. The insertion of organic entities acting as linkers usually results in more flexible structures. The synthesis of hybrid supertetrahedral gallium-sulphides structures is achieved under solvothermal conditions using pyridine derivates as solvents and templates, and elemental sulphur and gallium. The hybrid clusters consist of T3 gallium-sulphide supertetrahedra where the four terminal S atoms in the vertexes are substituted by N-covalently bonded pyridyl ligands (L), forming hybrid clusters of general stoichiometry $[Ga_{10}S_{16}L_4]^{4-}$.

Lutidine, 4-picoline and pyridine are effective solvents/templates for the synthesis of discrete hybrid clusters (see compounds: $[C_7H_{10}N]_2[Ga_{10}S_{18}(NC_7H_9)_4]$ **(5)**, $[C_4H_{12}N_2][C_7H_{10}N]_2[Ga_{10}S_{18}(NC_7H_9)_4]$ **(6)**, $[C_{12}H_{12}N_2]_2[C_{12}H_{14}N_2]_2[C_6H_7N]_6[Ga_{10}S_{16}(NC_6H_7)_4]_4$ **(7),** $[C_6H_8N]_2[Ga_{10}S_{16}(NC_6H_7)_4]$ **(8)**, $[C_{24}H_{20}P][C_6H_8N][Ga_{10}S_{16}(NC_6H_7)_4]$ **(9)**). Effective ligands can be associated with an approximate p$K_a \approx 6$. The position of the substituents in the pyridyl rings also affects the coordination to Ga. Ditopic ligands were used in the synthesis to produce extended structures. However, due to the physical characteristic of these materials, lutidine and 4-picoline were employed as solvents. The mixture of templates produces multi-functionalised clusters because the species compete to coordinate gallium. It has been observed that monotopic ligands are usually present in the structures as counter-

cations and ligands while the ditopic ligands are only observed acting as ligands. Therefore, the ditopic ligands can act as mono- and bidentate ligands. Clusters can be connected by one ligand forming dimeric species such as those contained in compounds $[C_7H_{10}N]_6[Ga_{20}S_{34}H_2(NC_7H_9)_4(N_2C_{12}H_{10})]$ **(10)**, $[C_6H_8N]_2[Ga_{20}S_{32}(N_2C_{12}H_{12})(NC_{12}H_{13}N)_2(NC_6H_7)_4]$ **(11)** or $[C_7H_{10}N]_6[Ga_{10}S_{16}(NC_7H_9)(N_2C_{10}H_8)_3][Ga_{20}S_{32}(NH_3)_2(NC_6H_7)_4(N_2C_{10}H_8)]$ **(12)** and extended structures containing infinite chains (see compounds $[C_6H_8N]_2[Ga_{10}S_{16}(NC_6H_7)_2(N_2C_{12}H_{12})]$ **(13)**, $[C_2H_8N]_2[Ga_{10}S_{16}(N_2C_{12}H_{12})(NC_2H_7)_2]$ **(14)** and $[C_5H_6N]_4[C_6H_8N]_4[Ga_{10}S_{16}(NC_6H_7)_2(N_2C_{12}H_{12})][Ga_{10}S_{16}(N_2C_{12}H_{10})_{1/2}(NC_6H_7)_3]$ **(15)**) and two-dimensional layers (see compounds $[C_7H_{10}N]_2[Ga_{10}S_{16}(NC_7H_9)(N_2C_{12}H_{10})_{3/2}]$ **(16)** and $[C_5H_6N]_3[Ga_{10}S_{16}(OH)(N_2C_{13}H_{14})]$ **(17)**). These extended structures can form complex and novel super-structures, such as the super β-helices $[Ga_{10}S_{16}(N_2C_{12}H_{12})(NC_2H_7)_2]^{2-}$ in **(14)**, which is one of the few examples of superchains constituted by four left-handed chains of supertetrahedra presenting chirality. Honey comb layers $[Ga_{10}S_{16}(NC_7H_9)(N_2C_{12}H_{10})_{3/2}]^{2-}$ in **(16)**, which form a net of channels of an approximate diameter of 3 Å and it has also been observed interpenetrated square grid layers $[Ga_{10}S_{16}(OH)(N_2C_{13}H_{14})]^{3-}$ in **(17)**, which are formed by chains of gallium-sulphide supertetrahedra sharing OH anions and connected by organic linkers. The formation of multi-functionalised clusters also indicates that the structure of the clusters and the organic ligands can be tuned to optimize desirable properties, by extending the range of connectivity and architectures. It has been demonstrated that several supertetrahedral species can coexist in solution under solvothermal conditions. These can co-crystallize, producing crystals containing two types of anions, such those found in **(12)** which contains $[Ga_{10}S_{16}(NC_7H_9)(N_2C_{10}H_8)_3]^{2-}$ discrete and $[Ga_{20}S_{32}(NH_3)_2(NC_6H_7)_4(N_2C_{10}H_8)]^{4-}$ dimeric anions or in **(15)**, where $[Ga_{10}S_{16}(NC_6H_7)_2(N_2C_{12}H_{12})]^{2-}$ dimeric units are alternated with $[Ga_{10}S_{16}(N_2C_{12}H_{10})_{1/2}(NC_6H_7)_3]^{2-}$ supertetrahedral one-dimensional chains.

The use of different amines such as second templates along with pyridyl ligands can result in structures containing the second template as counter-cations, as for example structures **(6)** or **(9)**, or favoring the synthesis of completely new structures, as was observed when the compounds **(7)** and **(8)** were compared.

Like supertetrahedral gallium-sulphide structures, hybrid functionalised supertetrahedral gallium-sulphide compounds also exhibit semiconducting properties. The semiconducting band system is produced by Ga and S orbitals, although N atoms introduce additional bands, which could be associated with the red-shifting of the band

gap values. Moreover, the optical and electronic properties in supertetrahedral structures could be attributed to interaction at the microscopic level between the organic and inorganic components in hybrid clusters. It was found that hybrid clusters of the same type of units (discrete clusters, dimeric unit, etc.) present large differences in the band gap values, depending on the functional group and the presence of organic molecules acting as counter cations. This effect is attributed to the non-equivalent environments of the supertetrahedral clusters; in other words no all the clusters are chemically equivalent. The presence of more than one type of counter-cation produces different interactions with each cluster the contribution to the band gap from each cluster turns on small changes in the energy levels. As a consequence, the ideal band gap value is not constant and the diffuse reflectance spectra can show transitions shifted to lower values. The shift in the band gap can also be associated with a lower symmetry as for example in compound **(7)** or the presence of different type of supertetrahedral anions as in compounds **(12)** and **(15)**. Additionally, the facility of charge-transfer processes between the organic components can shift the band gap values to low ranges in the UV-VIS spectrum and mask the real value of the band gap, for example in the case of compound **(9)**.

It is also demonstrated through this research, that under solvothermal conditions, slight changes in the reaction conditions yield different products. The reactivity increases mainly to the organic fraction, where dimerisation, hydrogenation and electrofilic/nucleofilic addition processes occur. The result of these reactions is the formation *in situ* of ligands that form part of the structure or potential ligands (see compound **(7)**) and the compounds described in Appendix V. The latter are a series of organic materials which were unexpectedly synthesised during the progress of the experimental part of this thesis. Some of them are potential molecules that can be use as ligand in the synthesis of hybrid cluster. This indicates that it is possible to synthesise *in situ* ligands to produce hybrid supertetrahedral structures.

Other gallium-sulphide structures obtained with primary and secondary amines under solvothermal conditions are one-dimensional chains, compounds $[C_4H_{11}N_2][GaS_2]$ **(18)** and $[C_6H_{16}N_2][GaS_2]_2$ **(19)**. Chains consist of GaS_4 tetrahedra sharing edges, which are separated by protonated amines. The orientation and packing of the chains is influenced by a number of factors such as hydrogen bonding between the counter cations, as well as between the counter cations and the chains. Additionally, the hybrid compound $[Ga_6S_9(N_2C_6H_{14})_2(NC_6H_{14}N)_2$ **(20)** consists of hybrid gallium-sulphide layers. In this case 1,2-DACH acts as a mono- and a bidentate ligand and the

layers consist of alternating GaS_4, GaS_3N and GaS_2N_2 tetrahedra. As a result, the layers are neutral and the stability of the structure is achieved by van der Waals interactions between the layers.

The conclusions cited above suggest that the gallium-sulphides system is still a source of novel materials, whose structure and properties can be tuned depending on ligands/template employed.

6.2. Further work

The compounds presented in this thesis are fully characterised, although it would be interesting to further study their fluorescence properties, similar to those carried out in other supertetrahedral materials [199].

Further efforts in the design of new materials based on gallium chalcogenides could be directed towards the preparation of non-interpenetrating structures, materials containing larger clusters and hybrid clusters; focusing in the reduction of the band gap and increasing the microporous size. A few strategies could be considered for the synthesis of novel tetrahedral gallium sulphides:

- Three-dimensional supertetrahedral structures may be produced using a suitable template to avoid interpenetration. These species are though to be able to fulfill the cavities produced. For this purpose, a combination of templates could be used, where one of the templates acts as directing agent and the other one acts as space filler.
- The use of optically active templates, which are believed to interact with the inorganic gallium-sulphide framework, reducing the band gap.
- Use of multi-topic ligands, to produce covalent organic-inorganic frameworks.
- Use of other ternary amines contained in conjugated systems as potential ligands, such as imidazol derivates. In a similar approach to produce metal organic frameworks succeed forming zeolitic imidazolate frameworks (ZIF) [311-313]. These compounds mimic the zeolitic angles through N-center-N bonds via the imidazol molecules.
- Preparation of ligands in situ. Ligands can be formed during the reaction process and form part of the structures. Additionally in Appendix V, the synthesis of a few organic compounds, which could act as potential ligands, was described.
- Insertion of metal cations into the structure, in order to produce larger clusters and reduce the band gap values.

- To explore other hybrid supertetrahedral systems using gallium chalcogenides (selenium or tellurium) or mixtures of chalcogenides. This could lead to the synthesis of hybrid supertetrahedral clusters exhibiting lower band gap values.

Solvothermally prepared gallium sulphides still hold large potential to produce structures exhibiting interesting physical and electric properties. These properties can be tuned using organic templates, providing an alternative to traditional inorganic framework structures.

References

[1] J. K. Lilienfield, **US patent 1745175**, (1925).

[2] C. Michael, B. Raveau, *Rev. Chim. Miner.*, **21**, 407-425 (1984).

[3] J. G. Bednorz, K. A. Müller, *Z. Physik B*, **64**, 189-193 (1986).

[4] M. G. Kanatzidis, K. R. Popelmeir, *Progress in solid state chemistry*, **36**, 1-133 (2007).

[5] A. J. Karkamkar, M. G. Kanatzidis, *J. Am. Chem. Soc.*, **128**, 6002-6003 (2006).

[6] R. E. Schaak, A. K. Sra, B. M. Leonard, R. E. Cable, J. C. Bauer, Y.-F. Han, J. Means, W. Teizer, Y. Vasquez, E. S. Funck, *J. Am. Chem. Soc.*, **127**, 3506-3515 (2005).

[7] X. Huang, J. Li, A. Mascarenhas, *J. Am. Chem. Soc.*, **125**, 7049-7055 (2003).

[8] P. A. Wright, *'Microporous frameworks solids'*, RCS materials monograph (2008).

[9] W. M. Meier, D. H. Olson, C. Baerlocher, Butterworth: London (1996).

[10] R. E. Morris, S. J. Weigel, *Chem. Soc. Rev.*, **26**, 309-317 (1997).

[11] P. J. Hagrman, D. Hagrman, J. Zubieta, *Angew. Chem. Int. Ed.*, **38**, 2638-2684 (1999).

[12] R. L. Berard, S. T. Wilson, L. D. Vail, J. M. Bennet, E. M. Flanigen, *Stud. Surf. Sci. Catal. A*, **49**, 375-387 (1989).

[13] D. Maspoch, D. Ruiz-Molina, J. Veciana, *Chem. Soc. Rev.*, **36**, 770-818 (2007).

[14] G. Férey, *Angew. Chem. Int. Ed.*, **42**, 2576-2579 (2003).

[15] O. M. Yaghi, H. Li, C. Davis, D. Richardson, T. L. Groy, *Acc. Chem. Res.*, **31**, 474-484 (1998).

[16] J. Gopalakrishnan, *Chem. Mater.*, **7**, 1265-1275 (1995).

[17] B. Krebs, *Angew. Chem. Ed. Engl.*, **22**, 113-134 (1983).

[18] G. Férey, *Chem. Mater.*, **13**, 3084-3098 (2001).

[19] R. I. Walton, F. Millange, T. Louiseau, D. O'Hare, G. Ferey, *Angew. Chem. Int. Ed.*, **39**, 4552-4555 (2000).

[20] R. I. Walton, F. Millange, D. O'Hare, T. Loiseau, C. Paulet, G. Férey, *Chem. Mater.*, **12**, 1977-1984 (2000).

[21] H. Dan, C. N. R. Rao, *Angew. Chem. Int. Ed.*, **45**, 281-285 (2006).

[22] B. Jandeleit, D. J. Schaefer, T. S. Powers, H. W. Turner, W. H. Weinberg, *Angew. Chem. Int. Ed.*, **38**, 2494-2535 (1999).

[23] X.-D. Xiang, P. G. Schiltz, *Physica C*, 282-287 (1998).

[24] G. Briceno, H. Chang, X.-D. Sun, P. G. Schultz, X. D. Xiang, *Science*, **270**, 273-275 (1995).

[25] J. J. Hanak, *J. Vac. Sci. Technol.*, **8**, 172-175 (1991).

[26] H. Chang, C. Gao, I. Takeuchi, Y. Yoo, J. Wang, P. G. Schultz, X.-D. Xiang, R. P. Sharma, M. Downes, T. Venkatesan, *Appl. Phys. Lett.*, **73**, 1820-1822 (1998).

[27] D. E. Akoporiaye, I. M. Dahl, A. Karlsson, R. Wendelbo, *Angew. Chem. Int. Ed.*, **37**, 609-611 (1998).

[28] J. Klein, C. W. Lehmann, H.-W. Schmidt, W. F. Maier, *Angew. Chem. Int. Ed.*, **37**, 3369-3372 (1998).

[29] D. W. Breck, E. M. Flanigem, *Molecular Sieves Soc. Chem.*, 47 (1968).

[30] R. M. Barrer, J. W. Baynham, F. W. Bultitude, W. M. Meier, *J. Chem. Soc.*, 195-195 (1959).

[31] S. P. Zhdanov, *Adv. Chem. Ser.*, **101**, 20-43 (1971).

[32] M. E. David, R. F. Lobo, *Chem.Mater.*, **4**, 756-768 (1992).

[33] G. Férey, *J. Fluorine Chem.*, **72**, 187-193 (1998).

[34] F. Taulelle, M. Haouas, C. Gerardin, C. Estournes, T. Loiseau, G. Férey, *Colloids Surf.*, **158**, 299-311 (1999).

[35] C. Gerardin, M. Haouas, F. Lorentz, F. Taulelle, *Magnetic Resonance Chem.*, **38**, 429-435 (2000).

[36] J. Shi, M. W. Anderson, S. W. Carr, *Chem. Mater.*, **8**, 369-375 (1996).

[37] R. I. Walton, D. O'Hare, *Chem. Comm.*, 2283-2292 (2000).

[38] M. J. Zaworotko, *Nature*, **402**, 242-243 (1999).

[39] M. O'Keeffe, M. Eddaoudi, H. Li, R. T, O. M. Yaghi, *J. Solid State Chem.*, **152**, 3-20 (2000).

[40] S. R. Batten, R. Robson, *Angew. Chem. Int. Ed.*, **37**, 1461-1494 (1998).

[41] P. Feng, X. Bu, N. Feng, *Acc. Chem. Res.*, **38**, 293-303 (2005).

[42] I. D. Brown, *J. Appl. Crystallogr.*, **29**, 479-480 (1996).

[43] C. Wang, X. Bu, Z. Zheng, P. Feng, *J. Am. Chem. Soc.*, **124**, 10268-10269 (2002).

[44] H. Li, J. Kim, M. O'Keeffe, O. M. Yaghi, *Angew. Chem. Int. Ed.*, **42**, 1819-1821 (2003).

[45] H. Ahari, A. Lough, S. Petrov, G. A. Ozin, R. L. Berard, *J. Mater. Chem.,*, **9**, 1263-1274 (1999).

[46] J. B. Parise, Y. Ko, *Chem. Mater.*, **6**, 718-720 (1994).

[47] P. Feng, X. Bu, G. D. Stucky, *Nature*, **388**, 735-741 (1997).

[48] O. Palchik, R. G. Iyer, J. H. Liao, M. G. Kanatzidis, *Inorg. Chem.*, **42**, 5052-5054 (2003).

[49] N. Zheng, X. Bu, P. Feng, *Angew. Chem. Int. Ed.*, **43**, 4753-4755 (2004).

[50] I. G. Dance, *J. Am. Chem. Soc.*, **101**, 6264-6273 (1979).

[51] A. Choy, D. Craig, I. G. Dance, M. Scudder, *J. Chem. Soc., Chem. Comm.*, 1246-1247 (1982).

[52] K. S. Hagen, J. M. Berg, R. H. Holm, *Inorg. Chim. Acta*, **45**, L17 (1980).

[53] J. Xie, X. Bu, N. Zheng, P. Feng, *Chem. Comm.*, 4916-4918 (2005).

[54] S. Behrens, M. Bettenhausen, A. C. Devenson, A. Eichöfer, D. Fenske, A. lohde, U. Woggon, *Angew. Chem. Int. Ed. Engl.*, **35**, 2215-2218 (1996).

[55] M. Williams, R. M. Okasha, J. Naim, B. Twanley, T. H. Afifi, P. J. Shapiro, *Chem. Comm.*, 3177-3179 (2007).

[56] H. Schimdbaur, S. D. Nogai, *Z. Anorg. Allg. Chem.*, **630**, 2218-2225 (2002).

[57] Q. Zhang, T. Wu, X. Bu, T. Tran, P. Feng, *Chem. Comm.*, **20**, 4170-4172 (2008).

[58] G. S. H. Lee, D. C. Craig, I. Ma, M. I. Scudder, T. D. Bailey, I. G. Dance, *J. Am. Chem. Soc.*, **110**, 4863-4864 (1988).

[59] N. Zheng, X. Bu, H. Lu, Q. Zhang, P. Feng, *J. Am. Chem. Soc.*, **127**, 11963-11965 (2005).

[60] N. Zheng, X. Bu, J. Lauda, P. Feng, *Chem. Mater.*, **18**, 4307-4311 (2006).

[61] W. S. Sheldrick, *J. Chem. Soc., Dalton Trans.*, 3041-3052 (2000).

[62] J. K. Burdett, *Chem. Rev.*, **88**, 3-30 (1988).

[63] B. Krebs, D. Voelker, K. Stiller, *Inorganica Chemica Acta*, **65**, 101-102 (1982).

[64] W. Schiwy, S. Pohl, B. Krebs, *Z. Anorg. Allg. Chem.*, **402**, 77-86 (1973).

[65] S. Pohl, W. Schiwy, N. Weinstock, B. Krebs, *Z. Naturforsch. B*, **28**, 565-569 (1973).

[66] B. Krebs, H.-J. Jacobsen, *Z. Anorg. Allg. Chem.*, **421**, 97-104 (1976).

[67] B. Krebs, H.-U. Hürter, *Z. Anog. Allg. Chem.*, **462**, 143-151 (1980).

[68] B. Krebs, S. Pohl, *Z. Naturforsch. B*, **26**, 853-853 (1971).

[69] W. Schiwy, B. Krebs, *Angew. Chem. Int. Ed. Engl.*, **14**, 436 (1975).

[70] H.-J. Wallstab, Universität Bielefeld (1979).

[71] C. L. Cahill, J. B. Parise, *J. Chem. Soc., Dalton Trans.*, 1475-1482 (2000).

[72] C. Zimmermann, M. Melullis, S. Dehnen, *Angew. Chem. Int. Ed.*, **41**, 4269-4272 (2002).

[73] S. Dehnen, M. K. Bradmayer, *J. Am. Chem. Soc.*, **125**, 6618-6619 (2003).

[74] F. Bonhomme, M. G. Kanatzidis, *Chem. Mater.*, **10**, 1153-1159 (1998).

[75] B. Eisenmann, A. Hoffmann, *Z. fuer Kristallogr.*, **197**, 171-172 (1991).

[76] P. Lemoine, D. Carré, M. Guittard, *Acta Cryst. C*, **40**, 910-912 (1984).

[77] A. Kumari, K. Vidyasagar, *Acta Cryst. E*, i193-i195 (2005).

[78] J. Kim, T. Hughbanks, *J. Solid State Chem.*, **149**, 242-251 (2000).

[79] J. Zhou, Y. Zhang, G.-Q. Bian, C.-Y. Li, X.-X. Chen, J. Dai, *Crystal Growth & Design*, **8**, 2235-2240 (2008).

[80] X. Bu, N. Zheng, Y. Li, P. Feng, *J. Am. Chem. Soc.*, **124**, 12646-12647 (2002).

[81] W. Su, X. Huang, J. Li, H. Fu, *J. Am. Chem. Soc.*, **124**, 12944-12945 (2002).

[82] D. Pitzschke, C. Näther, W. Bensch, *Solid State Sciences*, **4**, 1167-1171 (2002).

[83] Q. Zhang, X. Bu, L. Han, P. Feng, *Inorg. Chem.*, **45**, 6684-6687 (2006).

[84] X. Bu, N. Zheng, X. Wang, B. Wang, P. Feng, *Angew. Chem. Int. Ed.*, **43**, 1502-1505 (2004).

[85] X. Bu, N. Zheng, Y. Li, P. Feng, *J. Am. Chem. Soc.*, **125**, 6024-6025 (2003).

[86] C. Wang, Y. Li, X. Bu, N. Zheng, O. Zivkoviv, C.-S. Yang, P. Feng, *J. Am. Chem. Soc.*, **123**, 11506-11507 (2001).

[87] W. Sum, X. Huang, J. Li, X. Fu, *J. Chem. Soc.*, **124**, 12944-12945 (2002).

[88] M. O'Keeffe, B. G. Hyde, Washington, DC (1996).

[89] S. Hansen, *Nature*, **346**, 799-800 (1990).

[90] H. Li, M. Eddaoudi, A. Laine, M. O'Keeffe, O. M. Yaghi, *J. Am. Chem. Soc.*, **121**, 6096-6097 (1999).

[91] D. Pitzschke, W. Bensch, *Z. Anorg. Allg. Chem.*, **639**, 2206-2210 (2003).

[92] H. Li, J. Kim, T. L. Groy, M. O'Keeffe, O. M. Yaghi, *J. Am. Chem. Soc.*, **123**, 4867-4868 (2001).

[93] H. Li, A. Laine, M. O'Keeffe, O. M. Yaghi, *Science*, **283**, 1145-1147 (1999).

[94] N. Zheng, X. Bu, B. Wang, P. Feng, *Science*, **298**, 2366-2369 (2002).

[95] Y. Yakéuchi, N. Haga, J. Ito, *Z. Kristallogr.*, **137**, 380-398 (1973).

[96] N. Zheng, X. Bu, H. Vu, P. Feng, *Angew. Chem. Int. Ed.*, **44**, 5299-5303 (2005).

[97] C. L. Cahill, J. B. Parise, *Chem. Mater.*, **9**, 807-911 (1997).

[98] M. J. MacLachlan, N. Coombs, G. A. Ozin, *Nature*, **397**, 681-684 (1999).

[99] G. Férey, C. Mellot-Draznieks, C. Serre, F. Millange, *Acc. Chem. Res.*, **38**, 217-225 (2005).

[100] O. M. Yaghi, Z. Sum, D. A. Richardson, T. L. Groy, *J. Am. Chem. Soc.*, **116**, 807-808 (1994).

[101] C. L. Bowes, W. U. Huynh, S. J. Kirby, A. Malek, G. A. Ozin, S. Petrov, M. Twardowski, D. Young, R. L. Berard, R. Broach, *Chem. Mater.*, **8**, 2147-2152 (1996).

[102] C. Wang, X. Bu, N. Zheng, P. Feng, *Chem. Comm.*, 1344-1345 (2002).

[103] N. Zheng, X. Bu, P. Feng, *J. Am. Chem. Soc.*, **125**, 1138-1139 (2003).

[104] Z. Su, X. Li, Y. Lan, J. Wen, G. Jin, J. Xie, C. Zheng, J. Jin, S. Li, *Material letters*, **62**, 2802-2805 (2008).

[105] N. Zheng, X. Bu, P. Feng, *Nature*, **426**, 428-432 (2003).

[106] M. J. Manos, J. I. Jang, J. B. Ketterson, M. G. Kanatzidis, *Chem. Comm.*, 972-974 (2008).

[107] A. K. Cheetham, C. N. R. Rao, R. K. Feller, *Chem. Comm.*, 4780-4795 (2006).

[108] P. Chini, *J. Organomet. Chem.*, **200**, 37-61 (1980).

[109] B. F. G. Johnson, J. Lewis, *Adv. Inorg. Chem. Radiochem.*, **24**, 225- 355 (1981).

[110] M. H. Chrisholm, J. C. Hoffman, C. C. Kirkpatrik, J. Leonelli, K. Folting, *J. Am. Chem. Soc.*, **103**, 6093-6099 (1981).

[111] J. L. Hencher, M. Khanm, F. F. Said, D. G. Tuck, *Inorg. Chem.* , **21**, 2787-2791 (1982).

[112] W. Hirpo, S. Dhingra, A. C. Sutorik, M. G. Kanatzidis, *J. Am. Chem. Soc.*, **115**, 1597-1599 (1993).

[113] I. Num, B. Eisen, R. Benedix, H. Kish, *Inorg. Chem.*, **33**, 5079-5085 (1994).

[114] H. Kirsh, *Coord. Chem. Rev.*, **125**, 155-171 (1993).

[115] M. Hofbauer, M. Möbius, F. Knoch, R. Benedix, *Inorg. Chim. Acta*, **247**, 147-154 (1996).

[116] G. Xu, P. Guo, S. Song, H. Zhang, C. Wang, *Inorg. Chem.*, **46**, 4628-4630 (2009).

[117] Q. Zhang, I. Chung, J. I. Jang, J. B. Ketterson, M. G. Kanatzidis, *Chem. Mater.*, **21**, 12-14 (2009).

[118] T. Vossmeyer, G. Reck, L. Katsikas, E. T. K. Haupt, B. Schulz, *Science*, **267**, 1476-1480 (1995).

[119] N. Zheng, H. Lu, X. Bu, P. Feng, *J. Am. Chem. Soc.*, **128**, 4528-4529 (2006).

[120] Q. Zhang, Y. Liu, X. Bu, T. Wu, P. Feng, *Angew. Chem. Int. Ed.*, **47**, 1113-1116 (2008).

[121] Q. Zhang, Z. Lin, X. Bu, T. Wu, P. Feng, *Chem. Mater.*, **20**, 3239-3241 (2008).

[122] Q. Zhang, X. Bu, J. Zhang, T. Wu, P. Feng, *J. Am. Chem. Soc.*, **129**, 8412-8413 (2007).

[123] J. Zhou, J. Dai, G.-Q. Bian, C.-Y. Li, *Coord. Chem. Rev.*, in press (2008).

[124] J. Peters, B. Krebs, *Acta Cryst. B*, **38**, 1270-1272 (1982).

[125] W. Broger, A. Kyas, P. Muller, *J. Solid State Chem.*, **70**, 262-279 (1987).

[126] H.-J. Deiseroth, H. Fu-Son, *Angew. Chem. Int. Ed.*, **93**, 1011-1012 (1981).

[127] H. Schubert, R. Hoppe, *Z. Naturforsch. B*, **25**, 886-887 (1970).

[128] R. Hoppe, W. Lidecke, F.-C. Frorath, *Z. Anorg. Allg. Chem. B*, **309**, 49-54 (1961).

[129] P. Vaqueiro, *Inorg. Chem.*, **45**, 4150-4156 (2006).

[130] H.-O. Stephan, M. G. Kanatzidis, *Inorg. Chem.*, **36**, 6050-6057 (1997).

[131] D.-X. Jia, J. Dai, Q.-Y. Zhu, L.-H. Cao, H.-H. Lin, *J. Solid State Chem.*, **178**, 874-881 (2005).

[132] P. Vaqueiro, *J. Solid State Chem.*, **179**, 302-307 (2006).

[133] J. Zhou, Y. Zhang, G.-Q. Bian, C.-Y. Li, X.-X. Chen, J. Dai, *Crystal Growth & Design*, **8**, 2235-2238 (2008).

[134] C.-Y. Li, J. Zhou, G.-Q. Bian, M.-H. Zhang, J. Dai, *Inorg. Chem. Comm.*, **11**, 1327-1329 (2008).

[135] J. Zhou, G. v.-Q. Bian, Y. Zhang, Q.-Y. Zhu, C.-Y. Li, J. Dai, *Inorg. Chem.*, **46**, 6347-6352 (2007).

[136] J. Do, M. G. Kanatzidis, *Z. Anog. Allg. Chem.*, **629**, 621-624 (2003).

[137] M. S. Devi, K. Vidyasagar, *J. Chem. Soc., Dalton Trans.*, 4751-4754 (2002).

[138] O. Conrad, C. Jansen, B. Krebs, *Angew. Chem. Int. Ed.*, **37**, 3208-3218 (1998).

[139] A. Lindemann, J. Kuper, W. Hamann, J. Kuchinke, C. Koster, B. Krebs, *J. Solid State Chem.*, **157**, 206-212 (2001).

[140] P. Vaqueiro, A. M. Chippindale, A. R. Cowley, A. V. Powell, *Inorg. Chem.*, **42**, 7846-7851 (2003).

[141] V. Spetzler, C. Näther, W. Bensch, *Inorg. Chem.*, **44**, 5805-5812 (2005).

[142] Z.-X. Deng, L. Li, Y. Li, *Inorg. Chem.*, **42**, 2331-2341 (2003).

[143] W. Bensch, M. Schur, *Eur. J. Solid State Inorg. Chem.*, **33**, 1149-1160 (1996).

[144] L. Engelke, M. Schaefer, M. Schur, W. Bensch, *Chem. Mater.*, **13**, 1383-1390 (2001).

[145] Y. Dong, Q. Peng, R. Wang, Y. Li, *Inorg. Chem.*, **42**, 1794-1796 (2003).

[146] C. Wang, X. Bu, Z. Zheng, P. Feng, *Angew. Chem. Inter. Ed.* , **41**, 1959-1961 (2002).

[147] P. Vaqueiro, *Inorg. Chem.*, **47**, 20-21 (2008).

[148] N. Zheng, X. Bu, P. Feng, *J. Am. Chem. Soc.*, **127**, 5286-5287 (2005).

[149] M. J. Manos, C. D. Malliakas, M. G. Kanatzidis, *Chem. Eur. J.*, **13**, 51-58 (2007).

[150] A. P. Alivisatos, *J. Phys. Chem.*, **100**, 13226-13239 (1996).

[151] M. Fuentes-Cabrera, H. Wang, B. Daniels, O. F. Sankey, *Phys. Rev. B* **66**, 045109-1 045109-9 (2002).

[152] J. Do, M. G. Kanatzidis, *Z. Anorg. Allg. Chem.*, **629**, 621-624 (2008).

[153] M. Suseela, K. Vidasagar, *Dalton transaction*, 4751-4754 (2002).

[154] L. Zhang, W. Zhang, J. Shi, Z. Hwa, Y. Li, J. Yan, *Chem. Comm.*, 210-211 (2003).

[155] J. Liu, X. Feng, G. E. Fryxell, L. Q. Wang, A. Y. Kim, M. Gong, *Adv. Mater.*, **10**, 161-165 (1998).

[156] M. J. Manos, K. Chrissafis, M. G. Kanatzidis, *J. Am. Chem. Soc.*, **128**, 8875-8883 (2006).

[157] D. Brunel, P. Sutra, F. Fajula, *Stud. Surf. Sci. Catal.*, **129**, 773-780 (2000).

[158] R. Ryoo, I.-S. Park, S. Jun, C. W. Lee, M. Kruk, M. Jaronier, *J. Am. Chem. Soc.*, **123**, 1650-1657 (2001).

[159] M. Kruk, M. Jaroniec, *Chem. Mater.*, **12**, 222-230 (2000).

[160] P. Feng, X. Bu, N. Zheng, *Acc. Chem. Res.*, **38**, 293-303 (2004).

[161] C.-S. Yang, Y.-H. Su, Y.-J. Wang, J.-H. Cheng, X.-H. Lin, *Materials letters*, **62**, 4015-4017 (2008).

[162] C.-J. Chen, C.-S. Yang, X.-H. Lin, *Inorg. Chem. Comm.*, **8**, 836-840 (2005).

[163] F. E. Osterloh, *Chem. Mater.*, **20**, 35-54 (2008).

[164] M. Matsumura, S. Furukawa, Y. Saho, T. Hiroshi, *J. Phys. Chem.*, **89**, 1327-1329 (1985).

[165] R. A. Laudise, *Chem. Eng. News*, **65**, 30-43 (1987).

[166] G. Demazeau, *C.R. Acad. Sci. Paris, T.2, Serie II C*, 685-692 (1999).

[167] R. L. Bedard, S. T. Wilson, L. D. Vail, J. M. Bennett, E. M. Flanigen, Elsevier (1989).

[168] K. Choi, D. Gardner, N. Hilbrandt, T. Bein, *Angew. Chem. Int. Ed.*, **38**, 2891-2894 (1999).

[169] Y. Song, J. Yu, M. Zhang, R. Xu, *Eur. J. Inorg. Chem.*, 3718-3723 (2004).

[170] S. Bauer, T. Bein, N. Stock, *Inorg. Chem.*, **44**, 5882-5889 (2005).

[171] S. Bauer, N. Stock, *Angew. Chem. Int. Ed.*, **46**, 6857-6860 (2007).

[172] S. N. Stock, T. Bien, *Solid State Sciences*, **5**, 1207-1210 (2003).

[173] R. J. Leeds, 'Doctoral Thesis, Heriot-Watt University' (2007).

[174] R. Gans, German Patent 197, 111 (1906); U.S. Patents 914, 405 (March 9, 1909), 943, 535 (Dec.. 14,1909); 1, 131, 503 (March 9, 1915)

[175] W. Kraus, G. Nozel, *Powder cell (version 2.4)*, (2000).

[176] TOPAS version 3 Bruker-AXS Inc. Madison, Wisconsin, USA (1999).

[177] D. A. Fletcher, R. F. McMeeking, D. J. Perkin, *J. Chem. Inf. Comput. Sci.*, **36**, 746-749 “The United Kingdom Chemical Database Service” (1996).

[178] PDF MaintEx Library, Version 9.0.1.33. (2007).

[179] Bruker X8 APEX 2, Version 1.0-8, Bruker-AXS Inc. Madison, Wisconsin, USA (2004).

[180] G. M. Sheldrick, SADABS, University of Göttingen, Germany (1996).

[181] A. Altomare, G. Cascarano, C. Gdi, M. C. Burla, G. Polidori, M. Carmeli, *J. Appl. Crystallogr. Sect. A.*, **27**, 435 (1994).

[182] D. J. Watkin, C. K. Prout, J. R. Carruthers, P. W. Betteridge, *Crystal Issue*, **10**, Chemical Crystallography Laboratory, University of Oxford, UK (1996).

[183] A. L. Spek, *Act. Cryst. A*, **46**, C34 (1990).

[184] W. W. Wendlant, H. G. Hecht, 'Reflectance spectroscopy', Ed. John Wiley and Sons, London (1966).

[185] H.-H. Perkampus, 'UV-VIS Spectroscopy and Its Applications', Ed. Springer-Verlag, New York (1992).

[186] S. I. Boldish, W. B. White, *Amer. Mineral.*, **83**, 865-871 (1998).

[187] S. P. Tandom, J. P. Gupta, *Phys. Stat. Sol.*, **38**, 363-367 (1970).

[188] D. Dollimore, G. P. Heal, *J. Colloid Interface Sci.*, **33**, 508 (1970).

[189] M. Marezio, J. P. Remeika, *J. Chem. Phys.*, **46**, 1862-1865 (1967).

[190] C. L. Cahill, Y. Ko, J. B. Parise, *Chem. Mater.*, **10**, 19-21 (1998).

[191] K. Nakanishi, T. Goto, M. Ohashi, *Infrared Spectra of Organic Compounds*, **30**, 403-408 (1957).

[192] M. Springford, *Proc. Phys. Soc.*, **82**, 1020-1028 (1963).

[193] X. Huang, J. Li, *J. Am. Chem. Soc.*, **122**, 8789-8790 (2000).

[194] A. N. Platonov, A. S. Marfunin, *Geochem. Int.*, **5**, 245-259 (1968).

[195] ATOMS v6.3.1, shape software (2006).

[196] J. R. Anderson, K. C. Pratt, 'Introduction to characterisation and testing of catalyst', Academic Press Australia (1985).

[197] H. H. Lee, 'Heterogeneous reactor design', Butterworth-Heinemann Ltd. (1985).

[198] I. M. S. Terminology, *Pure Appl. Chem.*, **31**, 578 (1972).

[199] X. Bu, N. Zheng, P. Feng, *Chem. Eur. J.*, **10**, 3356-3362 (2004).

[200] M. J. Manos, R. G. Iyer, E. Quarez, J. H. Liao, M. G. Kanatzidis, *Angew. Chem. Int. Ed.*, **44**, 3552-3555 (2005).

[201] H. S. Sherry, *J. Phy. Chem.*, **70**, 1158-1168 (1966).

[202] R. Kitaura, K. Seki, G. Akiyama, S. Kitagawa, *Angew. Chem. Int. Ed.*, **42**, 428-431 (2003).

[203] K. Seki, *Phys. Chem. Chem Phys.*, **4**, 1968-1971 (2002).

[204] A. Bondi, *J. Phys. Chem.*, **68**, 441-451 (1964).

[205] C. Janiak, *J. Chem. Soc., Dalton Trans.*, 3885-2896 (2000).

[206] R. M. Silverstein, G. C. Bassler, T. C. Morril, 'Spectrometric identification of organic compounds', John Wiley & Sons, Inc. (1981).

[207] T. L. Gilchrist, U. Linpel, *'Heterocyclic Chemistry'*, Ed. John Wiley and sons, 3rd edition (1992).

[208] G. B. Deacon, R. A. Jones, P. E. Rogash, *Australian Journal of Chem.*, **16**, 360-379 (1963).

[209] Q. Zhang, T. Wu, X. Bu, T. Tran, P. Feng, *Chem. Mater.*, **20**, 4170-4172 (2008).

[210] N. W. Alcock, P. R. Barker, J. M. Hannon, C. L. Paiting, Z. Pikramenou, E. A. Plummer, K. Rissanen, P. Saarenketo, *J. Chem. Soc., Dalton Trans.*, 1447-1461 (2000).

[211] J.-J. Wang, L.-F. Yan, Z.-X. Li, Z. Chang, T.-L. Hu, X.-H. Bu, *Inorg. Chim. Acta*, **362**, 3147-3154 (2009).

[212] G. Che, J. Wang, C. Liu, X. Li, B. Liu, J. Sun, Y. Liu, L. Lu, *Inorg. Chim. Acta*, **362**, 2756-2761 (2009).

[213] S. De, M. G. B. Drew, N. Aliaga-Alcalde, D. Datha, *Inorg. Chim. Acta*, **362**, 2879-2883 (2009).

[214] L. Han, M. Hong, *Inorg. Chem. Comm.*, **8**, 406-419 (2005).

[215] T. Ezuhuara, K. Endo, Y. Aoyama, *J. Am. Chem. Soc.*, **121**, 3279-3283 (1999).

[216] J.-P. Zhang, Y.-Y. Lin, X.-C. Huang, X.-M. Chen, *Chem. Comm.*, 1258-1260 (2005).

[217] R. M. Silvestein, G. C. Bassler, T. C. Morril, *Spectrometric identification of organic compounds*, John Wiley & Sons, Inc. (1981).

[218] M. Melullis, R. Clerac, S. Dehnen, *Chem. Commun.* , 6008-6010 (2005).

[219] L. Han, H. Valle, X. Bu, *Inorg. Chem.*, **46**, 1511-1513 (2007).

[220] L. Carlucci, G. Ciani, D. W. Gudeberg, D. M. Proserpio, *Inorg. Chem.*, **36**, 3812-3813 (1997).

[221] J. Li, Z. Chen, R.-J. Wang, D. M. Proserpio, *Coord. Chem. Rev.*, **190-192**, 707-735 (1999).

[222] A. R. Katritzky, Ed. Academic Press, New York (1963).

[223] M. R. Chkrabarty, C. S. Handloser, M. W. Mosher, *J.C.S. Perkin II*, 938-942 (1972).

[224] Q. Zhang, X. Bu, Z. Lin, P. Feng, *Inorg. Chem.*, **47**, 9724-9726 (2008).

[225] S. M. Shi, W. Qian, G. H. Li, L. Wang, H. M. Yuan, J. N. Xu, G. S. Zhu, T. Y. Song, S. L. Qiu, *J. Solid State Chem.*, **177**, 3038-3044 (2004).

[226] S. Fernandez-Armas, J. L. Mesa, J. L. Pizarro, M.-C. Chung, M. J. Arriortua, T. Rojo, *J. Solid State Chem.*, **178**, 3554-3562 (2005).

[227] D. Schmitz, W. Bronger, *Z. Naturforsch. B*, **B30**, 491-493 (1975).

[228] B. Eissenmann, A. Hoffmann, *Z. fuer Kristallogr.*, **197**, 143-144 (1991).

[229] K. O. Klepp, *Z. fuer Naturforschung*, **B47**, 937-941 (1992).

[230] R. G. Kostyanovsky, F. A. Lakhvich, P. M. Philipchenko, D. A. Lenev, V. Y. Torbeev, K. A. Lyssenko, *Mendeleev Commun.*, 147-149 (2002).

[231] L. Fan, H. Song, H. Zhao, G. Pan, H. Yu, X. Bai, S. Li, Y. Lei, Q. Dai, R. Qin, T. Wang, B. Dong, Z. Zheng, X. Ren, *J. Phys. Chem.*, **100**, 13226-13239 (1996).

[232] A. Nazzal, H. Fu, *Phys. Rev. B*, **72**, 075202 (2005).

[233] M. M. J. Treacy, J. M. Newsam, M. W. Deem, *Proc. R. Soc. London A*, **433**, 499-520 (1991).

[234] J. M. Cowley, *Acta Crystallogr. A*, **32**, 83-87 (1976).

[235] J. M. Cowley, *Acta Crystallogr. A*, **32**, 88-91 (1976).

[236] J. M. Cowley, A. Y. Au, *Acta Crystallogr. A*, **34**, 738-743 (1978).

[237] A. Puls, M. Schaefer, C. Näther, W. Bensch, A. V. Powell, S. Boissière, A. M. Chippindale, *J. Solid State Chem.*, **178**, 1171-1181 (2005).

[238] X. Wang, Y. Li, *J. Am. Chem. Soc.*, **124**, 2880-2881 (2002).

[239] X. Chem, H. Xu, N. Xu, F. Zhao, W. Lin, Y. Fu, Z. Huang, H. Wang, M. Wu, *Inorg. Chem.*, **44**, 3100-3106 (2003).

[240] M. Cote, M. L. Cohen, D. Chadi, *58*, **J. Phys. Rev., B**, 4277-4279 (1998).

[241] X. Huang, H. R. H. IV, V. Le, J. Li, *Chem. Mater.*, **13**, 3754-3759 (2001).

[242] A. Philippidis, T. Bakasb, P. N. Trikalitis, *Chem. Commun.*, 1556 - 1558 (2009).

[243] G. J. Long, P. J. Clark, *Inorg. Chem.*, **17**, 1394-1401 (1978).

[244] S. A. Bourne, M. Kilkenny, L. R. Nassimbeni, *J.Chem.Soc.,Dalton Trans.*, 1176-1179 (2001).

[245] G. S. Matouzenko, G. Molnar, N. Brefuel, M. Perrin, A. Bousseksou, S. A. Borshch, *Chem. Mater.*, **15**, 550-556 (2003).

[246] G. S. Matouzenko, M. Perrin, B. L. Guennic, C. Genre, G. Molnár, A. Bousseksou, S. Borsh, *Dalton Trans.*, 934-942 (2007).

[247] D. Mandon, A. Machkour, S. Goetz, R. Welter, *Inorg. Chem.*, **41**, 5364-5372 (2002).

[248] H. Xu, Y. Song, L. Mi, H. Hou, M. Tang, Y. Sang, Y. Fan, Y. Pan, *Dalton Trans.*, 838-845 (2006).

[249] I. Bernal, I. M. Jensen, K. B. Jensen, C. J. McKenzie, H. Toftlund, J. P. J. Tuchagues, *Chem. Soc., Dalton Trans.* , 3667-3675 (1995).

[250] K.-T. Youm, J. Ko, M.-J. Jun, *Polyhedron*, **25**, 2717-2720 (2006).

[251] T. J. Prior, M. J. Rosseinsky, *Chem. Commun.*, 495-496 (2001).

[252] J. C. MacDonald, P. C. Dorresten, M. M. Pelley, M. M. Foote, J. L. Lundburgh, R. W. Henning, A. J. Schultz, J. L. Manson, JACS, 122, , *J. Am. Chem. Soc.*, **122**, 11692-11702 (2000).

[253] J. A. Real, A. B. Gaspar, V. N. Niel, M. C. Munoz, *Coord. Chem. Rev.*, **236**, 121-141 (2003).

[254] T. Morita, S. Nakashima, K. Yamada, K. Inoue, *Chem. Lett.*, **35**, 1042-1043 (2006).

[255] R. Jooss, A. Kult, A. Lentz, L. Wals, *Z. fuer Kristallographie*, **210**, 766-768 (1995).

[256] M. S. Laesndy, X. Huang, R.-J. Wang, J. Li, J. Y. Lu, *Inorg. Chem.*, **38**, 5410-5414 (1999).

[257] M. Atsuchi, H. Higashikawa, Y. Yoshida, S. Nakashima, K. Inoue, *Chem. Lett.*, **36**, 1064-1065 (2007).

[258] H.-L. Sun, S. Gao, B.-Q. Ma, S. R. Batten, *Cryst. Eng. Comm*, **6**, 579-583 (2004).

[259] J. A. Real, A. B. Gaspar, M. C. Mun˜oz, *Dalton Trans.*, 2062-2079 (2005).

[260] D. F. Shriver, P. W. Atkins, 'Inorganic Chemistry', 3rd edition, Oxford University Press (2001).

[261] T. Zielinski, J. Jurczak, *Tetrahedron*, **61**, 4081-4089 (2005).

[262] L. S. Rao, B. K. Gupta, *Pramana*, **9**, 349-355 (1977).

[263] H.-J. Lee, Y.-S. Choi, K.-B. Lee, J. Park, C.-J. Yeem, *Phys. Chem. A*, **106**, 7010-7017 (2002).

[264] A. Michta, E. Chelmecka, H. Nowack, J. Kusz, *Acta Cryst. C.*, **64**, 411-413 (2008).

[265] R. H. Judge, D. C. Moule, *Can. J. Chem.*, **65**, 2100-2105 (1987).

[266] H. Takahata, T. Yamazaki, *Heterocycles*, **27**, 1953-1973 (1988).

[267] R. N. Hurd, G. T. Delamater, *Chem. Rev.*, **61**, 45-86 (1961).

[268] K. Kindler, *Liebigs Ann. Chem.*, **431**, 187-230 (1923).

[269] H. Z. Lecher, R. A. Greenwood, K. C. Whitehouse, T. H. Chao, *J. Am. Chem. Soc.*, **78**, 5018-5022 (1956).

[270] B. Kaboudin, D. Elhamifar, *Synthesis*, 224-226 (2006).

[271] R. S. Varma, D. Kurma, *Org. Lett.*, **1**, 697-700 (1999).

[272] Z. Kaleta, B. T. Makowski, T. Soos, R. Dembiski, *Org. Lett.*, **8**, 1625-1628 (2006).

[273] O. I. Zubruyev, N. Stiasni, C. O. Kappe, *J. Comb. Chem.*, **5**, 145-148 (2003).

[274] U. Kazmaier, S. Ackermann, *Org. Biomol. Chem.*, **3**, 3184-3187 (2005).

[275] T. S. Piper, A. G. Karipides, *J. Am. Chem. Soc.*, **86**, 5039-5040 (1964).

[276] C. Pariya, F.-L. Liao, S.-L. Wang, C.-S. Chung, *Polyhedron*, **17**, 547-554 (1998).

[277] S. E. Harnung, B. S. Sørensen, I. Creaser, H. Maegaard, U. Pfenninger, C. E. Schäffer, *Inorg. Chem.*, **15**, 2123-2126 (1976).

[278] S. Sato, Y. Saito, *Acta Crystallogr. B*, **33**, 860-865 (1977).

[279] A. Kobayashi, F. Marumo, Y. Saito, *Acta Crystallogr. B*, **28**, 2709-2715 (1972).

[280] M. Morooka, S. Ohba, Y. Saito, H. Miyamare, *Acta Crystallogr. B*, **47**, 910-917 (1991).

[281] R. J. Angelici, 'Synthesis and technique in Inorganic Chemistry', Saunders: Philadelphia (1969).

[282] R. E. Davis, H. F. Nakshbendi, *J. Am. Chem. Soc.*, **84**, 2079-2090 (1961).

[283] D. G. Crosby, R. V. Berthold, *J. Org. Chem.*, **25**, 1916-1919 (1960).

[284] J. P. Shoffner, L. Bauer, C. L. Bell, *J. Heterocycl. Chem.*, **7**, 487-490 (1970).

[285] D. E. O'Brien, L. T. Weistock, R. H. Springer, C. C. Cheng, *J. Heterocycl. Chem.*, **4**, 49-53 (1967).

[286] Y. Kubota, M. Kodaka, T. Tomohiro, H. Okuno, *J. Chem. Soc. Perkin Trans.*, **1**, 5-6 (1993).

[287] H. Matsuda, A. Baba, R. Nomura, M. Kori, S. Ogawa, *Ind. Eng. Chem. Prod. Res. Dev.*, **24**, 239-242 (1985).

[288] R. Nomura, M. Yamamoto, H. Matsura, *Ind. Eng. Chem. Res.*, **26**, 1056-1059 (1987).

[289] K. Tominaga, Y. Sasaki, *SynLett.*, 307-397 (2002).

[290] J. F. Mulvaney, R. L. Evans, *Ind. Eng. Chem.* , **40**, 393-397 (1948).

[291] F. Fichter, B. Becker, *Ber. Dtsch. Chem. Ges.*, **44**, 3473-3480 (1911).

[292] F. Fichter, B. Becker, *Ber. Dtsch. Chem. Ges.*, **44**, 3481-3485 (1911).

[293] B. M. Bhanage, S.-I. Fujita, Y. Ikushima, M. Arai, *Green Chemistry*, **5**, 340-342 (2003).

[294] J. Janczak, M. Sledz, R. Kubiak, *J. of Molecular Structure*, **659**, 71-79 (2003).

[295] B. F. Abrahams, S. R. Batten, M. J. Grannas, H. Hamit, B. F. Hoskins, R. Robson, *Angew. Chem. Int. Ed.* , **38**, 1475 -1477 (1999).

[296] S. R. Batten, B. F. Hoskins, B. Moubaraki, K. S. Murray, R. Robson, *Chem. Commun.*, 1095 -1096 (2000).

[297] M. X. Li, Z. X. Miao, M. Shao, S-W. Liang, S.-R. Zhu, *Inorg. Chem.*, **47**, 4481-4489 (2008).

[298] J. A. Joule, K. Mills, 'Heterocyclic Chemistry' 4th ed. Ed. Blackwell Science, Oxford (1992).

[299] F. W. Schaefer, G. A. Peters, *J. Org. Chem.*, **26**, 2778-2784 (1961).

[300] C. Chen, R. Daguino, J. R. McCarthy, *J. Org. Chem.*, **60**, 8428-8430 (1995).

[301] F. H. Case, E. Koft, *J. Am. Chem. Soc.*, **81**, 905-906 (1959).

[302] C. M. Fitchett, C. Richardson, P. J. Steel, *J. Org. Biomol. Chem.*, **3**, 498-502 (2004).

[303] O. N. Chupakhin, E. O. Sidorov, S. M. Shein, I. I. Bil'kis, *Zh. Org. Khim.*, **12**, 2464-2468 (1976).

[304] M. L. Castellanos, S. Oliveira, N. Roca, J. d. Mendoza, J. Elguero, *Can. J. Chem.*, **62**, 687-695 (1984).

[305] S. P. Singh, D. Kumar, D. Kumar, A. Martinez, J. Elguero, *J. Heterocycl. Chem.*, **33**, 323-326 (1996).

[306] C. Kaes, A. Katz, M. W. Hosseini, *Chem. Rev.*, **100**, 3553-3590 (2000).

[307] G. R. Newkome, A. K. Patri, E. Holder, U. S. Schubert, *Eur. J. Org. Chem.* , 235-254 (2004).

[308] P. J. Steel, *Adv. Heterocycl.*, **67**, 1-117 (2004).

[309] S. Neeraj, S. Natarajan, C. N. R. Rao, *Angew. Chem. Int. Ed.*, **38**, 3480-3483 (1999).

[310] J. Zhou, J. Dai, G.-Q. Bian, C.-Y. Li, *Coord. Chem. Rev.*, **253**, 1221-1247 (2009).

[311] K. S. Park, Z. Ni, A. P. Côte, J. Y. Choi, R. Huang, F. J. Uribe-Romero, H. K. Chae, M. O'Keeffe, O. M. Yaghi, *PNAS*, **103**, 10186-10191 (2006).

[312] B. Wang, A. P. Côte, H. Furukawa, M. O'Keeffe, O. M. Yaghi, *Nature*, **453**, 207-211 (2008).

[313] R. Banerjee, A. Phan, B. Wang, C. Knobler, H. Furukawa, M. O'Keeffe, O. M. Yaghi, *Science*, **319**, 939-943 (2008).